DEVELOPMENT OF MOLECULAR CATALYSTS FOR FUEL CELL APPLICATIONS

by

Jennifer Wood Eddy

A dissertation submitted to the Faculty of the University of Delaware in partial fulfillment of the requirements for the degree of Doctor of Philosophy in Chemistry and Biochemistry

Spring 2017

DEVELOPMENT OF MOLECULAR CATALYSTS

FOR FUEL CELL APPLICATIONS

by

Jennifer Wood Eddy

Approved: _____

Murray V. Johnston, Ph.D.
Chair of the Department of Chemistry and Biochemistry

Approved: _____

George H. Watson, Ph.D.
Dean of the College of Arts and Sciences

Approved: _____

Ann L. Ardis, Ph.D.
Senior Vice Provost for Graduate and Professional Education

I certify that I have read this dissertation and that in my opinion it meets the academic and professional standard required by the University as a dissertation for the degree of Doctor of Philosophy.

Signed: _____

Joel Rosenthal, Ph.D.
Professor in charge of dissertation

I certify that I have read this dissertation and that in my opinion it meets the academic and professional standard required by the University as a dissertation for the degree of Doctor of Philosophy.

Signed: _____

Donald A. Watson, Ph.D.
Member of dissertation committee

I certify that I have read this dissertation and that in my opinion it meets the academic and professional standard required by the University as a dissertation for the degree of Doctor of Philosophy.

Signed: _____

Charles G. Riordan, Ph.D.
Member of dissertation committee

I certify that I have read this dissertation and that in my opinion it meets the academic and professional standard required by the University as a dissertation for the degree of Doctor of Philosophy.

Signed: _____

Andrea E. Martin, Ph.D.
Member of dissertation committee

ACKNOWLEDGMENTS

Foremost, I would to thank my advisor, Professor Joel Rosenthal, whose guidance and support over the last several years has enabled me to become a better presenter, independent thinker and inspired researcher. He is clearly passionate about science, and it has been a great opportunity to be a member of his laboratory. I would also like to thank my thesis committee members, Professor Donald Watson, Professor Charles Riordan, and Professor Andrea Martin for their time, encouragement, feedback and insightful comments.

I would like to thank the members of the Rosenthal research lab, especially during my time as a new lab member, for their help and support. The opportunity to work in a collaborative and supportive environment was essential to my progress during my graduate studies. I would also like to thank my undergraduate research advisor, Dr. Felix Goodson, for inspiring me to pursue my graduate studies, and for his continued support and guidance over the years.

Finally, I would like to thank my parents, Richard and Lori Eddy, for their constant love and encouragement through my academic journey. And of course my husband, Dino, for his patience, love, support, understanding, guidance, and encouragement; this journey would not have been possible without you.

This thesis document is dedicated to my mother-in-law, Nagamani Gnanamgari.

TABLE OF CONTENTS

LIST OF TABLES

LIST OF FIGURES

LIST OF SCHEMES

ABSTRACT

Formic acid has been proposed as a hydrogen storage medium; however, this necessitates efficient and selective catalysts for the dehydrogenation of formic acid to produce H_2 and CO_2. Consequently, we have developed palladium based complexes supported by chelating bis-N-heterocyclic carbene (NHC) ligands and probed the activity of such complexes for the dehydrogenation of formic acid. The formic acid dehydrogenation properties of $[(MDC^{Mes})Pd(MeCN)_2](PF_6)_2$ in MeCN with triethylamine additive were monitored using water displacement and gas chromatography to show a 1:1 ratio of CO_2:H_2 production with no detection of CO, and a modest turnover frequency (TOF, 325 h^{-1}) and turnover number (TON, 185). The $[(MDC^{Mes})Pd(MeCN)_2](PF_6)_2$ catalyst was used under relatively mild conditions and is the first example of a homogenous palladium catalyst with any reasonable activity for formic acid dehydrogenation. The original catalyst motif was modified by changing either the NHC wingtip substituents or the coordinating ligands. This family of complexes was characterized by NMR spectroscopy, elemental analysis, and X-ray crystallography, and studied for formic acid dehydrogenation. The modified complexes were found to be less active than the parent catalyst.

From these initial studies, a mechanism was proposed and probed using several kinetic studies, including Eyring and Arrhenius analyses. These studies supported the proposed mechanism and suggested that the opening of a coordination site on palladium for subsequent β-hydride elimination was the rate determining step of H_2 liberation. Based on the proposed mechanism, the reaction system with

$[(MDC^{Mes})Pd(MeCN)_2](PF_6)_2$ as catalyst was further optimized by changing the base from triethylamine to Hünig's base. The initial TOF for the reaction with Hünig's base was determined to be 414 h^{-1} and the total TON was increased to 353. Additionally, formic acid could be added up to 18 times with catalytic activity.

The $4e^-/4H^+$ reduction of oxygen to water is an important reaction that takes place at the cathode of fuel cells; therefore, catalysts that are selective for this reaction are highly desired. The calix[4]phyrin is a tetrapyrrole macrocycle that exhibits unique properties due to the incorporation of two sp^3 hybridized *meso* carbons. We wished to explore these unique macrocycles and corresponding metal complexes with the goal of applications to catalysis, in particular the oxygen reduction reaction (ORR). The freebase calix[4]phyrin was synthesized by modifying a streamlined procedure for tetrapyrrole macrocycle synthesis previously utilized in our laboratory for the related phlorin macrocycle. The freebase calix[4]phyrin macrocycle was then metalated to give the corresponding zinc, copper, nickel and cobalt complexes. These metal complexes were characterized using a variety of methods, including X-ray crystallography, UV-vis spectroscopy, differential pulse voltammetry and cyclic voltammetry.

The cobalt calix[4]phyrin was studied as a catalyst for the ORR, both heterogeneously and homogeneously. The homogeneous ORR was monitored using UV-vis spectroscopy, and cobalt calix[4]phyrin was found to catalyze the reduction of O_2 to give approximately 50% water production (n = 3). A series of kinetic studies were also performed by varying the concentration of each species in solution, and from these studies a mechanism was proposed. The ORR with cobalt calix[4]phyrin was studied heterogeneously using rotating ring-disk electrode electrochemistry. By

using Koutecky-Levich analysis, cobalt calix[4]phyrin was found to reduce O_2 with 2.9 electron equivalents transferred under electrochemical conditions, which corresponds to ~50% water production. This selectivity for water production is promising for a monomeric cobalt complex. Initial attempts were made to further optimize the cobalt calix[4]phyrin using a hangman scaffold, however these modifications did not increase the selectivity as compared to the parent compound.

Chapter 1

INTRODUCTION

1.1 World Energy Consumption

World energy consumption has increased dramatically over the past half century and will continue to rise over the next 50 years. The Energy Information Administration estimates that global energy usage in 2012 was 18.4 TW and projects an increase of energy usage to 27 TW by 2040.[1,2] Some predictions are even more drastic with a doubling of the current energy usage by 2050 and tripling by the end of the 21st century.[3] This dramatic increase in energy demand is due to rising population levels with an increase to approximately 10 billion people by 2050.[3] This correlation between population levels and energy usage is exacerbated by population growth in emerging economies: as prosperity increases in these countries so does consumer consumption and, consequently, energy usage.[4]

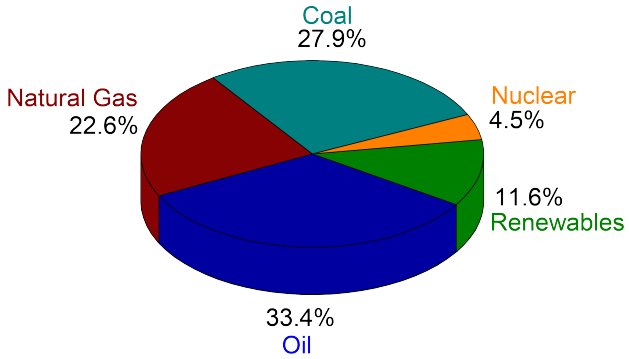

Figure 1.1: World Energy Profile, 2012[1]

Currently, our energy profile consists mainly of coal, oil and natural gas (Figure 1.1).[1,4] Even with increased use of alternative energy sources, predictions show fossil fuels to be the predominant source of energy, comprising approximately three quarters of total energy supplies in 2035.[4] As our fossil fuel consumption has increased, there has been a similar increase in the concentration of carbon dioxide in the atmosphere ($[CO_{2atm}]$), from 296 ppmv at the beginning of the last century to the benchmark 400 ppmv in 2015 (Figure 1.2).[5] This is the highest the $[CO_{2atm}]$ has been over the past 670,000 years.[6] As carbon emissions increase over the next few decades,[1,4] within 40 years, $[CO_{2atm}]$ will be over double its pre-industrial levels.[7] This dramatic increase in $[CO_{2atm}]$ has been shown to be caused by anthropogenic activities, largely from fossil fuel consumption.[3,7-9]

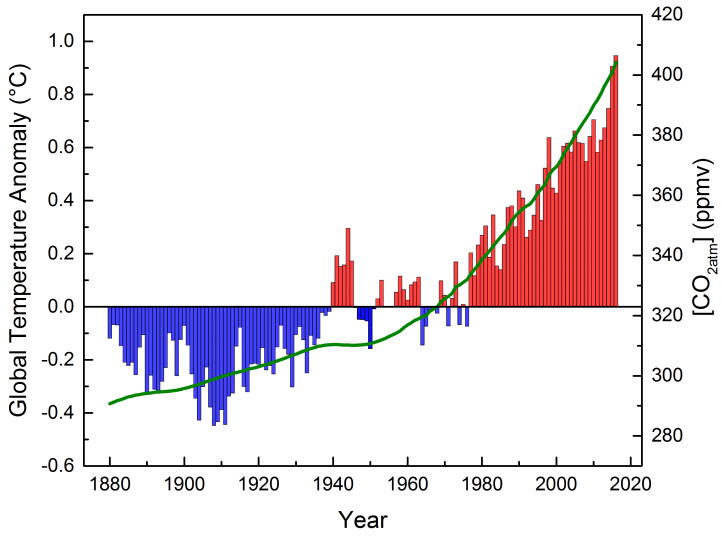

Figure 1.2: Global land and ocean temperature anomaly (°C, departure from 20th century average) with red bars indicating temperatures warmer than the average and blue bars cooler than the average temperature[10] and the carbon dioxide concentration in the atmosphere (green line)[5]

Furthermore, over the last several decades there has been a dramatic increase in the yearly average global temperature, which mirrors a rise in the carbon dioxide levels in the atmosphere (Figure 1.2).[11,12] Critical concerns as a result of global warming and overall climate change[13] caused by human influence are abrupt changes to glaciers, ice sheets, sea ice, oceanic flows and terrestrial ecosystems;[14-16] sea level rise;[15,16] extreme weather events including rainfall reductions leading to irreversible dry seasons and drought;[15-17] and loss of biodiversity.[16] The distribution of the impact of these critical concerns is an important consideration, as well as the monetary damages and lives affected by the events.[17]

These concerns are all projected for warming levels below 2 °C.[14] The Paris Agreement states as one of its objectives to halt the increase in global average temperature to approximately 1.5 °C above pre-industrial levels, in order to decrease the risk and impacts of climate change.[18] This objective can only be fulfilled by transitioning towards renewable, carbon neutral energy sources and away from fossil fuels on a global scale as soon as possible.[3,8,12] Furthermore, this transition is necessary for the United States to provide geopolitical and economic security, as renewable energy sources are typically widely distributed.[3]

1.1.1 The Hydrogen Economy

Hydrogen is desirable as an energy source since it does not contain carbon and the combustion of hydrogen produces no toxic products.[19-21] Hydrogen is also desirable in geopolitical terms as it is accessible around the globe. However, hydrogen is not found in nature as its diatomic gaseous form, H_2. Hydrogen is a secondary energy carrier, similar to electricity, and therefore needs to be produced from a natural source. Currently, the most common method of hydrogen production is steam

reforming from natural gas. Thus, in order to eliminate the use of fossil fuels from the hydrogen economy, methods are being developed to efficiently produce hydrogen from renewable resources.[20-23] These new methods include using solar energy coupled to the splitting of water for H_2 production, which would provide an alternative energy feedstock. Hydrogen has the advantage over electricity in that it can store energy, rather than having to be produced and used immediately. Two of the major obstacles for implementing a hydrogen economy on a large scale are the storage and transportation of hydrogen, and fuel cell efficiencies and cost.

1.2 Hydrogen Storage

One of the most promising applications of H_2 fuel is in transportation. In order for H_2 to be a useful transportation fuel, hydrogen storage needs to be further developed and optimized. In addition to the environmental and geopolitical benefits mentioned above, H_2 is also desirable as fuel since it contains more energy than any other known fuel based on mass, with an energy density of 33.3 $kWh \cdot kg^{-1}$.[21] However, H_2 has a very low energy density based on volume. This is true even with the most advanced methods for hydrogen storage of compression and liquefaction, which have volumetric energy densities of 0.53 $kWh \cdot L^{-1}$ (200 bar) and 2.37 $kWh \cdot L^{-1}$, respectively;[21] furthermore, these values exclude the weight and volume of the container. These values are especially low when compared to the volumetric energy density of commonly used fossil fuels, such as gasoline (9.5 $kWh \cdot L^{-1}$) and coal (7.6 $kWh \cdot L^{-1}$). Storage of H_2 in liquid form also requires severe energy costs (40%) to reach the required low temperatures.[20] Therefore, several different types of hydrogen storage materials are currently being developed to overcome these limitations. In general, solid hydrogen storage materials can be placed in two different categories:

highly porous solids that physically absorb molecular H_2 (physisorption), and metal hydrides and related compounds that store hydrogen through chemical bonds.[22-26] Both categories have disadvantages: first, since physisorption is based on weak van der Waals forces, the storage capacity of porous solids at room temperature is limited, requiring low temperatures for any reasonable storage capacity. Second, metal hydrides have a relatively high stability and therefore either require high temperatures for H_2 release or lack reversibility altogether. In addition to H_2 storage in solid materials, H_2 can also be stored in liquid hydrocarbons, such as formic acid (HCOOH, Scheme 1.1).

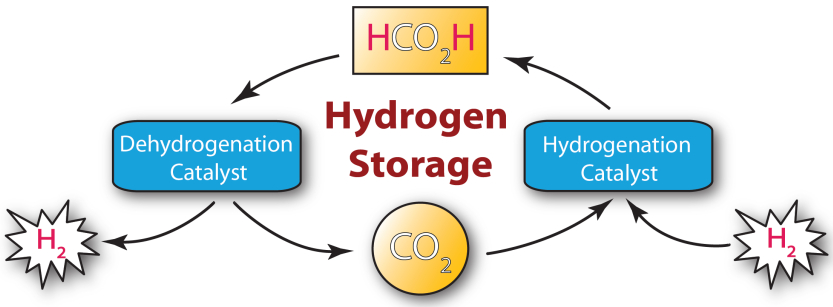

Scheme 1.1: Hydrogen storage system with formic acid

Formic acid (FA) has several advantages as a hydrogen storage material, the most prominent being the hydrogen content of formic acid (4.4 wt%) and the overall simplicity of the storage system. A general scheme for hydrogen storage using formic acid is shown in Scheme 1.1. In the first step, formic acid is dehydrogenated to produce hydrogen for the desired application. Carbon dioxide is also produced;

however, CO_2 can be captured[27] and hydrogenated back to formic acid once hydrogen needs to be stored or transported. This creates an overall carbon neutral cycle.[28-32]

The dehydrogenation of formic acid to produce carbon dioxide and hydrogen is thermodynamically downhill (Scheme 1.2); however, formic acid can also decompose to produce carbon monoxide and water.[33] The latter reaction is especially undesired since carbon monoxide is known to poison the Pt catalyst at the anode of polymer electrolyte membrane (PEM) fuel cells.[28,29] Therefore, catalysts that are selective for the production of carbon dioxide and hydrogen are essential.

$$HCOOH \longrightarrow CO_2 + H_2 \quad \Delta G^\circ = -33\ kJ \cdot mol^{-1}$$

$$HCOOH \longrightarrow CO + H_2O \quad \Delta G^\circ = -21\ kJ \cdot mol^{-1}$$

Scheme 1.2: Thermodynamic parameters for formic acid decomposition to carbon dioxide and hydrogen (top) or carbon monoxide and water (bottom)[33]

1.2.1 Catalysts for Formic Acid Dehydrogenation

The most common metals used for homogeneous formic acid dehydrogenation catalysts are ruthenium, iridium and iron.[28-32,34] These catalysts are typically assessed using two different parameters: turnover number (TON) and turnover frequency (TOF). Both parameters give an indication of the activity of the catalyst. The TON typically describes the lifetime of the catalyst, and is defined as the moles of product divided by the moles of catalyst (equation 1.1). The TOF is defined as the TON per unit of time, typically per hour for formic acid dehydrogenation, and gives an indication of the rate of reaction within the first several minutes (equation 1.2).

$$\mathrm{TON} = \frac{\text{mol product}}{\text{mol catalyst}} \qquad 1.1$$

$$\text{TOF} = \frac{\text{TON}}{\text{time (hr)}} \qquad 1.2$$

One of the first catalysts to show good activity for formic acid dehydrogenation was $Ru_2(\mu\text{-CO})(CO)_4(\mu\text{-dppm})_2$ (where dppm = $Ph_2PCH_2PPh_2$) (Figure 1.3a).[35,36] This catalyst operates in acetone with a TOF of 500 h^{-1}; further studies showed pH to be an important criterion to overall reactivity. The Beller group[37] tested several in-situ generated catalysts using different ruthenium sources with the addition of various amines or phosphines. The combination of $RuBr_3 \cdot xH_2O$ with 3.4 equivalents of PPh_3 pretreated in DMF was found to dehydrogenate formic acid with a TOF of 3630 h^{-1} and a total TON of 1475 at 40 °C in the presence of triethylamine as base (Figure 1.3b). A hydrophilic ruthenium catalyst was generated in-situ using a water-soluble ligand, meta-trisulfonated triphenylphosphine (TPPTS) and $RuCl_3$ (Figure 1.3c), and was shown by the Laurenczy group[38] to produce hydrogen from a formic acid/sodium formate solution with a TOF of 460 h^{-1} at 120 °C and total TON of ~40,000. The commercially available $RuCl_2(PPh_3)_3$ catalyst (Figure 1.3d) pretreated in DMF was shown to give an excellent TOF (2688 h^{-1}) at 40 °C in an azeotropic mixture of formic acid and triethylamine.[39] One of the highest catalytic activities reported with ruthenium was for $RuCl_2(DMSO)_4$ with PPh_3, with a TOF of 18,000 h^{-1} at 120 °C in an azeotropic mixture of formic acid and triethylamine; however, some carbon monoxide was detected using this system.[40] Further analysis showed the active catalyst in this system to be an in-situ generated dimer of ruthenium with two bridging formates (Figure 1.3e). Finally, a ruthenium catalyst with a polydentate phosphine ligand, $[Ru(\kappa^3\text{-triphos})(MeCN)_3](OTf)_3$ (Figure 1.3f) showed

excellent TONs of 100,000 after 6 hours at 80 °C (TOF = 1000 h^{-1}); however, it required the use of n-octyldimethylamine as base for these activities.[41,42]

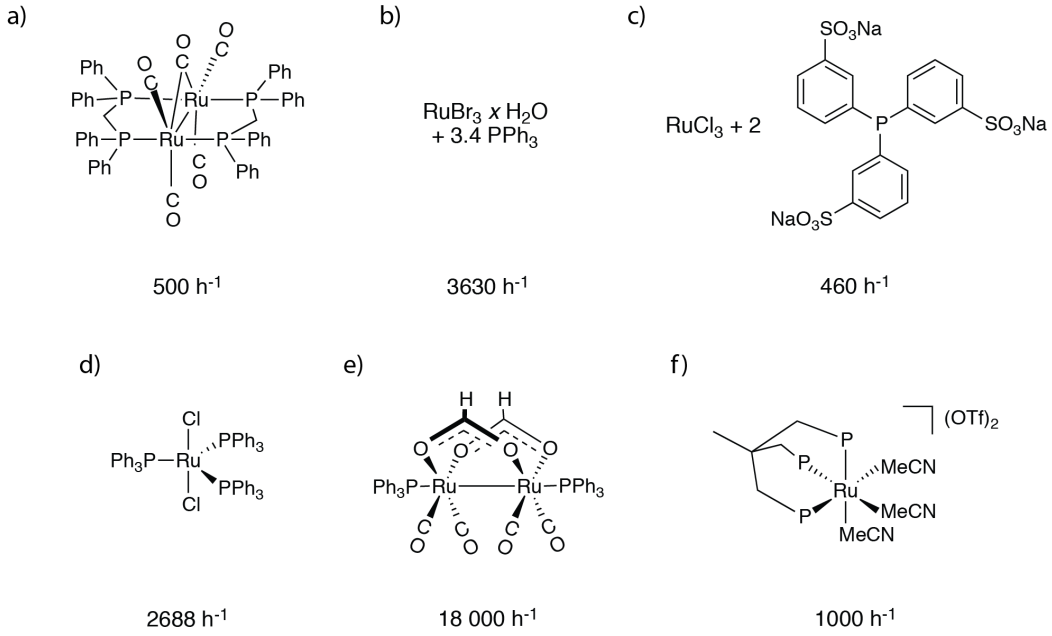

Figure 1.3: Homogeneous ruthenium catalysts for FA dehydrogenation with corresponding TOF

Iridium has also been shown to be very active for formic acid dehydrogenation. One of the initial studies to show iridium's superior activity was an iridium catalyst with bidentate 4,4'-dihydroxy-2,2'-bipyridine (dhpy) and pentamethyl cyclopentadienyl ligands (Cp*) ($[Ir^{III}(Cp^*)(dhpy)(H_2O)]SO_4$, Figure 1.4a). The aqueous formic acid dehydrogenation at 90 °C gave a TOF of 14,000 h^{-1}.[43] An iridium(III) trihydride catalyst with PNP-tridentate ligand developed by the Nozaki group (Figure 1.4b)[44] showed a TOF of 120,000 h^{-1} and a TON of 5,000 at 80 °C in *tert*-butanol with triethylamine as base. The highest TOF reported thus far for FA

dehydrogenation has been with a dinuclear Ir catalyst with 4,4',6,6'-tetrahydroxy-2,2' - bipyrimidine (thbpym) as a bridging ligand (Figure 1.4c). In an aqueous solution of formic acid and formate at 90 °C, an exceptional TOF of 228,000 h^{-1} was achieved.[45] Other interesting iridium based catalysts include an N-C cyclometallated iridium (III) catalyst developed from a 2-aryl imidazoline ligand (Figure 1.4d), which gave a TOF of 147,000 h^{-1} at 40 °C in an azeotropic mixture of formic acid and triethylamine.[46] This catalyst showed a unique long range metal-ligand bifunctional catalysis. Similarly, an iridium catalyst with a bifunctional ligand (bisMETAMORPhos, Figure 1.4e) showed good activity (TOF 3092 h^{-1} in toluene at 65°C) with the advantage that it could be used in base free conditions.[47]

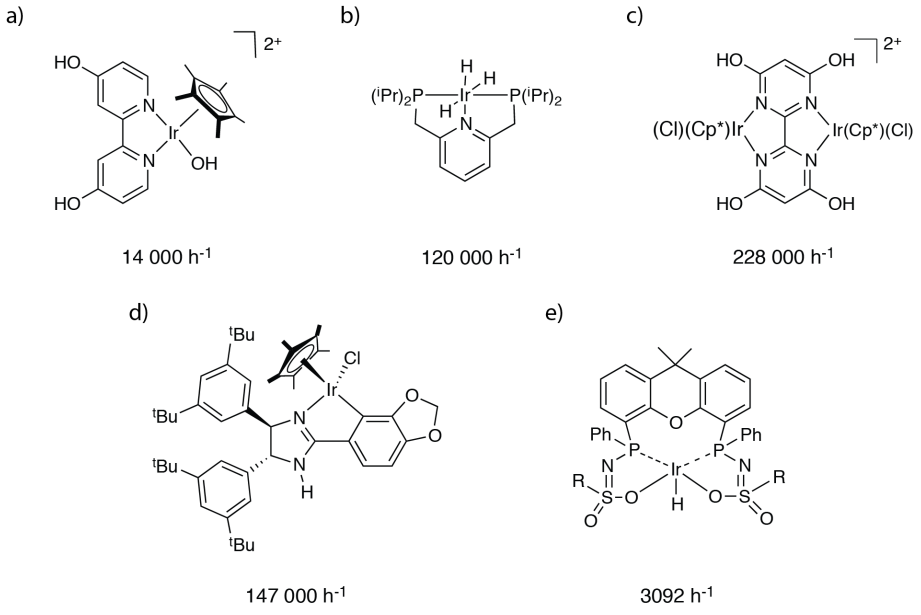

Figure 1.4: Homogeneous iridium catalysts for FA dehydrogenation with corresponding TOF

More recently, several iron complexes have also been shown to be promising catalysts for formic acid dehydrogenation. The first such example involved in-situ generated catalysts from various iron sources with the addition of phosphines and nitrogen based ligands, with the active catalyst determined to be $Fe(CO)_3(PPh_3)_2$. This catalyst gave a TOF of 200 h^{-1} at 60 °C (Figure 1.5a) in azeotropic formic acid and triethylamine. Irradiation with a lamp was also necessary for this activity and the addition of the nitrogen ligand tpy (6',6"-(phenyl)-2,2':6',2"-terpyridine, Figure 1.5a) was required to slow down deactivation of the catalyst.[48] From this initial finding with iron, further exploration by the Beller group gave even better activities by the catalyst generated in-situ from $Fe(BF_4)_2 \cdot 6H_2O$ and a tetradentate phosphine ligand, tris[(2-diphenylphosphino)ethyl phosphine, $(P(CH_2CH_2PPh_2)_3$, (Figure 1.5b). In propylene carbonate, this system produced a TOF of 9425 h^{-1} at 80 °C and an impressive TON of 92,000 without the need for additional base.[49] An iron catalyst with a PNP pincer ligand ([(^{t}Bu-PNP)$Fe(H)_2(CO)$], (^{t}Bu-PNP = 2,6-bis(di-*tert*-butyl phosphino-methyl)pyridine (Figure 1.5c), showed good TOF (836 h^{-1}) in THF with triethylamine as base[50] and TONs of up to 100,000. Another PNP pincer ($HN(CH_2CH_2(P^iPR_2)_2$) iron catalyst paired with a lewis acid co-catalyst (Figure 1.5d), produced a TOF of 196,728 h^{-1} in dioxane at 80 °C and the highest TON reported for a first row transition metal (1,000,000).[51]

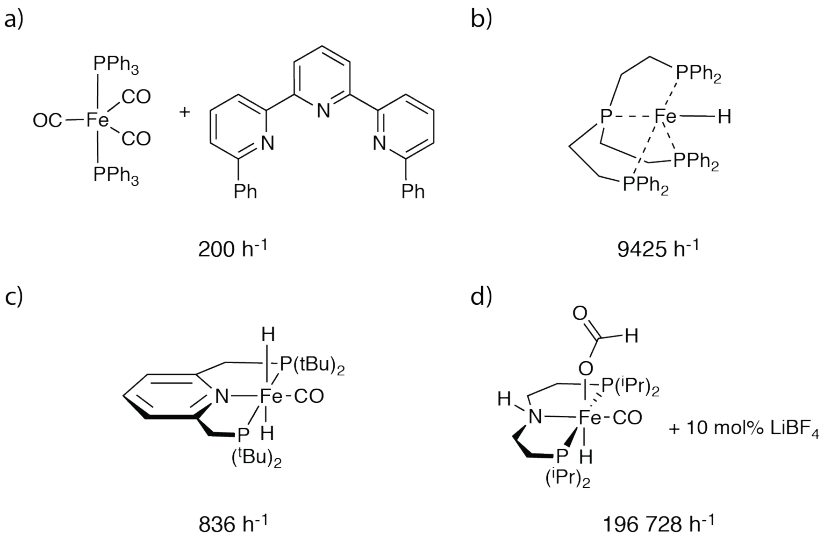

Figure 1.5: Homogeneous iron catalysts for FA dehydrogenation with corresponding TOF

Heterogeneous catalysts for formic acid dehydrogenation have been widely explored. However, these catalysts will only be briefly discussed below. A more thorough overview can be found in several excellent reviews on this topic.[29,30,34] The majority of heterogeneous formic acid dehydrogenation catalysts are supported mono-, bi-, or trimetallic nanoparticles with palladium as the main component. Dehydrogenation of formic acid using heterogeneous palladium catalysts was first studied in 1971, using Pd/C;[52] however, this catalyst was rather unselective for hydrogen production. Recently, more selective heterogeneous palladium catalysts have been developed.[53-55] The main disadvantage is that typically these heterogeneous catalysts are less active than their homogeneous counterparts, resulting in lower TOFs.

Chapters 2 and 3 discuss a unique homogeneous palladium catalyst with chelating N-heterocyclic carbene ligands for formic acid dehydrogenation. The

mechanism of the reaction with this homogeneous palladium catalyst was investigated and the reaction was further optimized with the use of a commercially available base.

1.3 Hydrogen Fuel Cells

Hydrogen can be used as a fuel for several different applications such as portable electronics, electricity and heat generation, and transportation. The latter is the most promising since hydrogen can be used efficiently in fuel cells to convert chemical energy to electrical energy.[19-21,56] By coupling a fuel cell to an electric motor, the chemical energy of H_2 can be converted without heat as an intermediate, which means that fuel cells are not limited by the Carnot cycle. This in turn means that fuel cell efficiencies (currently ~60% but theoretically higher) are fundamentally higher than internal combustion engine efficiencies (22% for gasoline and 45% for diesel).[20] Fuel cells generate electricity through the spatially separated oxidation of hydrogen fuel and reduction of oxygen from the air, which are continuously supplied to the cell (Figure 1.6). The polymer electrolyte membrane allows for the flow of ions between the electrodes, while the electrons are transported through an external load. The electrodes also provide a surface for the catalysts to facilitate the appropriate reaction.

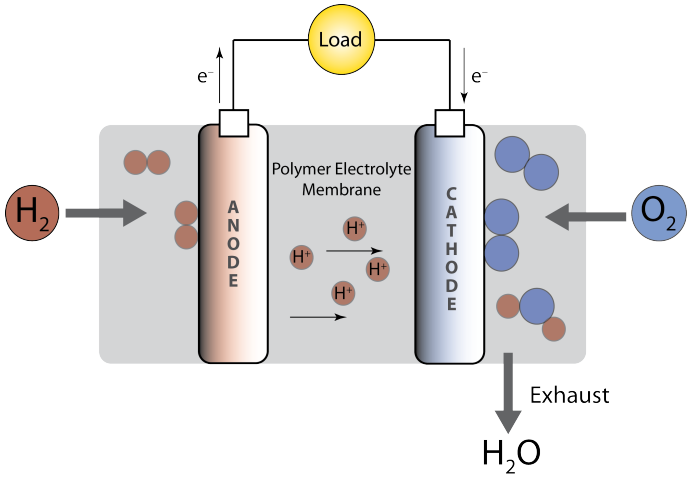

Figure 1.6: The polymer electrolyte membrane (PEM) hydrogen fuel cell

In a H_2 PEM fuel cell, hydrogen fuel is oxidized at the anode and oxygen is reduced at the cathode. Generally for fuel cells, different types of fuels besides H_2 can be used at the anode, but oxygen is always reduced at the cathode. The principal aspect limiting widespread implementation of fuel cells in transportation applications is the oxygen reduction reaction (ORR).[19,57] This is because the O=O bond is strong (498 kJ/mol), meaning activation of this bond is usually kinetically limiting.[19] Therefore, the selective 4 e^- and 4 H^+ reduction of oxygen is an important reaction that takes places at the cathode of fuel cells. Oxygen can also be reduced by 2 e^- and 2 H^+ to produce H_2O_2 (Scheme 1.3). Both reactions are energetically favorable but reduction to H_2O_2 squanders almost half a volt of energy (Scheme 1.4).[58] Additionally, H_2O_2 decomposes the Nafion electrolyte materials.[19] Consequently, catalysts that are selective for H_2O production are highly favorable. Currently, that catalyst is platinum nanoparticles supported on carbon black (Pt/C). Unfortunately, platinum is expensive and a high platinum loading is necessary for lower

overpotentials (a parameter indicative of energy efficiency) which limits the broad use and commercialization of fuel cells.[19,57] Hence, a major challenge is the design of inexpensive and efficient fuel cell catalysts at the cathode.

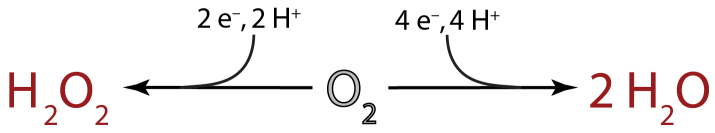

Scheme 1.3: Oxygen reduction by 4 e^- and 4 H^+ to water (right) or 2 e^- and 2 H^+ to hydrogen peroxide (left)

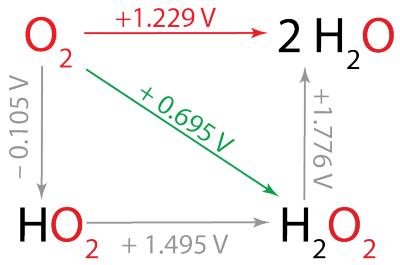

Scheme 1.4: Standard reduction potentials (E°) for oxygen in acidic solution[58,59]

1.3.1 Catalysts for Electrochemical Oxygen Reduction to Water

In the search for a more economical replacement of platinum at the cathode of fuel cells, cobalt catalysts have been promising, particularly cobalt porphyrins. In general, it is postulated that cobalt is active for this type of catalysis, because compared to other earth abundant metals, it has the most positive M^{II}/M^{III} redox potential while still being able to bind oxygen well.[56,60] The first example of a cobalt macrocycle to show activity for oxygen reduction was with cobalt phthalocyanine pressed on a nickel powder electrode, as reported by Jasinski in 1964.[61] However, this

catalyst was not necessarily selective for reduction of O_2 to H_2O. In fact, it has been generally shown that monomeric cobalt macrocycles, including cobalt porphyrins, are selective for the 2 e^-, 2H^+ reduction to hydrogen peroxide[62] and therefore are not good candidates for fuel cell applications.

Over the last several decades, it has been shown that cobalt macrocycles that are selective for reduction of O_2 to H_2O are cofacial bis(cobalt) diporphyrins.[56,58,62-65] Pioneering work by Collman[66-68] showed that a "face-to-face" porphyrin ([Co_2(FTF), Figure 1.7)] with flexible amide linkages, adsorbed on an EPG (edge plane graphite) electrode catalyzed the 4 e^-, 4 H^+ reduction of O_2 to H_2O (< 1% H_2O_2 production). It was found that this specific linkage motif was necessary, as changing the linking groups, metal centers, or metal-metal separation resulted in reduction of O_2 to undesired H_2O_2.

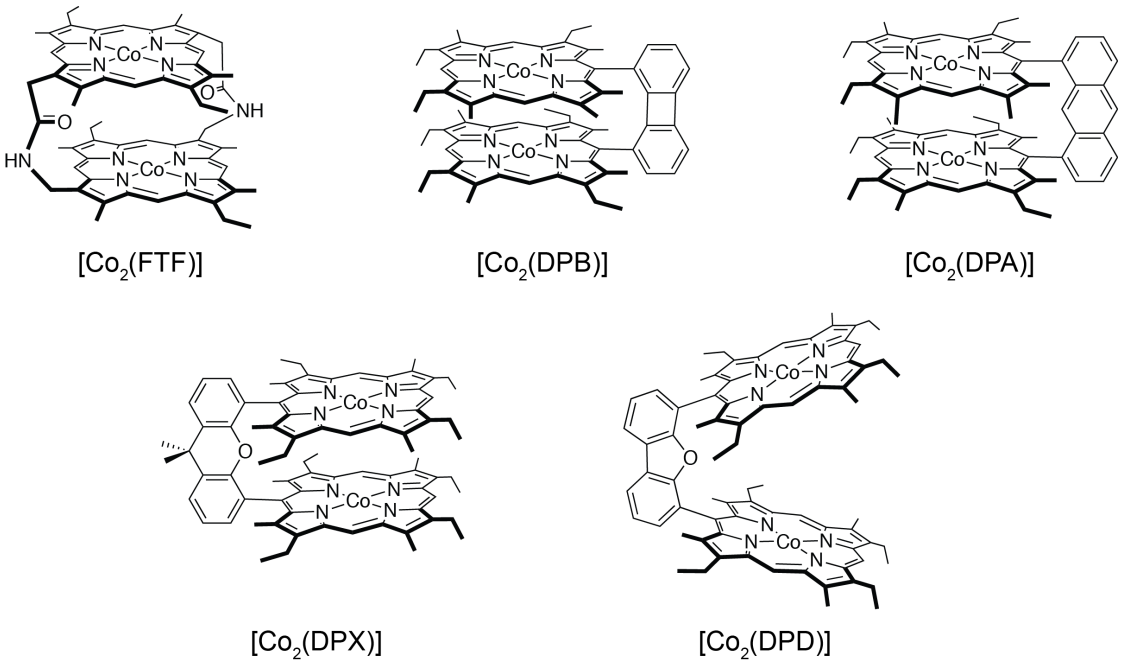

Figure 1.7: Cofacial bis(cobalt) diporphyrin catalysts for O_2 reduction to H_2O

This initial work was expanded to produce pillared cofacial bis(cobalt) diporphyrin catalysts.[69] This generation of catalysts was an improvement upon the previous amide linked porphyrins, as the pillared catalysts avoid slippage, where the two rings become laterally displaced. This is accomplished by using biphenylene and anthracene as linkers which provide a rigid pillar, [Co_2(DPB)] and [(Co_2(DPA)] (Figure 1.7), respectively. Catalysis with [Co_2(DPB)] or [(Co_2(DPA)] on a graphite electrode displayed oxygen reduction at $E_{1/2}$ of 0.43-0.46 V vs. SCE and <8% production of H_2O_2 corresponding to 3.7-3.8 electrons transferred per equivalent of O_2 reduced, respectively.

While this second generation of catalysts provided several advantages to the first, the structural limitations did not allow for the study of how a large range of motion between the cofacial porphyrins affects the oxygen reduction activity of the complex. This issue was addressed by developing a "Pacman" series of cofacial bis(cobalt) diporphyrins with flexible binding pockets. These Pacman porphyrins utilized xanthene ([Co_2(DPX)]) and dibenzofuran ([Co_2(DPD)]) (Figure 1.7), and had the added advantage of a more straightforward synthesis.

When adsorbed on EPG electrodes, both of these catalysts are selective for the 4 e^-, 4 H^+ reduction of O_2 to H_2O with an $E_{1/2}$ of 0.37 V (vs. Ag/AgCl).[70] This is especially interesting since there is an approximately 4 Å difference in their metal-metal bond distances. This would support the proposal of a flexible binding pocket that allows for structural accommodation of the reduction intermediates during catalysis and direction of the reaction pathway. Further studies were performed in which a sterically demanding aryl group was placed trans to the spacer (DPXM, diporphyrin xanthene methoxyaryl; and DPDM, diporphyrin dibenzofuran

methoxyaryl).[71] Although the structural flexibility and redox behavior was similar to the parent compounds, the [Co_2(DPXM)] and [Co_2(DPDM)] derivatives had decreased activity and selectivity towards the reduction of O_2 to produce H_2O. From DFT (density functional theory) calculations, it was shown that the HOMOs for the oxygen adducts were inverted between the modified and parent complexes. The $[Co_2(DPX)(O_2)]^+$ superoxo species exhibited localized molecular orbitals with substantial π^* (Co-O) and π^* (O-O) on the Co_2O_2 center, whereas the HOMO of $[Co_2(DPXM)(O_2)]^+$ was shown to lie on the porphyrin π system. Furthermore, no electron density for the HOMO was observed on the bound O_2 for $[Co_2(DPXM)(O_2)]^+$.

The mechanism proposed by the Nocera group[58,65] for O_2 reduction to H_2O or H_2O_2 by cofacial bis(cobalt) diporphyrins is shown in Figure 1.8. The comparative studies and DFT calculations with the methoxyaryl derivatives indicated that an important aspect of the overall mechanism was the pK_a of the bridging superoxo (highlighted structure in Figure 1.8). A more basic oxygen such as in [Co_2(DPX)] and [Co_2(DPD)] leads to protonation and eventual production of H_2O. Conversely, if the superoxo is not sufficiently basic, as in [Co_2(DPXM)] and [Co_2(DPDM)], a one electron reduction of the superoxo occurs to eventually produce H_2O_2. This highlights the important role of proton coupled electron transfer for O—O bond cleavage. Additionally, this mechanism addresses previous studies where it was shown that a second cobalt site is not always necessary for 4 e^-, 4 H^+ reduction to H_2O. Indeed, systems where the second functional site is a freebase porphyrin or is a porphyrin metalated with a Lewis acid have also been shown to produce H_2O.[65,72-75] As implied by the mechanism below, the second functional site is required to tune the pK_a of the superoxo intermediate.

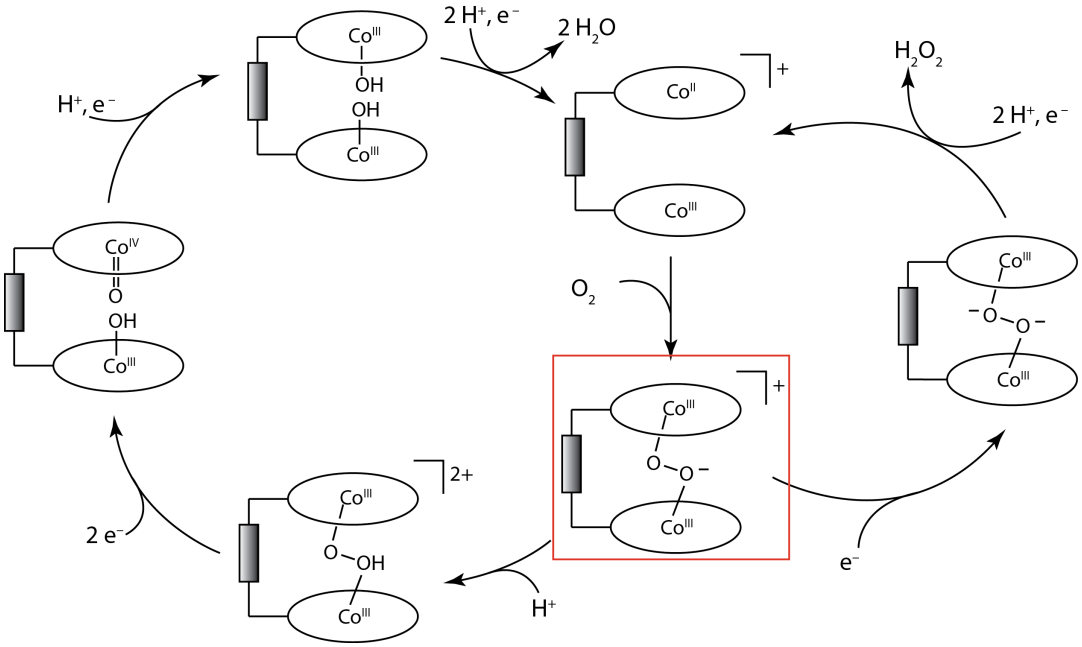

Figure 1.8: Mechanism for cofacial bis(cobalt) diporphyrin catalysts for O_2 reduction to H_2O or H_2O_2. Figure adapted from Nocera et. al.[58,65]

In addition to cofacial bis(cobalt) diporphyrins, a few additional tetraaza-macroycles have been developed as selective ORR catalysts, including cofacial binuclear cobalt Schiff base calixpyrrole macrocycles[76] and mixed Co^{III}corrole/ Co^{II}porphyrin complexes.[77] Each of the systems mentioned above aimed to promote H_2O production selectivity by constructing elaborate di-macrocycle platforms.

Chapter 4 will discuss the synthesis and characterization of a unique family of first row transition metal tetrapyrrole complexes. Chapter 5 will discuss the oxygen reduction activity and selectively of the monomeric cobalt tetrapyrrole catalyst, both homogeneously and heterogeneously. Finally, Chapter 6 will discuss further development of this catalyst towards better H_2O selectivity.

1.4 References and Notes

(1) U.S. Energy Information Administration: *International Energy Outlook 2016*

(2) For a comparison of energy outlooks, see *BP Energy Outlook*, 2017 pg. 100

(3) Cook, T. R.; Dogutan, D. K.; Reece, S. Y.; Surendranath, Y.; Teets, T. S.; Nocera, D. G. *Chem. Rev.* **2010**, *110* (11), 6474.

(4) *BP Energy Outlook*, 2017

(5) Atmospheric CO_2 concentration data from http://cdiac.ornl.gov/ftp/trends/co2/lawdome.combined.dat and ftp://aftp.cmdl.noaa.gov/products/trends/co2/co2_annmean_mlo.txt, accessed February 27, 2017

(6) *Climate Change 2014: Synthesis Report. Contribution of Working Groups I, II and III to the Fifth Assessment Report of the Intergovernmental Panel on Climate Change*, Intergovernmental Panel on Climate Change (IPCC), 2014

(7) Lewis, N. S. *Energy Environ. Sci.* **2016**, *9* (7), 2172.

(8) Lewis, N. S.; Nocera, D. G. *Proc. Natl. Acad. Sci.* **2006**, *103* (43), 15729.

(9) Karl, T. R.; Trenberth, K. E. *Science* **2003**, *302* (5651), 1719.

(10) Global land and ocean temperature anomalies for January-December from https://www.ncdc.noaa.gov/cag/time-series/global/globe/land_ocean/ytd/12/1880-2016, accessed February 27, 2017

(11) Feldman, D. R.; Collins, W. D.; Gero, P. J.; Torn, M. S.; Mlawer, E. J.; Shippert, T. R. *Nature* **2015**, *519* (7543), 339.

(12) Olah, G. A.; Prakash, G. K. S.; Goeppert, A. *J. Am. Chem. Soc.* **2011**, *133* (33), 12881.

(13) Hansen, J.; Sato, M.; Ruedy, R. *Proc. Natl. Acad. Sci.* **2012**, *109* (37), 2415.

(14) Drijfhout, S.; Bathiany, S.; Beaulieu, C.; Brovkin, V.; Claussen, M.; Huntingford, C.; Scheffer, M.; Sgubin, G.; Swingedouw, D. *Proc. Natl. Acad. Sci.* **2015**, *112* (43), 5777.

(15) Solomon, S.; Plattner, G.-K.; Knutti, R.; Friedlingstein, P. *Proc. Natl. Acad. Sci.* **2009**, *106* (6), 1704.

(16) Lenton, T. M.; Held, H.; Kriegler, E.; Hall, J. W.; Lucht, W.; Rahmstorf, S.; Schellnhuber, H. J. *Proc. Natl. Acad. Sci.* **2008**, *105* (6), 1786.

(17) Smith, J. B.; Schneider, S. H.; Oppenheimer, M.; Yohe, G. W.; Hare, W.; Mastrandrea, M. D.; Patwardhan, A.; Burton, I.; Corfee-Morlot, J.; Magadza, C. H. D.; Füssel, H.-M.; Pittock, A. B.; Rahman, A.; Suarez, A.; van Ypersele, J.-P. *Proc. Natl. Acad. Sci.* **2009**, *106* (11), 4133.

(18) United Nations. Adoption of the Paris Agreement. Proposal by the President, Paris Climate Change Conference – November 2015, COP 21, Paris, France, 2015.

(19) Gewirth, A. A.; Thorum, M. S. *Inorg. Chem.* **2010**, *49* (8), 3557.

(20) Crabtree, G.W.; Dresselhaus, M.S.; Buchanan, M.V. *Phys. Today* **2004**, *57* (12), 39.

(21) Edwards, P. P.; Kuznetsov, V. L.; David, W. I. F. *Philos. Trans. R. Soc. A Math. Phys. Eng. Sci.* **2007**, *365* (1853), 1043.

(22) Armaroli, N.; Balzani, V. *ChemSusChem* **2011**, *4* (1), 21.

(23) Sigfusson, T.I. *Philos. Trans. R. Soc. A Math. Phys. Eng. Sci.* **2007**, *365* (1853), 1025.

(24) Van den Berg, A. W. C.; Arean, C. O. *Chem. Commun.* **2008**, 668.

(25) Dalebrook, A. F.; Gan, W.; Grasemann, M.; Moret, S.; Laurenczy, G. *Chem. Commun.* **2013**, *49* (78), 8735.

(26) Lai, Q.; Paskevicius, M.; Sheppard, D. A.; Buckley, C. E.; Thornton, A. W.; Hill, M. R.; Gu, Q.; Mao, J.; Huang, Z.; Liu, H. K.; Guo, Z.; Banerjee, A.; Chakraborty, S.; Ahuja, R.; Aguey-Zinsou, K.-F. *ChemSusChem* **2015**, *8* (17), 2789.

(27) Choi, S.; Drese, J. H.; Jones, C. W. *ChemSusChem* **2009**, *2* (9), 796.

(28) Loges, B.; Boddien, A.; Gärtner, F.; Junge, H.; Beller, M. *Top. Catal.* **2010**, *53* (13), 902.

(29) Singh, A. K.; Singh, S.; Kumar, A. *Catal. Sci. Technol.* **2016**, *6* (1), 12.

(30) Grasemann, M.; Laurenczy, G. *Energy Environ. Sci.* **2012**, *5* (8), 8171.

(31) Joó, F. *ChemSusChem* **2008**, *1* (10), 805.

(32) Johnson, T. C.; Morris, D. J.; Wills, M. *Chem. Soc. Rev.* **2010**, *39* (1), 81.

(33) P.G. Jessop, *The Handbook of Homogeneous Hydrogenation*, Wiley-VCH Verlag GmbH, Weinheim, 2008, p 489-511

(34) Enthaler, S.; von Langermann, J.; Schmidt, T. *Energy Environ. Sci.* **2010**, *3* (9), 1207.

(35) Gao, Y.; Kuncheria, J.; Puddephatt, R. J.; Yap, G. P. A. *Chem. Commun.* **1998**, *21*, 2365.

(36) Gao, Y.; Kuncheria, J. K.; Jenkins, H. A.; Puddephatt, R. J.; Yap, G. P. A. *J. Chem. Soc., Dalt. Trans.* **2000**, *18*, 3212.

(37) Boddien, A.; Loges, B.; Junge, H.; Beller, M. *ChemSusChem* **2008**, *1* (8–9), 751.

(38) Fellay, C.; Yan, N.; Dyson, P. J.; Laurenczy, G. *Chem. – A Eur. J.* **2009**, *15* (15), 3752.

(39) Loges, B.; Boddien, A.; Junge, H.; Beller, M. *Angew. Chemie Int. Ed.* **2008**, *47* (21), 3962.

(40) Morris, D. J.; Clarkson, G. J.; Wills, M. *Organometallics* **2009**, *28* (14), 4133.

(41) Mellone, I.; Peruzzini, M.; Rosi, L.; Mellmann, D.; Junge, H.; Beller, M.; Gonsalvi, L. *Dalt. Trans.* **2013**, *42* (7), 2495.

(42) Manca, G.; Mellone, I.; Bertini, F.; Peruzzini, M.; Rosi, L.; Mellmann, D.; Junge, H.; Beller, M.; Ienco, A.; Gonsalvi, L. *Organometallics* **2013**, *32* (23), 7053.

(43) Himeda, Y. *Green Chem.* **2009**, *11* (12), 2018.

(44) Tanaka, R.; Yamashita, M.; Chung, L. W.; Morokuma, K.; Nozaki, K. *Organometallics* **2011**, *30* (24), 6742.

(45) Hull, J. F.; Himeda, Y.; Wang, W.-H.; Hashiguchi, B.; Periana, R.; Szalda, D. J.; Muckerman, J. T.; Fujita, E. *Nat Chem* **2012**, *4* (5), 383.

(46) Barnard, J. H.; Wang, C.; Berry, N. G.; Xiao, J. *Chem. Sci.* **2013**, *4* (3), 1234.

(47) Oldenhof, S.; de Bruin, B.; Lutz, M.; Siegler, M. A.; Patureau, F. W.; van der Vlugt, J. I.; Reek, J. N. H. *Chem. – A Eur. J.* **2013**, *19* (35), 11507.

(48) Boddien, A.; Loges, B.; Gärtner, F.; Torborg, C.; Fumino, K.; Junge, H.; Ludwig, R.; Beller, M. *J. Am. Chem. Soc.* **2010**, *132* (26), 8924.

(49) Boddien, A.; Mellmann, D.; Gärtner, F.; Jackstell, R.; Junge, H.; Dyson, P. J.; Laurenczy, G.; Ludwig, R.; Beller, M. *Science* **2011**, *333* (6050), 1733.

(50) Zell, T.; Butschke, B.; Ben-David, Y.; Milstein, D. *Chem. – A Eur. J.* **2013**, *19* (25), 8068.

(51) Bielinski, E. A.; Lagaditis, P. O.; Zhang, Y.; Mercado, B. Q.; Würtele, C.; Bernskoetter, W. H.; Hazari, N.; Schneider, S. *J. Am. Chem. Soc.* **2014**, *136* (29), 10234.

(52) Ruthven, D. M.; Upadhye, R. S. *J. Catal.* **1971**, *21* (1), 39.

(53) Zhou, X.; Huang, Y.; Xing, W.; Liu, C.; Liao, J.; Lu, T. *Chem. Commun.* **2008**, *30*, 3540.

(54) Wang, Z.-L.; Yan, J.-M.; Ping, Y.; Wang, H.-L.; Zheng, W.-T.; Jiang, Q. *Angew. Chemie Int. Ed.* **2013**, *52* (16), 4406.

(55) Zhang, S.; Metin, Ö.; Su, D.; Sun, S. *Angew. Chemie Int. Ed.* **2013**, *52* (13), 3681.

(56) Collman, J. P.; Wagenknecht, P. S.; Hutchison, J. E. *Angew. Chemie Int. Ed. English* **1994**, *33* (15–16), 1537.

(57) Gasteiger, H. A.; Marković, N. M. *Science* **2009**, *324* (5923), 48.

(58) Rosenthal, J.; Nocera, D. G. *Acc. Chem. Res.* **2007**, *40* (7), 543.

(59) Milazzo, G.; Caroli, S. *Tables of Standard Electrode Potentials*, p. 229, Wiley-Interscience, New York, 1978.

(60) Jones, R.D.; Summerville, D.A.; Basolo, F. *Chem. Rev.* **1979**, *79*, 139.

(61) Jasinski, R. *Nature* **1964**, *201* (4925), 1212.

(62) Zhang, W.; Lai, W.; Cao, R. *Chem. Rev.* **2017**, *117* (4), 3717

(63) Collman, J.P.; Boulatov, R.; Sunderland, C.J. In *The Porphyrin Handbook*; Kadish, K. M.; Smith, K.M.; Guilard, R., Eds.; Academic Press: San Diego, CA, 2003, Vol. 11, pp 1-49.

(64) Scherson, D. A.; Palencsár, A.; Tolmachev, Y.; Stefan, I. In *Electrochemical Surface Modification*; Wiley-VCH Verlag GmbH & Co. KGaA, 2008; pp 191–288.

(65) Rosenthal, J.; Nocera, D. G. In *Progress in Inorganic Chemistry*; John Wiley & Sons, Inc., 2007; pp 483–544.

(66) Collman, J. P.; Marrocco, M.; Denisevich, P.; Koval, C.; Anson, F. C. *J. Electroanal. Chem. Interfacial Electrochem.* **1979**, *101* (1), 117.

(67) Collman, J. P.; Denisevich, P.; Konai, Y.; Marrocco, M.; Koval, C.; Anson, F. C. *J. Am. Chem. Soc.* **1980**, *102* (19), 6027.

(68) Collman, J. P.; Anson, F. C.; Barnes, C. E.; Bencosme, C. S.; Geiger, T.; Evitt, E. R.; Kreh, R. P.; Meier, K.; Pettman, R. B. *J. Am. Chem. Soc.* **1983**, *105* (9), 2694.

(69) Chang, C. K.; Liu, H. Y.; Abdalmuhdi, I. *J. Am. Chem. Soc.* **1984**, *106* (9), 2725.

(70) Chang, C. J.; Deng, Y.; Shi, C.; Chang, C. K.; Anson, F. C.; Nocera, D. G. *Chem. Commun.* **2000**, *15*, 1355.

(71) Chang, C. J.; Loh, Z.-H.; Shi, C.; Anson, F. C.; Nocera, D. G. *J. Am. Chem. Soc.* **2004**, *126* (32), 10013.

(72) Liu, H. Y.; Abdalmuhdi, I.; Chang, C. K.; Anson, F. C. *J. Phys. Chem.* **1985**, *89* (4), 665.

(73) Ni, C. L.; Abdalmuhdi, I.; Chang, C. K.; Anson, F. C. *J. Phys. Chem.* **1987**, *91* (5), 1158.

(74) Collman, J. P.; Hendricks, N. H.; Kim, K.; Bencosme, C. S. *J. Chem. Soc., Chem. Commun.* **1987**, *20*, 1537.

(75) Guilard, R.; Brandes, S.; Tardieux, C.; Tabard, A.; L'Her, M.; Miry, C.; Gouerec, P.; Knop, Y.; Collman, J. P. *J. Am. Chem. Soc.* **1995**, *117* (47), 11721.

(76) Devoille, A. M. J.; Love, J. B. *Dalt. Trans.* **2012**, *41* (1), 65.

(77) Kadish, K. M.; Frémond, L.; Shen, J.; Chen, P.; Ohkubo, K.; Fukuzumi, S.; El Ojaimi, M.; Gros, C. P.; Barbe, J.-M.; Guilard, R. *Inorg. Chem.* **2009**, *48* (6), 2571.

Chapter 2

DEHYDROGENATION OF FORMIC ACID WITH A SERIES OF CHELATING N-HETEROCYCLIC CARBENE PALLADIUM COMPLEXES

2.1 Introduction

Previously, our group had synthesized a palladium dimethyl complex with a chelating *M*ethylene bridged *D*i*C*arbene (MDC) ligand scaffold ($(MDC^{Mes})PdMe_2$). This palladium complex was explored for its reactivity towards carbon dioxide in comparison to related dimethyl palladium species with bisphosphine or diamine ligands. $(MDC^{Mes})PdMe_2$ was found to give the corresponding methyl bicarbonate species $(MDC^{Mes})Pd(O_2COH)CH_3$) in the presence of carbon dioxide and trace water in solution (Scheme 2.1).[1]

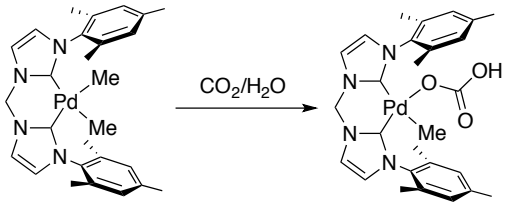

$(MDC^{Mes})PdMe_2$ $(MDC^{Mes})Pd(O_2COH)$

Scheme 2.1: Reaction of $(MDC^{Mes})PdMe_2$ with carbon dioxide and trace water

The MDC ligand was chosen because N-heterocyclic carbenes (NHCs) form strong NHC-metal bonds with strong electron rich σ-donating properties, as well as weak π -accepting properties.[2,3] These stable NHC-metal bonds give NHC metal

complexes robustness against air, moisture and elevated temperatures.[4,5] We wished to employ the same strategy of using this chelating NHC ligand as a robust supporting ligand for palladium to promote an analogous binding of formate with the ultimate goal of dehydrogenation to yield hydrogen and carbon dioxide.

Several different types of supporting ligands have been used on mental centers for formic acid dehydrogenation catalysts; however, the most prevalent type of ligand is the phosphine.[6] Therefore, we wished to study what effect using the more strongly σ-donating MDC ligand would have on the stability and reactivity of the catalyst in comparison to more labile supporting ligands, such as phosphine. In terms of the reactive metal center, palladium was chosen due to its known compatibility with the MDC ligand. Additionally, homogeneous palladium catalysts for formic acid dehydrogenation had not been widely explored in the literature; catalysts are typically developed using metals such as ruthenium and iridium,[6] and more recently iron.[7] Indeed, while numerous examples of heterogeneous palladium catalysts have been explored for formic acid dehydrogenation,[6,8] to the best of our knowledge only one example of a homogeneous palladium catalyst for this reaction has been reported: the Cazin group[9] reported [Pd(SIPr)(PCy_3)] (SIPr = *N*,*N*'-bis(2,6-diisopropylphenyl) imidazolidin-2-ylidene) for the production of hydrogen and carbon dioxide. However, this catalyst was not very efficient for formic acid dehydrogenation, reporting only a relatively small amount of gas production.

We initially proposed studying an analogous complex to our previously developed dimethyl palladium complex ((MDC^{Mes})$PdMe_2$), using the robust MDC ligand on Pd(II) with the acetonitrile solvato complex. We proposed using this complex, [(MDC^{Mes})Pd($CH_3CN)_2$]($PF_6)_2$, with more labile acetonitrile ligands at the

palladium center to promote the catalytic dehydrogenation of formic acid to form hydrogen and carbon dioxide (Scheme 2.2). While this complex is known in the literature, it has not been extensively used as a catalyst. One of the few examples of the catalytic reactivity of $[(MDC^{Mes})Pd(MeCN)_2](PF_6)_2$ and the related $[(MDC^{Me})Pd(MeCN)_2](BF_4)_2$ complex are for the copolymerization of ethylene and carbon monoxide.[10] Additionally, the related $[(MDC^{Me})Pd(MeCN)_2](BF_4)_2$ and $[(MDC^{iPr})Pd(MeCN)_2](BF_4)_2$ complexes were studied as catalysts for the Nazarov cyclization reaction[11] and for the hydrogenation of cyclooctene,[12] respectively.

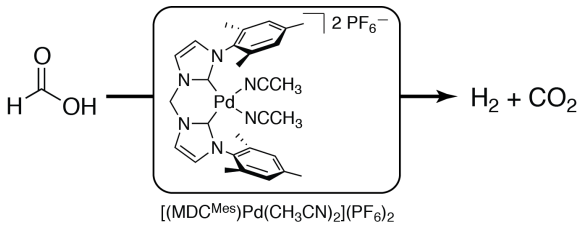

Scheme 2.2: Proposed palladium MDC catalyst for formic acid dehydrogenation

We initially developed an optimized procedure for formic acid dehydrogenation with $[(MDC^{Mes})Pd(MeCN)_2](PF_6)_2$ to determine the overall efficiency of the catalyst and analyzed the reaction products. Once these initial parameters were established, we then proposed studying various modifications of the catalyst (modifying the solvato ligands and nitrogen wingtip groups) to see what effect, if any, this had on the reactivity of the catalyst.

2.2 Formic Acid Dehydrogenation with $[(MDC^{Mes})Pd(CH_3CN)_2](PF_6)_2$

2.2.1 Synthesis of $[(MDC^{Mes})Pd(CH_3CN)_2](PF_6)_2$ via Zinc Transmetalation

The catalyst we chose for our initial studies, $[(MDC^{Mes})Pd(CH_3CN)_2](PF_6)_2$, was first synthesized in the literature using an exchange reaction between $Na[PF_6]$ and the corresponding $(MDC^{Mes})PdBr_2$ complex in acetonitrile and water.[10] Previously in our group we developed a new method to synthesize this palladium complex via a transmetalation from $(MDC^{Mes})ZnBr_2$ using $[(CH_3CN)_4Pd](PF_6)_2$ (Scheme 2.3).[13] This is analogous to a common method of transmetalation using silver;[14,15] however, our method does not involve the use of a precious metal as transfer reagent. Additionally, this is the first example of zinc being used as a transfer reagent for the synthesis of a transition metal NHC complex. Several mono- and di-N-heterocyclic carbene Zn complexes have been synthesized,[16] and have mainly been used as hydrogenation[17,18] or polymerization[19-22] catalysts. Conversely, there are few examples of Zn complexes with NHCs as one of the units on a chelating ligand;[23-28] to the best of our knowledge $(MDC^{Mes})ZnBr_2$ is the first example of a Zn complex with a neutral chelating dicarbene. The Zn complex reported here was synthesized in good yield from the methylene bridged diimidazolium salt and $ZnEt_2$ (Scheme 2.3).

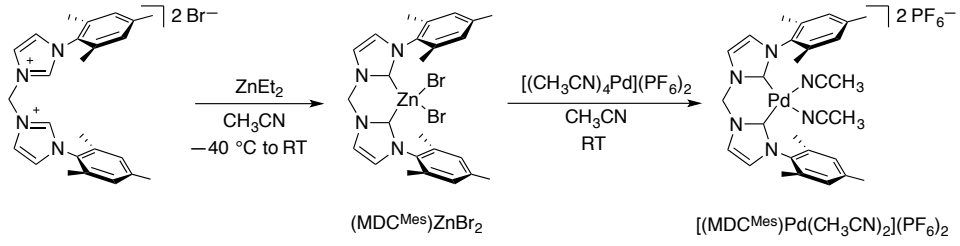

Scheme 2.3: Synthesis of $(MDC^{Mes})ZnBr_2$ and $[(MDC^{Mes})Pd(CH_3CN)_2](PF_6)_2$

2.2.2 Catalytic Activity of $[(MDC^{Mes})Pd(CH_3CN)_2](PF_6)_2$

With the catalyst in hand, $[(MDC^{Mes})Pd(CH_3CN)_2](PF_6)_2$ was tested for its activity for the production of hydrogen and carbon dioxide from formic acid. This activity was first tested using an aqueous solution of 5M formic acid with sodium formate as base. Even at elevated temperatures, the system gave minimal gas production (as measured using water displacement). The reaction system was then modified to use an organic base, triethylamine (a common additive for this type of reaction). This was done starting with 1 mL of a 5M solution of formic acid and triethylamine (2:1 ratio of acid to base) in acetonitrile. The solution was heated to the desired temperature, then 100 μL of a 200 mM solution of $[(MDC^{Mes})Pd(CH_3CN)_2](PF_6)_2$ in acetonitrile (0.4 mol% catalyst) was added to the formic acid solution. Gas production was observed at 55 °C, with increasing gas production at increasing temperatures to give an optimized reaction temperature of 70 °C (Figure 2.1). The turnover number (TON) and turnover frequency (TOF) were calculated under these conditions (Figure 2.2) from an average of at least three trials. After 80 minutes, the total TON was 185 (±10) with 80% conversion of formic acid. Addition of more formic acid once gas production had plateaued did not increase the TON. The initial TOF taken within the first 10 minutes was determined to be 325 (±35) h^{-1}. These metrics are comparable to some formic acid dehydrogenation catalysts that have been reported in the literature,[29-34] but (unfortunately) are well below some of the most active formic acid dehydrogenation catalysts.[35-38] However, this catalyst can be used under relatively simple conditions; the temperature of the reaction is comparatively mild and the reaction can be set-up under air.

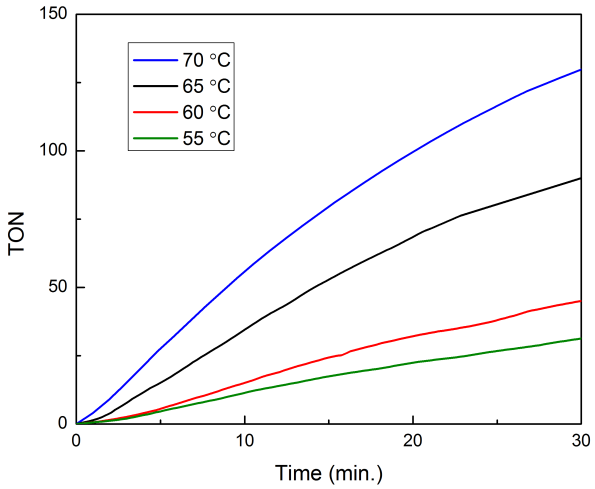

Figure 2.1: Gas production from formic acid and triethylamine at various temperatures

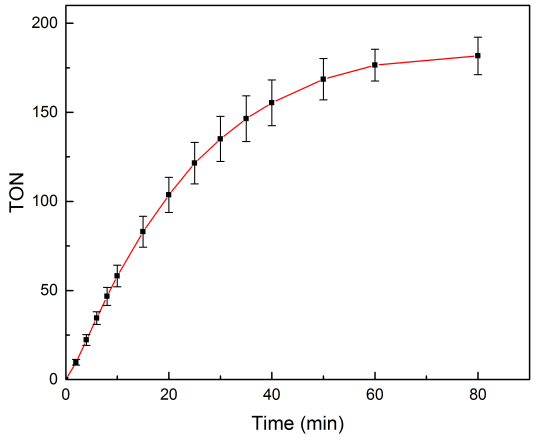

Figure 2.2: Gas production from 5 M formic acid and triethylamine (2:1) with 0.4 mol% $[(MDC^{Mes})Pd(CH_3CN)_2](PF_6)_2$ catalyst

Additionally, several control reactions with varying palladium sources ($PdCl_2$, $Pd(OAc)_2$, $(CH_3CN)_4Pd(PF_6)_2$) were also performed. In each case, only a minimal amount of gas production occurred (TON < 5), indicating that simple heterogeneous

Pd sources, or homogeneous Pd sources without the NHC ligand scaffold, are not active in catalysis for this reaction. Also, the reaction with the zinc precursor $(MDC^{Mes})ZnBr_2$ as catalyst and the reaction with $[(MDC^{Mes})Pd(CH_3CN)_2](PF_6)_2$ but without base did not proceed.

2.2.3 Determination of Products via Gas Chromatography

The gaseous products of the reaction were analyzed by gas chromatography in a separate experimental set-up (see Section 2.7.1.4). The results show a 1:1 ratio of hydrogen to carbon dioxide (Figure 2.3a), with no production of carbon monoxide within the limits of the gas chromatograph (< 5 ppm). A carbon monoxide standard is shown in Figure 2.3b for comparison. Since carbon monoxide is known to be detrimental to fuel cells, minimal or no production of any CO by-product is essential for any practical application of the catalyst.

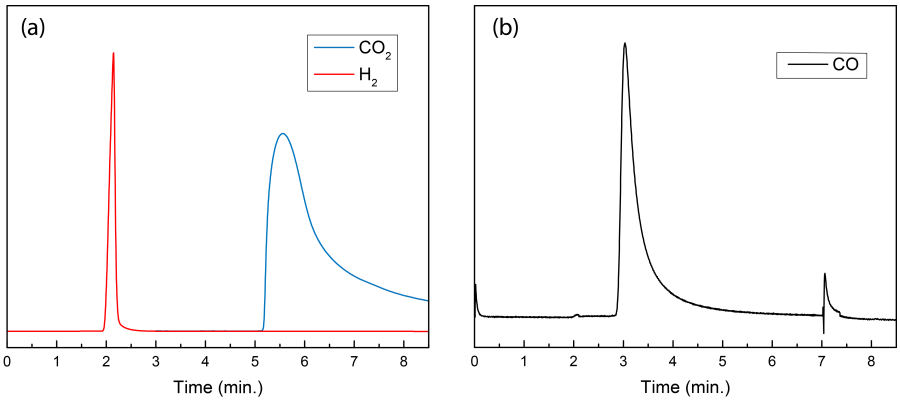

Figure 2.3: Gas chromatograms showing production of (a) carbon dioxide and hydrogen from formic acid and (b) carbon monoxide standard

2.3 Formic Acid Dehydrogenation with $[(MDC^{Mes})Pd(L)_2](PF_6)_2$ (L= PMe_3, CH_3CN; py; ^tBuNC)

From the initial finding of $[(MDC^{Mes})Pd(CH_3CN)_2](PF_6)_2$ as an efficient catalyst, we proposed modifying various aspects of this catalyst motif to see what effect these changes have on the activity of the catalyst. Our goal is to further optimize the catalyst, as well as gain insights into a possible mechanism of this reaction. The first type of modification was to substitute the labile acetonitrile ligands on the palladium center with other "L" type or neutral ligands. The ligand types we chose to study were phosphine (PMe_3), isonitrile (^{t}BuNC) and pyridine (py) to see what effect, if any, the identity of these various ligands have on the reactivity of the catalyst.

2.3.1 Synthesis of $[(MDC^{Mes})Pd(L)_2](PF_6)_2$

The synthesis of this family of palladium MDC complexes was previously developed in our laboratory (Scheme 2.4).[39] The palladium MDC catalyst with phosphine ligand was synthesized by reacting the $[(MDC^{Mes})Pd(CH_3CN)_2](PF_6)_2$ complex with one equivalent of trimethylphosphine (PMe_3) in acetonitrile at room temperature, resulting in a complex with one acetonitrile and one phosphine ligand bound to the palladium center ($[(MDC^{Mes})Pd(CH_3CN)(PMe_3)](PF_6)_2$) in 80% yield. If the synthesis was attempted with any additional amounts of phosphine added, the resulting product was always $[(MDC^{Mes})Pd(CH_3CN)(PMe_3)](PF_6)_2$, and not the species with two phosphines bound to palladium. The isonitrile complex, $[(MDC^{Mes})Pd(^tBuNC)_2](PF_6)_2$, was synthesized by reacting $[(MDC^{Mes})Pd(CH_3CN)_2](PF_6)_2$ with two equivalents of *tert*-butyl isocyanide in acetonitrile at room temperature to give the desired product in 70% yield. A different strategy was employed for the synthesis of $[(MDC^{Mes})Pd(py)_2](PF_6)_2$:

$[(MDC^{Mes})Pd(CH_3CN)_2](PF_6)_2$ was dissolved in an excess of pyridine in CH_3CN and heated to 60 °C to give the desired compound in 50% yield.

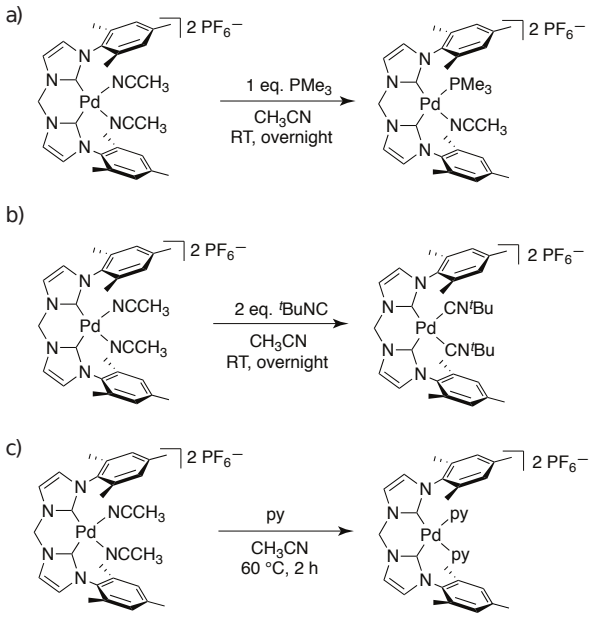

Scheme 2.4: Synthesis of **a)** $[(MDC^{Mes})Pd(CH_3CN)(PMe_3)](PF_6)_2$
b) $[(MDC^{Mes})Pd(^tBuNC)_2](PF_6)_2$ **c)** $[(MDC^{Mes})Pd(py)_2](PF_6)_2$

2.3.2 Catalytic Activity of $[(MDC^{Mes})Pd(L)_2](PF_6)_2$

The dehydrogenation of formic acid with each of the $[(MDC^{Mes})Pd(L)_2](PF_6)_2$ type catalysts was studied using the optimized experimental parameters determined for $[(MDC^{Mes})Pd(CH_3CN)_2](PF_6)_2$ (70 °C; 1 mL of 5M formic acid solution in acetonitrile; 2:1 acid: triethylamine; 100 μL of 200 mM catalyst solution (0.4 mol% catalyst)). The evolution of gaseous products was monitored via water displacement; TON and TOF were calculated based on the measured volume of gaseous products. The results are shown in Table 2.1.

Table 2.1: TON and TOF with $[(MDC^{Mes})Pd(L)_2](PF_6)_2$

Catalyst	TON	TOF (h^{-1})
$[(MDC^{Mes})Pd(CH_3CN)_2](PF_6)_2$	185 (±10)	325 (±35)
$[(MDC^{Mes})Pd(CH_3CN)(PMe_3)](PF_6)_2$	30 (±5)	119 (±25)
$[(MDC^{Mes})Pd(py)_2](PF_6)_2$	180 (±40)	256 (±60)
$[(MDC^{Mes})Pd(CN^tBu)_2](PF_6)_2$	0	0
$[(MDC^{Mes})Pd(CH_3CN)_2](PF_6)_2$ + 40 eq py	50 (±18)	24 (±11)
$[(MDC^{Mes})Pd(CH_3CN)_2](PF_6)_2$ + 10 eq PMe_3	5 (±0.5)	43 (±6)

The isonitrile complex, $[(MDC^{Mes})Pd(CN^tBu)_2](PF_6)_2$, was not active for formic acid dehydrogenation as no gaseous products were collected and the phosphine complex, $[(MDC^{Mes})Pd(CH_3CN)(PMe_3)](PF_6)_2$, gave only minimal gas production compared to the acetonitrile complex. However, the pyridine complex $[(MDC^{Mes})Pd(py)_2](PF_6)_2$ showed similar activities to $[(MDC^{Mes})Pd(CH_3CN)_2](PF_6)_2$. A possible explanation for the similar results is that in the excess of acetonitrile in solution, the pyridine ligands dissociate from the palladium center and form $[(MDC^{Mes})Pd(CH_3CN)_2](PF_6)_2$ in situ. In order to probe this theory further, the formic acid dehydrogenation reaction was set-up using $[(MDC^{Mes})Pd(CH_3CN)_2](PF_6)_2$ with an excess of pyridine added in order to form the $[(MDC^{Mes})Pd(py)_2](PF_6)_2$ complex in situ. Indeed, with 40 equivalents of pyridine added, the TON and TOF were much decreased (Table 2.1, Figure 2.4) from using the isolated $[(MDC^{Mes})Pd(py)_2](PF_6)_2$ complex. A similar trend was seen when an excess of phosphine was added to the solution with $[(MDC^{Mes})Pd(CH_3CN)_2](PF_6)$. From these studies, it appears that a labile ligand at the palladium center is necessary for reasonable formic acid dehydrogenation activity.

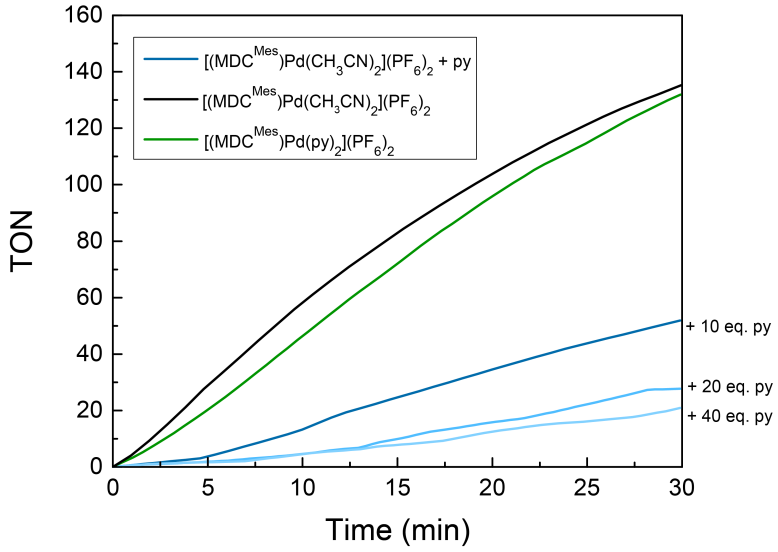

Figure 2.4: Comparison of gas production using isolated $[(MDC^{Mes})Pd(py)_2](PF_6)_2$ and the in-situ generated catalyst from $[(MDC^{Mes})Pd(CH_3CN)_2](PF_6)_2$ and excess pyridine

2.4 Formic Acid Dehydrogenation with $[(MDC^{Mes})Pd(L)Br]Br$ (L= PMe_3, ^{t}BuNC)

Having explored complexes similar to the initial catalyst, $[(MDC^{Mes})Pd(CH_3CN)_2](PF_6)_2$, with two neutral ligands on the open coordination site of palladium and hexafluorophosphate counterion for the Pd(II) species, we wanted to further modify the catalyst structure. We proposed studying a catalyst with both an "L" type neutral ligand as well as an "X" type anionic ligand (specifically bromide). coordinated to the palladium center, with a bromide counterion.

2.4.1 Synthesis of $[(MDC^{Mes})Pd(L)Br]Br$

The synthesis of this family of palladium MDC bromide complexes was previously developed in our laboratory (Scheme 2.5),[39] with the exception of $(MDC^{Mes})PdBr_2$ which is known in the literature.[10] The phosphine complex was

synthesized by reacting $(MDC^{Mes})PdBr_2$ with an excess of PMe_3 in tetrahydrofuran at room temperature to give the desired compound, $[(MDC^{Mes})Pd(PMe_3)Br]Br$, in 20% yield. Similarly, the isonitrile complex was synthesized by reacting $(MDC^{Mes})PdBr_2$ with an excess of *tert*-butyl isocyanide in tetrahydrofuran at room temperature to give the desired compound, $[(MDC^{Mes})Pd(CN^tBu)Br]Br$, in 95% yield.

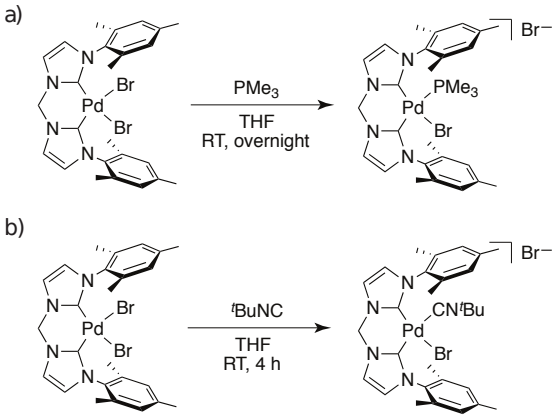

Scheme 2.5: Synthesis of **a)** $[(MDC^{Mes})Pd(PMe_3)Br]Br$ and
b) $[(MDC^{Mes})Pd(CN^tBu)Br]Br$

2.4.2 Catalytic Activity of $[(MDC^{Mes})Pd(L)Br]Br$

The dehydrogenation of formic acid with each of the $[(MDC^{Mes})Pd(X)Br]Br$ type complexes was studied using the same optimized experimental parameters as the previous catalysts (see Section 2.3.2). The volume of gaseous products was measured via water displacement and TONs and TOFs were calculated from these volumes. The results are shown in Table 2.2. While $[(MDC^{Mes})Pd(CN^tBu)Br]Br$ gave a modest initial TOF, the overall TON was very low, indicating quick deactivation of the catalyst. Both the TONs and TOFs for $(MDC^{Mes})PdBr_2$ and $[(MDC^{Mes})Pd(PMe_3)Br]Br$ catalysts were very low. The minimal activity of these $[(MDC^{Mes})Pd(X)Br]Br$ type

catalysts would indicate that having two labile ligands on the palladium center is essential to the reactivity of the catalyst.

Table 2.2: TON and TOF with [(MDC^{Mes})Pd(L)Br]Br

Catalyst	TON	TOF (h^{-1})
(MDC^{Mes})$PdBr_2$	4.0 (±0.7)	27 (±2)
[(MDC^{Mes})Pd(CN^tBu)Br]Br	11 (±2)	75 (±10)
[(MDC^{Mes})Pd(PMe_3)Br]Br	1.2 (±0.3)	7.0 (±0.8)

2.5 Formic Acid Dehydrogenation with [(MDC^R)Pd($MeCN)_2$]($PF_6)_2$ (R = Me, iPr, Ph, Cy, DIPP)

A variety of palladium MDC^R complexes were synthesized and studied for formic acid dehydrogenation. Variation of the wingtip groups on the imidazole nitrogens allowed us to determine what effect, if any, the steric nature of the groups surrounding the palladium center had on the activity of the catalyst for production of carbon dioxide and hydrogen in terms of TON and TOFs.

2.5.1 Synthesis of [(MDC^R)Pd($MeCN)_2$]($PF_6)_2$

Synthesis of the [(MDC^R)Pd($MeCN)_2$]($PF_6)_2$ complexes was performed using a modified procedure from Herrmann for the synthesis of [(MDC^{Mes})Pd($MeCN)_2$]($PF_6)_2$.[10] Chen and Qiu noted that these complexes could be synthesized by reacting $NaPF_6$ with the corresponding palladium bromide complex; however, no characterization data or crystal structures were provided.[40]

The series of [(MDC^R)Pd($MeCN)_2$]($PF_6)_2$ complexes were synthesized from the corresponding (MDC^R)$PdBr_2$ complexes, which are known in the literature.[41-43] This was accomplished by reacting the appropriate (MDC^R)$PdBr_2$ with two equivalents of $AgPF_6$ in acetonitrile at 65 °C for 4 hours (Scheme 2.6). The

corresponding $[(MDC^R)Pd(MeCN)_2](PF_6)_2$ complexes were obtained in good yield (40–75%).

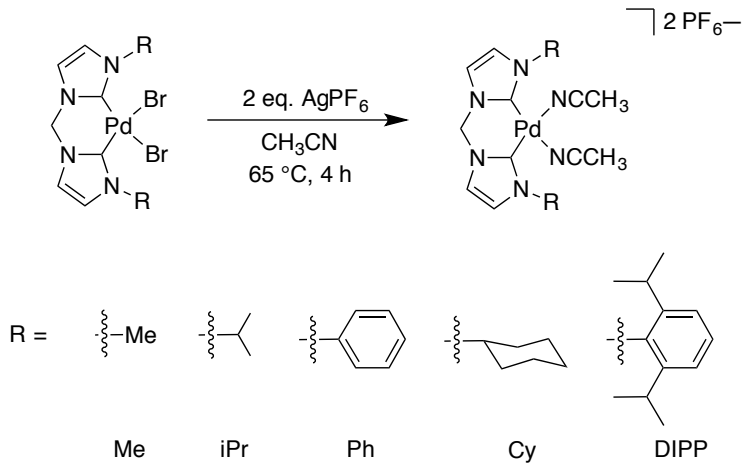

Scheme 2.6: Synthesis of a series of methylene bridged chelating N-heterocyclic carbene palladium complexes with differing substitutions at the NHC nitrogen

2.5.2 Molecular Structures of $[(MDC^R)Pd(MeCN)_2](PF_6)_2$

The crystal structures for each of the $[(MDC^R)Pd(MeCN)_2](PF_6)_2$ complexes are shown in Figure 2.5. Crystals for each complex were grown by slow evaporation of Et_2O into a supersaturated solution of the complex in CH_3CN. The structures are similar to other reported analogous palladium MDC complexes;[10,44] the Pd–C distances, shown in Table 2.3, are comparable to the distances reported for the analogous $[(MDC^{Mes})Pd(MeCN)_2](PF_6)_2$ complex (1.9653(8) and 1.9893(5) Å).[44] The Pd center in each structure is slightly distorted from the expected square planar geometry, due to the chelating effect of the MDC ligand. As shown in Table 2.3, the C–Pd–C bond angle is reduced to below 83.9° for almost all of the structures, with the

exception of $[(MDC^{DIPP})Pd(MeCN)_2](PF_6)_2$ which has a bond angle much closer to 90 °C. The *cis*- and *trans*-N–Pd–C bond angles are also affected by the chelate ring; the cis angles are relatively larger, between 92.52° and 95.6°, with the trans angles reduced to between 172.09° to the more ideal 178.1°.

Table 2.3: Selected bond lengths and angles for $[(MDC^{R})Pd(MeCN)_2](PF_6)_2$

R	Pd–C (Å)	C–Pd–C (°)	N–Pd–C (°) (*cis*)	N–Pd–C (°) (*trans*)	N–Pd–N (°)
Me	1.973(6) 1.973(6)	83.8(3)	95.0(2) 95.0(2)	177.7(2) 177.7(2)	86.2(3)
iPr	1.974(4) 1.979(3)	83.90(15)	94.01(14) 94.74(14)	176.26(13) 174.95(13)	87.08(13)
Ph	1.965(4) 1.973(4)	83.55(15)	92.52(14) 93.15(14)	172.09(14) 176.55(14)	90.87(13)
Cy	1.971(6) 1.971(6)	83.5(4)	95.6(3) 95.6(3)	178.1(2) 178.1(2)	85.3(3)
DIPP	1.972(5) 1.990(5)	88.0(2)	93.70(19) 94.35(19)	177.91(18) 177.12(18)	84.00(18)

2.5.3 Catalytic Activity of $[(MDC^{R})Pd(MeCN)_2](PF_6)_2$

The dehydrogenation of formic acid with each of the $[(MDC^{R})Pd(MeCN)_2](PF_6)_2$ catalysts was studied using the same optimized experimental parameters as the previous catalysts (see Section 2.3.2). The volume of gaseous products was measured via water displacement and TONs and TOFs were calculated from these volumes. The results are shown in Table 2.4.

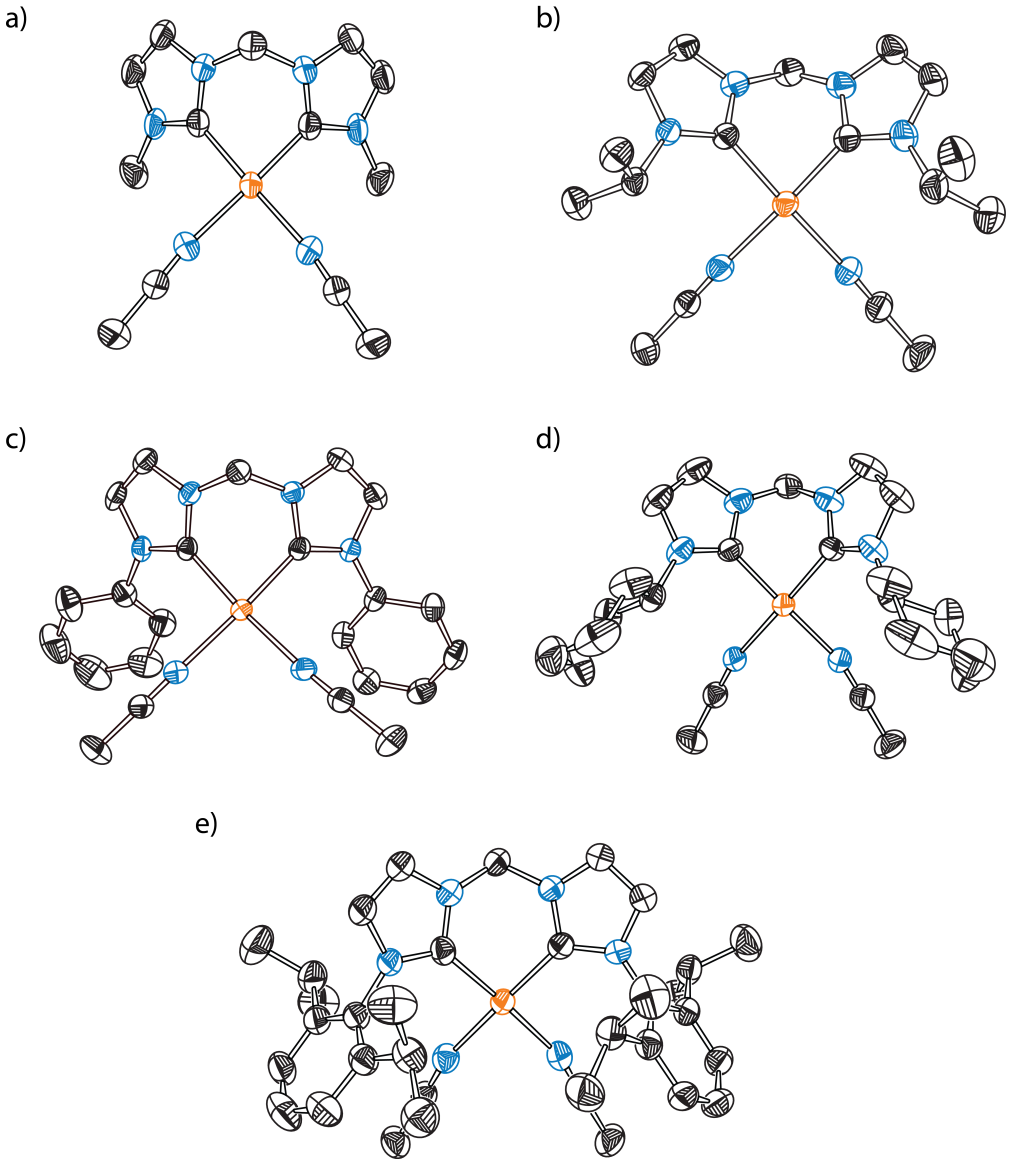

Figure 2.5: Crystal structure of **a)** [(MDC^{Me})Pd(MeCN)$_2$](PF$_6$)$_2$ **b)** [(MDC^{iPr})Pd(MeCN)$_2$](PF$_6$)$_2$ **c)** [(MDC^{Ph})Pd(MeCN)$_2$](PF$_6$)$_2$ **d)** (MDC^{Cy})Pd(MeCN)$_2$ **e)** [(MDC^{DIPP})Pd(MeCN)$_2$](PF$_6$)$_2$. Thermal ellipsoids are shown at the 50% probability level. All hydrogen atoms and counterions have been omitted for clarity.

Table 2.4: TON and TOF with $[(MDC^{R})Pd(MeCN)_2](PF_6)_2$

Catalyst	TON	TOF (h^{-1})
$[(MDC^{Me})Pd(MeCN)_2](PF_6)_2$	13 (±0.5)	72 (±3)
$[(MDC^{iPr})Pd(MeCN)_2](PF_6)_2$	6 (±0.5)	56 (±10)
$[(MDC^{Ph})Pd(MeCN)_2](PF_6)_2$	8 (±0.6)	62 (±5)
$[(MDC^{Cy})Pd(MeCN)_2](PF_6)_2$	10 (±2)	67 (±27)
$[(MDC^{DIPP})Pd(MeCN)_2](PF_6)_2$	35 (±20)	112 (±30)
$[(MDC^{Mes})Pd(MeCN)_2](PF_6)_2$	185 (±10)	325 (±35)

In general, it appears that the catalysts with a smaller steric size (Me, iPr, Ph, Cy) than the initially studied catalyst with the mesityl groups are much less active for the production of carbon dioxide and hydrogen from formic acid, based on the very low overall TONs (<20) and modest TOFs (56-72 h^{-1}). Interestingly, the catalyst with the most sterically hindering diisopropylphenyl groups on the NHC nitrogens ($[(MDC^{DIPP})Pd(MeCN)_2](PF_6)_2$) gave higher TONs and TOFs than the previously mentioned catalysts (Me, iPr, Ph, Cy), but was not as good as the original $[(MDC^{Mes})Pd(MeCN)_2](PF_6)_2$ catalyst. It appears the mesityl groups provide the correct steric environment around palladium for optimal catalysis. A further explanation and analysis of these results related to the proposed mechanism will be discussed in the next chapter (see Chapter 3).

2.6 Summary

We have shown the first example of a homogeneous palladium catalyst, $[(MDC^{Mes})Pd(MeCN)_2](PF_6)_2$, with any reasonable activity for formic acid dehydrogenation. This catalyst shows modest TONs and TOFs, but can be used under relatively mild conditions. It also produces minimal, if any, carbon monoxide, a potential byproduct of formic acid dehydrogenation that is detrimental to fuel cells. By

varying the original catalyst motif, we were able to synthesize a new family of MDC complexes with various phosphine, isonitrile and pyridine ligands coordinated to palladium. These modifications show that having two labile acetonitrile ligands coordinated to the palladium center give the optimal catalyst performance. In addition, we modified the mesityl group at the wingtip position of the MDC ancillary ligand, to understand what effect changing the steric nature around the palladium catalyst center has on the catalytic activity. From these modifications, mesityl appears to give the best catalyst performance, with both larger and smaller steric modifications giving decreased catalyst activity. From these catalyst modifications, we are able to begin hypothesizing a possible mechanism for formic acid dehydrogenation to produce hydrogen and carbon dioxide with $[(MDC^{Mes})Pd(MeCN)_2](PF_6)_2$ as catalyst. A proposed mechanism, and further studies to probe this mechanism, will be discussed in the following chapter (Chapter 3).

2.7 Experimental Methods

2.7.1 General Methods

Unless otherwise stated, reactions were performed in oven-dried glassware either under a positive pressure of nitrogen with flasks fitted with Suba-Seal rubber septa or in a nitrogen-filled glovebox. Air- and moisture-sensitive reagents were transferred using standard Schlenk techniques.

2.7.1.1 Materials

Reagents and solvents were purchased from Acros Organics, Cambridge Isotopes Laboratories, Fisher Scientific, Sigma-Aldrich, VWR or Strem Chemicals, Inc. Solvents for synthesis were of reagent grade or better; solvents for air- or

moisture-sensitive reactions were dried by passage through activated alumina and then stored over 4 Å molecular sieves prior to use.[45] Formic acid (99%) was obtained from Acros Organics; formic acid and CH_3CN (VWR) for dehydrogenation studies were used from the supplier without further purification.

2.7.1.2 Compound Characterization

^1H NMR and ^{13}C NMR spectra were recorded at 25 °C on a Bruker 400 MHz spectrometer. Proton spectra are referenced to the residual proton resonance of the deuterated solvent ($CDCl_3$ = δ 7.26, CD_3CN = δ 1.94), and carbon spectra are referenced to the carbon resonances of the solvent ($CDCl_3$ = δ 77.16, CD_3CN = δ 118.69). All chemical shifts are reported using the standard δ notation in parts-per-million; positive chemical shifts are to higher frequency from the given reference. High-resolution mass spectrometry analyses were performed by the Mass Spectrometry Laboratory in the Department of Chemistry and Biochemistry at the University of Delaware. Elemental analyses were performed by Robertson Microlit Laboratories, Ledgewood, NJ.

2.7.1.3 Procedure for Formation of Hydrogen from Formic Acid

A typical experiment involved the addition of 1 mL of a 5 M formic acid/base (2:1) acetonitrile solution to a septum capped vial. The solution was allowed to stir at desired temperature in a pre-heated sand bath. Once the solution was at a constant temperature, the vial was injected with 100 μL of the catalyst solution in acetonitrile. Any gas produced was measured using water displacement and (in a separate experimental set-up) identified using gas chromatography (vide infra). Water displacement measurements were performed using an inverted graduated cylinder

(typically 250 mL to 500 mL) and TONs were calculated from moles of gas produced (48 mol·L^{-1}). Instantaneous TOFs were calculated within the first ten minutes of the reaction. Standard deviations for TONs and TOFs were determined from multiple (at least 3) trials of each run.

2.7.1.4 Procedure for GC Analysis

A cell (Figure 2.6) containing 1 mL of the standard formic acid/base solution (vide supra) was heated in a sand bath at 70°C while stirring, during which time a continuous supply of argon gas was passed through the headspace of the cell at a rate of 20 cm^3/min. Any gaseous products of the cell were vented directly into the sampling loop of a SRI Instruments gas chromatograph (SRI-8610C). Following injection of the 100 μL catalyst solution into the cell, a GC acquisition was started every 5 minutes by placing the sampling loop in line with a packed HeySep D column and a packed MoleSieve 13X column. Argon (Keen, 99.999%) was used as the GC carrier gas. Hydrogen was quantified using a thermal conductivity detector (TCD), and carbon monoxide and carbon dioxide were quantified using a flame ionization detector (FID).

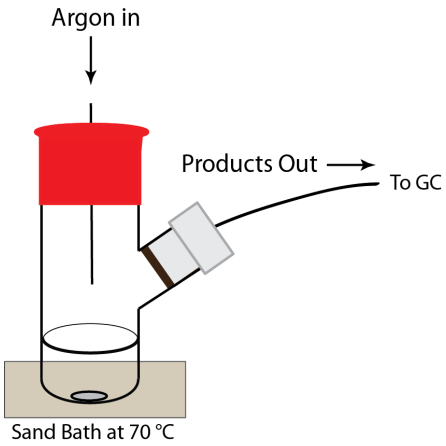

Figure 2.6: Experimental set-up for determination of gaseous products from formic acid via gas chromatography

2.7.2 Synthesis of (MDC^{R})PdBr$_2$ (R = Me, iPr, Ph, Cy, DIPP)

The synthesis of (1,1'-dicyclohexyl-3,3'-methylenediimidazolin-2,2'-diylidene)palladium(II)bromide, (1,1'-diphenyl-3,3'-methylenediimidazolin-2,2'-diylidene)palladium(II)bromide, (1,1'-dimethyl-3,3'-methylenediimidazolin-2,2'-diylidene)palladium(II)bromide, (1,1'-diisopropyl-3,3'-methylenediimidazolin-2,2'-diylidene)palladium(II)bromide was accomplished using a slight modification of literature procedures.[41,42]

Higher yields were found for the synthesis of (1,1'-di-2,6-diisopropylphenyl-3,3'-methylenediimidazolin-2,2'-diylidene)palladium(II)bromide by using an alternative metalation route common for N-heterocyclic carbenes.[15] Under an air atmosphere, a solution of 1,1'-methylene-3,3'-di-2,6-diisopropylphenylimidazolium dibromide[46] (300 mg, 0.47 mmol) and Ag_2O (109 mg, 0.47 mmol) was stirred in 15 mL of dimethylsulfoxide in the dark at room temperature for 2 days. To this solution was added 160 mg (0.47 mmol) $PdBr_2(MeCN)_2$ and the mixture was allowed to stir for an additional 2 h in the dark at room temperature. The solution was filtered through

celite and solvent was removed *in vacuo* to yield a yellow-gray solid. The solid was washed with dichloromethane and diethyl ether to give an off-white solid in 65% yield (227 mg). The ^{1}H-NMR and other spectroscopic characterizations were in accordance with the previously reported product.[43]

2.7.3 Synthesis of $[(MDC^{Mes})Pd(L)_2](PF_6)_2$ (L = CH_3CN, PMe_3; ^{t}BuNC; py)

$[(MDC^{Mes})Pd(CH_3CN)(PMe_3)](PF_6)_2$, $[(MDC^{Mes})Pd(^{t}BuNC)_2](PF_6)_2$ and $[(MDC^{Mes})Pd(py)_2](PF_6)_2$ were synthesized according to methods previously developed in our laboratory.[39]

2.7.3.1 [(1,1'-di(mesityl)-3,3'-methylenediimidazolin-2,2'-diylidene) palladium(II)-(acetonitrile)(trimethylphosphine)][$(PF_6)]_2$, $[(MDC^{Mes})Pd(CH_3CN)(PMe_3)](PF_6)_2$

A mixture of 250 mg $[(MDC^{Mes})Pd(CH_3CN)_2](PF_6)_2$ (0.30 mmol) and 1 equivalent of trimethylphosphine (30 μL, 0.30 mmol) was stirred in 10 mL of acetonitrile at room temperature, overnight. The solvent was removed *in vacuo* and the remaining solid was dissolved in a minimal amount of acetonitrile then added to 200 mL of diethyl ether. The resulting precipitate was collected and dried *in vacuo* to give 205 mg (80% yield) of a white solid. ^{1}H NMR (400 MHz; CD_3CN, 25 °C) δ/ppm: 7.72 (d, J = 10.6 Hz, 2H), 7.21 (d, J=104 Hz, 2H), 7.14 (m, 4H), 6.42 (dd, J=52.0 Hz, 13.3 Hz, 2H), 2.40 (s, 3H), 2.35 (s, 3H), 2.33 (s, 3H), 2.17 (s, 3H), 2.01 (s, 3H), 1.96 (s, 3H), 1.88 (s, 3H), 0.94 (d, J=11.6 Hz, 9 H). ^{13}C NMR (101 MHz; CD_3CN, 25 °C) δ/ppm: 165.38 (d, $J_{P,C}$=152.13), 156.04 (d, $J_{P,C}$=6.88), 141.68, 141.16, 136.93, 136.25, 136.19, 135.32, 135.10, 134.24, 131.61, 131.36, 130.31, 129.71, 126.95, 125.30, 124.13, 123.41, 64.14, 21.86, 21.03, 20.87, 19.69, 17.70, 17.62, 14.24 (d, $J_{P,C}$=32.2 Hz). ^{31}P NMR (162 MHz; $CDCl_3$, 25 °C) δ/ppm: -11.68, -144.59 (sept). Anal. Calc.

for $C_{30}H_{40}F_{12}N_5P_3Pd \cdot 0.5\ C_4H_{10}O$: C, 41.10; H, 4.85; N 7.49. Found: C, 40.83; H, 4.75; N, 7.48.

2.7.3.2 [(1,1'-di(mesityl)-3,3'-methylenediimidazolin-2,2'-diylidene) palladium(II)-bis(*tert*-butyl isocyanide)][$(PF_6)]_2$, [$(MDC^{Mes})Pd(^tBuNC)_2](PF_6)_2$

A mixture of 300 mg [$(MDC^{Mes})Pd(CH_3CN)_2](PF_6)_2$ (0.35 mmol) and two equivalents of *tert*-butyl isocyanide (0.7 mmol, 80 μL) were stirred in 10 mL of acetonitrile at room temperature overnight. The solvent was removed *in vacuo* and the remaining solid was dissolved in a minimal amount of acetonitrile then added to 200 mL of diethyl ether. The resulting precipitate was collected and dried *in vacuo* to give 232 mg (70% yield) of a white solid. ^{1}H NMR (400 MHz; CD_3CN, 25 °C) δ/ppm: 7.76 (s, 2H), 7.25 (s, 2H), 7.14 (s, 4H), 6.34 (s, 2H), 2.36 (s, 6H), 2.05 (s, 12H), 1.28 (s, 18H). ^{13}C NMR (101 MHz; CD_3CN, 25 °C) δ/ppm: 157.75, 141.51, 136.00, 135.51, 130.80, 126.01, 124.58, 63.91, 61.57, 29.68, 21.08, 18.87. ^{31}P NMR (162 MHz; CD_3CN, 25 °C) δ/ppm: -144.60 (sept). Anal. Calc. for $C_{35}H_{46}F_{12}N_6P_2Pd$: C, 44.38; H, 4.90; N 8.87. Found: C, 44.45; H, 4.96; N, 8.80.

2.7.3.3 [(1,1'-di(mesityl)-3,3'-methylenediimidazolin-2,2'-diylidene) palladium(II)-bis(pyridine)][$(PF_6)]_2$, [$(MDC^{Mes})Pd(py)_2](PF_6)_2$

A mixture of 180 mg [$(MDC^{Mes})Pd(CH_3CN)_2](PF_6)_2$ (0.20 mmol) and 100 μL pyridine were stirred in 15 mL of acetonitrile at 60 °C for 2 h. The solvent was removed *in vacuo* and the remaining solid was dissolved in a minimal amount of acetonitrile then added to 200 mL of diethyl ether. The resulting precipitate was collected and dried *in vacuo* to give 98 mg (50% yield) of a white solid. ^{1}H NMR (400 MHz; CD_3CN, -10 °C) δ/ppm: 8.43 (broad s, 2H), 7.75 (s, 2H), 7.58 (t, J=7.8 Hz, 2H), 7.49 (broad s, 2H), 7.19 (broad s, 2H), 7.10 (s, 4H), 6.76 (m, 3H), 6.45 (m, 1H), 6.28

(s, 2H), 2.29 (s, 6H), 2.22 (s, 6H), 1.36 (s, 6H). ^{13}C NMR (101 MHz; CD_3CN, -10 °C) δ/ppm: 153.04, 150.52, 149.76, 140.73, 139.79, 135.18, 134.93, 134.26, 130.17, 126.70, 126.41, 125.40, 123.84, 63.65, 20.72, 18.83, 17.92. ^{31}P NMR (162 MHz; CD_3CN, 25 °C) δ/ppm: -144.56 (sept). Anal. Calc. for $C_{35}H_{38}F_{12}N_6P_2Pd \cdot 1\ C_2H_3N$: C, 45.35; H, 4.22; N 10.00. Found: C, 45.55; H, 3.94; N, 10.24.

2.7.4 Synthesis of [(MDC^{Mes})Pd(L)Br]Br (L = PMe_3, ^{t}BuNC)

[(1,1'-di(mesityl)-3,3'-methylenediimidazolin-2,2'-diylidene)palladium(II) dibromide] ((MDC^{Mes})$PdBr_2$) was synthesized according to a literature procedure.[10]

2.7.4.1 [(1,1'-di(mesityl)-3,3'-methylenediimidazolin-2,2'-diylidene) palladium(II)-(trimethylphosphine)bromide]bromide, [(MDC^{Mes})Pd(PMe_3)Br]Br

A mixture of 130 mg (0.2 mmol) (MDC^{Mes})$PdBr_2$ and 200 μL PMe_3 were stirred in 7 mL THF at room temperature, overnight. The solvent was removed *in vacuo* and the remaining solid was dissolved in dichloromethane and added to 200 mL of diethyl ether. The product was an off-white solid (29 mg, 20% yield). ^{1}H NMR (400 MHz; $CDCl_3$, 25 °C) δ/ppm: 8.85 (s, 1H), 8.37 (s, 1H), 8.21 (d, J=12.9 Hz, 1H), 7.01 (s, 2H), 6.98 (d, J=1.9 Hz, 1H), 6.90 (s, 2H), 6.71 (s, 1H), 6.28 (d, J=12.8 Hz, 1H), 2.44 (s, 3H), 2.31 (d, J=2.5 Hz, 6H), 2.14 (s, 3H), 2.08 (s, 3H), 1.74 (s, 3H), 1.03 (d, J=10.9 Hz, 9H). ^{13}C NMR (101 MHz; $CDCl_3$, 25 °C) δ/ppm: 166.55 (d, $J_{P,C}$=174.5 Hz) 164.81 (d, $J_{P,C}$=6.6 Hz), 140.26, 139.23, 137.39, 135.76, 135.51, 133.98, 133.64, 133.49, 130.44, 129.00, 128.40, 124.33, 124.19, 124.13, 123.61, 122.58, 62.64, 21.91, 21.29, 21.00, 19.77, 19.37, 17.71, 16.31 (d, $J_{P,C}$=33.1 Hz). ^{31}P NMR (162 MHz; $CDCl_3$, 25 °C) δ/ppm: -15.56. HR-LIFDI-MS: $[M]^+$−Br m/z calc: 647.0972. Found: 647.0959

2.7.4.2 [(1,1'-di(mesityl)-3,3'-methylenediimidazolin-2,2'-diylidene) palladium(II)-(*tert*-butyl isocyanide)bromide]bromide, [(MDC^{Mes})Pd(^{t}BuNC)Br]Br

A mixture of 65 mg of (MDC^{Mes})PdBr$_2$ (0.1 mmol) and 50 μL *tert*-butyl isocyanide were allowed to stir in 7 mL of THF at room temperature for 4 h. After an hour, a precipitate formed and was eventually collected and dried *in vacuo* to give an off-white solid (70 mg, 95% yield). ^{1}H NMR (400 MHz; $CDCl_3$, 25 °C) δ/ppm: 7.82 (s, 1H), 7.77 (s, 1H), 7.18 (s, 1H), 7.11 (s, 2H), 7.08 (s, 1H), 6.95 (s, 2H), 6.46 (broad s, 2H), 2.35 (s, 3H), 2.30 (s, 3H), 2.04 (s, 6H), 2.00 (broad s, 6H), 1.22 (s, 9H). ^{13}C NMR (101 MHz; $CDCl_3$, 25 °C) δ/ppm: 159.62, 157.99, 140.31, 140.26, 139.37, 139.32, 135.64, 134.92, 129.71, 129.68, 124.47, 124.30, 123.11, 122.86, 61.86, 58.73, 29.56, 29.50, 21.24, 21.19. ν (^{t}BuNC): 2218 cm^{-1} HR-LIFDI-MS: $[M]^{+}$−Br m/z calc: 654.1266. Found: 654.1268.

2.7.5 Synthesis of [(MDC^{R})Pd($CH_3CN)_2$]($PF_6)_2$ (R = Mes, Me, iPr, Ph, Cy, DIPP)

2.7.5.1 [(1,1'-di(mesityl)-3,3'-methylenediimidazolin-2,2'-diylidene) palladium(II)-bis(acetonitrile)][$(PF_6)]_2$, [(MDC^{Mes})Pd($CH_3CN)_2$](PF_6)

[(MDC^{Mes})Pd($CH_3CN)_2$](PF_6) was synthesized according to a method developed in our laboratory.[13]

2.7.5.2 [(1,1'-dimethyl-3,3'-methylenediimidazolin-2,2'-diylidene) palladium(II)-bis(acetonitrile)][$(PF_6)]_2$, [(MDC^{Me})Pd($CH_3CN)_2$](PF_6)

A mixture of (1,1'-dimethyl -3,3'-methylenediimidazolin-2,2'-diylidene)palladium(II)bromide (123 mg, 0.28 mmol) and $AgPF_6$ (140 mg, 0.56 mmol) in acetonitrile was stirred at 65 °C for 4 h in the dark. The mixture was filtered through celite, then solvent was removed *in vacuo*. The resulting light yellow solid

was dissolved in a minimal amount of acetonitrile (~2 mL) and added to 200 mL of diethyl ether, resulting in a light yellow precipitate. The precipitate was collected and dried under vacuum to give a light yellow solid (106 mg, 58% yield). ^{1}H NMR (400 MHz; CD_3CN, 25 °C) δ/ppm: 7.43 (d, J=1.9 Hz, 2H), 7.17 (d, J=1.9 Hz, 2H), 6.19 (d, J=12.1 Hz, 1H), 6.07 (d, J=12.4 Hz, 1H), 3.86 (s, 6H), 1.96 (s, 6H). ^{13}C NMR (101 MHz; CD_3CN, 25 °C) δ/ppm: 147.88, 124.94, 123.71, 63.68, 38.79. ^{31}P NMR (162 MHz, CD_3CN, 25 °C) δ/ppm: -144.63 (sept). Anal. Calc. for $C_{13}H_{18}F_{12}N_6P_2Pd$: C, 23.85; H, 2.77; N 12.84. Found: C, 23.95; H, 2.70; N, 12.57.

2.7.5.3 [(1,1'-diisopropyl-3,3'-methylenediimidazolin-2,2'-diylidene) palladium(II)-bis(acetonitrile)][$(PF_6)]_2$, [$(MDC^{iPr})Pd(CH_3CN)_2](PF_6)$

A mixture of 1,1'-diisopropyl -3,3'-methylenediimidazolin-2,2'-diylidene)palladium(II)bromide (200 mg, 0.40 mmol) and $AgPF_6$ (203 mg, 0.80 mmol) in acetonitrile was stirred at 65 °C for 4 h in the dark. The mixture was filtered through celite, then solvent was removed *in vacuo*. The resulting yellow solid was dissolved in a minimal amount of acetonitrile (~2 mL) and added to 200 mL of diethyl ether, resulting in a light yellow precipitate. The precipitate was collected and dried under vacuum to give a light yellow solid (212 mg, 75% yield). ^{1}H NMR (400 MHz; CD_3CN, 25 °C) δ/ppm: 7.48 (d, J=2.0 Hz, 2H), 7.28 (d, J=2.0 Hz, 2H), 6.19 (d, J=13.2 Hz, 1H), 6.05 (d, J=13.2 Hz, 1H), 4.83 (sept, J=6.7 Hz, 2H), 1.96 (s, 6H), 1.50 (d, J=6.7 Hz, 6H), 1.38 (d, J=6.7 Hz, 6H). ^{13}C NMR (101 MHz; CD_3CN, 25 °C) δ/ppm: 146.25, 124.55, 119.79, 63.55, 54.36, 23.81, 22.69. ^{31}P NMR (162 MHz; CD_3CN, 25 °C) δ/ppm: -144.65 (sept). Anal. Calc. for $C_{17}H_{26}F_{12}N_6P_2Pd$: C, 28.73; H, 3.69; N 11.82. Found: C, 28.92; H, 3.77; N, 11.53.

2.7.5.4 [(1,1'-diphenyl-3,3'-methylenediimidazolin-2,2'-diylidene) palladium(II)-bis(acetonitrile)][$(PF_6)]_2$, [$(MDC^{Ph})Pd(CH_3CN)_2](PF_6)$

A mixture of (1,1'-diphenyl-3,3'-methylenediimidazolin-2,2'-diylidene) palladium(II)bromide (100 mg, 0.175 mmol) and $AgPF_6$ (89 mg, 0.35 mmol) in acetonitrile was stirred at 65 °C for 4 h in the dark. The mixture was filtered through celite, then solvent was removed *in vacuo*. The resulting off-white solid was dissolved in a minimal amount of acetonitrile (~2 mL) and added to 200 mL of diethyl ether, resulting in an off-white precipitate. The precipitate was collected and dried under vacuum to give an off-white solid (55 mg, 40% yield). ^{1}H NMR (400 MHz; CD_3CN, 25 °C) δ/ppm: 7.66-7.78 (m, 12H), 7.55 (s, 2H), 6.38 (s, 2H), 1.96 (s, 6H). ^{13}C NMR (101 MHz; CD_3CN, 25 °C) δ/ppm: 147.78, 139.27, 131.27, 131.05, 126.21, 124.86, 124.37, 64.04. ^{31}P NMR (162 MHz, CD_3CN, 25 °C) δ/ppm: -144.64 (sept). Anal. Calc. for $C_{23}H_{22}F_{12}N_6P_2Pd$: C, 35.47; H, 2.85; N 10.79. Found: C, 35.42; H, 2.85; N, 10.57.

2.7.5.5 [(1,1'-di(cyclohexyl)-3,3'-methylenediimidazolin-2,2'-diylidene) palladium(II)-bis(acetonitrile)][$(PF_6)]_2$, [$(MDC^{Cy})Pd(CH_3CN)_2](PF_6)$

A mixture of (1,1'-dicyclohexyl-3,3'-methylenediimidazolin-2,2'-diylidene) palladium(II)bromide (200 mg, 0.35 mmol) and $AgPF_6$ (175 mg, 0.70 mmol) in acetonitrile was stirred at 65 °C for 4 h in the dark. The mixture was filtered through celite, then solvent was removed *in vacuo*. The resulting off-white solid was dissolved in a minimal amount of acetonitrile (~2 mL) and added to 200 mL of diethyl ether, resulting in an off-white precipitate. The precipitate was collected and dried under vacuum to give an off-white solid (143 mg, 52% yield). ^{1}H NMR (400 MHz; CD_3CN, 25 °C) δ/ppm: 7.47 (d, J=2.0 Hz, 2H), 7.26 (d, J=2.0 Hz, 2H), 6.18 (d, J=13.3 Hz, 1H), 6.06 (d, J=13.3 Hz, 1H), 4.46 (td, J=10.0, 8.3, 3.6 Hz, 2H), 1.96 (s, 6H) 1.24-1.86 (m, 20H). ^{13}C NMR (101 MHz; CD_3CN, 25 °C) δ/ppm: 146.35, 124.39, 120.44, 63.65,

61.30, 34.71, 33.88, 26.05, 25.58. ^{31}P NMR (162 MHz; CD_3CN, 25 °C) δ/ppm: -144.64 (sept). Anal. Calc. for $C_{23}H_{34}F_{12}N_6P_2Pd$: C, 34.93; H, 4.33; N 10.63. Found: C, 34.70; H, 4.25; N, 10.34.

2.7.5.6 [(1,1'-di-2,6-diisopropylphenyl -3,3'-methylenediimidazolin-2,2'-diylidene) palladium(II)-bis(acetonitrile)][(PF_6)]$_2$, [$(MDC^{DIPP})Pd(CH_3CN)_2$](PF_6)

A mixture of (1,1'-di-2,6-diisopropylphenyl-3,3'-methylenediimidazolin-2,2'-diylidene)palladium(II)bromide (200 mg, 0.27 mmol) and $AgPF_6$ (137 mg, 0.54 mmol) in acetonitrile was stirred at 65 °C for 4 h in the dark. The mixture was filtered through celite, then solvent was removed *in vacuo*. The resulting off-white solid was dissolved in a minimal amount of acetonitrile (~2 mL) and added to 200 mL of diethyl ether, resulting in a white precipitate. The precipitate was collected and dried under vacuum to give a white solid (140 mg, 55% yield). ^{1}H NMR (400 MHz; CD_3CN, 25 °C) δ/ppm: 7.69 (d, J=2.0 Hz, 2H), 7.54 (m, 2H), 7.41 (d, J=7.8 Hz, 4H), 7.35 (d, J=2.0 Hz, 2H), 2.52 (sept, J=6.8 Hz, 4H), 1.96 (s, 6H), 1.30 (d, J=6.8 Hz, 12H), 1.09 (d, J=6.8 Hz, 12H). ^{13}C NMR (101 MHz; CD_3CN, 25 °C) δ/ppm: 146.93, 144.74, 135.53, 132.74, 128.09, 125.37, 123.80, 63.37, 29.20, 25.26, 23.78. ^{31}P NMR (162 MHz; CD_3CN, 25 °C) δ/ppm: -144.65 (sept). Anal. Calc. for $C_{35}H_{46}F_{12}N_6P_2Pd$: C, 44.38; H, 4.90; N 8.87. Found: C, 44.59; H, 4.64; N, 9.06.

2.7.6 X-ray Crystallography

2.7.6.1 X-ray Structure Solution and Refinement for [$(MDC^{R})Pd(CH_3CN)_2$]$(PF_6)_2$

Crystals were mounted using viscous oil onto a plastic mesh and cooled to the data collection temperature. Data were collected on a Smart APEX diffractometer with

Mo-Kα radiation (λ = 0.71073 Å) monochromated with graphite except $[(MDC^{DIPP})Pd(CH_3CN)_2](PF_6)_2$ which was collected using Cu- Kα radiation (λ = 1.54178 Å) focused using Goebel mirrors. Unit cell parameters were obtained from 36 data frames, 0.5º ω, from three different sections of the Ewald sphere. The unit-cell parameters, equivalent reflections, and systematic absences in the diffraction data are consistent, uniquely, with $P2_1/c$ (or $P2_1/n$ no. 14) for $[(MDC^{Ph})Pd(CH_3CN)_2](PF_6)_2$; uniquely; *Pbca* (no. 61) for $[(MDC^{DIPP})Pd(CH_3CN)_2](PF_6)_2$; $P2_1/m$ (no. 11) and $P2_1$ for $[(MDC^{Me})Pd(CH_3CN)_2](PF_6)_2$; and for *Pnma* (no. 62) and $Pna2_1$ ($Pn2_1a$) for $[(MDC^{Cy})Pd(CH_3CN)_2](PF_6)_2$. No symmetry higher than triclinic was observed in $[(MDC^{iPr})Pd(CH_3CN)_2](PF_6)_2$. Solutions in the centrosymmetric space group options yielded chemically reasonable and computationally stable results of refinement. The data sets were treated with multi-scan absorption corrections.[47] The structures were solved using direct methods and refined with full-matrix, least-squares procedures on F^2.[48] The compound was located at a mirror plane for $[(MDC^{Cy})Pd(CH_3CN)_2](PF_6)_2$ and $[(MDC^{Me})Pd(CH_3CN)_2](PF_6)_2$. An acetonitrile molecule of solvation was located in $[(MDC^{DIPP})Pd(CH_3CN)_2](PF_6)_2$. A half-occupied, disordered diethylether molecule of solvation was located near the origin in $[(MDC^{iPr})Pd(CH_3CN)_2](PF_6)_2$. All non-hydrogen atoms were refined with anisotropic displacement parameters. H-atoms were placed in calculated positions with U_{iso} equal to 1.2 (1.5 for methyl H) U_{eq} of the attached atom. Atomic scattering factors are contained in the SHELXTL program library. Crystallographic data were collected by Gabriel Andrade or Dr. Glenn Yap, Department of Chemistry and Biochemistry, University of Delaware.

2.7.6.2 Crystallography Tables

Table 2.5: Crystallographic data for $[(MDC^{R})Pd(CH_3CN)_2](PF_6)_2$

Formula	R = Me	iPr	Ph
Fw	736.78	747.84	519.20
Crystal System	monoclinic	triclinic	monoclinic
Space Group	$P2_1/m$	P-1	$P2_1/c$
a	7.7500(11) Å	11.4987(8) Å	11.3482(13) Å
b	10.0188(14) Å	11.8131(8) Å	20.928(2) Å
c	18.175(3) Å	13.0125(9) Å	12.9218(15) Å
α	90°	78.1353(9)°	90°
β	90.175(2)°	71.5338(10)°	106.868(2)°
γ	90°	67.8588(9)°	90°
Volume	1411.2(3) $Å^3$	1545.42(18) $Å^3$	2939.1(6) $Å^3$
Z	2	2	6
Temp	293(2)K	200(2) K	200(2) K
D_{calcd}	1.734 g/cm^3	1.607 g/cm^3	1.760 g/cm^3
2Θ range	2.03 to 27.65°	1.98 to 27.82°	1.88 to 27.76°
μ (Mo Kα)	0.874 mm^{-1}	0.798 mm^{-1}	0.843 mm^{-1}
Reflections	18349	20528	55830
Unique	3427	7257	6855
R (int)	0.0624	0.0254	0.1032
R_1	0.0574	0.0526	0.0446
wR_2	0.1492	0.1655	0.1062

Table 2.5: (cont.)

Formula	R = Cy	DIPP
Fw	790.90	988.17
Crystal System	orthorhombic	orthorhombic
Space Group	Pnma	Pbca
a	17.019(3) Å	21.5523(6) Å
b	13.722(2) Å	17.0961(5) Å
c	14.020(2) Å	23.8470(6) Å
α	90°	90°
β	90°	90°
γ	90°	90°
Volume	3274.2(9) $Å^3$	8786.7(4) $Å^3$
Z	4	8
Temp	200(2) K	200(2) K
D_{calcd}	1.604 g/cm^3	1.494 g/cm^3
2Θ range	1.88 to 27.61°	3.79 to 74.60°
μ (Mo Kα)	0.758 mm^{-1}	4.872 mm^{-1}
Reflections	37489	104104
Unique	3952	8956
R (int)	0.0538	0.1450
R_1	0.0923	0.0648
wR_2	0.2828	0.1958

2.8 References and Notes

(1) Ariyananda, P. W. G.; Yap, G. P. A.; Rosenthal, J. *Dalton Trans.* **2012**, *41* (26), 7977.

(2) Díez-González, S.; Nolan, S. P. *Coord. Chem. Rev.* **2007**, *251* (5–6), 874.

(3) Jacobsen, H.; Correa, A.; Poater, A.; Costabile, C.; Cavallo, L. *Coord. Chem. Rev.* **2009**, *253* (5–6), 687.

(4) Glorius, F. In *N-Heterocyclic Carbenes in Transition Metal Catalysis*; Springer Berlin Heidelberg: Berlin, Heidelberg. **2007**, *21*, 1–20.

(5) Díez-González, S.; Marion, N.; Nolan, S. P. *Chem. Rev.* **2009**, *109* (8), 3612.

(6) (a) Singh, A. K.; Singh, S.; Kumar, A. *Catal. Sci. Technol.* **2016**, *6* (1), 12. (b) Enthaler, S.; von Langermann, J.; Schmidt, T. *Energy Environ. Sci.* **2010**, *3* (9), 1207.

(7) For example: (a) Boddien, A.; Loges, B.; Gärtner, F.; Torborg, C.; Fumino, K.; Junge, H.; Ludwig, R.; Beller, M. *J. Am. Chem. Soc.* **2010**, *132* (26), 8924. (b) Boddien, A.; Mellmann, D.; Gärtner, F.; Jackstell, R.; Junge, H.; Dyson, P. J.; Laurenczy, G.; Ludwig, R.; Beller, M. *Science.* **2011**, *333* (6050), 1733. (c) Bielinski, E. A.; Lagaditis, P. O.; Zhang, Y.; Mercado, B. Q.; Würtele, C.; Bernskoetter, W. H.; Hazari, N.; Schneider, S. *J. Am. Chem. Soc.* **2014**, *136* (29), 10234. (d) Zell, T.; Butschke, B.; Ben-David, Y.; Milstein, D. *Chem. – A Eur. J.* **2013**, *19* (25), 8068.

(8) Grasemann, M.; Laurenczy, G. *Energy Environ. Sci.* **2012**, *5* (8), 8171.

(9) Broggi, J.; Jurčík, V.; Songis, O.; Poater, A.; Cavallo, L.; Slawin, A. M. Z.; Cazin, C. S. J. *J. Am. Chem. Soc.* **2013**, *135* (12), 4588.

(10) Gardiner, M. G.; Herrmann, W. A.; Reisinger, C.-P.; Schwarz, J.; Spiegler, M. *J. Organomet. Chem.* **1999**, *572* (2), 239.

(11) Subramanium, S. S.; Handa, S.; Miranda, A. J.; Slaughter, L. M. *ACS Catal.* **2011**, *1* (10), 1371.

(12) Heckenroth, M.; Khlebnikov, V.; Neels, A.; Schurtenberger, P.; Albrecht, M. *ChemCatChem* **2011**, *3* (1), 167.

(13) Eddy, J. W.; Ariyananda, P. W. G.; Yap, G. P. A.; Rosenthal, J. *Manuscript in Prep*. **2016**

(14) Wang, H. M. J.; Lin, I. J. B. *Organometallics* **1998**, *17* (5), 972.

(15) Wanniarachchi, Y. A.; Khan, M. A.; Slaughter, L. M. *Organometallics* **2004**, *23* (25), 5881.

(16) Budagumpi, S.; Endud, S. *Organometallics* **2013**, *32* (6), 1537.

(17) Jochmann, P.; Stephan, D. W. *Angew. Chem. Int. Ed.* **2013**, *52* (37), 9831.

(18) Jochmann, P.; Stephan, D. W. *Chem. – A Eur. J.* **2014**, *20* (27), 8370.

(19) Fliedel, C.; Mameri, S.; Dagorne, S.; Avilés, T. *Appl. Organomet. Chem.* **2014**, *28* (7), 504.

(20) Schnee, G.; Fliedel, C.; Avilés, T.; Dagorne, S. *Eur. J. Inorg. Chem.* **2013**, (21), 3699.

(21) Bantu, B.; Manohar Pawar, G.; Wurst, K.; Decker, U.; Schmidt, A. M.; Buchmeiser, M. R. *Eur. J. Inorg. Chem.* **2009**, (13), 1970.

(22) Wang, D.; Wurst, K.; Buchmeiser, M. R. *J. Organomet. Chem.* **2004**, *689* (12), 2123.

(23) Jensen, T. R.; Schaller, C. P.; Hillmyer, M. A.; Tolman, W. B. *J. Organomet. Chem.* **2005**, *690* (24–25), 5881.

(24) Lee, Y.; Li, B.; Hoveyda, A. H. *J. Am. Chem. Soc.* **2009**, *131* (32), 11625.

(25) Merle, N.; Törnroos, K. W.; Jensen, V. R.; Le Roux, E. *J. Organomet. Chem.* **2011**, *696* (8), 1691.

(26) Zheng, X.-X.; Zhang, C.; Wang, Z.-X. *J. Organomet. Chem.* **2015**, *783*, 105.

(27) Xu, S.; Everett, W. C.; Ellern, A.; Windus, T. L.; Sadow, A. D. *Dalton Trans.* **2014**, *43* (38), 14368.

(28) Rit, A.; Spaniol, T. P.; Okuda, J. *Chem. – Asian J.* **2014**, *9* (2), 612.

(29) Laine, R. M.; Rinker, R. G.; Ford, P. C. *J. Am. Chem. Soc.* **1977**, *99* (1), 252.

(30) Gao, Y.; Kuncheria, J.; J. Puddephatt, R.; P. A. Yap, G. *Chem. Commun.* **1998**, 21, 2365.

(31) Fellay, C.; Dyson, P. J.; Laurenczy, G. *Angew. Chemie Int. Ed.* **2008**, *47* (21), 3966.

(32) Loges, B.; Boddien, A.; Junge, H.; Beller, M. *Angew. Chemie Int. Ed.* **2008**, *47* (21), 3962.

(33) Berger, M. E. M.; Assenbaum, D.; Taccardi, N.; Spiecker, E.; Wasserscheid, P. *Green Chem.* **2011**, *13* (6), 1411.

(34) Enthaler, S.; Junge, H.; Fischer, A.; Kammer, A.; Krackl, S.; Epping, J. D. *Polym. Chem.* **2013**, *4* (9), 2741.

(35) Morris, D. J.; Clarkson, G. J.; Wills, M. *Organometallics* **2009**, *28* (14), 4133.

(36) Tanaka, R.; Yamashita, M.; Chung, L. W.; Morokuma, K.; Nozaki, K. *Organometallics* **2011**, *30* (24), 6742.

(37) Hull, J. F.; Himeda, Y.; Wang, W.-H.; Hashiguchi, B.; Periana, R.; Szalda, D. J.; Muckerman, J. T.; Fujita, E. *Nat Chem* **2012**, *4* (5), 383.

(38) Boddien, A.; Mellmann, D.; Gärtner, F.; Jackstell, R.; Junge, H.; Dyson, P. J.; Laurenczy, G.; Ludwig, R.; Beller, M. *Science.* **2011**, *333* (6050), 1733.

(39) Ariyananda, P. W. G.; Rosenthal, J. *Unpublished Results*.

(40) Chen, C.; Chen, W.; Qiu, H. *Dalton Trans.* **2012**, *41* (43), 13405.

(41) Okuyama, K.; Sugiyama, J.; Nagahata, R.; Asai, M.; Ueda, M.; Takeuchi, K. *J. Mol. Catal. A Chem.* **2003**, *203* (1–2), 21

(42) Slootweg, J. C.; Chen, P. *Organometallics* **2006**, *25* (25), 5863.

(43) Micksch, M.; Strassner, T. *Eur. J. Inorg. Chem.* **2012**, (35), 5872.

(44) Scherg, T.; Schneider, S. K.; Frey, G. D.; Schwarz, J.; Herdtweck, E.; Herrmann, W. A. *Synlett* **2006**, (18), 2894.

(45) Pangborn, A. B.; Giardello, M. A.; Grubbs, R. H.; Rosen, R. K.; Timmers, F. J. *Organometallics.* **1996,** *15* (5), 1518.

(46) Kreisel, K. A.; Yap, G. P. A.; Theopold, K. H. *Organometallics* **2006**, *25* (19), 4670.

(47) Apex3 software suite, Madison, WI, 2015

(48) Sheldrick, G. M. *Acta Crystallogr. Sect. A* **2008**, *64* (1), 112.

Chapter 3

MECHANISTIC STUDIES AND TURNOVER STUDIES OF FORMIC ACID DEHYDROGENATION

3.1 Introduction

The mechanism for formic acid dehydrogenation to produce hydrogen and carbon dioxide has been studied by several groups. Of those studies[1-5] that appeared most relevant to our work (see Chapter 2), a general scheme can be derived: (A) binding of formate to the catalyst, M^+, to give a metal formato complex, (B) β-hydride elimination of the formate to generate the metal hydride and release carbon dioxide, (C) protonation of the hydride and release of hydrogen with concomitant regeneration of the starting catalyst (Figure 3.1).

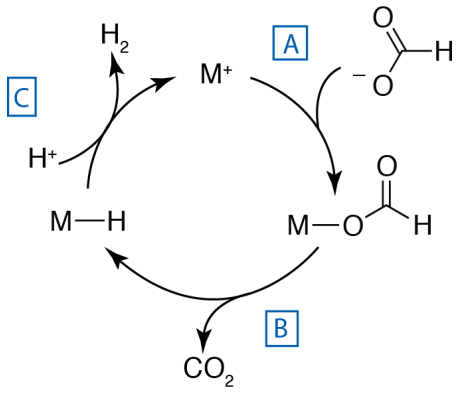

Figure 3.1: General catalytic cycle for production of hydrogen and carbon dioxide from formic acid

The mechanisms from these previous studies were proposed based on findings from deuterium labeling studies,[1,6] NMR spectroscopy studies,[2,4,6] and density functional theory (DFT) calculations.[3,5] Several studies[2,4-6] also propose competing cycles where the first step of the cycle is protonation of the metal hydride catalyst, followed by release of hydrogen, binding of formate, and finally β-hydride elimination to produce carbon dioxide and regenerate the starting metal hydride complex. However, since our active catalyst is not proposed to be a metal hydride, we did not find this competing reaction cycle to be relevant to our work.

In addition to the methods described above, Arrhenius and Eyring analyses can also be useful in mechanistic studies. More specifically, the plots derived from these analyses can be useful in determining the activation parameters for a reaction. The Arrhenius rate law (equation 3.1) shows that the rates of reactions increase exponentially as temperature is increased, where A is the Arrhenius pre-exponential factor, E_a is the activation energy, T is the temperature and R is the gas constant. By using the logarithmic form of the Arrhenius rate law plotting ln k versus T^{-1} yields a slope that is equal to $-E_a/R$ (equation 3.2). Therefore, the E_a for a reaction can be derived using an Arrhenius plot.

$$k = \mathrm{A}e^{(-\mathrm{E_a}/\mathrm{RT})} \tag{3.1}$$

$$\ln(k) = -\left(\frac{\mathrm{E_a}}{\mathrm{R}}\right)\left(\frac{1}{\mathrm{T}}\right) + \ln(\mathrm{A}) \tag{3.2}$$

A complimentary method to the Arrhenius analysis is the Eyring analysis.[7] As shown in equation 3.3, the Eyring analysis is used to determine the entropy and enthalpy of activation, where k_B is Boltzmann's constant, h is Planck's constant, R is

the gas constant, T is temperature, $\Delta H^{\ddagger}$ is the enthalpy of activation and $\Delta S^{\ddagger}$ is the entropy of activation. By taking the natural log of both sides of equation 3.3, plotting $\ln(kh/k_BT)$ versus T^{-1} gives a line with a slope equal to $-\Delta H^{\ddagger}/R$ and intercept equal to $\Delta S^{\ddagger}/R$ (equation 3.4).

$$k = \frac{k_B T}{h} \exp\left(-\frac{\Delta H^{\ddagger}}{RT} + \frac{\Delta S^{\ddagger}}{R}\right) \quad 3.3$$

$$\ln\left(\frac{kh}{k_B T}\right) = -\frac{\Delta H^{\ddagger}}{R}\left(\frac{1}{T}\right) + \frac{\Delta S^{\ddagger}}{R} \quad 3.4$$

The previous chapter explored our work in the development of a new type of formic acid dehydrogenation catalyst, $[(MDC^{Mes})Pd(MeCN)_2](PF_6)_2$. This catalyst was modified by varying the wingtip groups on the NHC nitrogens or replacing the MeCN ligands around the palladium center with a variety of different types of ligands. In this chapter, we will take the observations from these studies, as well as several kinetic and ^{1}H NMR spectroscopy studies, to propose and study a mechanism for the formic acid dehydrogenation reaction with our catalyst. In addition, from this proposed mechanism, we will explore ways to increase the overall activity of our catalyst.

3.2 Proposed Mechanism

Our previous studies show lower activity for formic acid dehydrogenation when acetonitrile (MeCN) is replaced with a less labile coordinating ligand (Chapter 2). Therefore, it is concluded that an open coordination site is necessary to produce the desired hydrogen and carbon dioxide products. The need for open coordination sites is presumed due to the β-hydride elimination step following binding of formate to the

metal center. A traditional β-hydride elimination would necessitate the use of two open coordination sites; however, DFT calculations of other formic acid reaction cycles showed that a non-classical intramolecular β-hydride elimination was more favorable in some cases.[3,8] This non-classical mechanism proposes the dissociation of the formate ion and reorganization so that the formate ion is coordinated to the metal via the hydrogen atom, followed by production of the metal hydride and carbon dioxide through a hydride transfer. Consequently, this mechanism does not require the need for a second open coordination site. Therefore, to explore if this latter mechanism is feasible in our catalytic cycle we also tested the pyridyl and lutidyl spaced complexes, shown in Figure 3.2, for formic acid dehydrogenation using the optimized reaction conditions (see Section 3.5.2.1). These complexes, with an analogous ligand motif to our most active catalyst ($[(MDC^{Mes})Pd(MeCN)_2](PF_6)_2$) but with only one open coordination site at the palladium center, are not active for formic acid dehydrogenation (TON = 0). This supports the conclusion that two open coordination sites are necessary for the desired production of hydrogen and carbon dioxide from formic acid.

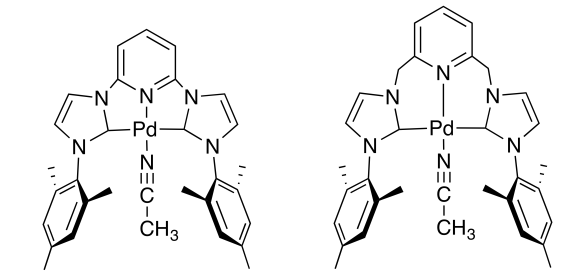

Figure 3.2: Structures of pyridyl (left) and lutidyl (right) spaced NHC palladium complexes

Based on the studies mentioned thus far and previous literature mechanisms,[1-6] we propose the mechanism shown in Figure 3.3. The proposed steps of the mechanism are as follows: binding of formate to the palladium center via an associative addition (step A in Figure 3.3), dissociation of an MeCN ligand (B), loss of the second MeCN ligand to provide an open coordination site on palladium (C), β - hydride elimination to produce carbon dioxide and the corresponding palladium hydride species (D), coordination of an MeCN ligand at the open coordination site (E), and finally protonation of the hydride species to produce hydrogen and regenerate the active catalyst (F).

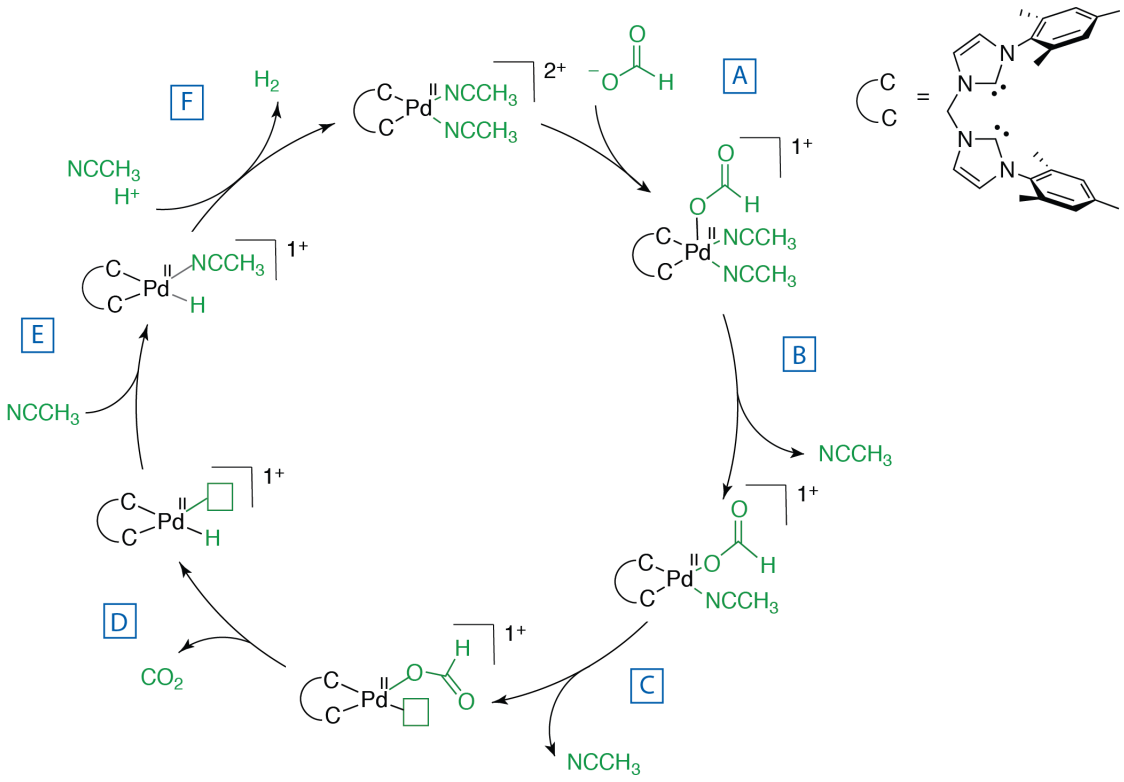

Figure 3.3: Proposed mechanism for formic acid dehydrogenation to produce hydrogen and carbon dioxide with $[(MDC^{Mes})Pd(MeCN)_2](PF_6)_2$

3.2.1 Mechanistic Kinetic Studies

In order to better understand and support our proposed mechanism, studies were performed to determine the effect that varying the concentration of formic acid and catalyst has on the reaction rate. Additionally, Eyring and Arrhenius analyses were performed to determine the activation parameters of the reaction, which ultimately led to the proposal of a rate determining step for the catalytic cycle.

3.2.1.1 Relationship of Reaction Rate to Concentration of Formic Acid and Catalyst

The concentration of catalyst in solution was varied between 4.5 and 90 mM and the rate of production of carbon dioxide and hydrogen was measured via water displacement. A double logarithmic plot of the initial rate versus the concentration of catalyst shows a linear dependence on the palladium catalyst concentration (Figure 3.4). Furthermore, the plot yields a straight line with a slope of 0.94, indicating that the reaction is first order in palladium. This suggests that the active catalyst is homogeneous, and no catalytically active palladium nanoparticles are formed during the reaction.

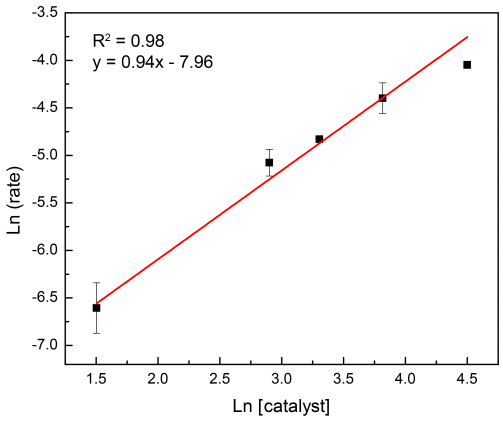

Figure 3.4: Double logarithmic plot of the initial rate versus the catalyst concentration

The dependence of the reaction rate on the concentration of formic acid was determined by varying the concentration of formic acid between 0.91 M and 9.09 M, while maintaining a constant concentration of catalyst. The double logarithmic plot showed a linear dependence between the reaction rate and formic acid at lower concentrations of the latter (Figure 3.5). At higher concentrations of formic acid, there was no further increase in reaction rate due to saturation kinetics. The linear dependence at lower concentrations suggests that one molecule of formate binds to the palladium catalyst. This most likely occurs before the rate determining step with an equilibrium between the initial palladium catalyst ($[(MDC^{Mes})Pd(MeCN)_2](PF_6)_2$) and the palladium catalyst with formate bound ($[(MDC^{Mes})Pd(MeCN)_2(OCHO)](PF_6)$ (step A).

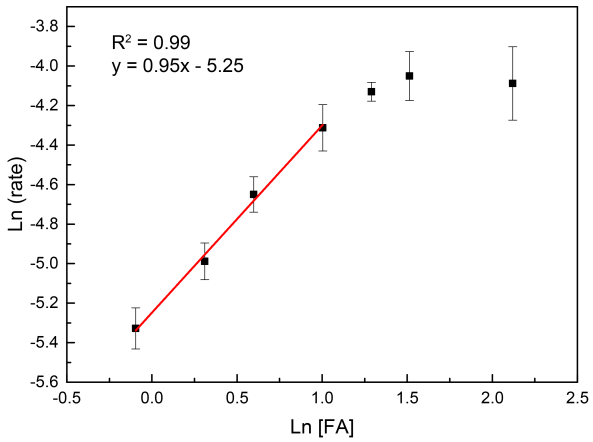

Figure 3.5: Double logarithmic plot of the initial rate versus the formic acid (FA) concentration

3.2.1.2 Eyring and Arrhenius Analysis

The temperature dependence of the reaction was monitored and studied using two different plots: Arrhenius and Eyring. From the slope of the Arrhenius plot (Figure 3.6) the energy of activation, E_a, was determined to be 101.9 (± 6.9) kJ·mol^{-1}. This is comparable to activation energies for other homogeneous formic acid dehydrogenation catalysts (77-110 kJ·mol^{-1}),[5,9] and well below the uncatalyzed reaction (325 kJ·mol^{-1}).[10]

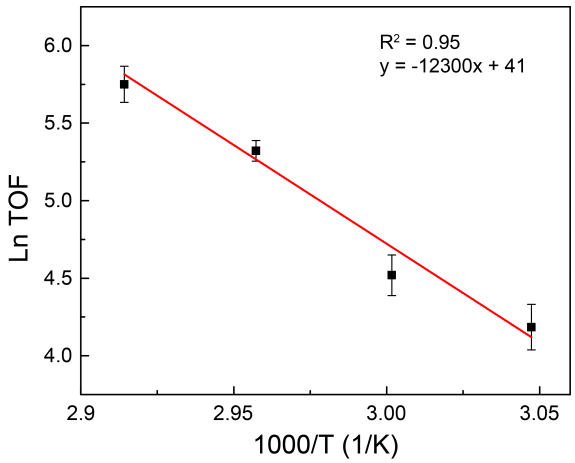

Figure 3.6: Arrhenius plot for formic acid dehydrogenation with $[(MDC^{Mes})Pd(MeCN)_2](PF_6)_2$

The enthalpy ($\Delta H^{\ddagger}$) and entropy ($\Delta S^{\ddagger}$) of activation were determined from the slope and y-intercept of the Eyring plot, respectively (Figure 3.7). The enthalpy of activation was determined to be 105.2 (± 6.2) kJ·mol^{-1} and the entropy of activation was determined to be 108.5 (± 18.5) J·mol^{-1}K^{-1}. A summary of the activation parameters for production of hydrogen from formic acid using $[(MDC^{Mes})Pd(MeCN)_2](PF_6)_2$ is listed in Table 3.1.

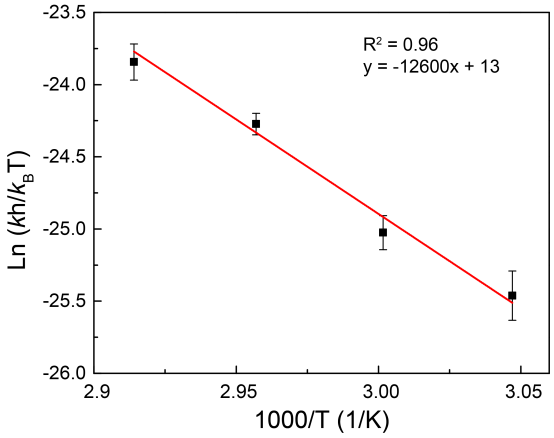

Figure 3.7: Eyring plot for formic acid dehydrogenation with $[(MDC^{Mes})Pd(MeCN)_2](PF_6)_2$

Table 3.1: Activation parameters for formic acid dehydrogenation with $[(MDC^{Mes})Pd(MeCN)_2](PF_6)_2$

E_a	101.9 (± 6.9) kJ·mol^{-1}
$\Delta H^{‡}$	105.2 (± 6.2) kJ·mol^{-1}
$\Delta S^{‡}$	108.5 (± 18.5) J·mol^{-1}K^{-1}

In general, the $\Delta H^{‡}$ of the reaction provides information on the formation and cleavage of bonds in the transition state. The large value of $\Delta H^{‡}$ for this reaction (105 kJ·mol^{-1}) indicates not only a net bond cleavage at the transition state for the rate determining step, but also transitioning from a stable complex to a less stable intermediate. The $\Delta S^{‡}$ indicates the amount of disorder in the transition state. The large, positive value of $\Delta S^{‡}$ (108.5 J·mol^{-1}K^{-1}) represents an increase in the degree of disorder at the transition state resulting from an overall increase in the number of molecules. This increase in the number of molecules can be indicative of a dissociative mechanism.

3.2.1.3 Rate Determining Step

Based on these kinetic studies, the rate determining step was proposed as the production of an open coordination site on the palladium complex, step C in Figure 3.3 and shown in Scheme 3.1. This is in agreement with the results of the double logarithmic plot of reaction rate versus concentration of formic acid, since we propose one molecule of formate binds before this rate determining step (step A in Figure 3.3). The large $\Delta H^{\ddagger}$ (105 $kJ \cdot mol^{-1}$) from the Eyring analysis also supports this rate determining step since the intermediate is transitioning from a stable four coordinate, 16 e^{-}, d^{8} square planar complex to a much less stable three coordinate, 14 e^{-} species. The large, positive value of $\Delta S^{\ddagger}$ (108.5 $J \cdot mol^{-1}K^{-1}$) is in agreement with the dissociation of MeCN and the increasing degrees of disorder caused by the increase in the number of molecules.

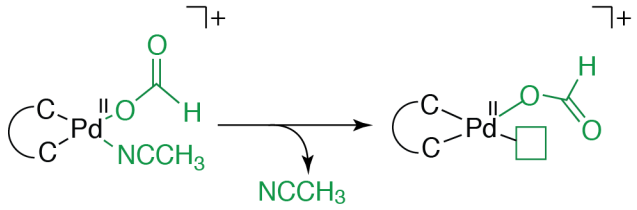

Scheme 3.1: Proposed rate determining step

3.2.2 Calculation of pK_as in MeCN

For the final step of the proposed mechanism (Figure 3.3, step F), the palladium hydride species is protonated to generate hydrogen gas and reform the starting catalyst. The identity of the protonating species in the mechanism is shown as a general "H^{+}". There are two possible species in solution which most likely protonate the hydride: either formic acid or the conjugate acid of triethylamine formed from

deprotonation of formic acid in solution, triethylammonium. In order to gain a better understanding of the species more likely to protonate the hydride, DFT calculations were performed to determine the pK_a of formic acid in MeCN, since this value could not be found in the literature. The pK_a of the triethylammonium in MeCN is a literature value.[11] The pK_a of formic acid in MeCN was determined to be 19.00 through DFT calculations, which is very similar to the literature pK_a of triethylammonium at 18.82. Therefore, it is reasonable to assume that the source of the proton in step F can be provided from either formic acid or triethylammonium.

3.2.3 Determination of Reaction Intermediates via NMR

In order to identify the reaction intermediates of our proposed catalytic cycle, the reaction of tetraethylammonium formate with $[(MDC^{Mes})Pd(CH_3CN)_2](PF_6)_2$ was analyzed by ^{1}H NMR spectroscopy. The use of tetraethylammonium formate in place of triethylamine and formic acid was necessary in order to be able to monitor the reaction intermediates at elevated temperatures. Not having available protons in solution allowed the catalytic cycle to be stopped at the palladium hydride species, since the hydride will not be protonated to produce hydrogen, which makes the reaction intermediates easier to detect by ^{1}H NMR spectroscopy. Additionally, the use of $(CD_3)_2SO$ was necessary because upon heating the solution in CD_3CN a complex mixture of products was obtained. Further analysis using flow gas chromatography showed undesired hydrogen production, most likely due to protonation of the hydride in CD_3CN.

3.2.3.1 Formation of MDC Palladium Formato Species

The ^{1}H NMR spectrum of tetraethylammonium formate in comparison to the spectrum for $[(MDC^{Mes})Pd(CH_3CN)_2](PF_6)_2$ (both in $(CD_3)_2SO$) is shown in Figure 3.8. The ^{1}H NMR spectrum of the reaction between tetraethylammonium formate and $[(MDC^{Mes})Pd(CH_3CN)_2](PF_6)_2$ in $(CD_3)_2SO$ at 25° in a J-Young NMR tube is shown in Figure 3.9 and is consistent with formation of a MDC palladium formato species. Formation of the species is indicated by the upfield shift of all peaks compared to the starting species, in particular the shift of the proton on formate from 8.55 ppm to 7.20 ppm. The symmetrical nature of ^{1}H NMR spectrum suggests the formation of a bidentate formato complexes in $(CD_3)_2SO$, $[(MDC^{Mes})Pd(\eta^2\text{-}OCHO)](PF_6)$ (Scheme 3.2). This is distinct from the same reaction in CD_3CN: the same upfield shifts occurs, however, the peaks in CD_3CN are much broader suggesting an equilibrium between the η^1-formato species.

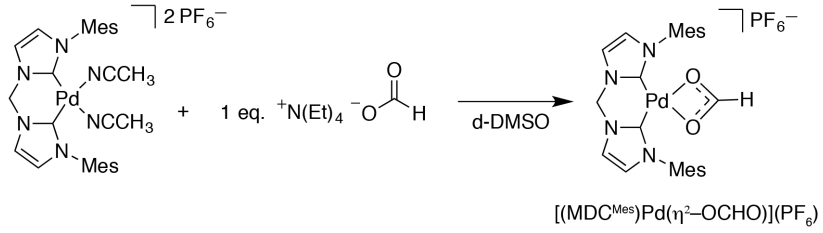

Scheme 3.2: Formation of formato complex from $[(MDC^{Mes})Pd(CH_3CN)_2](PF_6)_2$ and tetraethylammonium formate in $(CD_3)_2SO$

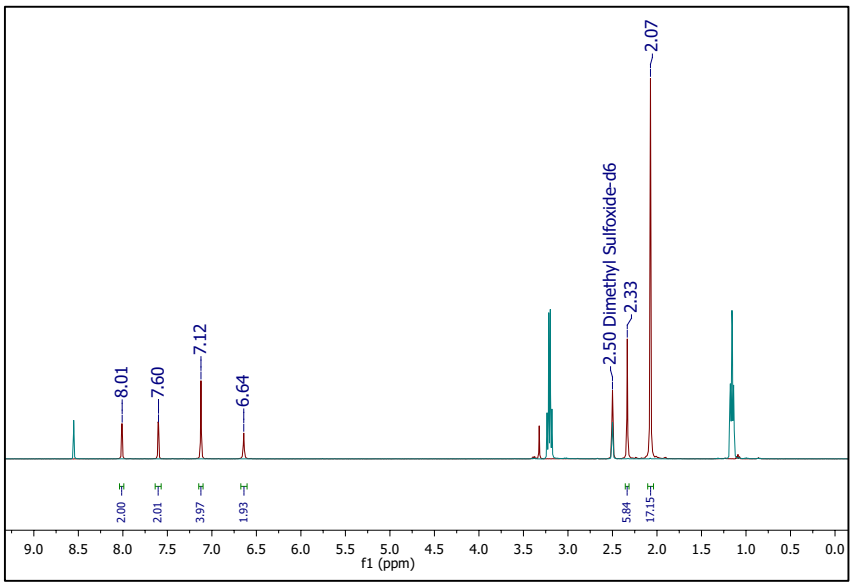

Figure 3.8: ^{1}H NMR spectrum at 25 °C of tetraethylammonium formate (shown in green) overlaid with ^{1}H NMR spectrum of $[(MDC^{Mes})Pd(CH_3CN)_2](PF_6)_2$ (shown in red) in $(CD_3)_2SO$.

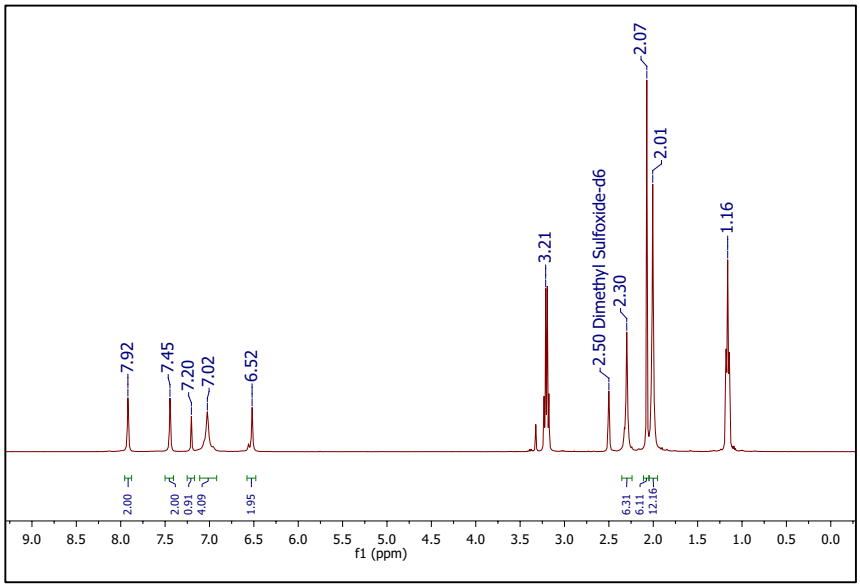

Figure 3.9: ^{1}H NMR spectrum of $[(MDC^{Mes})Pd(\eta^2\text{-}OCHO)](PF_6)$ formed from the reaction of $[(MDC^{Mes})Pd(CH_3CN)_2](PF_6)_2$ with tetraethylammonium formate at 25 °C in $(CD_3)_2SO$.

3.2.3.2 Formation of Hydride Species

The formation of a hydride intermediate is an important step in the proposed mechanism (Figure 3.3) as it is protonated to produce hydrogen. In order to study the formation of a hydride intermediate, the reaction of the Pd NHC formato complex at increasing temperature was monitored by VT-NMR (variable temperature) in a J-Young tube. As the temperature was warmed to 50 °C, a peak at approximately -9.61 ppm began to appear. As the temperature was increased to 60 °C and 70 °C, the intensity of the peak at -9.61 ppm increased (Figure 3.10). An NMR peak in this ppm range is indicative of the formation of a palladium hydride (Scheme 3.3). Unfortunately, the exact nature of the hydride species could not be ascertained due to formation of additional undesired byproducts causing overlapping NMR signals in the aliphatic and aromatic regions of the NMR spectrum; however, a proposed structure is shown in Scheme 3.3.

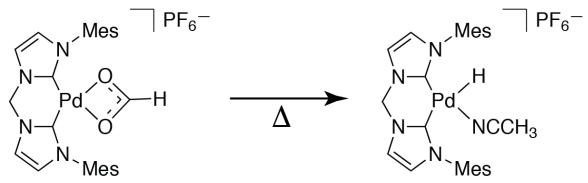

Scheme 3.3: Formation of hydride species upon heating of [(MDC^{Mes})Pd(η^2-OCHO)](PF_6) in $(CD_3)_2SO$

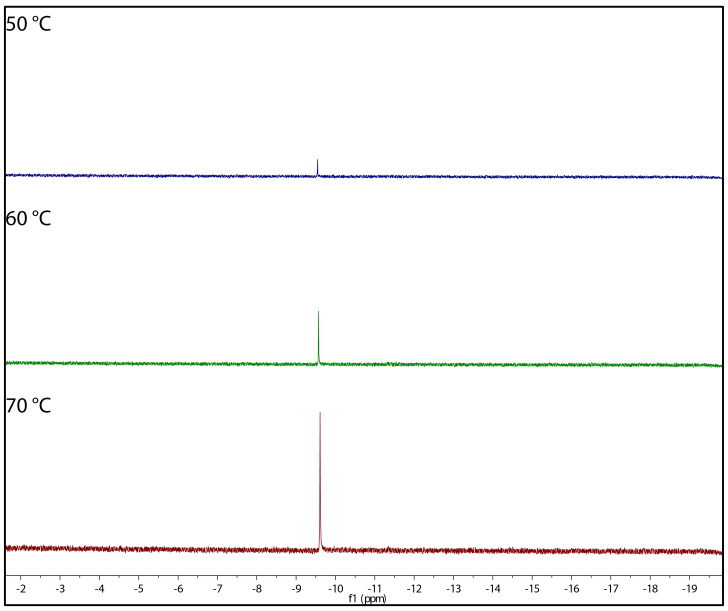

Figure 3.10: ^{1}H NMR spectrum of hydride region at 50 °C (blue), 60 °C (green) and 70 °C (red) of the proposed [(MDC^{Mes})Pd(CH_3CN)(H)](PF_6) species in $(CD_3)_2SO$

3.3 Formic Acid Dehydrogenation with Hünig's Base

As mentioned briefly (see Chapter 2), for the formic acid reaction system with triethylamine as base, addition of more formic acid to the solution once catalysis had plateaued did not lead to the formation of more gaseous products (Figure 3.11). Additionally, after the first several minutes of the reaction a black precipitate began to appear in solution. We attributed this to the formation of a catalytically inactive decomposition species formed from the palladium catalyst. Indeed, the formation of palladium black from decomposition pathways has been previously observed for palladium NHC complexes.[12]

From our proposed mechanism (Figure 3.3), we wanted to explore possible catalyst decomposition pathways that contribute to lowered TONs through off cycle reactions. One possible explanation for lower TONs involves the palladium hydride

intermediate in the proposed mechanism. A competing reaction to the protonation of this species is the deprotonation of the hydride by triethylamine to give a palladium (0) or palladium black species. Deprotonation of the hydride would hinder catalysis, as the Pd(0) species is no longer catalytically active. Additional evidence to support this theory is the lowered TONs with $[(MDC^{R})Pd(CH_3CN)_2](PF_6)_2$, where R is a less sterically hindering group around the palladium center (see Chapter 2). Having a small steric group around the palladium center allows triethylamine to more easily deprotonate the hydride species, leading to catalyst decomposition and lower overall TONs (Scheme 3.4).

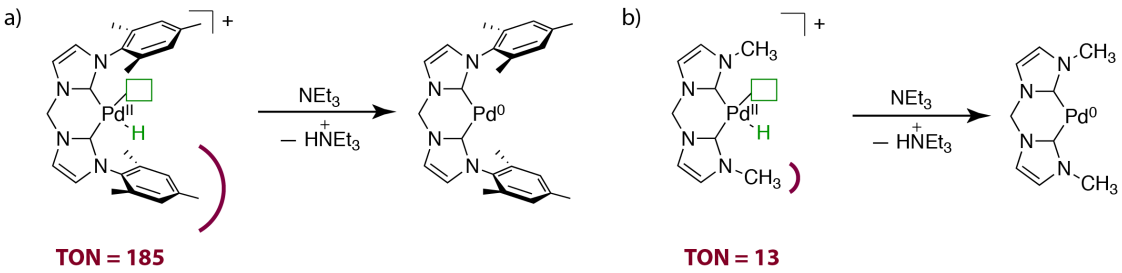

Scheme 3.4: Deprotonation with triethylamine shown for a) $[(MDC^{Mes})Pd(H)](PF_6)$ and b) $[(MDC^{Me})Pd(H)](PF_6)$. The red semi-circles are shown to illustrate the difference in size between the two wingtip groups of the MDC ligand. The TONs are for the production of hydrogen and carbon dioxide with a) $[(MDC^{Mes})Pd(CH_3CN)_2](PF_6)_2$ and b) $[(MDC^{Me})Pd(CH_3CN)_2](PF_6)_2$ as catalyst.

Since the catalyst has already been optimized, we instead looked at modifying the base to prevent this deprotonation reaction from occurring and increase TONs. More specifically, we proposed using the same reaction conditions, but with the bulkier Hünig's base (*N*,*N*-diisopropylethylamine) in place of triethylamine. We chose

a base with a conjugate acid pK_a similar to triethylammonium, since a suitable balance between the ability to deprotonate formic acid and protonate the Pd-hydride species is important to the overall reaction cycle. The pK_a for *N*,*N*-diisopropylethylammonium was calculated using DFT (see Section 3.5.4) and determined to be 20.02 in MeCN, which is fairly similar to the pK_a for triethylammonium (18.82).

First, the initial TOF for the reaction with Hünig's base was determined to be 414 (± 30) h^{-1} (optimized reaction conditions, see Section 3.5.2.1). This was a modest increase compared to the TOF with triethylamine as base (325 (± 35) h^{-1}). The percent conversion of formic acid was essentially the same under both conditions (~80%). In order to determine the TON, a similar experiment to the one previously mentioned with triethylamine was set-up with Hünig's base: once catalysis plateaued an additional 0.1 mL of formic acid was added to the solution. In this case, the catalytic activity continued with the addition of more reactant (Figure 3.11). From this initial finding, the experimental parameters were adjusted to produce optimal TONs. This was accomplished with 0.05 mL additions of formic acid to give a TON of 353 (±35). This is a significant increase from the TON with triethylamine at 185 (±10). Modifying the reaction conditions by starting with a lower concentration of formic acid (see Section 3.5.2.1), resulted in lower overall activity but allowed formic acid to be added up to 18 times (0.02 mL increment additions, Figure 3.12).

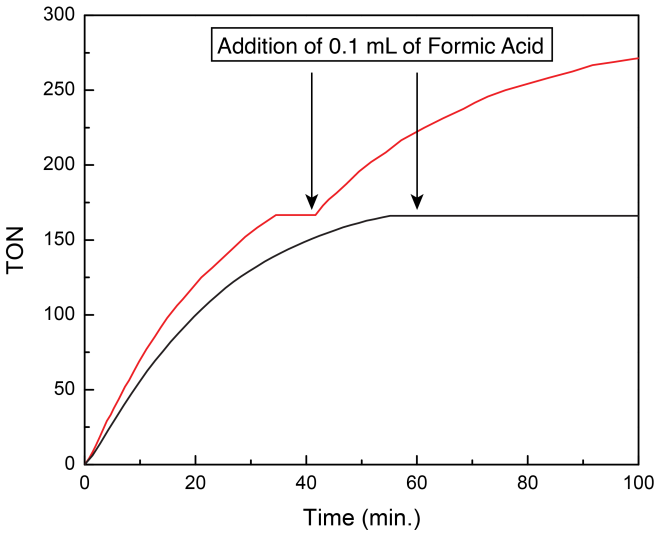

Figure 3.11: Total TON for formic acid dehydrogenation (0.1 mL additions of formic acid) with either Hünig's base (red) or triethylamine (black).

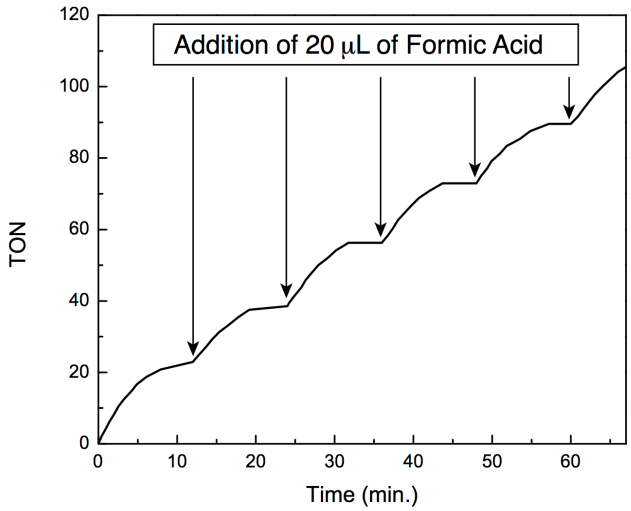

Figure 3.12: TON experiment with Hunig's base (initial 60 min) and 0.02 mL additions of formic acid

Hünig's base was initially chosen as a comparison to triethylamine for TON studies, since it is a commonly used base and commercially available. Subsequently, we wanted to compare another base in this series, diethylisopropylamine, which was synthesized according to a literature procedure.[13] Diethylisopropylamine was used as base for formic acid dehydrogenation and gave very similar results to that of triethylamine: diethylisopropylamine gave a TON of 172 (±12) and TOF of 300 (±60) h^{-1}, triethylamine gave a TON of 185 (±10) and a TOF of 325 (±35) h^{-1}. Also, similar to the reaction with triethylamine, addition of 0.1 mL formic acid when catalysis plateaued produced little to no additional gaseous products. This indicates that two bulky isopropyl groups, as with Hünig's base, are necessary to slow deprotonation of the palladium hydride and subsequent catalyst decomposition. According to this assumption, an analogous base, triisopropylamine, should increase TONs even further. Unfortunately, to the best of our knowledge, triisopropylamine is not known in the literature, and attempts to synthesize this base were unsuccessful.

The TON for formic acid dehydrogenation with Hünig's base was also determined for a series of catalysts related to $[(MDC^{Mes})Pd(MeCN)_2](PF_6)_2$, where the mesityl group on the wingtip of the NHCs has been modified. The syntheses of these complexes and formic acid dehydrogenation activity results with triethylamine were discussed in Chapter 2; Table 3.2 shows a comparison between the results obtained with Hünig's base and triethylamine using these catalysts. Similar to the results with $[(MDC^{Mes})Pd(MeCN)_2](PF_6)_2$, for each catalyst the TON was greater with Hünig's base compared with triethylamine, by almost double in some cases.

Table 3.2: Comparison of TON with Hünig's base versus triethylamine for $[(MDC^{R})Pd(MeCN)_2](PF_6)_2$ catalysts

Catalyst	TON with Hünig's Base	TON with Triethylamine
$[(MDC^{Me})Pd(MeCN)_2](PF_6)_2$	16 (±0.5)	13 (±0.5)
$[(MDC^{iPr})Pd(MeCN)_2](PF_6)_2$	10 (±0.6)	6 (±0.5)
$[(MDC^{Ph})Pd(MeCN)_2](PF_6)_2$	15 (±2)	8 (±0.6)
$[(MDC^{Cy})Pd(MeCN)_2](PF_6)_2$	14 (±1)	10 (±2)
$[(MDC^{DIPP})Pd(MeCN)_2](PF_6)_2$	65 (±5)	35 (±20)

3.4 Summary

In this chapter, we have further explored our formic acid dehydrogenation catalyst, $[(MDC^{Mes})Pd(MeCN)_2](PF_6)_2$. We proposed a mechanism based on the findings from the previous chapter, as well as several literature examples and then probed this mechanism through several kinetic studies. First, varying the concentration of catalyst or formic acid and monitoring the reaction rate for each showed that the reaction was homogeneous in palladium, and a one to one binding of formate occurred before the rate determining step. Arrhenius analysis revealed that the energy of activation for the reaction was similar to other homogeneous formic acid dehydrogenation catalysts. Eyring analysis provided a large positive enthalpy and entropy of activation, from which we concluded that the rate determining step of the reaction is the creation of an open coordination site on palladium. Finally, we were able to observe several reaction intermediates using variable temperature ^{1}H-NMR spectroscopy.

From the proposed mechanism, we were also able to determine possible side reactions which contributed to lowered TONs. One possible side reaction was determined to be the deprotonation of the palladium-hydride species which would deactivate the catalyst. In order to hinder this process from occurring, we proposed

using a bulkier base, *N*,*N*-diisopropylethylamine or Hunig's base, in place of triethylamine. Indeed, by using this base we were able to improve TONs for the reaction.

3.5 Experimental Methods

3.5.1 General Methods

NMR experiments were carried out in a nitrogen-filled glovebox in a J-Young NMR tube. Deuterated dimethylsulfoxide ($(CD_3)_2SO$) was stored over 4 Å molecular sieves prior to use.

3.5.1.1 Materials

Reagents and solvents were purchased from Alfa Aesar, Cambridge Isotopes Laboratories, Fisher Scientific or Sigma-Aldrich. Solvents for synthesis were of reagent grade or better; solvents for air- or moisture-sensitive reactions were dried by passage through activated alumina and then stored over 4 Å molecular sieves prior to use.[14] The synthesis of $[(PDC^{Mes})Pd(CH_3CN)](PF_6)_2$ and $[(LDC^{Mes})Pd(CH_3CN)](PF_6)_2$ was previously developed in our laboratory.[15]

3.5.1.2 Compound Characterization

^1H NMR and ^{13}C NMR spectra were recorded at 25 °C on a Bruker 400 MHz spectrometer. Proton spectra are referenced to the residual proton resonance of the deuterated solvent ($(CD_3)_2SO$ = δ 2.50, CD_3CN = 1.94), and carbon spectra are referenced to the carbon resonances of the solvent ($(CD_3)_2SO$ = δ 39.51, CD_3CN = 118.69). All chemical shifts are reported using the standard δ notation in parts-per-million; positive chemical shifts are to higher frequency from the given reference.

3.5.1.3 Procedure for Formation of Hydrogen from Formic Acid

A typical experiment involved the addition of 1 mL of a 5 M formic acid/base (2:1) MeCN solution to a septum capped vial. The solution was allowed to stir at the desired temperature in a pre-heated sand bath. Once the solution was at a constant temperature, the vial was injected with 100 μL of the catalyst solution in MeCN. Any gas produced was measured using water displacement (see Section 2.7.1.3). Initial rates of formic acid dehydrogenation were determined from gas evolution in the first several minutes of the reaction (mol gas/min). For reaction rate studies where the concentration of catalyst is varied (Figure 3.4), the initial concentration of formic acid is 4.55 M for each trial. For reaction rate studies where the concentration of formic acid is varied (Figure 3.5), the concentration of catalyst is 18 mM for each trial.

The reaction conditions were modified for TON experiments with Hünig's base and multiple additions of formic acid: to a septum capped vial was added 0.435 mL of Hunig's base, 0.376 mL of MeCN and 0.02 mL of formic acid. The solution was allowed to stir at 70 °C in a pre-heated sand bath. Once the solution was at a constant temperature, the vial was injected with 0.10 mL of 200 mM $[(MDC^{Mes})Pd(CH_3CN)](PF_6)_2$ in MeCN. After 12 minutes (once gas production decreased), 0.02 mL of formic acid was added to the reaction. This procedure was repeated until the addition of more formic acid no longer produced any gaseous products.

3.5.1.4 NMR Variable Temperature Experiments

In a nitrogen filled glovebox, 5 mg (0.029 mmol) of tetraethylammonium formate was added to 25 mg (0.029 mmol) of $[(MDC^{Mes})Pd(CH_3CN)_2](PF_6)_2$ in 1 mL of $(CD_3)_2SO$. This mixture was added to a J-Young NMR tube and an initial ^1H NMR

spectrum was obtained at 25 °C to show formation of [(MDC^{Mes})Pd(η^2-OCHO)](PF$_6$). ^{1}H NMR (400 MHz; (CD$_3$)$_2$SO, 25 °C) δ/ppm: 7.92 (s, 2H), 7.45 (s, 2H), 7.20 (broad s, 1H), 7.02 (s, 4H), 6.52 (s, 2H), 2.30 (s, 6H), 2.07 (s, 6H), 2.01 (s, 12H). The internal temperature of the NMR instrument was then increased to 50, 60 and 70 °C and ^{1}H NMR spectra were obtained at each of these temperatures to show a hydride peak at -9.61 ppm.

3.5.2 Synthesis of Tetraethylammonium Formate

To a mixture of 262 mg (1.58 mmol) tetraethylammonium chloride in 15 mL MeCN was added 400 mg (1.58 mmol) thalium(I)formate. The mixture was allowed to stir at 25 °C for 14 h. The solution was filtered through celite and solvent was removed *in vacuo* to yield an off-white solid. The solid was dried *in vacuo* to give 267 mg (96%) of the desired product. ^{1}H NMR (400 MHz; CD$_3$CN, 25 °C) δ/ppm: 8.55 (s, 1H), 3.21 (q, J = 7.2 Hz, 8H), 1.15 (t, J = 7.3 Hz, 12 H). ^{13}C NMR (101 MHz; CD$_3$CN, 25 °C) δ/ppm: 164.86, 51.35 (t, J = 3.0 Hz), 7.12.

3.5.3 Computations

The calculations were performed with density functional theory (DFT) methods by using M062X exchange correlation functionals[16] and a 6-311+G(d,p) basis set in the Gaussian 09 software.[17] All geometry optimizations were performed in C1 symmetry with subsequent frequency analysis to confirm that each stationary point was a minimum on the potential energy surface. The solvent effects of MeCN for geometry optimizations have been accounted for using the SMD universal continuum model with ε =35.688.[18]

3.5.3.1 Solvent Free Energy Calculations

The free energy in MeCN solution (G_{MeCN}) and gas phase free energy (G_{gas}) were determined for formic acid, acetic acid, triethylamine and Hünig's base (*N*,*N*-diisopropylethylamine) (and their corresponding conjugate bases or acids) using the methods described above on the geometry-optimized molecules (Table 3.3). The solvation free energy (ΔG_{sol}) for each species was calculated based on the difference between these two values, as shown in the equation below:

$$\Delta G_{sol} = G_{gas} - G_{MeCN}$$

Table 3.3: Calculated solvation energies in MeCN

Compound	Solvation Energy (kcal/mol)
Formic Acid	–5.5
Formate	–59.5
Acetic Acid	–7.2
Acetate	–61.2
Triethylamine	–6.3
Triethylammonium	–61.6
N,*N*-Diisopropylethylamine (Hünig's Base)	–6.1
N,*N*-Diisopropylethylammonium	–58.5

3.5.3.2 pK_a Calculations using the Isodesmic Reaction

The pK_a of formic acid and *N*,*N*-diisopropylethylammonium (the conjugate acid of Hünig's base) in MeCN were determined using a calculation based on the isodesmic reaction.[19,20] This method uses a thermodynamic cycle (Scheme 3.5) which involves several parts: **(1)** the donation of a proton by an acid species (AH) to a base

(B^-) to give the corresponding conjugate base (A^-) and conjugate acid (BH) in both the gaseous and solvent phases, **(2)** the free energies of deprotonation in the gas phase (ΔG_{gas}) and in solution (ΔG_{MeCN}), and **(3)** the free energy of solvation (ΔG_{sol}).

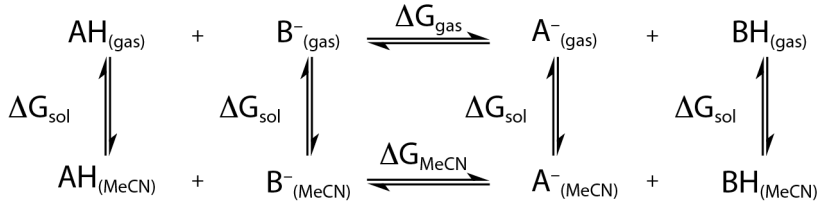

Scheme 3.5: Thermodynamic cycle for isodesmic reaction

The pK_a of the acid AH can be calculated from the equations shown below and the known literature pK_a value of the reference species BH.[21-23] The pK_a of formic acid in MeCN was determined using acetic acid as a reference[24] and the pK_a of *N*,*N*-diisopropylethylammonium in MeCN was determined using triethylammonium as a reference.[24] These references were chosen based on the similarity in structure to the acid for which pK_a is being determined. The gas phase free energies and solvation energies were calculated using Gaussian09 software as described above.

$$\Delta G_{gas} = G_{(g)}BH + G_{(g)}A^- - G_{(g)}AH - G_{(g)}B^-$$

$$\Delta G_{MeCN} = \Delta G_{gas} + \Delta G_{sol}A^- + \Delta G_{sol}BH - \Delta G_{sol}AH - \Delta G_{sol}B^-$$

$$pK_a = \frac{\Delta G_{MeCN}}{\ln(10)RT} + pK_a(BH)$$

The pK_a obtained either from theoretical calculations or literature values for formic acid, acetic acid, *N*,*N*-diisopropylethylammonium and triethylammonium are shown in Table 3.4.

Table 3.4: Literature and calculated pK_a values in MeCN

Compound	**Literature pK_a**	**Calculated pK_a**
Formic Acid	—	19.00
Acetic Acid	22.3	—
N,*N*-diisopropylethylammonium	—	20.02
Triethylammonium	18.82	—

3.6 References and Notes

(1) Fukuzumi, S.; Kobayashi, T.; Suenobu, T. *ChemSusChem* **2008**, *1* (10), 827.

(2) Manca, G.; Mellone, I.; Bertini, F.; Peruzzini, M.; Rosi, L.; Mellmann, D.; Junge, H.; Beller, M.; Ienco, A.; Gonsalvi, L. *Organometallics* **2013**, *32* (23), 7053.

(3) Sánchez-de-Armas, R.; Xue, L.; Ahlquist, M. S. G. *Chem. – Eur. J.* **2013**, *19* (36), 11869.

(4) Mellone, I.; Peruzzini, M.; Rosi, L.; Mellmann, D.; Junge, H.; Beller, M.; Gonsalvi, L. *Dalton Trans.* **2013**, *42* (7), 2495.

(5) Boddien, A.; Mellmann, D.; Gärtner, F.; Jackstell, R.; Junge, H.; Dyson, P. J.; Laurenczy, G.; Ludwig, R.; Beller, M. *Science.* **2011**, *333* (6050), 1733.

(6) Rieckborn, T. P.; Huber, E.; Karakoc, E.; Prosenc, M. H. *Eur. J. Inorg. Chem.* **2010**, 30, 4757.

(7) Eyring, H. *J. Chem. Phys.* **1935**, *3* (2), 107.

(8) Zell, T.; Butschke, B.; Ben-David, Y.; Milstein, D. *Chem. – Eur. J.* **2013**, *19* (25), 8068

(9) Fukuzumi, S.; Kobayashi, T.; Suenobu, T. *J. Am. Chem. Soc.* **2010**, *132* (5), 1496.

(10) Ruelle, P.; Kesselring, U. W.; Ho Nam-Tran. *J. Am. Chem. Soc.* **1986**, *108* (3), 371.

(11) Izutsu, K. *Acid-Base Dissociation Constants in Dipolar Aprotic Solvents*; Blackwell Science, 1990.

(12) *N-Heterocyclic Carbenes in Transition Metal Catalysis*; Glorius, F., Ed.; Springer-Verlag Berlin: Heidelberg, Germany, 2007; Topics in Organometallic Chemistry Vol. 21, pp 1-20.

(13) Caspe, S. *J. Am. Chem. Soc.* **1932**, *54* (11), 4457.

(14) Pangborn, A. B.; Giardello, M. A.; Grubbs, R. H.; Rosen, R. K.; Timmers, F. J. *Organometallics.* **1996,** *15* (5), 1518.

(15) Andrade, G.A.; Rosenthal, J. Unpublished Results.

(16) Zhao, Y.; Truhlar, D. G. *Theor*. *Chem*. *Acc*. **2008**, *120*, 215.

(17) Frisch, M. J.; Trucks, G. W.; Schlegel, H. B.; Scuseria, G. E.; Robb, M. A.; Cheeseman, J. R.; Scalmani, G.; Barone, V.; Mennucci, B.; Petersson, G. A.; Nakatsuji, H.; Caricato, M.; Li, X.; Hratchian, H. P.; Izmaylov, A. F.; Bloino, J.; Zheng, G.; Sonnenberg, J. L.; Hada, M.; Ehara, M.; Toyota, K.; Fukuda, R.; Hasegawa, J.; Ishida, M.; Nakajima, T.; Honda, Y.; Kitao, O.; Nakai, H.; Vreven, T.; Montgomery Jr., J. A.; Peralta, J. E.; Ogliaro, F.; Bearpark, M.; Heyd, J. J.; Brothers, E.; Kudin, K. N.; Staroverov, V. N.; Kobayashi, R.; Normand, J.; Raghavachari, K.; Rendell, A.; Burant, J. C.; Iyengar, S. S.; Tomasi, J.; Cossi, M.; Rega, N.; Millam, J. M.; Klene, M.; Knox, J. E.; Cross, J. B.; Bakken, V.; Adamo, C.; Jaramillo, J.; Gomperts, R.; Stratmann, R. E.; Yazyev, O.; Austin, A. J.; Cammi, R.; Pomelli, C.; Ochterski, J. W.; Martin, R. L.; Morokuma, K.; Zakrzewski, V. G.; Voth, G. A.; Salvador, P.; Dannenberg, J. J.; Dapprich, S.; Daniels, A. D.; Farkas, Ö.; Foresman, J. B.; Ortiz, J. V; Cioslowski, J.; Fox, D. J. Gaussian09 Revision A.01, 2009.

(18) Marenich, A. V.; Cramer, C. J.; Truhlar, D. G. *J*. *Phys*. *Chem*. *B* **2009**, *113*, 6378.

(19) Sastre, S.; Casasnovas, R.; Muñoz, F.; Frau, J. *Phys. Chem. Chem. Phys.* **2016**, *18* (16), 11202.

(20) Sastre, S.; Casasnovas, R.; Muñoz, F.; Frau, J. *Theor. Chem. Acc.* **2012**, *132* (2), 1310.

(21) Liptak, M. D.; Shields, G. C. *J. Am. Chem. Soc.* **2001**, *123* (30), 7314.

(22) Ho, J.; Coote, M. L. *Wiley Interdiscip. Rev. Comput. Mol. Sci.* **2011**, *1* (5), 649.

(23) Ho, J. *Aust. J. Chem.* **2014**, *67* (10), 1441.

(24) Izutsu, K. *Acid-Base Dissociation Constants in Dipolar Aprotic Solvents*; Blackwell Science, 1990.

Chapter 4

SYNTHESIS AND CHARACTERIZATION OF A SERIES OF METALATED CALIX[4]PHYRINS

4.1 Introduction

Calix[4]phyrins, also known in earlier work as porphodimethenes,[1-9] are hybrid macrocycles containing both sp^2 and sp^3 hybridized bridging *meso* carbons and thus combine features from both conjugated porphyrins and non-conjugated calixpyrroles (Figure 4.1). Since various types of calixphyrins are found in the literature, Sessler[10] proposed a systematic nomenclature in which the "trans-like" type of calix[4]phyrin shown in Figure 4.1 is designated with (**1**,*1*,**1**,*1*),[11] which represents the order of *meso* carbons with sp^2 centers in bold and sp^3 centers in italics. The bracketed number in calix[4]phyrin refers to the macrocycle containing four pyrrole units, which is used to differentiate the calix[4]phyrin from higher homologues of calixphyrin.

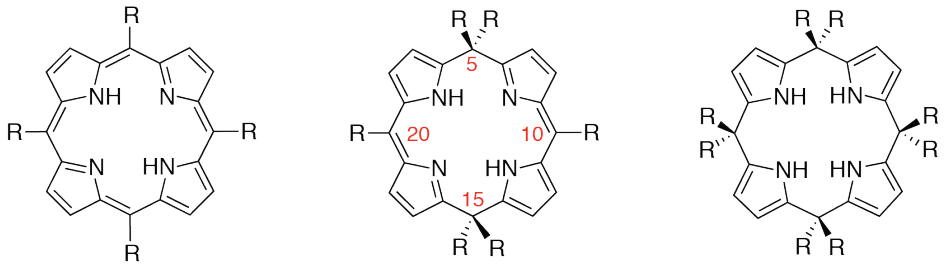

Figure 4.1: Structures of representative porphyrin, calix[4]phyrin and calixpyrrole, with common number scheme shown in red for calix[4]phyrin

Initially, calix[4]phyrins were merely identified as intermediates in the stepwise oxidation of porphyrinogen to produce porphyrin.[12,13] It has only been over the last decade and a half that these macrocycles have gained attention because of the unique physicochemical properties and flexibility of the molecule in comparison to analogous tetrapyrrole macrocycles.[10] Calix[4]phyrins have been explored for applications in anion[14-16] and cation binding,[17-19] as electrochemical sensors,[20,21] and intramolecular proton transfer.[22] A likely reason for the recent interest and exploration of these unique characteristics has been the development of directed synthetic strategies for calix[4]phyrins. A targeted synthesis for calix[4]phyrin was first pioneered by the Floriani group;[23] this method produced the calix[4]phyrin by dealkylation from a corresponding calix[4]pyrrole through a series of organometallic reactions which were followed by hydrolysis to give the free acid. Additional strategies include reductive alkylation of metalated porphyrin (however, this method is limited to production of metalated symmetric calixphyrins);[24] coupling of an aromatic dipyrrylmethane with acetone catalyzed by an acid at room temperature;[14,25] reduction of monoacyl dipyrromethane to monocarbinol dipyrromethane, then self-condensation catalyzed by a Lewis acid;[26] reaction of an aromatic aldehyde with dialkyldipyrromethane;[15,27,28] and [2+2] McDonald type condensation reactions.[29]

Despite the development of efficient syntheses, the use of calix[4]phyrins as ligand scaffolds in metal catalysts has not been widely explored. This is especially surprising since the analogous metalloporphyrins have been extensively developed to catalyze a variety of reactions. Indeed, to the best of our knowledge, the only example of metallocalixphyrins as catalysts utilizes hybrid calix[4]phyrins (**1**,**1**,*1*,*1* type) where one or two pyrrole nitrogens are replaced with S, O or P atoms. The palladium and

rhodium complexes of these macrocycles were used to catalyze Heck and hydrosilylation reactions, respectively.[30,31] Therefore, with the lack of exploration in this area, there is a great potential in catalysis for this unique and relatively unexplored porphyrinoid.

Our group wished to synthesize, characterize and metalate the free base calix[4]phyrin in order to explore metallocalix[4]phyrins as unique catalysts for significant reactions. Previously in our group,[32,33] we synthesized and analyzed the phlorin, a tetrapyrrole macrocycle similar to the calix[4]phyrin but with only one sp^3-hybridized *meso* carbon. By combining the multi-electron redox properties of the porphyrinogen with the photophysical properties of the porphyrin, the phlorin framework was proposed as a potential dye for dye-sensitized solar cells. Initial studies[32] utilized a phlorin with 5,5-dimethyl substituents at the sp^3 carbon and pentafluorophenyl groups at the sp^2 carbons. By developing a highly modular synthetic strategy for the phlorin, we proposed adopting a similar strategy for the synthesis of calix[4]phyrin. Analogous to the phlorin, we proposed beginning our studies with the synthesis of 5,5,15,15-tetramethyl-10,20-bis(pentafluorophenyl) calix[4]phyrin ($C4P^{PF}$, M = 2H in Figure 4.2). In addition to the convenience of working with similar starting materials as the phlorin, these particular *meso* substituents were chosen since the electron-withdrawing pentafluorophenyl groups at the sp^2 centers are proposed to give the macrocycle better stability[34] and the dimethyl substituents at the sp^3 centers are shown to support multielectron redox oxidations.[35,36] The latter characteristic is desired as we would like to use the calix[4]phyrin as a unique multi-electron redox ligand in catalysis, which will be further discussed and explored in the chapters to follow.

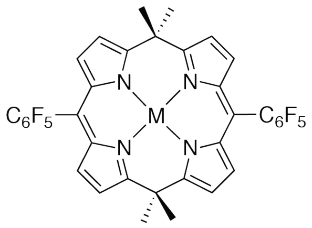

C4P^{PF}
M = 2H, Zn, Cu, Ni, Co

Figure 4.2: Freebase and metallocalix[4]phyrins explored in this work

In this chapter the synthesis of the freebase calix[4]phyrin and corresponding metallocalixphyrins metalated with a variety of first row transitions metals (Ni, Cu, Zn, Co, Figure 4.2) will be discussed. These unique complexes were characterized and analyzed by crystallography, UV-vis spectroscopy, time-dependent density functional theory (TTDFT) calculations, differential pulse voltammetry and cyclic voltammetry.

4.2 Synthesis of Freebase Calix[4]phyrin

Several syntheses of freebase C4P^{PF} have already been outlined in the literature. The first was developed by the Sessler group and involved the condensation between 5-(pentafluorophenyl)dipyrromethane and acetone in the presence of acid, followed by oxidation with 2,3-dichloro-5,6-dicyano-1,4-benzoquinone (DDQ). While the reaction was very high yielding, it required an impractical reaction time (6 days).[25] Shortly thereafter, Androletti proposed a condensation reaction between 5,5-dimethyldipyrromethane and pentafluorobenzaldehyde under acidic conditions. The yield for this reaction was approximately 40%; however, it required the use of a basic magnesium silicate support.[15] Additionally, the Geier group showed that calix[4]phyrin could be synthesized by reduction of 1-pentafluorobenzoyl-5,5-

dimethyldipyrromethane to the corresponding monocarbinol dipyrromethane, followed by self-condensation under Lewis acidic conditions and oxidation with DDQ.[26] This synthetic strategy, however, was much lower yielding than the previous two methods.

Since each of the syntheses detailed above could be improved upon, our group decided to take the synthetic strategy we had previously optimized in our lab for phlorin and apply it to the synthesis of our desired $C4P^{PF}$. This synthesis is shown in Scheme 4.1: 5,5'-dimethyldipyrromethane[37] (1) is deprotonated with Grignard's reagent, followed by addition of pentafluorobenzoyl chloride to yield the corresponding diacylated dipyrromethane (2). The isolated diacylated dipyrromethane is then reduced with $NaBH_4$ to give the dicarbinol product. To this product is added 5,5'-dimethyldipyrromethane (1) with indium chloride as Lewis acid to catalyze the condensation reaction, followed by oxidation with DDQ and quenching with triethylamine. Following purification with column chromatography the desired calix[4]phyrin product was obtained in good yield (45%).

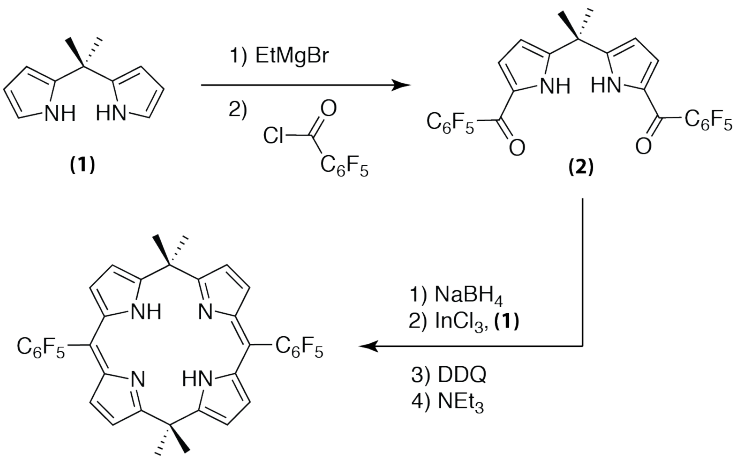

Scheme 4.1: Reaction scheme for synthesis of $C4P^{PF}$

4.3 Synthesis of M Calix[4]phyrin (M = Co, Ni, Cu, Zn)

There are relatively few examples for the synthesis of metallocalix[4]phyrins in the literature. There are even fewer examples of metallocalix[4]phyrins synthesized directly from the free base calix[4]phyrin; metallocalix[4]phyrins have been commonly synthesized by metal-assisted dealkylation of porphyrinogen[19] or reductive methylation of metalloporphyrins.[1,38] Synthesis of metallocalix[4]phyrins directly from the freebase calix[4]phyrin has been previously accomplished by two different methods: reacting freebase calix[4]phyrin with $ZnBr_2$ or $Cu(NO_3)_2{\cdot}H_2O$ to give the zinc or copper calix[4]phyrin complexes, respectively,[20] and by refluxing the appropriate metal acetate with the freebase calix[4]phyrin in a chloroform-methanol mixture to obtain the zinc, copper or cobalt calix[4]phyrin.[39]

Previously in our group, we had success metalating 5,5-dimethylbiladiene, a tetrapyrrole related to calix[4]phyrin, by reacting the free base with the appropriate metal acetate;[40] therefore, we employed a similar strategy for the metallocalix[4]phyrins as outlined in Scheme 4.2. The zinc derivative of $C4P^{PF}$ was synthesized by reacting $C4P^{PF}$ with an excess (20 equivalents) of $Zn(OAc)_2{\cdot}2\ H_2O$ in *N*,*N*-dimethylformamide (DMF) at 60 °C for sixteen hours to obtain $Zn(C4P^{PF})$ in 90 % yield. A large excess of zinc acetate was used to drive the reaction to completion. This is necessary because column chromatography cannot be use for purification since the zinc center is removed on the column. The nickel derivative is synthesized in a similar manner by reacting $Ni(OAc)_2$ with $C4P^{PF}$ for twelve hours, except that an elevated temperature (130 °C) was required to give the desired product in 45% yield. The copper derivative was synthesized by reacting $Cu(OAc)_2$ with $C4P^{PF}$ at 130 °C for four hours to give $Cu(C4P^{PF})$ in 73% yield. The cobalt derivative was also synthesized with $Co(OAc)_2$ using these reaction conditions (DMF, 130°C, 12 hours), but while the

previous derivatives could be synthesized under an air atmosphere, the cobalt synthesis was performed under a nitrogen atmosphere to prevent the production of the undesired Co(III) product. The Co(C4P^{PF}) product was obtained in 75% yield.

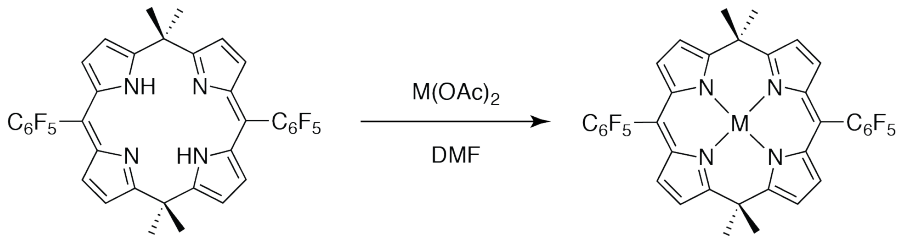

Scheme 4.2: General reaction scheme for M(C4P^{PF}), where M = Zn, Cu, Ni or Co

4.3.1 Solid State Structure of M Calix[4]phyrin (M = Co, Cu, Zn)

The solid state structure of Zn(C4P^{PF}) (Figures 4.3 and 4.4) was obtained by slow evaporation of a saturated solution of the complex in THF and MeOH (1:1) with a small amount of pyridine added to the solution. The structure crystallized with pyridine bound to the zinc center, as shown in Figure 4.3b. The average Zn-N bond distance was 2.08 Å (Table 4.1), which is comparable to reported Zn-N bond distances in other zinc calix[4]phyrins.[20,39,41,42] The complex with pyridine bound to the zinc center is square pyramidal at zinc, with N-M-N bond angles slightly less than 90° which is due to a puckering at the metal center with a deviation of 0.41 Å from the N4 plane (Table 4.1). This deviation is greater for the zinc complex than the copper and cobalt derivatives (*vide infra*).

Table 4.1: Selected bond lengths and angles for Zn(C4P^{PF})

Atoms	Bond Lengths (Å)	Atoms	Bond Angle (°)
Zn-N(1)	2.090(5)	N(2)-Zn-N(1)	89.67(19)
Zn-N(2)	2.083(5)	N(4)-Zn-N(2)	158.80(19)
Zn-N(3)	2.083(5)	N(4)-Zn-N(1)	85.5(2)
Zn-N(4)	2.079(5)	N(3)-Zn-N(1)	156.06(19)

The solid state structure of Cu(C4P^{PF}) is shown in Figures 4.5 and 4.6. The structure was obtained by slow evaporation of a saturated solution of the complex in THF and MeOH (1:1) with a small amount of pyridine added to the solution. The average Cu-N bond length is 1.98 Å (Table 4.2), which is comparable to other Cu-N bond lengths reported for copper calix[4]phyrins.[19,20,41] The average metal-nitrogen bond length for the copper complex is shorter than that for the analogous zinc complex (2.08 Å), which suggests a less strained conformation. The complex is square pyramidal at copper with a pyridine group bound to the copper center (Figure 4.5b), with a deviation of 0.04 Å of the metal from the N4 plane and N-M-N bond angles slightly less than 90° (Table 4.2).

Table 4.2: Selected bond lengths and angles for Cu(C4P^{PF})

Atoms	Bond Lengths (Å)	Atoms	Bond Angle (°)
Cu-N(1)	1.986(2)	N(2)-Cu-N(1)	89.66(9)
Cu-N(2)	1.978(2)	N(2)-Cu-N(4)	177.40(10)
Cu-N(3)	1.979(2)	N(4)-Cu-N(1)	89.99(9)
Cu-N(4)	1.980(2)	N(3)-Cu-N(1)	177.96(9)

The cobalt complex was crystallized by slow evaporation of a saturated solution of the complex in $CHCl_3$ and MeOH (1:1) with a small amount of pyridine added to the solution. The complex is square pyramidal at cobalt with pyridine bound

at the cobalt center (Figures 4.7 and 4.8) and the bond angles between the cobalt center and macrocyclic nitrogens approximately 90° (Table 4.3). The cobalt center is only slightly displaced from the N4 plane (0.05 Å). The average Co-N bond length is 1.93 Å (Table 4.3), which is similar to the Co-N bond length reported for an analogous cobalt calix[4]phyrin.[19]

Table 4.3: Selected bond lengths and angles for Co(C4P^{PF})

Atoms	Bond Lengths (Å)	Atoms	Bond Angle (°)
Co-N(1)	1.9334(19)	N(2)-Co-N(1)	90.08(8)
Co-N(2)	1.9249(19)	N(4)-Co-N(2)	176.10(8)
Co-N(3)	1.9273(19)	N(4)-Co-N(1)	90.37(8)
Co-N(4)	1.9239(19)	N(3)-Co-N(1)	177.69(8)

Additionally, each of the metal calix[4]phyrin complexes described above shows a puckering at the sp^3 hybridized *meso* carbons. This is a feature that is unique from the analogous porphyrin, which is planar, and highlights the flexibility of this ligand scaffold.

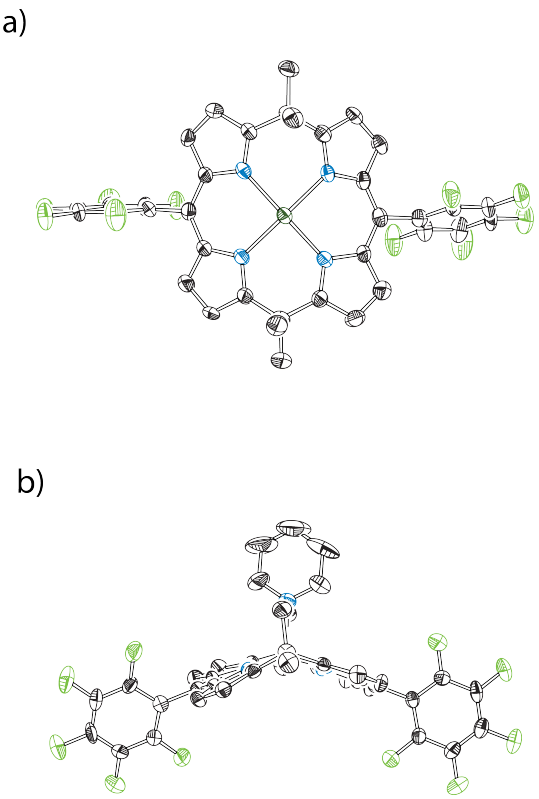

Figure 4.3: Solid state structure of Zn(C4P^{PF}) with a view from (a) top and (b) side on. All hydrogen atoms were omitted for clarity and thermal ellipsoids are shown at 50% probability. The pyridine group is also omitted for clarity in the top view (a)

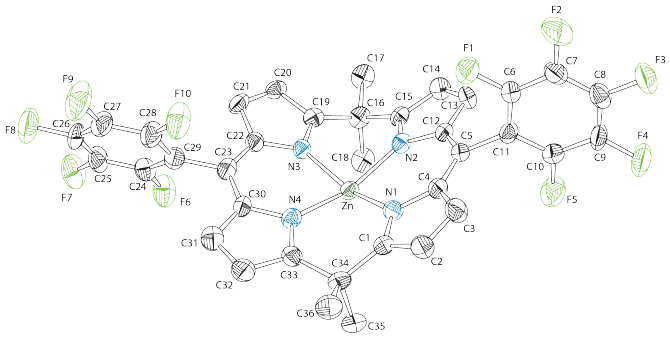

Figure 4.4: Numbered solid state structure of Zn(C4P^{PF}) with all hydrogen atoms omitted for clarity and thermal ellipsoids shown at 50% probability. The pyridine group is also omitted for clarity

a)

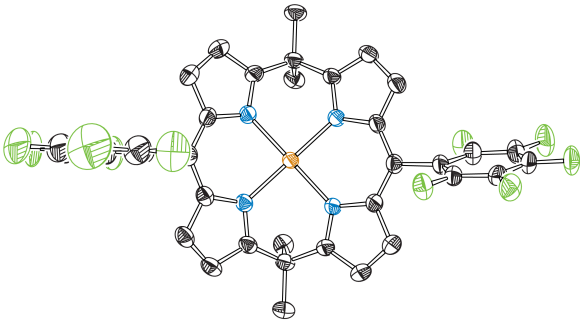

b)

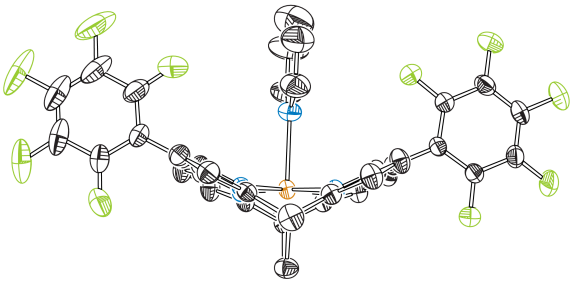

Figure 4.5: Solid state structure of Cu(C4P^{PF}) with a view from (a) top and (b) side on. All hydrogen atoms were omitted for clarity and thermal ellipsoids are shown at 50% probability. The pyridine group is also omitted for clarity in the top view (a)

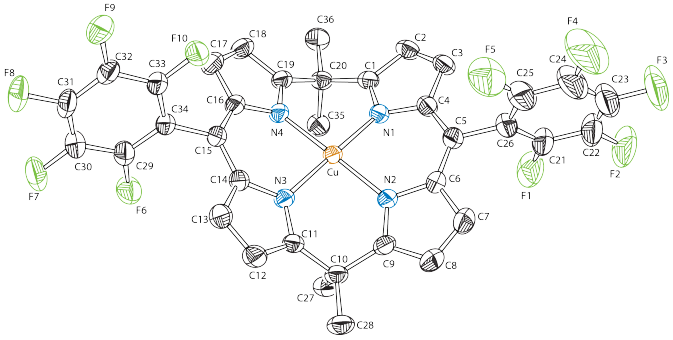

Figure 4.6: Numbered solid state structure of Cu(C4P^{PF}) with all hydrogen atoms omitted for clarity and thermal ellipsoids shown at 50% probability. The pyridine group is also omitted for clarity

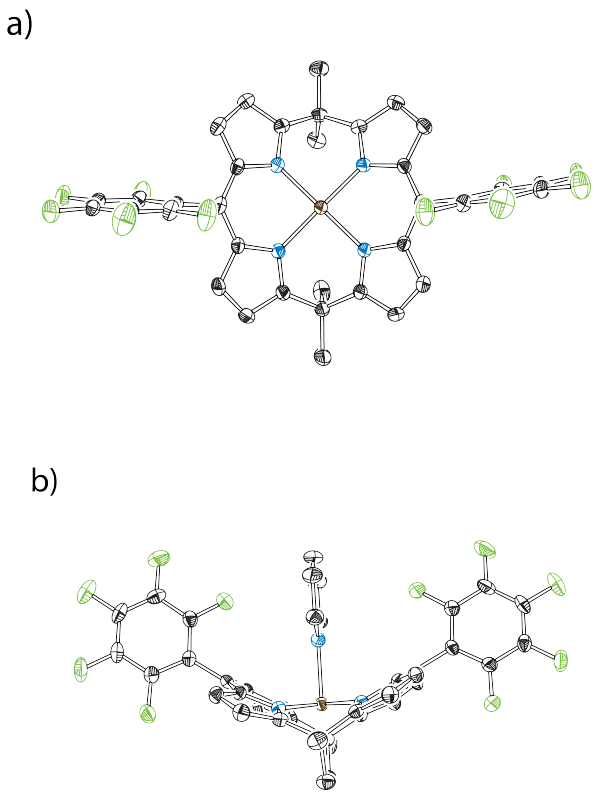

Figure 4.7: Solid state structure of Co(C4P^{PF}) with a view from (a) top and (b) side on. All hydrogen atoms were omitted for clarity and thermal ellipsoids are shown at 50% probability. The pyridine group is also omitted for clarity in the top view (a)

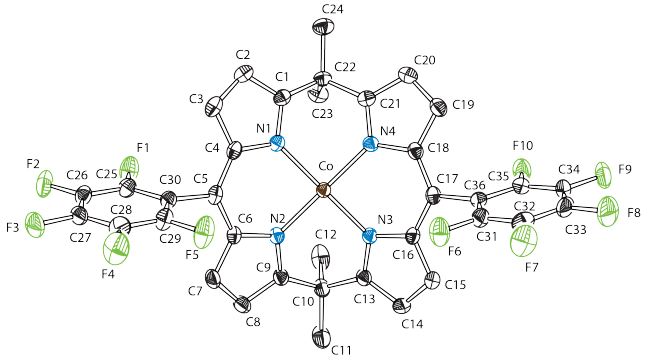

Figure 4.8: Numbered solid state structure of Co(C4P^{PF}) with all hydrogen atoms omitted for clarity and thermal ellipsoids shown at 50% probability. The pyridine group is also omitted for clarity

4.4 Absorption Profile

The UV-vis absorption spectra for free base C4P^{PF} and each of the metal derivatives was obtained in CH_2Cl_2 (Figure 4.9). The freebase C4P^{PF} and Zn, Cu, and Ni derivatives are dark red in color when dissolved in CH_2Cl_2, while the Co derivative is a dark yellow-brown color in CH_2Cl_2. The λ_{max} of the freebase C4P^{PF} is 422 nm and the λ_{max} of the metal derivatives (440-468 nm) is red shifted as compared to the freebase (Table 4.4). The cobalt and copper derivatives also have a shoulder at longer wavelengths (500 nm) and the nickel derivative has a second weaker band at 544 nm. These absorbance features are comparable to those that were reported for related metallocalix[4]phyrins.[19]

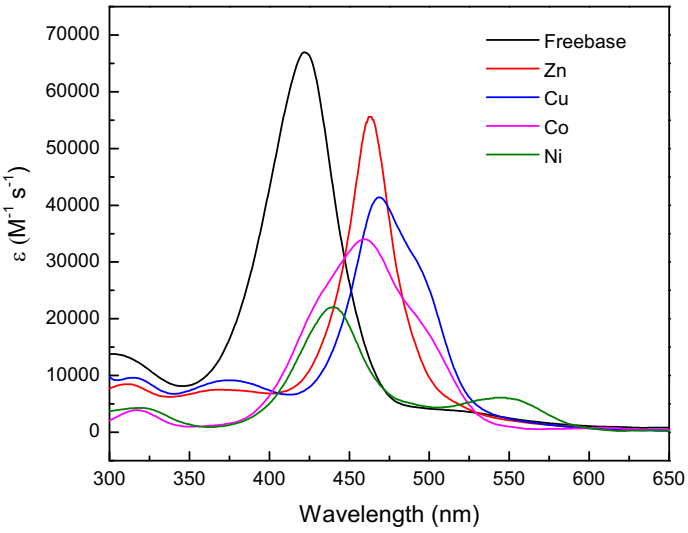

Figure 4.9: UV-vis absorbance spectra for M(C4P^{PF}) (where M = 2H (black), Zn (red), Cu (blue), Ni (green), Co (pink)) in CH_2Cl_2

Table 4.4: Maximum absorbance(s) for M(C4P^{PF}) (where M = 2H, Zn, Cu, Ni, Co)

	λ_{max} (nm)	ε (cm^{-1}, M^{-1})	λ (nm)	ε (cm^{-1}, M^{-1})
C4P^{PF}	422	67000	–	–
Zn(C4P^{PF})	463	55600	–	–
Cu(C4P^{PF})	468	41400	500	25200
Ni(C4P^{PF})	440	22100	544	6100
Co(C4P^{PF})	460	34000	500	17200

4.4.1 TDDFT Calculations

Time-dependent density functional theory (TDDFT) calculations were implemented for the metallocalix[4]phyrins in order to gain better insight into the nature of the electronic transitions of the UV-vis spectra discussed above. The major calculated transitions (f > 0.02) are shown in comparison to the experimental spectra in Figure 4.10. Overall, the calculated transitions were in reasonable agreement with the experimental results, apart from a small yet consistent deviation of approximately 50 nm of the excitation energy.

Additionally, natural transition orbital (NTO)[43] analysis was applied to provide an orbital representation for the electronic transitions. This analysis provides a simple, qualitative depiction of the electronic transitions by producing a particle-hole pair for each excitation. Due to the paramagnetic nature of Co(C4P^{PF}) and Cu(C4P^{PF}), the unrestricted calculation method was implemented for these complexes, which produced both alpha (α) and beta (β) spin states for each excitation. The NTO pairs for the most prominent electronic transitions for Zn-, Cu-, Ni- and Co- (C4P^{PF}) are shown in Figure 4.11. The NTO analysis shows that the major transitions arise from π to π* energy excitation, with some involvement of the metal d orbitals for the cobalt and nickel complexes.

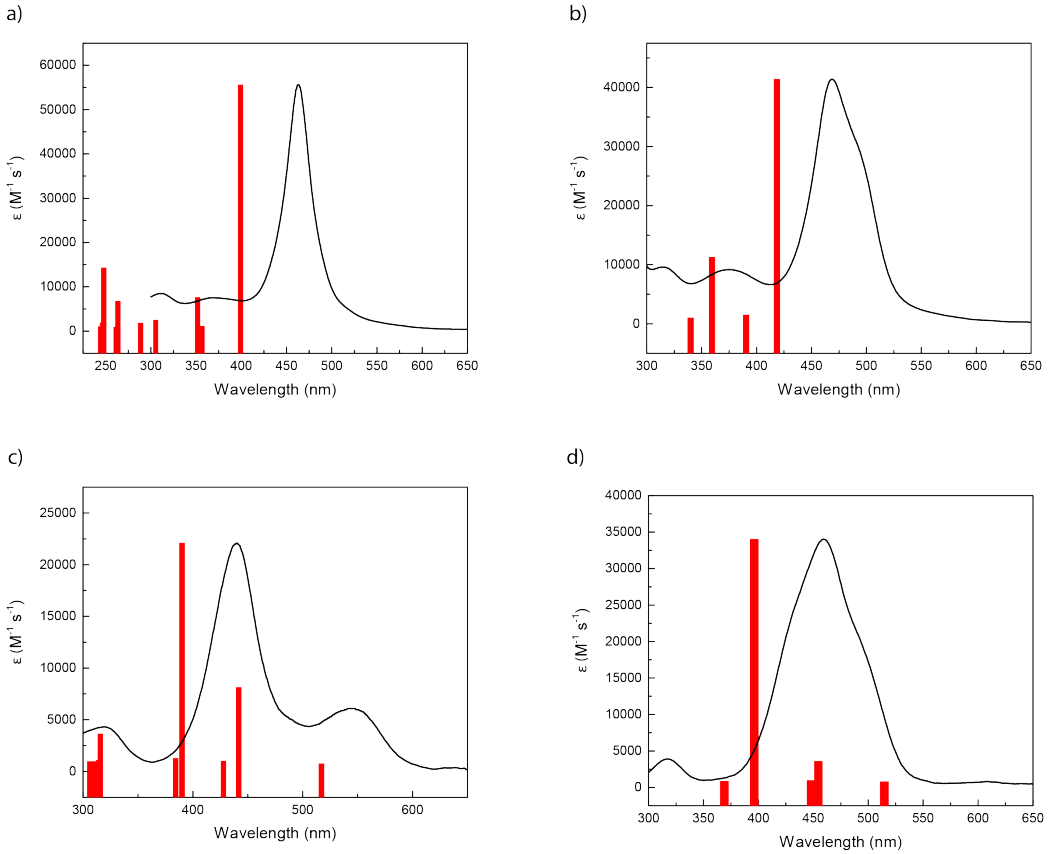

Figure 4.10: The red bars represent the most intense computed transitions (f > 0.02) as calculated by TD-DFT for a) Zn(C4P^{PF}) b) Cu(C4P^{PF}) c) Ni(C4P^{PF}) d) Co(C4P^{PF}) with the corresponding experimental UV-vis absorbance spectrum overlaid for comparison (black).

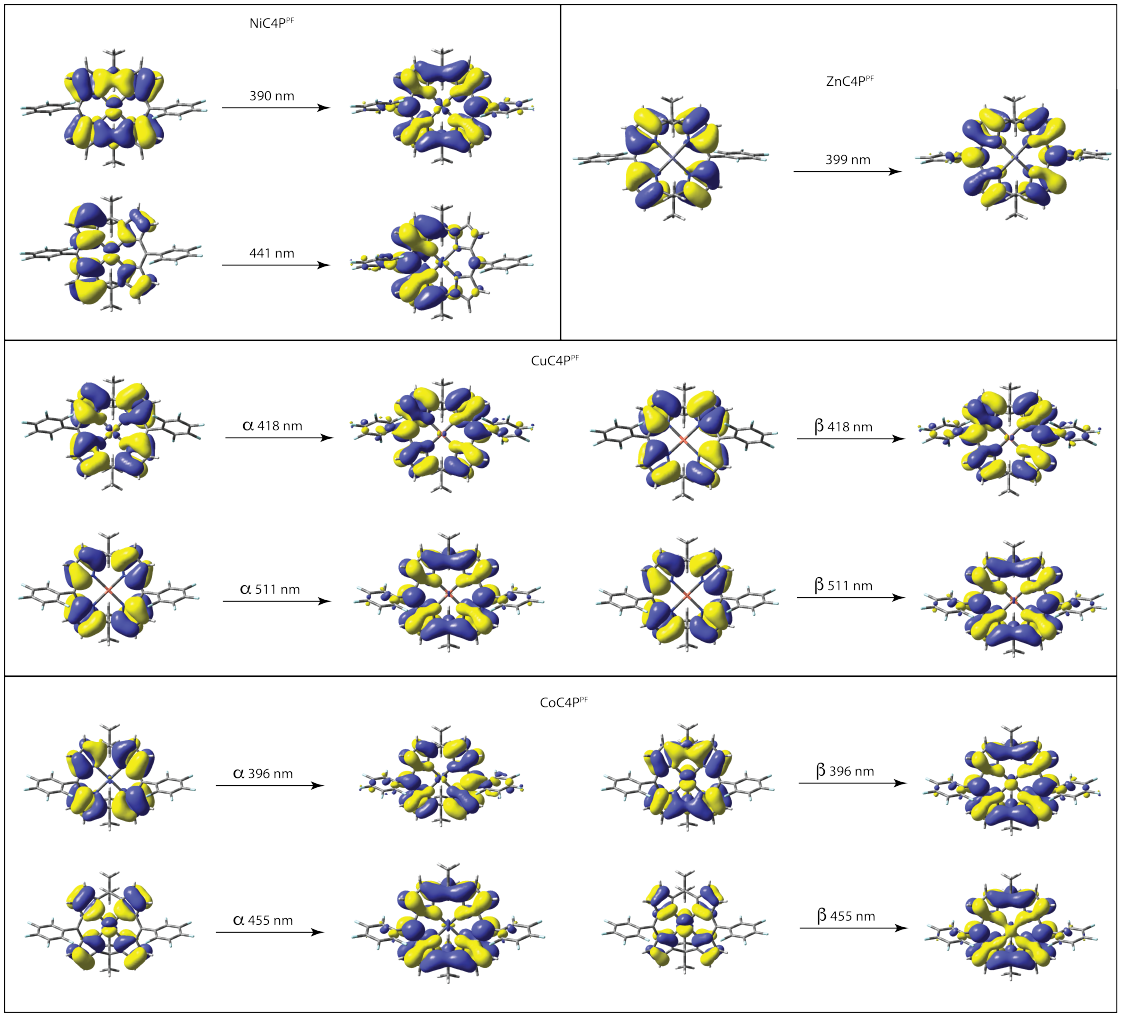

Figure 4.11: Orbital illustrations of the dominant NTO pairs for excited states at the absorption maxima of Zn-, Cu-, Ni- and Co- ($C4P^{PF}$). For each pair, the "hole" is shown to the left of the arrow, and the "particle" is to the right. Both the α and β states are shown for Cu- and Co- ($C4P^{PF}$)

4.5 Electrochemical Characterization

The redox properties of the metallocalix[4]phyrins were assessed using cyclic voltammetry (CV) and differential pulse voltammetry (DPV). The experiments were performed using 1 mM of the appropriate metallocalix[4]phyrin, 0.1 M $TBAPF_6$ (tetrabutylammonium hexafluorophosphate) as supporting electrolyte and decamethylferrocene (Fc*) as an internal standard in either dichloromethane (CH_2Cl_2) or acetonitrile (MeCN). The cyclic voltammograms of Zn-, Cu-, Ni- and Co- ($C4P^{PF}$) in MeCN are shown in Figure 4.12. The voltammograms show two quasi-reversible reductions, most likely ligand based with some influence from the metal, for each metallocalix[4]phyrin derivative. From the differential pulse voltammograms (Figure 4.13), the first reduction ranges from -0.88 to -1.15 V for each derivative with nickel having the most positive reduction potential and zinc the most negative, while the second reduction is more consistent for each derivative at -1.32 or -1.33 V (Table 4.5). In the oxidative region of the cyclic voltammograms (Figure 4.12), the redox events are less defined but typically display two or more irreversible oxidations. The oxidative potentials obtained from the differential pulse voltammogram (Figure 4.14) are given in Table 4.5, with the cobalt derivative having the least positive initial oxidation event.

Table 4.5: Summary of redox properties for $M(C4P^{PF})$ in MeCN

	$E_{ox}(1)$, V	$E_{ox}(2)$, V	$E_{red}(1)$, V	$E_{red}(2)$, V
$Zn(C4P^{PF})$	1.02	1.25	-1.15	-1.33
$Cu(C4P^{PF})$	1.17	~1.27	-0.91	-1.32
$Ni(C4P^{PF})$	1.23	—	-0.88	-1.32
$Co(C4P^{PF})$	0.94	1.36	-1.01	-1.33

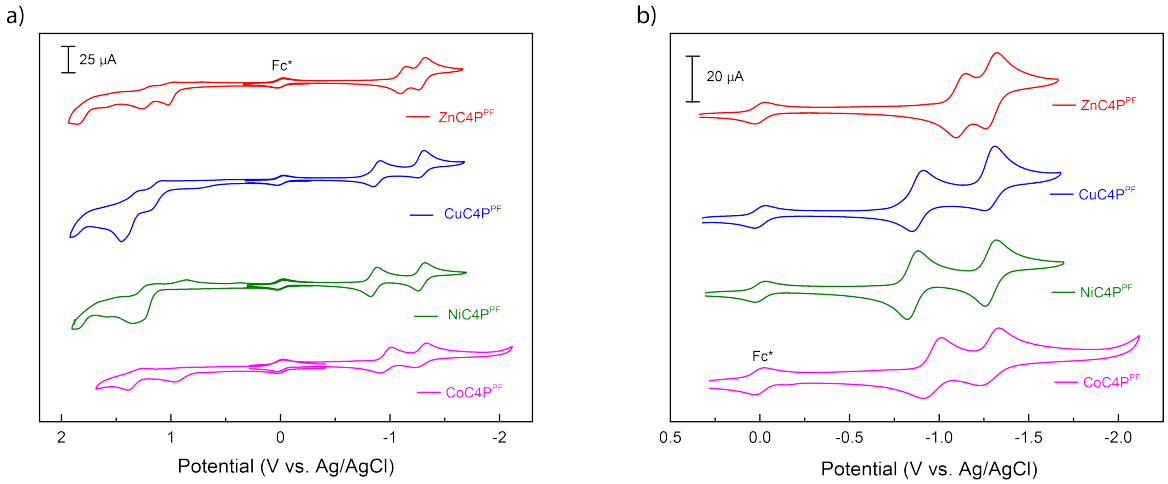

Figure 4.12: Cyclic voltammograms for Zn(C4P^{PF}) (red), Cu(C4P^{PF}) (blue), Ni(C4P^{PF}) (green) and Co(C4P^{PF}) (pink) recorded in MeCN containing 0.1 M $TBAPF_6$, 1.0 mM analyte and an internal reference (decamethylferrocene, Fc*). Scan rate 100 mV/s

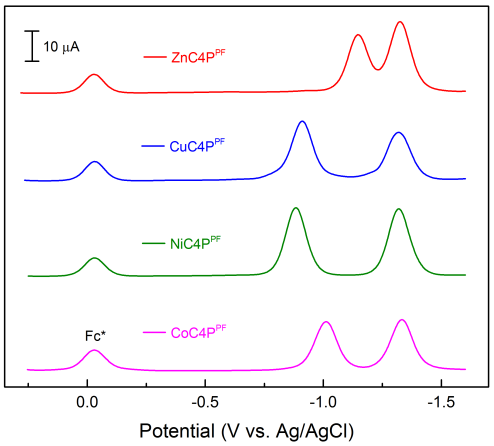

Figure 4.13: Differential pulse voltammograms of the reductive region of Zn(C4P^{PF}) (red), Cu(C4P^{PF}) (blue), Ni(C4P^{PF}) (green) and Co(C4P^{PF}) (pink) recorded in MeCN containing 0.1 M $TBAPF_6$, 1.0 mM analyte and an internal reference (decamethylferrocene, Fc*)

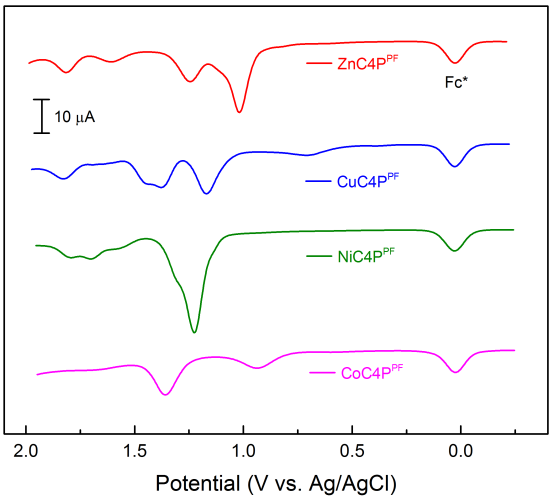

Figure 4.14: Differential pulse voltammograms of the oxidative region for Zn(C4P^{PF}) (red), Cu(C4P^{PF}) (blue), Ni(C4P^{PF}) (green) and Co(C4P^{PF}) (pink) recorded in MeCN containing 0.1 M $TBAPF_6$, 1.0 mM analyte and an internal reference (decamethylferrocene, Fc*)

The cyclic voltammograms and differential pulse voltammograms obtained in CH_2Cl_2 for the oxidative regions of Zn(C4P^{PF}), Cu(C4P^{PF}) and Ni(C4P^{PF}) are shown in Figures 4.15 and 4.16, respectively. The redox events in CH_2Cl_2 for this region are much more defined for these derivatives than the corresponding redox events in MeCN. The zinc derivative shows two ligand-based quasi-reversible oxidations at 1.04 V and 1.28 V (from DPV) (Table 4.6). The copper and nickel derivatives both show two quasi-reversible oxidations, followed by a third irreversible oxidation most likely owing to the $M^{II/III}$ event. The values of the first oxidation and third oxidation for both copper and nickel from the differential pulse voltammograms are 1.22 V and 1.80 V, respectively, and the second oxidation is 1.48 V for copper and 1.43 V for nickel (Table 4.6). The reductions for each complex in CH_2Cl_2, shown in Figure 4.15a and Figure 4.17, follow a similar trend to the reductions in MeCN.

Table 4.6: Summary of redox properties for $M(C4P^{PF})$ in CH_2Cl_2

	$E_{ox}(1)$, V	$E_{ox}(2)$, V	$E_{ox}(3)$, V	$E_{red}(1)$, V	$E_{red}(2)$, V
$Zn(C4P^{PF})$	1.04	1.28	—	-1.11	-1.42
$Cu(C4P^{PF})$	1.22	1.48	1.80	-1.03	-1.43
$Ni(C4P^{PF})$	1.22	1.43	1.80	-1.01	-1.42

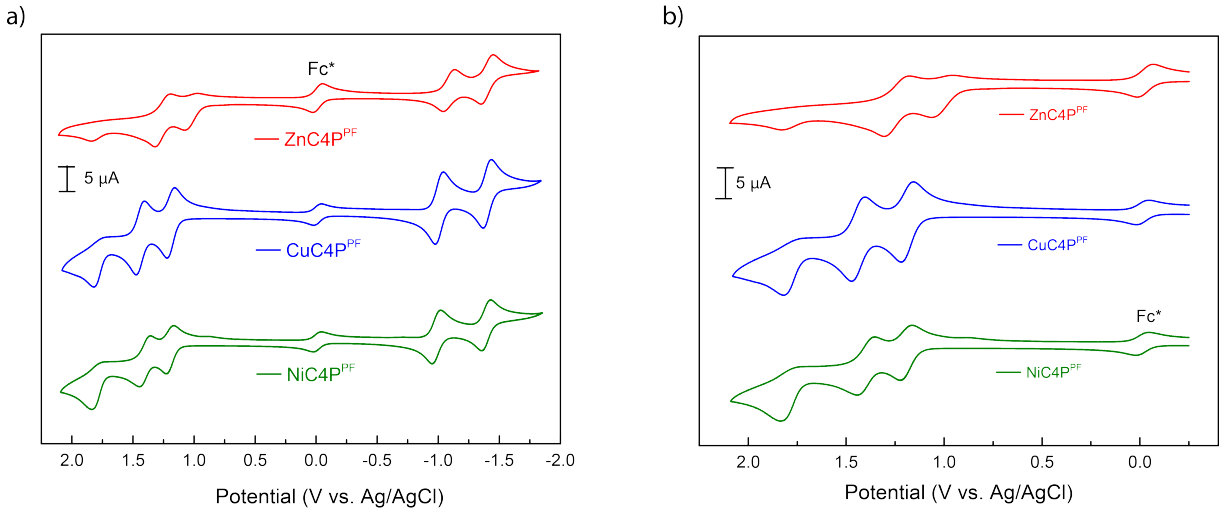

Figure 4.15: Cyclic voltammograms for $Zn(C4P^{PF})$ (red), $Cu(C4P^{PF})$ (blue), $Ni(C4P^{PF})$ (green) recorded in CH_2Cl_2 containing 0.1 M $TBAPF_6$, 1.0 mM analyte and an internal reference (decamethylferrocene, Fc*). Scan rate 100 mV/s

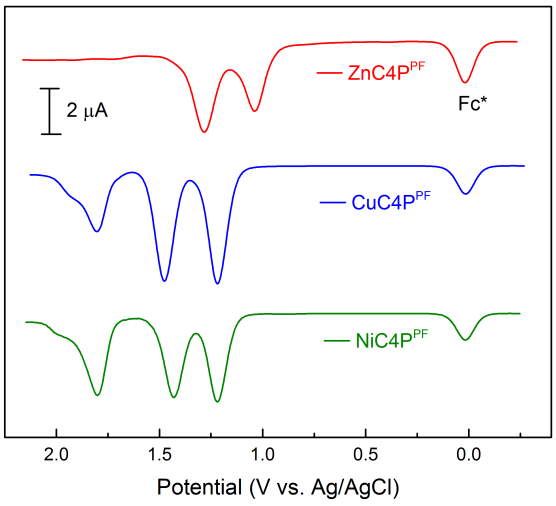

Figure 4.16: Differential pulse voltammograms of the oxidative region for Zn($C4P^{PF}$) (red), Cu($C4P^{PF}$) (blue), Ni($C4P^{PF}$) (green) recorded in CH_2Cl_2 containing 0.1 M $TBAPF_6$, 1.0 mM analyte and an internal reference (decamethylferrocene, Fc*)

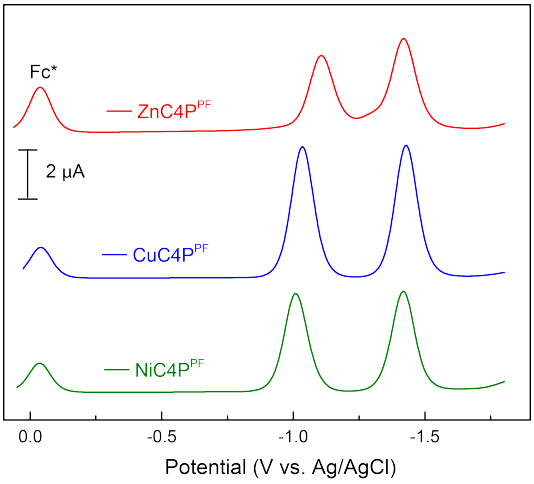

Figure 4.17: Differential pulse voltammograms of the reductive region for Zn($C4P^{PF}$) (red), Cu($C4P^{PF}$) (blue), Ni($C4P^{PF}$) (green) recorded in CH_2Cl_2 containing 0.1 M $TBAPF_6$, 1.0 mM analyte and an internal reference (decamethylferrocene, Fc*)

4.6 Summary

The calix[4]phyrin is a tetrapyrrole macrocycle that has been relatively unexplored as a ligand. In this work, we synthesized the freebase $C4P^{PF}$ by modifying a streamlined procedure previously utilized in our laboratory and explored the metalation of this macrocycle with zinc, copper, nickel and cobalt. These metallocalix[4]phyrin were then characterized using a variety of methods. These complexes show unique characteristics compared to other tetrapyrrole macrocycles; the solid state structures obtained for these complexes highlight the flexibility of the macrocycle and voltammetry shows these complexes exhibit a rich multielectron redox chemistry. The chapters to follow will explore how these metallocalix[4]phyrins, specifically the cobalt complex, act as a unique catalyst in the oxygen reduction reaction.

4.7 Experimental Methods

4.7.1 General Methods

Unless otherwise stated, reactions were performed in oven-dried glassware either under a positive pressure of nitrogen with flasks fitted with Suba-Seal rubber septa or in a nitrogen-filled glovebox.

4.7.1.1 Materials

Reagents and solvents were purchased from Acros Organics, Cambridge Isotopes Laboratories, Fisher Scientific, Sigma-Aldrich, or Strem Chemicals, Inc. Solvents for synthesis were of reagent grade or better; solvents for air- or moisture-sensitive reactions were dried by passage through activated alumina and then stored over 4 Å molecular sieves prior to use.[44] Tetrabutylammonium hexafluorophosphate

($TBAPF_6$) was purchased from Tokyo Chemical Industry Co. LTD and further purified by recrystallization from ethanol, then dried *in vacuo* at 40 °C for several days prior to use.

4.7.1.2 Compound Characterization

^1H NMR and ^{13}C NMR spectra were recorded at 25 °C on a Bruker 400 MHz spectrometer. Proton spectra are referenced to the residual proton resonance of the deuterated solvent ($CDCl_3$ = δ 7.26), and carbon spectra are referenced to the carbon resonances of the solvent ($CDCl_3$ = δ 77.16). All chemical shifts are reported using the standard δ notation in parts-per-million; positive chemical shifts are to higher frequency from the given reference. High-resolution mass spectrometry analyses were performed by the Mass Spectrometry Laboratory in the Department of Chemistry and Biochemistry at the University of Delaware.

4.7.1.3 Electrochemical Measurements

Cyclic voltammetry (CV) and differential pulse voltammetry (DPV) measurements were performed using a CHI-620D potentiostat and voltammograms were recorded in a nitrogen filled glovebox using a standard three-electrode assembly (glassy carbon working electrode, a platinum wire auxiliary electrode, and a silver wire quasi-reference electrode). A decamethylferrocene–decamethylferrocenium internal standard was used for all stated potentials, referenced to 1 mV versus Ag/AgCl in CH_3CN and -12 mV versus Ag/AgCl in CH_2Cl_2.[45] The supporting electrolyte was 0.1 M $TBAPF_6$ with an analyte concentration of 1 mM; a scan rate of 100 mV/s with iR drop compensation was maintained during data acquisition.

4.7.1.4 UV-Vis Absorption

UV-vis spectroscopy was carried out on a StellarNet CCD array UV- vis spectrometer at room temperature using screw cap quartz cuvettes from Starna (path length = 1 cm). The concentration of the complex in CH_2Cl_2 was between 2 and 20 μM.

4.7.1.5 Computations

The computations were performed with density functional theory (DFT) methods by using Becke three-parameter hybrid exchange and Lee-Yang-Parr correlation functional (B3LYP)[46-48] or the analogous unrestricted method (UB3LYP) in the Gaussian 09 software.[49] The 6-31G(d) basis set was utilized for the ligand (C, H, N, and F atoms) and LANL2DZ[50] basis set was utilized for the metal center (Cu, Co, Ni, Zn). All geometry optimizations were performed in C_1 symmetry with subsequent frequency analysis to confirm that each stationary point was a minimum on the potential energy surface. The solvent effects of CH_2Cl_2 for geometry optimizations have been accounted for using the SMD universal continuum model with $\varepsilon = 8.93$.[51] The electronic transitions of the complexes were calculated using the time-dependent density functional theory (TD-DFT) from the optimized ground-state structure and natural transition orbital (NTO)[43] analysis was performed to provide a visualization for better interpretation of these results.

4.7.2 Synthesis of M[bis(pentafluorophenyl)calix[4]phyrin] (M= 2H, Zn, Cu, Ni, Co)

The synthesis of the free base bis(pentafluorophenyl)calix[4]phyrin was accomplished using a method previously developed in our group.[52] The syntheses of Zn, Cu and Ni [bis(pentafluorophenyl)calix[4]phyrin] were performed under air.

4.7.2.1 5,5,15,15-Tetramethyl-10,20-bis(pentafluorophenyl)calix[4]phyrin

To a solution of 281 mg (0.5 mmol) of 5,5-dimethyl-1,9-bis(pentafluorobenzoyl)dipyrromethane[34] dissolved in 30 mL THF and 9 mL MeOH was added 946 mg $NaBH_4$ (25.0 mmol). This solution was allowed to stir at room temperature for 2 hours, followed by addition of distilled water to quench the reaction. The solution was extracted with CH_2Cl_2 twice then the organic layers were combined and rinsed with water and brine. The organic layer was collected and CH_2Cl_2 was removed *in vacuo* to give a pale-yellow oil. The oil was dissolved in 200 mL of CH_2Cl_2 and sparged with nitrogen for 0.5 hours. To the solution was then added 87 mg (0.5 mmol) of 5,5-dimethyldipyrromethane[37] and 30 mg of $InCl_3$. The reaction was allowed to stir under a nitrogen atmosphere for 0.5 hours. To the reaction mixture was added 226 mg DDQ (2,3-dichloro-5,6-dicyano-1,4-benzoquinone) and after 5 minutes, 14 mL of triethylamine was also added. The reaction was allowed to stir for an additional 15 minutes, followed by removal of solvent *in vacuo* to give a dark red solid. The solid was purified by column chromatography on silica using hexanes and CH_2Cl_2 (5:1) to give 158 mg of the desired compound (45% yield). Characterization by ^1H and ^{13}C NMR matched previously reported results.[15,25,26]

4.7.2.2 Zinc[bis(pentafluorophenyl)calix[4]phyrin]

A mixture of bis(pentafluorophenyl)calix[4]phyrin (100 mg, 0.14 mmol) and 600 mg $Zn(OAc)_2 \cdot 2\ H_2O$ was allowed to stir in 30 mL N,N-dimethylformamide (DMF) at 60 °C for 16 h. The solvent was removed *in vacuo*. The remaining solid was dissolved in dichloromethane and rinsed several times with a brine solution. The organic layers were combined and dried over sodium sulfate. The solvent was removed *in vacuo* to give a dark red solid (98 mg, 90% yield). ^1H NMR (400 MHz;

$CDCl_3$, 25 °C) δ/ppm: 6.44 (q, J=4.2 Hz, 8H), 1.81 (s, 12 H). ^{13}C NMR (101 MHz; $CDCl_3$, 25 °C) δ/ppm: 171.48, 144.94 (dm, 4xCF), 141.47 (dm, 4xCF), 140.72, 137.35 (dm, 2xCF), 130.52, 127.25, 115.96, 113.26 (t), 39.09, 31.63. HR-LIFDI-MS: $[M]^+$ m/z calc for $C_{36}H_{20}F_{10}N_4Zn$: 762.0820. Found: 762.0836.

4.7.2.3 Nickel[bis(pentafluorophenyl)calix[4]phyrin]

A mixture of bis(pentafluorophenyl)calix[4]phyrin (35 mg, 0.05 mmol) and 10 mg $Ni(OAc)_2$ was allowed to stir in 15 mL DMF at 130 °C for 16 h. The solvent was removed *in vacuo*. The remaining solid was dissolved in dichloromethane and rinsed several times with a brine solution. The organic layers were combined and dried over sodium sulfate. The solvent was removed *in vacuo* and the crude material was purified by column chromatography on basic alumina using hexanes and chloroform (20:1) as the eluent to give a dark red solid (22 mg, 56% yield). ^1H NMR (400 MHz; $CDCl_3$, 25 °C) δ/ppm: 6.29 (d, 4.3 Hz, 4H), 6.21 (d, 4.3 Hz, 4H), 2.68 (s, 6 H), 1.62 (s, 6 H). ^{13}C NMR (101 MHz; $CDCl_3$, 25 °C) δ/ppm: 168.13, 144.97 (dm, 4xCF), 141.55 (dm, 4xCF), 137.32 (dm, 2xCF), 135.57, 130.12, 126.40, 115.69, 111.43 (t), 39.4, 38.59, 23.94. HR-LIFDI-MS: $[M]^+$ m/z calc for $C_{36}H_{20}F_{10}N_4Ni$: 756.0882. Found: 756.0900.

4.7.2.4 Copper[bis(pentafluorophenyl)calix[4]phyrin]

A mixture of bis(pentafluorophenyl)calix[4]phyrin (30 mg, 0.04 mmol) and 8 mg $Cu(OAc)_2$ was allowed to stir in 10 mL DMF at 130 °C for 4 h. The solvent was removed *in vacuo*. The remaining solid was dissolved in dichloromethane and rinsed several times with a brine solution. The organic layers were combined and dried over sodium sulfate. The solvent was removed *in vacuo* and the crude material was purified by column chromatography on silica using hexanes and chloroform (4:1) as the eluent

to give a dark red solid (24 mg, 73% yield). HR-LIFDI-MS: $[M]^+$ m/z calc for $C_{36}H_{20}F_{10}N_4Cu$: 761.0824. Found: 761.0804

4.7.2.5 Cobalt[bis(pentafluorophenyl)calix[4]phyrin]

A mixture of bis(pentafluorophenyl)calix[4]phyrin (25 mg, 0.036 mmol) and 10 mg $Co(OAc)_2$ was allowed to stir in 15 mL DMF at 130 °C for 16 h. The solvent was removed *in vacuo*. The remaining solid was dissolved in dichloromethane and rinsed several times with a brine solution. The organic layers were combined and dried over sodium sulfate. The solvent was removed *in vacuo* and the crude material was purified by column chromatography on basic alumina using hexanes and chloroform (20:1) as the eluent to give a dark yellow brown solid (21 mg, 75%). HR-LIFDI-MS: $[M]^+$ m/z calc for $C_{36}H_{20}F_{10}N_4Co$: 757.0860. Found: 757.0883. Anal. Calc. for $C_{36}H_{20}F_{10}N_4Co \cdot C_4H_8O$: C, 57.91; H, 3.40; N 6.75. Found: C, 58.28; H, 3.10; N, 6.87.

4.7.3 X-ray Crystallography

4.7.3.1 X-ray Structure Solution and Refinement for M Calix[4]phyrin

Crystals were mounted using viscous oil onto a plastic mesh and cooled to the data collection temperature. Data were collected on a Smart APEX diffractometer with Mo-Kα radiation (λ = 0.71073 Å) monochromated with graphite except Cu($C4P^{PF}$) which were collected using Cu- Kα radiation (λ = 1.54178 Å) focused using Goebel mirrors. Unit cell parameters were obtained from 36 data frames, 0.5º ω, from three different sections of the Ewald sphere. The unit-cell parameters, equivalent reflections, and systematic absences in the diffraction data are consistent, uniquely, with $P2_1/c$ (or $P2_1/n$ no. 14). Solutions in the centrosymmetric space group options yielded chemically reasonable and computationally stable results of refinement. The data sets

were treated with multi-scan absorption corrections.[53] The structures were solved using direct methods and refined with full-matrix, least-squares procedures on F^2.[54] Two compound molecules were located in the asymmetric unit of Cu(C4P^{PF}). The data for Cu(C4P^{PF}) was treated with Squeeze to model disordered solvent molecules as diffused contributions.[55] Despite repeated attempts, Zn(C4P^{PF}) consistently deposited as multiple crystals with preferential cleavage precluding sectioning a single data crystal leading to a level B alert from an R_{int} of 0.18. All non-hydrogen atoms were refined with anisotropic displacement parameters. H-atoms were placed in calculated positions with U_{iso} equal to 1.2 (1.5 for methyl H) U_{eq} of the attached atom. Atomic scattering factors are contained in the SHELXTL program library. Crystallographic data were collected by Gabriel Andrade or Dr. Glenn Yap, Department of Chemistry and Biochemistry, University of Delaware.

4.7.3.2 Crystallographic Information Tables

Table 4.7: Crystallographic data for M Calix[4]phyrin

Formula	M = Zn	M = Cu	M = Co
Fw	843.03	949.35	836.59
Crystal System	monoclinic	monoclinic	monoclinic
Space Group	P 1 2_1/n 1	P 1 2_1/c 1	P 1 2_1/n 1
a	14.057(2) Å	10.7917(2) Å	14.7547(14) Å
b	13.745(2) Å	31.5139(8) Å	15.4489(15) Å
c	19.062(3) Å	25.3954(6) Å	15.5827(15) Å
α	90°	90°	90°
β	96.001(4)°	90.1850(13)°	93.857(2)°
γ	90°	90°	90°
Volume	3662.9(9) $Å^3$	8636.6(3) $Å^3$	3543.9(6) $Å^3$
Z	4	8	4
Temp	200(2) K	200(2) K	200(2) K
D_{calcd}	1.529 g/cm^3	1.460 g/cm^3	1.568 g/cm^3
2Θ range	1.90 to 27.53°	3.75 to 73.94°	1.84 to 27.55°
μ	0.760 mm^{-1}	1.484 mm^{-1}	0.577 mm^{-1}
Reflections	35803	108076	53616
Unique	8396	17057	8151
R (int)	0.1812	0.0917	0.0817
R_1	0.0745	0.0563	0.0413
wR_2	0.2339	0.1665	0.0901

4.8 References and Notes

(1) Dwyer, P. N.; Buchler, J. W.; Scheidt, W. R. *J. Am. Chem. Soc.* **1974**, *96* (9), 2789.

(2) Dwyer, P. N.; Puppe, L.; Buchler, J. W.; Scheidt, W. R. *Inorg. Chem.* **1975**, *14* (8), 1782.

(3) Buchler, J. W.; Lay, K. L.; Smith, P. D.; Scheidt, W. R.; Rupprecht, G. A.; Kenny, J. E. *J. Organomet. Chem.* **1976**, *110* (1), 109.

(4) Buchler, J. W.; Lay, K. L.; Lee, Y. J.; Scheidt, W. R. *Angew. Chemie Int. Ed. Engl.* **1982**, *21* (6), 432.

(5) Buchler, J. W.; Dreher, C.; Lay, K. L.; Lee, Y. J.; Scheidt, W. R. *Inorg. Chem.* **1983**, *22* (6), 888.

(6) Botulinski, A.; Buchler, J. W.; Tonn, B.; Wicholas, M. *Inorg. Chem.* **1985**, *24* (20), 3239.

(7) Botulinski, A.; Buchler, J. W.; Wicholas, M. *Inorg. Chem.* **1987**, *26* (10), 1540.

(8) Botulinski, A.; Buchler, J. W.; Lee, Y. J.; Scheidt, W. R.; Wicholas, M. *Inorg. Chem.* **1988**, *27* (5), 927.

(9) Renner, M. W.; Buchler, J. W. *J. Phys. Chem.* **1995**, *99* (20), 8045.

(10) Sessler, J.L.; Zimmerman, R.S.; Bucher, C.; Král, V.; Andrioletti, B. *Pure Appl. Chem.* **2001**, *73* (7), 1041.

(11) The focus of our work will mainly be on the calix[4]phyrin-(**1**,*1*,**1**,*1*) type scaffold, and as such in later sections if the (**1**,*1*,**1**,*1*) notation is not indicated it should be assumed to be this type.

(12) Scheer, H.; Wolf, H. *Justus Liebigs Ann. Chem.* **1973**, *1973* (10), 1741.

(13) Furhop, J.-H.; Salek, A.; Subramanian, J.; Mengersen, C.; Besecke, S. *Justus Liebigs Ann. Chem.* **1975**, *1975* (6), 1131.

(14) Král, V.; Sessler, J. L.; Zimmerman, R. S.; Seidel, D.; Lynch, V.; Andrioletti, B. *Angew. Chemie Int. Ed.* **2000**, *39* (6), 1055.

(15) Bernátková, M.; Andrioletti, B.; Král, V.; Rose, E.; Vaissermann, J. *J. Org. Chem.* **2004**, *69* (23), 8140.

(16) Finnigan, E. M.; Giordani, S.; Senge, M. O.; McCabe, T. *J. Phys. Chem. A* **2010**, *114* (7), 2464.

(17) Da Silva, C.; Bonomo, L.; Solari, E.; Scopelliti, R.; Floriani, C.; Re, N. *Chem. – A Eur. J.* **2000**, *6* (24), 4518.

(18) Bonomo, L.; Solari, E.; Scopelliti, R.; Floriani, C.; Re, N. *J. Am. Chem. Soc.* **2000**, *122* (22), 5312.

(19) Re, N.; Bonomo, L.; Da Silva, C.; Solari, E.; Scopelliti, R.; Floriani, C. *Chem. – A Eur. J.* **2001**, *7* (12), 2536.

(20) Bucher, C.; Devillers, C. H.; Moutet, J.-C.; Pecaut, J.; Royal, G.; Saint-Aman, E.; Thomas, F. *Dalton Trans.* **2005**, (22), 3620.

(21) Salini, P. S.; Thomas, A. P.; Sabarinathan, R.; Ramakrishnan, S.; Sreedevi, K. C. G.; Reddy, M. L. P.; Srinivasan, A. *Chem. – A Eur. J.* **2011**, *17* (24), 6598.

(22) Horníček, J.; Dvořáková, H.; Bouř, P. *J. Phys. Chem. A* **2010**, *114* (10), 3649.

(23) Benech, J.-M.; Bonomo, L.; Solari, E.; Scopelliti, R.; Floriani, C. *Angew. Chemie Int. Ed.* **1999**, *38* (13–14), 1957.

(24) Bischoff, I.; Feng, X.; Senge, M. O. *Tetrahedron* **2001**, *57* (26), 5573.

(25) Dolenský, B.; Kroulík, J.; Král, V.; Sessler, J. L.; Dvořáková, H.; Bouř, P.; Bernátková, M.; Bucher, C.; Lynch, V. *J. Am. Chem. Soc.* **2004**, *126* (42), 13714.

(26) Flint, D. L.; Fowler, R. L.; LeSaulnier, T. D.; Long, A. C.; O'Brien, A. Y.; Geier, G. R. *J. Org. Chem.* **2010**, *75* (3), 553.

(27) Orlewska, C.; Toppet, S.; Dehaen, W. *Synth. Commun.* **2005**, *35* (14), 1953.

(28) Guchhait, T.; Jha, V. K.; Mani, G. *Org. Biomol. Chem.* **2013**, *11* (17), 2818.

(29) Orlewska, C.; Maes, W.; Toppet, S.; Dehaen, W. *Tetrahedron Lett.* **2005**, *46* (36), 6067.

(30) Matano, Y.; Miyajima, T.; Nakabuchi, T.; Imahori, H.; Ochi, N.; Sakaki, S. *J. Am. Chem. Soc.* **2006**, *128* (36), 11760.

(31) Matano, Y.; Miyajima, T.; Ochi, N.; Nakabuchi, T.; Shiro, M.; Nakao, Y.; Sakaki, S.; Imahori, H. *J. Am. Chem. Soc.* **2008**, *130* (3), 990.

(32) Pistner, A. J.; Yap, G. P. A.; Rosenthal, J. *J. Phys. Chem. C* **2012**, *116* (32), 16918.

(33) Pistner, A. J.; Lutterman, D. A.; Ghidiu, M. J.; Ma, Y.-Z.; Rosenthal, J. *J. Am. Chem. Soc.* **2013**, *135* (17), 6601.

(34) O'Brien, A. Y.; McGann, J. P.; Geier, G. R. *J. Org. Chem.* **2007**, *72* (11), 4084.

(35) Bachmann, J.; Nocera, D. G. *J. Am. Chem. Soc.* **2004**, *126* (9), 2829.

(36) Bachmann, J.; Nocera, D. G. *J. Am. Chem. Soc.* **2005**, *127* (13), 4730.

(37) Littler, B. J.; Miller, M. A.; Hung, C.-H.; Wagner, R. W.; O'Shea, D. F.; Boyle, P. D.; Lindsey, J. S. *J. Org. Chem.* **1999**, *64* (4), 1391.

(38) Bischoff, I.; Feng, X.; Senge, M. O. *Tetrahedron* **2001**, *57* (26), 5573.

(39) Harmjanz, M.; Gill, H. S.; Scott, M. J. *J. Org. Chem.* **2001**, *66* (16), 5374.

(40) Pistner, A. J.; Pupillo, R. C.; Yap, G. P. A.; Lutterman, D. A.; Ma, Y.-Z.; Rosenthal, J. *J. Phys. Chem. A* **2014**, *118* (45), 10639.

(41) Ema, T.; Senge, M. O.; Nelson, N. Y.; Ogoshi, H.; Smith, K. M. *Angew. Chemie Int. Ed. English* **1994**, *33* (18), 1879.

(42) Senge, M. O.; Bischoff, I.; Nelson, N. Y.; Smith, K. M. *J. Porphyins. Phthalocyanines* **1999**, *3* (2), 99.

(43) Martin, R. L. *J. Chem. Phys.* **2003**, *118* (11), 4775.

(44) Pangborn, A. B.; Giardello, M. A.; Grubbs, R. H.; Rosen, R. K.; Timmers, F. J. *Organometallics* **1996,** *15* (5), 1518-1520.

(45) Noviandri, I.; Brown, K. N.; Fleming, D. S.; Gulyas, P. T.; Lay, P. A.; Masters, A. F.; Phillips, L. *J. Phys. Chem. B* **1999,** *103* (32), 6713-6722.

(46) Becke, A. D. *J. Chem. Phys.* **1993**, *98* (7), 5648.

(47) Becke, A. D. *Phys. Rev. A* **1988**, *38* (6), 3098.

(48) Lee, C.; Yang, W.; Parr, R. G. *Phys. Rev. B* **1988**, *37* (2), 785.

(49) Frisch, M. J.; Trucks, G. W.; Schlegel, H. B.; Scuseria, G. E.; Robb, M. A.; Cheeseman, J. R.; Scalmani, G.; Barone, V.; Mennucci, B.; Petersson, G. A.; Nakatsuji, H.; Caricato, M.; Li, X.; Hratchian, H. P.; Izmaylov, A. F.; Bloino, J.; Zheng, G.; Sonnenberg, J. L.; Hada, M.; Ehara, M.; Toyota, K.; Fukuda, R.; Hasegawa, J.; Ishida, M.; Nakajima, T.; Honda, Y.; Kitao, O.; Nakai, H.; Vreven, T.; Montgomery Jr., J. A.; Peralta, J. E.; Ogliaro, F.; Bearpark, M.; Heyd, J. J.; Brothers, E.; Kudin, K. N.; Staroverov, V. N.; Kobayashi, R.; Normand, J.; Raghavachari, K.; Rendell, A.; Burant, J. C.; Iyengar, S. S.; Tomasi, J.; Cossi, M.; Rega, N.; Millam, J. M.; Klene, M.; Knox, J. E.; Cross, J. B.; Bakken, V.; Adamo, C.; Jaramillo, J.; Gomperts, R.; Stratmann, R. E.; Yazyev, O.; Austin, A. J.; Cammi, R.; Pomelli, C.; Ochterski, J. W.; Martin, R. L.; Morokuma, K.; Zakrzewski, V. G.; Voth, G. A.; Salvador, P.; Dannenberg, J. J.; Dapprich, S.; Daniels, A. D.; Farkas, Ö.; Foresman, J. B.; Ortiz, J. V; Cioslowski, J.; Fox, D. J. Gaussian09 Revision A.01, 2009.

(50) Wadt, W. R.; Hay, P. J. *J. Chem. Phys.* **1985**, *82* (1), 284.

(51) Marenich, A. V.; Cramer, C. J.; Truhlar, D. G. *J. Phys. Chem. B* **2009**, *113*, 6378.

(52) Lefler, B.; Eddy, J.W.; Rosenthal, J. *Unpublished Results* **2014**.

(53) Apex3 software suite, Madison, WI, 2015.

(54) Sheldrick, G. M. *Acta Crystallogr. Sect. A* **2008**, *64* (1), 112.

(55) Spek, A. L. *J. Appl. Crystallogr.* **2003**, *36* (1), 7.

Chapter 5

OXYGEN REDUCTION REACTION CATALYZED BY COBALT CALIX[4]PHYRIN

5.1 Introduction

Over the last several decades, cobalt catalysts have been explored as inexpensive replacements for platinum at the cathode of fuel cells.[1-6] Platinum has been the traditional cathode catalyst since it selectivity reduces O_2 by a $4e^-/4H^+$ process to give H_2O. Oxygen can also be reduced by $2e^-$ and $2H^+$ to produce H_2O_2, however, this process wastes approximately half a volt of energy (Figure 1.6)[6] and is not compatible with PEM fuel cells.[7] Therefore, as viable replacements for platinum these cobalt complexes must catalyze the oxygen reduction reaction (ORR) to selectively produce water. Rotating ring disk electrodes (RRDE) are typically employed to electrochemically determine the selectivity of H_2O production.

A typical RRDE for ORR studies is shown in Figure 5.1.[8,9] The electrode consists of a glassy carbon disk at the center of the electrode and a platinum ring surrounding the disk, with a small separation between the two. A cobalt catalyst is adsorbed on the glassy carbon disk; adsorbing the catalyst on the electrode is advantageous over solution catalysis, since less catalyst is required and electron transfer is faster.[5] The electrode is placed in an oxygenated aqueous electrolyte solution and the potential of the glassy carbon disk is swept from a positive potential to a more negative potential. Additionally, the entire electrode assembly is rotated at various rates. This allows substrate to be replenished at the glassy carbon disk surface,

as well as any H_2O or H_2O_2 produced at the glassy carbon disk to be swept across the platinum ring electrode. While the glassy carbon disk potential is changed at a constant rate, the platinum ring is set at a fixed potential (+ 1.4 V vs. NHE), where any catalytically produced H_2O_2 is oxidized. This provides a means of detection for H_2O_2 product at the platinum ring electrode.

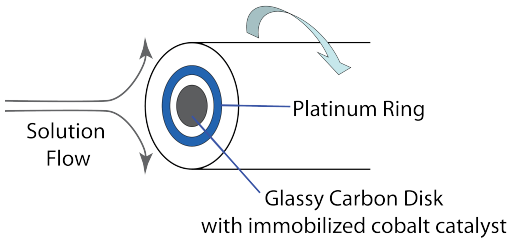

Figure 5.1: Rotating Ring-Disk Electrode

The number of electrons (n) and the % H_2O_2 can be calculated based on the ring and disk currents, shown in equation 5.1 and 5.2:

$$\% \, H_2O_2 = \frac{(2I_r/N)}{I_d+(I_r/N)} \text{ x } 100 \qquad 5.1$$

$$n = \frac{4I_d}{I_d+(I_r/N)} \qquad 5.2$$

where I_d is the disk current, I_r is the ring current, and N is the collection efficiency.

The number of electrons can also be determined using the Koutecky-Levich (KL) equation:[8]

$$\frac{1}{i} = \frac{1}{i_K} + \frac{1}{i_{l,c}} = \frac{1}{i_K} + \left(\frac{1}{0.62nFAD_O^{2/3}\nu^{-1/6}C_O^*}\right)\omega^{-1/2} \qquad 5.3$$

where i_i is the measured current density, i_K is kinetic current density, $i_{l,c}$ is limiting current density, n is electrons transferred, F is Faraday's constant (96485 C/mol), A is the electrode area (0.2475 cm^2), D_O is the diffusion coefficient of O_2 (1.15 x 10^{-5} mol/cm^3), v is the kinematic viscosity of electrolyte (1.0 x 10^{-2} V s^{-1}), C_O is concentration of O_2 (1.4 x 10^{-6} M), and ω is the angular rotation rate of the electrode ($2\pi f$, f is revolutions per second). The number of electrons transferred can be determined from the slope of a plot of inverse measured current density versus the inverse square root of the rotation rate and the kinetic current density can be extracted from the y-intercept.

The most selective cobalt catalysts for O_2 reduction to H_2O are elaborate cofacial bis(cobalt) diporphyrin motifs. The cofacial structure was found to be necessary to direct protonation of the bound superoxo (Figure 1.8). Our group wanted to explore a different approach by using cobalt tetrapyrroles with multielectron redox ligands to provide selectivity for H_2O production using a simple monomeric cobalt species. In this chapter, the homogeneous and heterogeneous oxygen reduction capabilities of one such cobalt complex, cobalt calix[4]phyrin or Co(C4P^{PF}), is explored and compared to the analogous cobalt porphyrin, Co(Por^{PF}) (Figure 5.2)

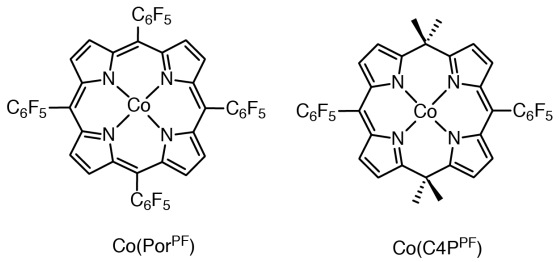

Figure 5.2: Cobalt catalysts studied for the homogenous and heterogeneous ORR: cobalt porphyrin (Co(Por^{PF}), left) and cobalt calix[4]phyrin (Co(C4P^{PF}), right)

5.2 Homogeneous O_2 Reduction

The ORR with cobalt calix[4]phyrin was first carried out under homogeneous conditions using an experimental set-up developed by Fukuzumi and co-workers,[10] which involves monitoring the reaction progress via UV-vis spectroscopy. Using homogeneous conditions for the ORR is advantageous since the reaction can be studied stoichiometrically as well as providing mechanistic insight into the catalytic reaction. The reaction was probed using ferrocene as a one electron chemical reductant and perchloric acid as a proton source in benzonitrile (PhCN), a solvent with a known oxygen concentration (Scheme 5.1).

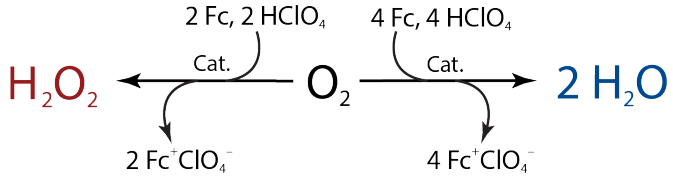

Scheme 5.1: Potential pathways for O_2 reduction by Co(C4P^{PF}) catalyst. On the left is a 2 e^-, 2 H^+ process that generates H_2O_2, while on the right is 4 e^- and 4 H^+ process that generates two equivalents of H_2O

The cobalt calix[4]phyrin catalyst and $HClO_4$ were added to an air-saturated PhCN solution of ferrocene. The resulting oxidation of ferrocene by O_2 was monitored by absorption spectroscopy with a rise in the absorbance of ferrocenium ion (Fc^+) product (λ = 620 nm) over time (Figure 5.3). The concentration of ferrocenium can be determined from the extinction coefficient of ferrocenium (330 $M^{-1}cm^{-1}$ in PhCN), which in turn allows for the calculation of the number of electron equivalents transferred during the reaction. The total number of e^- equivalents transferred indicates either H_2O_2 production (2 e^- equivalents), H_2O production (4 e^- equivalents)

or a combination of both pathways (between 2 and 4 e^- equivalents) (Scheme 5.1). Therefore, the e^- equivalents can be determined by the ratio of final concentration of Fc^+ in solution to the known concentration of O_2 in solution (1.7 mM). For example, a final Fc^+ concentration of 6.8 mM indicates H_2O production, since dividing 6.8 mM by 1.7 mM gives 4 e^- equivalents.

For the reaction catalyzed by Co(C4P^{PF}), the final absorbance at 620 nm was determined to be 1.69 (±0.06), which corresponds to a final Fc^+ concentration of 5.12 (±0.17) mM. This corresponds to 3.01 (±0.1) electron equivalents, which is almost half to the production of H_2O and half to the production of H_2O_2 (Table 5.1). The concentration of H_2O_2 was confirmed by a standard sodium iodide assay.[11] Additionally, no production of Fc^+ occurs in the presence of O_2 and $HClO_4$ in PhCN without catalyst.

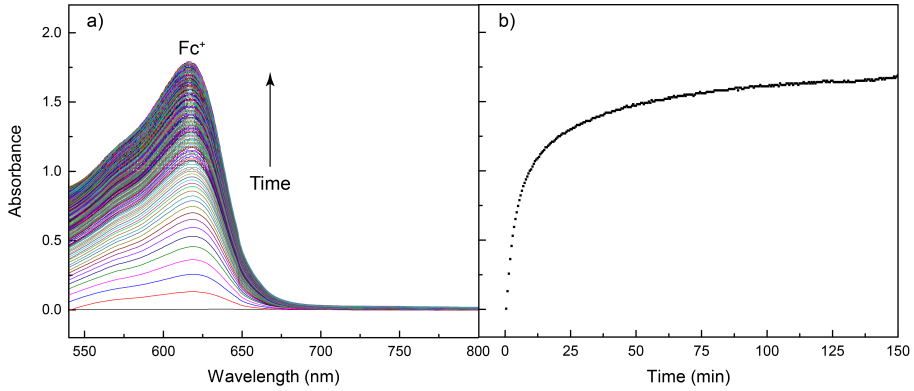

Figure 5.3: a) Absorption spectral change of Fc^+ produced from oxidation of Fc by O_2 and $HClO_4$ catalyzed by Co(C4P^{PF}) b) Time course of absorbance at 620 nm due to Fc oxidation catalyzed by Co(C4P^{PF})

Table 5.1: Homogeneous O_2 reduction catalyzed by Co(C4P^{PF})

Final Abs	1.69 (±0.06)
[Fc^+]	5.12 (±0.17) mM
e^- equiv.	3.01 (±0.1)
% H_2O	51
% H_2O_2	49

5.2.1 Kinetic Studies of Oxygen Reduction with Co(C4P^{PF})

The dependence of the observed rate constant (k_{obs}) for the production of Fc^+ on concentrations of Co(C4P^{PF}), Fc, $HClO_4$ and O_2 were determined in order to gain insight into the mechanism of the homogeneous O_2 reduction catalyzed by Co(C4P^{PF}). The k_{obs} for various concentrations of each species was determined from the slope of ln (A_∞-A_o) versus time; the k_{obs} is taken from the first ~20 seconds of the reaction, where the slope is a straight line. This is illustrated with various concentrations of $HClO_4$ in Figure 5.4. Additionally, the concentration of Fc and $HClO_4$ is kept 10 times greater than the concentration of O_2, so that the reaction is pseudo-first order in $HClO_4$ and Fc.

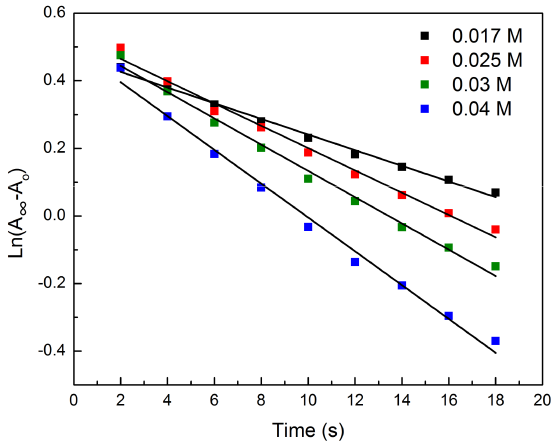

Figure 5.4: First order plots of various concentrations of $HClO_4$

The observed rate constant (k_{obs}) versus concentration is shown for each species in Figure 5.5; the k_{obs} values increased linearly with increasing concentrations of Co(C4P^{PF}) and $HClO_4$. The plot of k_{obs} versus [O_2] increases linearly at lower concentrations of O_2, and remains constant at higher concentrations of O_2, exhibiting saturation kinetics (Figure 5.5d). The plot of k_{obs} versus [Fc] (Figure 5.5c) shows that the k_{obs} remains constant with increasing concentrations of Fc. Accordingly, the kinetic equation for the reduction of O_2 catalyzed by Co(C4P^{PF}) is shown by equation 5.4, below.

$$\frac{d[Fc^+]}{dt} = k_{cat}[CoC4P^{PF}][HClO_4][O_2] \qquad 5.4$$

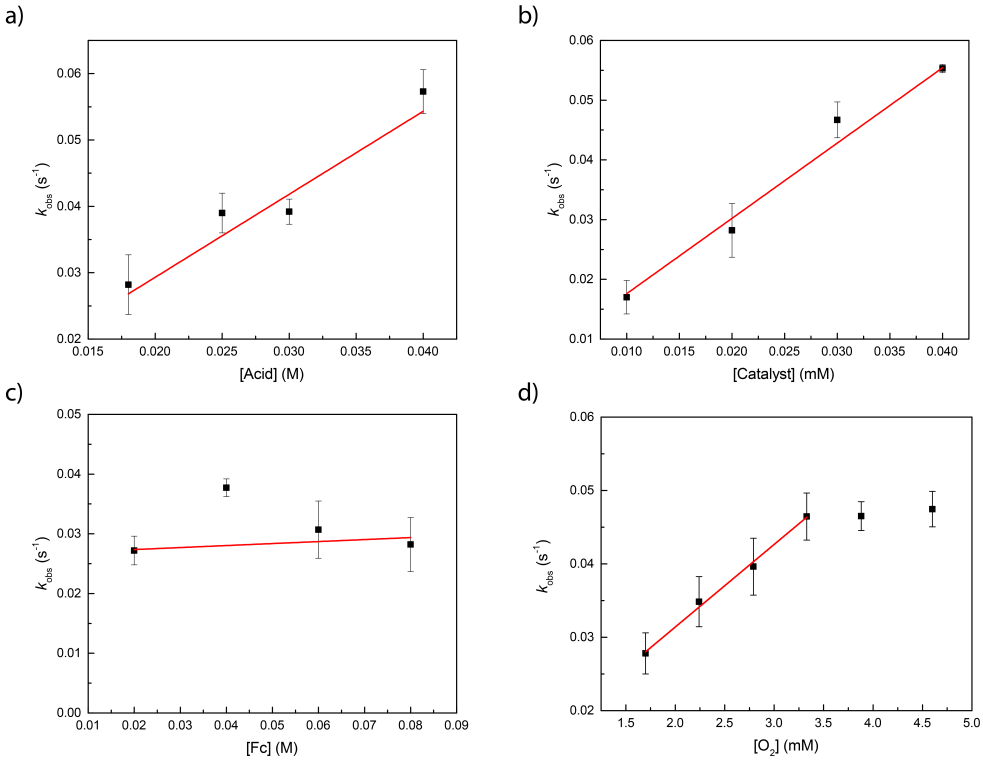

Figure 5.5: Plots of k_{obs} vs [$HClO_4$] (a), [Co(C4P^{PF})] (b), [Fc] (c), or [O_2] (d) for the reduction of O_2 to H_2O_2 or H_2O in PhCN

5.2.2 Proposed Mechanism

Based on the above kinetic studies the proposed mechanism is shown in Figure 5.6. The rate determining step is proton assisted binding of O_2 to the $Co^{II}(C4P^{PF})$ catalyst to give a Co(III) hydroperoxo radical intermediate. The difference in reactivity occurs after the addition of another electron: the protonation of the Co(III) hydroperoxo intermediate at either the α or β oxygen. Protonation at the α oxygen (green, inner circle of Figure 5.6) produces H_2O_2 and following reduction regenerates the $Co^{II}(C4P^{PF})$ catalyst, producing an overall 2 e^-, 2H^+ reduction to yield 1 equivalent of H_2O_2. Alternatively, protonation of the distal β oxygen yields the first equivalent of water and gives the Co(IV)oxo complex (blue, outer circle of Figure 5.6). This step is proposed to be assisted by the multielectron redox capabilities of the C4P ligand scaffold. The Co(IV)oxo complex is then protonated to yield the Co(III)hydroxo intermediate, which after the addition of another proton and electron regenerates the $Co^{II}(C4P^{PF})$ catalyst and produces the second equivalent of water. Overall, this yields a 4 e^-, 4H^+ reduction to give 2 equivalents of H_2O.

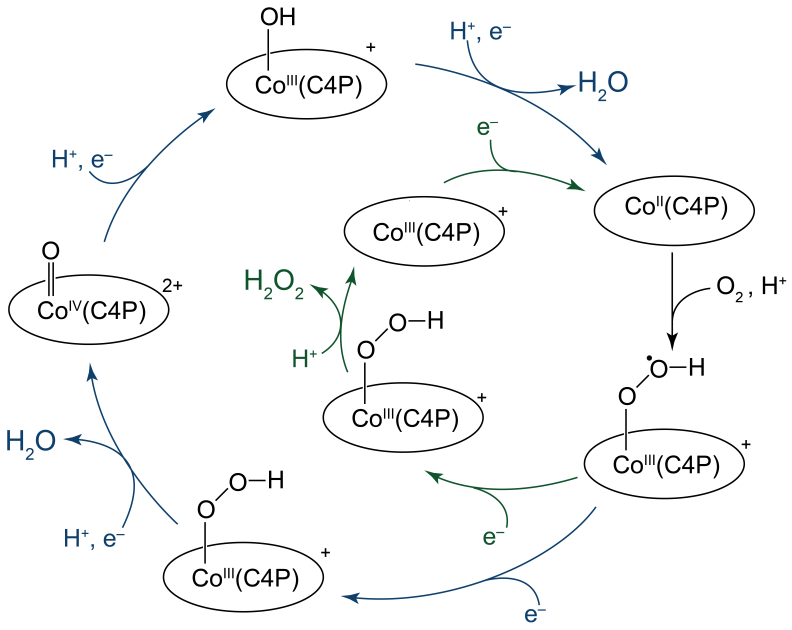

Figure 5.6: Proposed mechanism for O_2 reduction to H_2O_2 (green inner circle) or H_2O (blue outer circle) with Co(C4P^{PF})

5.2.2.1 Control Experiments

In order to eliminate other possible mechanistic pathways two different control experiments were also performed. First, instead of the direct 4 e^-, 4 H^+ pathway to produce H_2O (top equation in Scheme 5.2), another possible pathway is the 2 e^-, 2 H^+ production of H_2O_2 followed by an additional 2 e^- and 2 H^+ to produce H_2O as the final product (bottom two equations in Scheme 5.2).

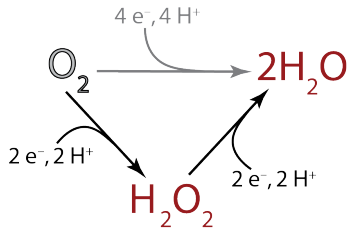

Scheme 5.2: Direct 4 e^-, 4 H^+ reduction of O_2 to H_2O (top) and stepwise pathway for H_2O production with H_2O_2 as an intermediate (bottom)

In order to determine if the latter is a viable pathway, the oxidation of Fc with H_2O_2 and $HClO_4$ catalyzed by Co(C4P^{PF}) was investigated using UV-vis spectroscopy. The experimental parameters for this reaction were the same as with the oxidation of Fc with O_2, with the exception that the reaction was performed and monitored under an N_2 atmosphere in the absence of O_2. The UV-vis spectrum of a trial of this experiment is shown in Figure 5.7. From the final absorbance of Fc^+, the number of electron equivalents produced was determined to be only 0.20 (±0.01); therefore, this 2 e^- pathway contributed to minimal, if any, water production.

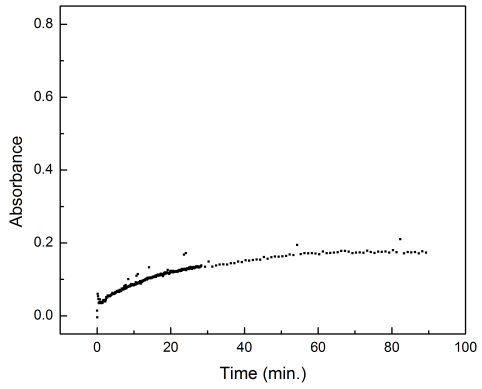

Figure 5.7: Time course of absorbance at 620 nm due to Fc oxidation by H_2O_2 catalyzed by Co(C4P^{PF}) in PhCN

Another possible pathway for H_2O production is the 2 e^-, 2 H^+ production of H_2O_2 followed by dismutation of H_2O_2 to produce O_2 and H_2O (Scheme 5.3). The produced O_2 can then reenter into the 2 e^-, 2 H^+ reduction to H_2O_2, so that the final e– equivalents produced (based on the initial concentration of O_2) can be greater than two.

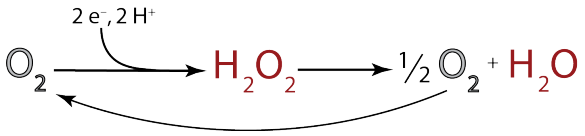

Scheme 5.3: Dismutation of H_2O_2 intermediate

This alternative pathway was investigated by monitoring the dismutation of H_2O_2 catalyzed by Co(C4P^{PF}) in PhCN under N_2. The reaction was monitored for the production of O_2 gas using water displacement. The results are shown in Figure 5.8; the reaction produced a TON of 4 ± 3, which corresponds to < 1% yield of O_2. Therefore, since 2 e^-, 2 H^+ reduction of H_2O_2 and H_2O_2 dismutation have been determined not to be relevant pathways for our system, the most likely pathway for the production of H_2O catalyzed by Co(C4P^{PF}) is the direct 4 e^-, 4 H^+ pathway.

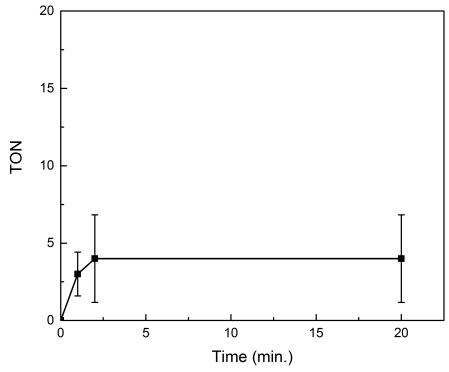

Figure 5.8: TON for dismutation of H_2O_2 catalyzed by Co(C4P^{PF}) in PhCN at 25 °C

5.2.3 Comparison of Homogenous O_2 Reduction for Co(C4P^{PF}) and Co(Por^{PF})

The homogenous O_2 reduction for Co(C4P^{PF}) was compared to the reduction of O_2 catalyzed by the analogous cobalt porphyrin, Co(Por^{PF}). The comparison of the absorbance versus time plot for Co(C4P^{PF}) and Co(Por^{PF}) is shown in Figure 5.9. From this plot, it is shown that the final absorbance of both species is relatively the same. However, the initial rate of the Co(C4P^{PF}) appears to be faster than the analogous porphyrin. Therefore, the k_{cat} for Co(Por^{PF}) was determined from the slope of k_{obs} versus catalyst concentration (as described in Section 5.2.1). The plot of k_{obs} versus catalyst concentration for both Co(C4P^{PF}) and Co(Por^{PF}) is shown in Figure 5.10. As shown in Figure 5.10, Co(C4P^{PF}) is almost tenfold faster than the analogous Co(Por^{PF}), with k_{cat} of 1247 s^{-1} mM^{-1} and 121.7 s^{-1} mM^{-1}, respectively. The results are summarized in Table 5.2.

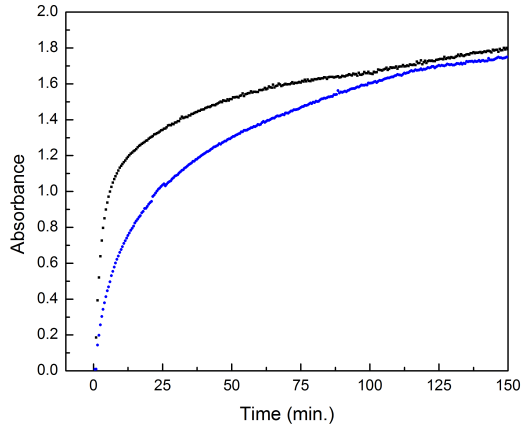

Figure 5.9: Time course of absorbance at 620 nm due to Fc oxidation catalyzed by Co(C4P^{PF}) (black) and Co(Por^{PF}) (blue)

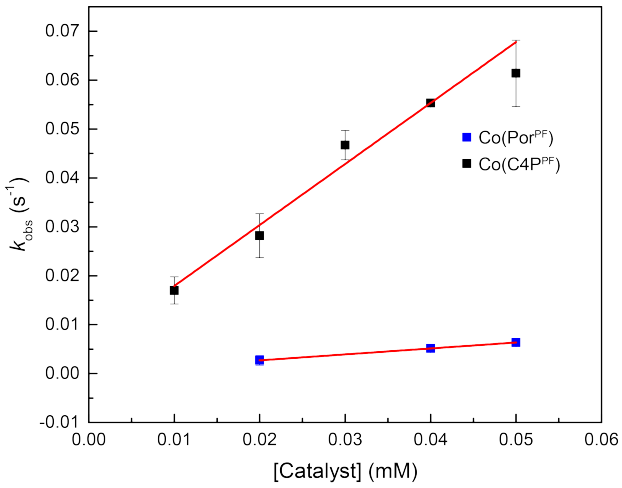

Figure 5.10: Plot of k_{obs} vs [Co(C4P^{PF})] (black) and [Co(Por^{PF})] (blue) for reduction of O_2 by Fc in the presence of $HClO_4$ in PhCN

Table 5.2: Comparison of results for homogenous O_2 reduction catalyzed by Co(C4P^{PF}) and Co(Por^{PF})

	Co(C4P^{PF})	**Co(Por^{PF})**
Final Absorbance	1.69 (±0.06)	1.75 (±0.04)
% H_2O	51	55
k_{cat} (s^{-1} mM^{-1})	1247 (±84)	121.7 (±0.2)

5.3 Heterogeneous O_2 Reduction

The cobalt calix[4]phyrin was also studied under heterogeneous conditions for the ORR, which better mimics fuel cell conditions. The number of electrons transferred (n) and selectivity for water production were determined under these conditions using RRDE. These results were obtained by immobilizing the cobalt catalyst on the glassy carbon disk portion of the RRDE using MWCNTs (multi-walled carbon nanotubes) and Nafion. MWCNTs were used as a high surface area catalyst support and as such have been shown to produce high current densities for ORR.[12] Nafion acted as a mechanical binder for adhesion to the electrode, as well as a

surfactant to promote electrostatic interaction.[13,14] A solution mixture of cobalt catalyst, Nafion and MWCNT in THF was drop cast onto the glassy carbon disk of the RRDE, and after evaporation of THF a thin catalyst film was adhered to the glassy carbon electrode. The supporting electrolyte for the experiment was 0.5 M H_2SO_4, which was saturated with O_2 prior to data collection. The linear sweep voltamograms (LSVs) for O_2 reduction were collected at an electrode rotation rate of 0, 100, 400, 900, and 1600 rpm. The glassy carbon disk electrode was swept from 0.8 to -0.2 V (vs Ag/AgCl); the platinum ring electrode was set at a fixed potential (1.22 V vs Ag/AgCl).

The LSVs obtained under these parameters for Co(C4P^{PF}) are shown in Figure 5.11. The scan rate of the LSV was 20 mV/s. As the rotation rate is increased, the disk current density at catalytically relevant potentials also increases. This current response is predicted, since at higher rotation rates the rate of transfer of O_2 from the bulk solution to the surface of the electrode is greater. This increases the overall rate of catalytic reduction of O_2 and leads to the observed increased current densities. The E_{onset} for ORR was shown to be approximately 470 mV (vs NHE).

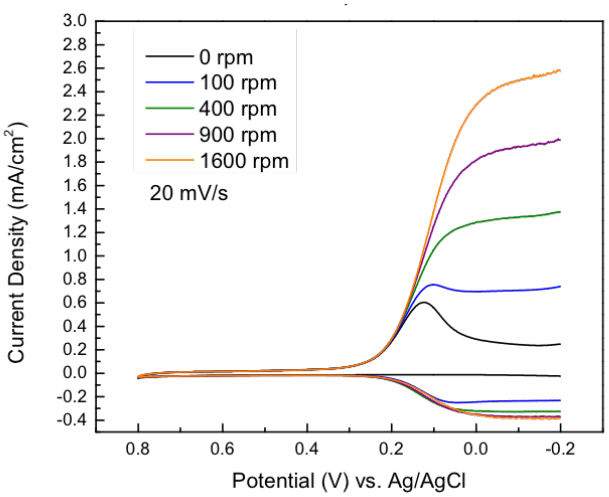

Figure 5.11: LSVs of ORR activity of Co(C4P^{PF}) at a RRDE at different rotation rates in O_2 saturated 0.5 M H_2SO_4, with a scan rate of 20 mV/s

The % H_2O_2 and n were calculated from the disk and ring current densities of the LSV using equations 5.1 and 5.2. The results at various rotation rates are shown in Table 5.3; data was collected at a potential of 0 mV (vs Ag/AgCl). Similarly, the LSVs for the analogous Co(Por^{PF}) were also collected (Figure 5.12) and the results of % H_2O_2 and n were compared to Co(C4P^{PF}) (Table 5.3). At the slowest rotation rate of 100 rpm, Co(Por^{PF}) appears to have a much better selectivity for H_2O (n = 2.70) than Co(C4P^{PF}) (n = 2.34). Moreover, Co(C4P^{PF}) appears to produce mostly H_2O_2 (83%). As the rotation rate is increased, n increases for both catalysts. However, the amount of increase for Co(C4P^{PF}) is greater than Co(Por^{PF}), so that at 1600 rpm the number of electrons transferred is more comparable. The number of electrons transferred at 1600 rpm is also more comparable to the results obtained homogeneously (*vide supra*). The increase in the number of electrons transferred as the rotation rate increased was unexpected, since typically as rotation rate increases, the % H_2O_2 increases (and n

decreases). This is because at higher rotation rates any H_2O_2 that is produced is swept more quickly past the ring electrode, and therefore does not have an opportunity to be further reduced to H_2O. Additionally, the current response at the platinum ring has been known to be low and irreproducible in some cases.[15]

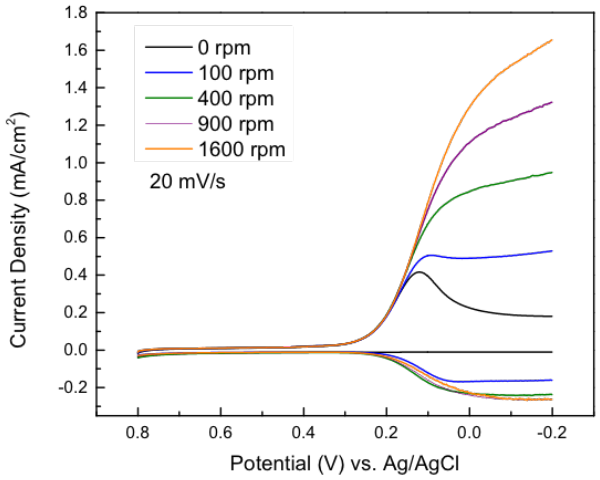

Figure 5.12: LSV of ORR activity of Co(Por^{PF}) at a RRDE at different rotation rates in O_2 saturated 0.5 M H_2SO_4, with a scan rate of 20 mV/s

Table 5.3: Comparison of results for heterogeneous O_2 reduction catalyzed by Co($C4P^{PF}$) and Co(Por^{PF}), based on ring and disk currents

	Co($C4P^{PF}$)[a]		**Co(Por^{PF})[a]**	
rpm	**n[b]**	**% H_2O_2[c]**	**n[b]**	**% H_2O_2[c]**
100	2.34 (±0.02)	83 (±1)	2.70 (±0.27)	65 (±13)
400	2.58 (±0.10)	71 (±5)	2.91 (±0.27)	54 (±14)
900	2.80 (±0.11)	60 (±5)	3.13 (±0.28)	44 (±14)
1600	3.14 (±0.36)	43 (±18)	3.31 (±0.30)	35 (±15)

[a] E(mV)=0 (Ag/AgCl), 20 mV/s
[b] n = number of electrons calculated from RRDE data using equation 5.2
[c] % H_2O_2 produced from ORR calculated from RRDE data using equation 5.1

5.3.1 KL Analysis

Due to the discrepancy in results at various rotation rates using the ratio of currents at the ring and disk to calculate n, an additional method to calculate the number of electrons which takes into account all rotation rates was also explored. This method, Koutecky-Levich (KL) analysis, involves plotting the inverse current density versus the inverse square root of the rotation rate. From the slope of the plot, the number of electrons transferred can be calculated, based on equation 5.3. Additionally, the kinetic current density can be determined from the y-intercept (equation 5.3).

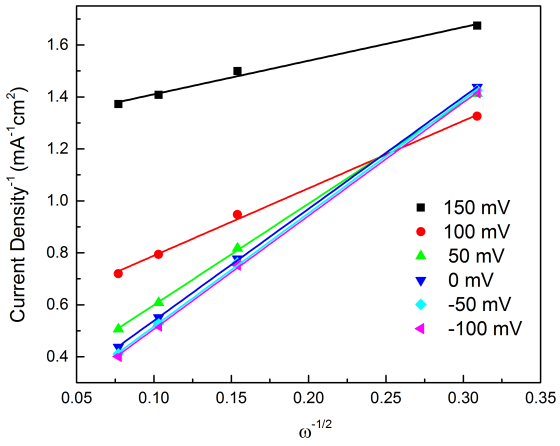

Figure 5.13: Koutecky-Levich analysis of Co(C4P^{PF}) at various potentials. Scan rate 20 mV/s

The KL plot for Co(C4P^{PF}) at various potentials is shown in Figure 5.13. KL plots for potentials that correspond to the maximum current response for O_2 reduction have parallel slopes. These slopes correspond to approximately 3 e^- equivalents. The KL plot analysis was also performed for Co(Por^{PF}) and compared to Co(C4P^{PF}); the results at 0 mV are shown in Figure 5.14 (orange and blue plots, respectively). The plot in Figure 5.14 also shows a theoretical slope for n = 2 (dashed green) and n =4

(dashed black). The slopes for Co(Por^{PF}) and Co(C4P^{PF}) lie in between the theoretical slopes and correspond to n = 2.3 (±0.3) and n = 2.9 (±0.3), respectively. From the y-intercept, the kinetic current densities were determined to be i_K = 2.0 (±0.3) mA/cm^2 (Co(C4P^{PF})) and 2.4 (±0.5) mA/cm^2 (Co(Por^{PF})).

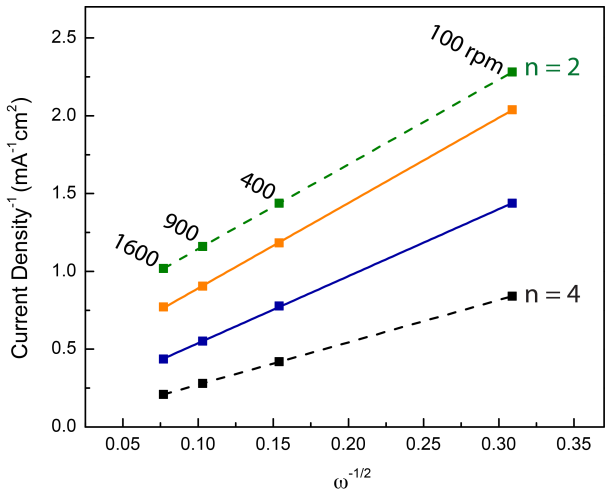

Figure 5.14: KL plots for Co(C4P^{PF}) (blue) and Co(Por^{PF}) (orange) compared to the theoretical slopes for the two-electron (green dash) and four-electron (black dash) ORR. E= 0 mV vs Ag/AgCl; scan rate is 20 mV/s

The number of electrons transferred as determined by KL analysis for Co(C4P^{PF}) is comparable to n calculated based on the ring and disk current responses at higher rotation rates (Table 5.3). It is also comparable to the homogeneous results discussed in Section 5.2 (Table 5.1). From the KL analysis, Co(C4P^{PF}) also appears to be more selective for H_2O (n closer to 4) than Co(Por^{PF}).

5.3.2 Comparison of KL Analysis with Different Cobalt Tetrapyrroles

The proposed increased reactivity of the cobalt calix[4]phyrin as compared to the analogous cobalt porphyrin was the addition of two sp^3-hybridized *meso* centers, with electron redox functionality, into the tetrapyrrole ligand scaffold. Therefore, to gain a better understanding of the effect this modification to the ligand scaffold has toward the oxygen reduction reactivity of the cobalt complex, a series of related tetrapyrroles were also studied. These derivatives all contain dimethyl substituents at the sp^3 *meso* positions and pentafluoro groups at the sp^2 *meso* centers: Co(DMIC) (cobalt dimethylisocorrole, Figure 5.15a), Co(Phl) (cobalt phlorin Figure 5.15b), Co(DMBIL) (cobalt dimethylbiladiene, Figure 5.15c). These complexes were synthesized and studied for their ORR reactivity previously in our group.[16]

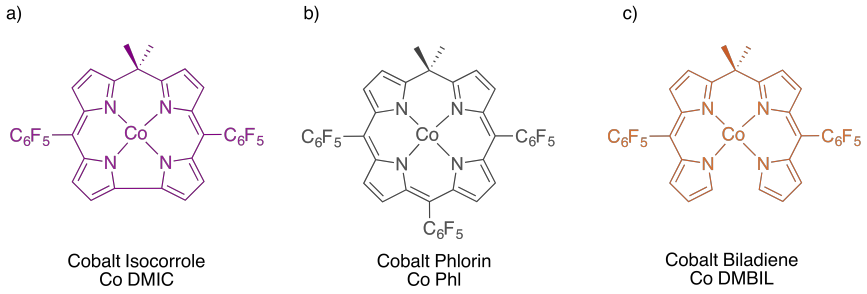

Figure 5.15: A series of cobalt tetrapyrroles with sp^3 hybridized *meso* centers

The results of the KL analysis for the ORR for all cobalt tetrapyrrole complexes in this series is shown in Figure 5.16. The n for each cobalt catalyst was determined from the slopes of these plots and the results are shown in Table 5.4. The % H_2O was also calculated based on n (see Section 5.5.3). The selectivity for O_2 reduction to H_2O decreases in the order of Co(DMIC) > Co(C4P^{PF}) > Co(Phl) >

Co(DMBil) ≈ Co(Por^{PF}). The porphyrin without tetrahedral *meso* positions, Co(Por^{PF}), had the lowest selectively for water production (15%). Co(DMIC) had the highest selectivity for water production (85%), followed by Co(C4P^{PF}) (45%). Additionally, Co(DMBil) and Co(DMIC) display the most significant kinetic current densities at 9.0 ± 0.4 mA/cm^2 and 8.7 ± 2.5 mA/cm^2, respectively, which indicates the fastest rates for ORR catalysis in this series. Additionally, the catalyst most selective for H_2O production, Co(DMIC), also has the most positive onset potential (E_{onset}, Table 5.4).

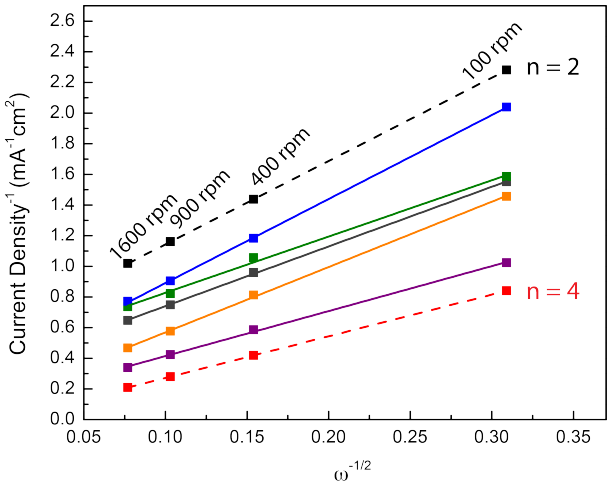

Figure 5.16: KL plots for Co(DMIC) (purple), Co(C4P^{PF}) (green), Co(DMBil) (orange), Co(Por^{PF}) (blue), and Co(Phl) (gray) compared to the theoretical slopes for the two-electron (black dash) and four-electron (red dash) ORR. E= 0 mV vs Ag/AgCl; scan rate is 20 mV/s

Table 5.4: Results of KL analysis for heterogeneous O_2 reduction catalyzed by various cobalt tetrapyrroles

Compound	n	% H_2O	i_K	E_{onset} (mV)[a]
Co(Por^{PF})	2.3 (±0.3)	15	2.4 (±0.5)	440
Co(DMBil)	2.4 (±0.1)	20	9.0 (±0.4)	430
Co(Phl)	2.6 (±0.1)	30	4.8 (±1.3)	410
Co($C4P^{PF}$)	2.9 (±0.3)	45	2.0 (±0.3)	470
Co(DMIC)	3.7 (±0.2)	85	8.7 (±2.5)	600

[a] mV versus NHE

As discussed in Chapter 4 for the calix[4]phyrin, we believe that the multielectron redox properties of these tetrapyrrole ligands with sp^3 hybridized *meso* carbons contributes to the improvement in selectivity towards H_2O production for the ORR. However, we do not yet fully understand the improved selectivity with the Co(DMIC) catalyst over each of the other tetrapyrroles of this type. One possible explanation is the trend in onset potential: Co(DMIC) has the most positive E_{onset} at 600 mV and the best selectivity for water production (85%), Co($C4P^{PF}$) has the second most positive E_{onset} (470 mV) and second best selectivity for water production (45%), and each of the remaining catalyst have the most negative E_{onset} (440-410 mV) and lowest selectivities for water production (30-15%). We are also currently investigating the mechanism of the ORR computationally for the Co(DMIC) to better understand this difference in reactivity.

5.4 Summary

A unique cobalt catalyst with a multielectron redox ligand, Co($C4P^{PF}$), was studied for the ORR. This catalyst was first investigated homogeneously by monitoring the concentration of ferrocenium ion in solution by UV-vis spectroscopy. Based on the final concentration of ferrocenium ion, the number of electron equivalents transferred was determined to be 3.01 which corresponds to 51% H_2O

production. Mechanistic studies were also performed by varying the concentration of acid, ferrocene, catalyst and oxygen in solution. From a plot of the k_{obs} versus concentration of each of these species, a first order dependence was shown for acid, catalyst and oxygen, while ferrocene showed a zero order dependence. From these kinetic studies a mechanism was proposed. This mechanism suggests that protonation at the β oxygen of the hydroperoxo intermediate is a key aspect of H_2O production. The results of the homogeneous O_2 reduction for Co(C4P^{PF}) were compared to the analogous cobalt porphyrin, Co(Por^{PF}), and showed a similar selectivity for H_2O production. However, Co(C4P^{PF}) had a ~10-fold increase in reaction rate compared to Co(Por^{PF}).

The Co(C4P^{PF}) was also studied heterogeneously for the ORR using a rotating ring disk electrode. From the linear sweep voltamograms, the number of electrons transferred and the % H_2O_2 produced was determined based on the current density response of the platinum ring and glassy carbon disk electrodes at various rotation rates. These results were compared to Co(Por^{PF}); at lower rotation rates Co(Por^{PF}) has better selectivity for H_2O production and at higher rotation rates the selectivities are more comparable between the two catalysts. Therefore, an additional method was also explored for determining the number of electrons transferred: Koutecky-Levich analysis. Using KL analysis, the number of electrons transferred for Co(C4P^{PF}) and Co(Por^{PF}) was determined to be 2.3 and 2.9, respectively, with higher selectivity for H_2O production for Co(C4P^{PF}). These results were compared to a series of cobalt catalysts related to Co(C4P^{PF}).

5.5 Experimental Methods

Reagents and solvents were purchased from Acros Organics, Cambridge Isotopes Laboratories, Fisher Scientific, Sigma-Aldrich, or Strem Chemicals, Inc. Solvents for synthesis were of reagent grade or better; solvents for air- or moisture-sensitive reactions were dried by passage through activated alumina and then stored over 4 Å molecular sieves prior to use.[17] Ferrocene was purified by sublimation. $Co(Por^{PF})$ was synthesized using a literature procedure.[18]

5.5.1 Homogeneous O_2 Reduction Experiments

UV-vis spectroscopy was carried out on a StellarNet CCD array UV- vis spectrometer at room temperature using screw cap quartz cuvettes from Starna (path length = 1 cm). The reduction of O_2 in benzonitrile (PhCN) with ferrocene (Fc), $HClO_4$ and a catalytic amount of $Co(C4P^{PF})$ was monitored by the rise in ferrocenium (Fc^+) ion concentration at λ = 620 nm (ε = 330 M^{-1} in PhCN). The concentration of O_2 in air-saturated PhCN is a known value ($1.7x10^{-3}$ M).[19]

A typical experiment for catalytic homogeneous reduction of O_2 by Fc and $HClO_4$ is as follows: To a quartz cuvette (volume ~ 4.6 mL) with a screw cap fitted with a rubber septum was added 3.6 mL of a solution of Fc (0.10 M) in PhCN. To this solution was simultaneously added 46 μL of $HClO_4$ in PhCN (2.0 M) and 1 mL of $Co(C4P^{PF})$ (1.0×10^{-4} M) in PhCN. All PhCN solutions were saturated with air prior to preparation. The rise in the absorbance of Fc^+ was recorded every 2 or 30 seconds. At least three trials were carried out and reported results were an average of these trials.

5.5.2 Homogeneous H_2O_2 Reduction and Dismutation Experiments

For the reduction of H_2O_2, the experiment was set-up as above, with the exception that all samples were prepared under a N_2 atmosphere and 200 μL of 0.04 M H_2O_2 in PhCN was added to the solution, so that the concentration is the same as the concentration of dissolved O_2 (1.7 mM) in the set-up described above.

The dismutation of H_2O_2 was also set-up under nitrogen with 3.6 mL of PhCN, 46 μL of 2.0 M $HClO_4$ and 1 mL of $Co(C4P^{PF})$ (1.0×10^{-4} M). After addition of 200 μL of 0.04 M H_2O_2 in PhCN, the volume of O_2 gas produced was measured by water displacement. Water displacement measurements were performed using an inverted graduated cylinder (25 mL) and TONs were calculated from moles of gas produced (48 $mol \cdot L^{-1}$).

5.5.3 Rotating Ring Disk Electrode Voltammetry

Rotating ring disk electrode (RRDE) and rotating disk electrode (RDE) experiments were performed using a CHI-720D bipotentiostat with a Pine Research Instrumentation modulated speed rotator (AFE6M). The linear sweep voltammetry (LSV) measurements were performed with a four-electrode assembly: a glassy carbon working electrode (0.2475 cm^2), a platinum ring working electrode (0.1866 cm^2), a platinum mesh auxiliary electrode, and a Ag/AgCl (1.0 M KCl) reference electrode. In some instances, the reference electrode was adjusted to the normal hydrogen electrode (NHE) according to the relationship Ag^+/Ag = 235 mV + NHE. The platinum ring working electrode was set at a fixed potential of 1.46 V vs. NHE. The designated catalyst was immobilized on the glassy carbon working electrode using a previously reported literature procedure:[12] a 3.9 mL THF solution was prepared by combining 4 mg MWCNT, 45 μL 5% Nafion and 0.47 mL of a 2.5 mM solution of the cobalt

compound in THF. The prepared solution was sonicated for 30 min, then 10 μL of the solution was drop cast onto the surface of the glassy carbon disk electrode. Subsequent evaporation of the solution provided an immobilized catalyst film. A 0.5 M H_2SO_4 in Millipore water solution was employed as supporting electrolyte and was saturated with O_2 for a minimum of 30 minutes prior to acquisition of LSVs. Collection efficiencies were calibrated against a ferricyanide standard.[20] Unless otherwise noted, a constant scan rate of 20 mV/s with iR drop compensation was maintained for LSV data acquisition. E_{onset} was taken at current density equal to 0.15 mA/cm^2. The number of electrons transferred (n) was calculated using equation 5.2 and the % H_2O_2 was calculated using equation 5.1. The % H_2O was calculated from (1- % H_2O_2). The number of electrons transferred (n) was also determined using the KL analysis (equation 5.3); the corresponding % H_2O and % H_2O_2 were calculated using n = 2(1-x) + 4x.

5.6 References

(1) Zhang, W.; Lai, W.; Cao, R. *Chem. Rev.* **2017**, *117* (4), 3717

(2) Collman, J.P.; Boulatov, R.; Sunderland, C.J. In *The Porphyrin Handbook*; Kadish, K. M.; Smith, K.M.; Guilard, R., Eds.; Academic Press: San Diego, CA, 2003, Vol. 11, pp 1-49.

(3) Scherson, D. A.; Palencsár, A.; Tolmachev, Y.; Stefan, I. In *Electrochemical Surface Modification*; Wiley-VCH Verlag GmbH & Co. KGaA, 2008; pp 191–288.

(4) Rosenthal, J.; Nocera, D. G. In *Progress in Inorganic Chemistry*; John Wiley & Sons, Inc., 2007; pp 483–544.

(5) Collman, J. P.; Wagenknecht, P. S.; Hutchison, J. E. *Angew. Chemie Int. Ed. English* **1994**, *33* (15–16), 1537.

(6) Rosenthal, J.; Nocera, D. G. *Acc. Chem. Res.* **2007**, *40* (7), 543.

(7) Gewirth, A. A.; Thorum, M. S. *Inorg. Chem.* **2010**, *49* (8), 3557.

(8) Bard, A. J.; Faulkner, L. R. In *Electrochemical Methods: Fundamentals and Applications, 2nd edition*; Wiley: New York, 2001; pp 517-518.

(9) Du, C.; Sun, Y.; Shen, T.; Yin, G.; Zhang, J. In *Rotating Electrode Methods and Oxygen Reduction Electrocatalysts*; Xing, W., Yin, G., Zhang, J., Eds.; Elsevier: Amsterdam, 2014; pp 231–277.

(10) Fukuzumi, S.; Okamoto, K.; Gros, C. P.; Guilard, R. *J. Am. Chem. Soc.* **2004**, *126* (33), 10441.

(11) Mair, R. D.; Graupner, A. J. *Anal. Chem.* **1964**, *36* (1), 194.

(12) McGuire Jr., R.; Dogutan, D. K.; Teets, T. S.; Suntivich, J.; Shao-Horn, Y.; Nocera, D. G. *Chem. Sci.* **2010**, *1* (3), 411.

(13) Choi, A.; Jeong, H.; Kim, S.; Jo, S.; Jeon, S. *Electrochim. Acta* **2008**, *53* (5), 2579.

(14) Qu, J.; Shen, Y.; Qu, X.; Dong, S. *Electroanalysis* **2004**, *16* (17), 1444.

(15) Collman, J. P.; Wagenknecht, P. S.; Hutchison, J. E. *Angew. Chemie Int. Ed. English* **1994**, *33* (15–16), 1537.

(16) (a) Qiu, T. Electrochemical CO_2 and O_2 Reduction using Nickel and Cobalt Macrocyclic Complexes. Ph.D. Thesis, University of Delaware, 2016 (b) Eddy, J. W.; Qiu, T.; Rosenthal, J. Manuscript in Prep.

(17) Pangborn, A. B.; Giardello, M. A.; Grubbs, R. H.; Rosen, R. K.; Timmers, F. J. *Organometallics.* **1996,** *15* (5), 1518.

(18) Kadish, K. M.; Han, B. C.; Franzen, M. M.; Araullo-McAdams, C. *J. Am. Chem. Soc.* **1990**, *112* (23), 8364.

(19) Fukuzumi, S.; Imahori, H.; Yamada, H.; El-Khouly, M. E.; Fujitsuka, M.; Ito, O.; Guldi, D. M. *J. Am. Chem. Soc.* **2001**, *123* (11), 2571.

(20) Hancock, C. A.; Ong, A. L.; Slater, P. R.; Varcoe, J. R. *J. Mater. Chem. A* **2014**, *2* (9), 3047.

Chapter 6

HANGMAN COBALT CALIX[4]PHYRINS AS CATALYSTS FOR O_2 REDUCTION

6.1 Introduction

It has been shown that some of the most selective catalysts for the ORR are cofacial bis(cobalt) diporphyrin catalysts.[1-6] Further studies revealed that the function of the second cobalt porphyrin is to tune the pK_a of the bound superoxo intermediate and promote O–O bond cleavage. Moreover, systems in which the second functional site is an unmetalated porphyrin or a porphyrin metalated with a Lewis acid have also been shown to be selective for H_2O production.[6-10] This work inspired the Nocera group[11] to explore catalyst designs that did not incorporate a second porphyrin unit, but instead incorporated an acid/base group to lie above the cobalt center of a porphyrin, aptly named "hangman" groups. A series of such cobalt complexes with a carboxylic acid hangman group and various electronic substituents on the porphyrin macrocycle (Figure 6.1) were synthesized and studied for the ORR. It was shown that these hangman functionalized cobalt porphyrins can be selective for the reduction of O_2 to H_2O, with the electronic properties of the macrocycle affecting the selectivity of the reaction. The pentafluorophenyl derivative had the best selectivity with 71% H_2O production (n = 3.4), as determined by RRDE (rotating ring disk electrode) analysis.

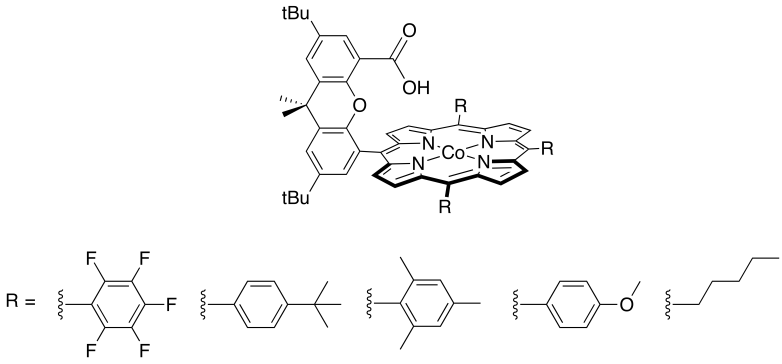

Figure 6.1: Hangman cobalt catalysts with various electronic substituents on the porphyrin core[11]

Electronic structure calculations of the hydroperoxo intermediate of the cobalt hangman porphyrin showed that the hydrogen bond between the hydroperoxo ligand and the hanging acid group is aligned towards the β oxygen (Figure 6.2).[12] This interaction results in H_2O production due to protonation at the β oxygen, whereas alignment with the α oxygen leads to H_2O_2 production. Therefore, protonation of the hydroperoxo intermediate at the distal oxygen is proposed to be vital to efficient O–O bond cleavage and the ultimate production of water.

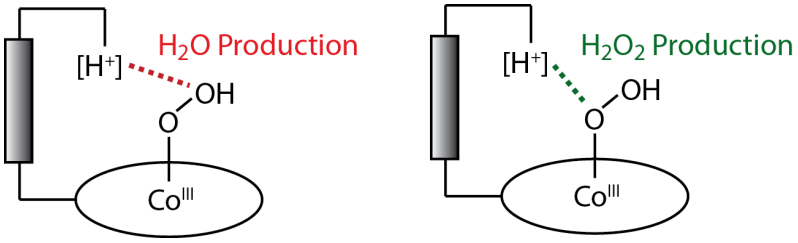

Figure 6.2: Proposed interaction of the hangman group with the β oxygen for H_2O production (left) and with the α oxygen for H_2O_2 production (right)

This chapter will explore employing a similar strategy for the cobalt calix[4]phyrin. First, a cobalt calix[4]phyrin with an analogous carboxylic acid hangman moiety was synthesized and investigated for O_2 reduction (both homogenously and heterogeneously). These studies led to the additional development of cobalt[4]phyrin catalysts with pyridine and pyrimidine hangman groups.

6.2 Synthesis of Cobalt Hangman Catalysts

6.2.1 Synthesis of Co(C4P*HM*^{COOH})

A synthetic strategy similar to that of the unmodified Co(C4P^{PF}) (Chapter 4) was utilized for the cobalt calix[4]phyrin with carboxylic acid hangman group (Co(C4P*HM*^{COOH})); however, the hangman functionality was incorporated into the dipyrromethane unit (Scheme 6.1). First, 3-acetylbenzoic acid was reacted with methanol under acidic conditions to protect the benzoic acid functional group as a methyl ester.[13] Then methyl 3-acetylbenzoate was reacted with an excess of pyrrole catalyzed by trifluoroacetic acid to give dipyrromethane **(1)** in 63 % yield. For the synthesis of the free base calix[4]phyrin, diacylated pentafluorophenyl dipyrromethane is reduced with $NaBH_4$ to give the dicarbinol product. To this product is added **(1)** with indium chloride to catalyze the condensation reaction, followed by oxidation with DDQ and quenching with triethylamine. Following purification with column chromatography the calix[4]phyrin with methyl ester hangman group was obtained in good yield (30 %). The hydrolysis of the methyl ester to the corresponding carboxylic acid was accomplished under strongly acidic conditions.[14] The calix[4]phyrin with carboxylic acid hangman group was metalated with cobalt acetate in acetonitrile at 60 °C to give quantitative conversion to CoC4P*HM*^{COOH}.

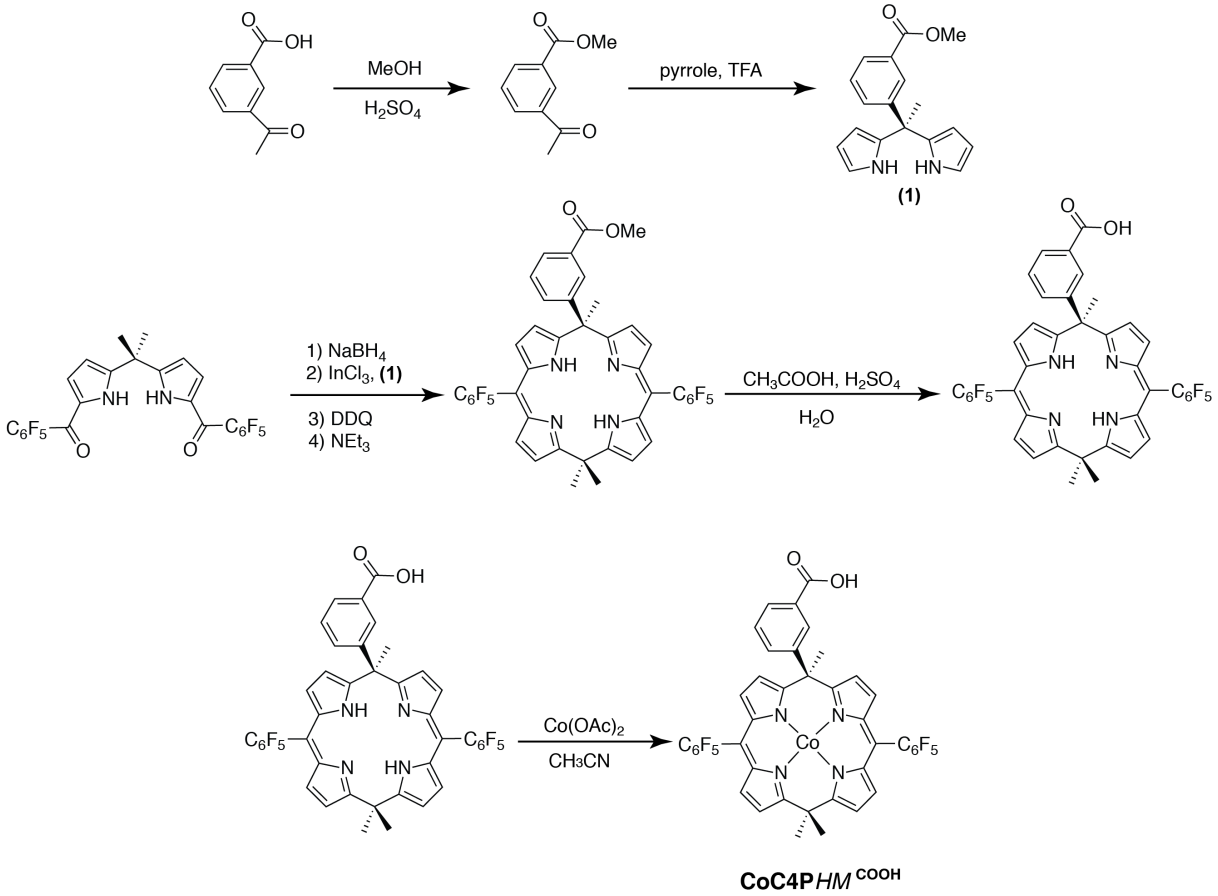

Scheme 6.1: Synthesis of a cobalt calix[4]phyrin catalyst with a carboxylic acid hangman group, Co(C4P*HM*^{COOH})

6.2.1.1 Solid State Structure of Co(C4P*HM*^{COOH})

The solid state structure of Co(C4P*HM*^{COOH}) is shown in Figures 6.3 and 6.4. The complex was crystallized by slow evaporation of a saturated solution of the complex in Et_2O and MeOH (1:1). The solid state structure shows that the carboxylic acid hanging group is directed away from the cobalt center. The cobalt center for Co(C4P*HM*^{COOH}) is almost entirely in line with the N4 plane (0.01 Å displacement), as compared to a displacement of 0.05 Å from the N4 plane for Co(C4P^{PF}). The average Co-N bond length is 1.93 Å (Table 6.1), which is the same as the unmodified Co(C4P^{PF}). Additionally, a molecule of ether was found to be coordinated to the cobalt center on the face opposite of the hangman group.

Table 6.1: Selected bond lengths and angles for Co(C4P*HM*^{COOH})

Atoms	Bond Lengths (Å)	Atoms	Bond Angle (°)
Co-N(1)	1.919(3)	N(2)-Co-N(1)	90.28(11)
Co-N(2)	1.932(3)	N(4)-Co-N(2)	179.61(11)
Co-N(3)	1.930(3)	N(4)-Co-N(1)	89.33(11)
Co-N(4)	1.921(2)	N(3)-Co-N(1)	178.84(12)

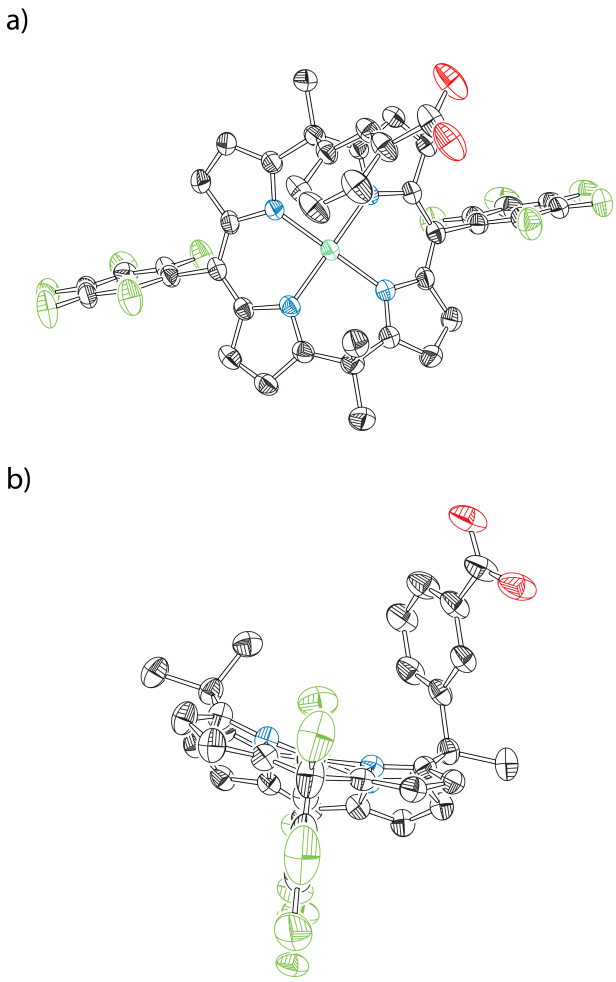

Figure 6.3: Solid state structure of Co(C4P*HM*^{COOH}) with (a) top and (b) side on views. All hydrogen atoms were omitted for clarity and thermal ellipsoids are shown at 50% probability. A coordinating ether is also omitted for clarity

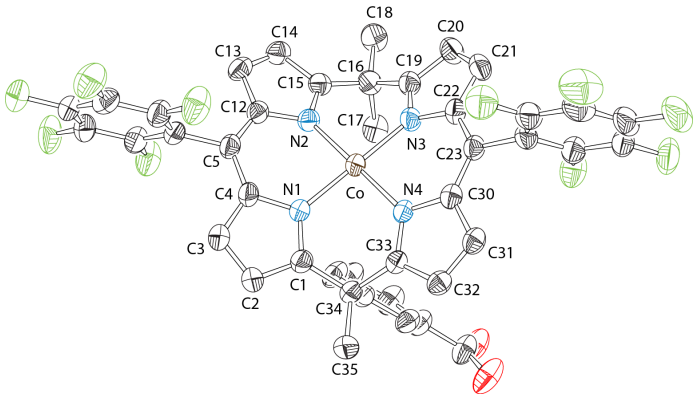

Figure 6.4: Partially numbered solid state structure of Co(C4P*HM*^{COOH}) with all hydrogen atoms omitted for clarity and thermal ellipsoids shown at 50% probability. A coordinating ether is also omitted for clarity

6.2.2 Synthesis of Co(C4P*HM*^{py}) and Co(C4P*HM*^{pyrm})

Analysis of the solid state structure of Co(C4P*HM*^{COOH}) prompted our group to explore additional cobalt calix[4]phyrin hangman derivatives. We proposed that cobalt calix[4]phyrins with pyridine and pyrimidine hangman groups (Co(C4P*HM*^{py}) and Co(C4P*HM*^{pyrm}), respectively) would provide the ideal alignment for hydrogen bonding with the bound hydroperoxo, which is desired for selective reduction to H_2O.

The synthesis of Co(C4P*HM*^{py}) and Co(C4P*HM*^{pyrm}) both followed similar routes, except for the synthesis of the functionalized dipyrromethane unit (Scheme 6.2). The dipyrromethane unit with pyridine functionality was synthesized using a literature procedure:[15] 1-(2-pyridyl)-1-ethanone was reacted with excess pyrrole catalyzed by methanesulfonic acid in ethanol at reflux to yield 5-methyl-5-(2-pyridyl)-dipyrromethane **(2)**. For the dipyrromethane unit with pyridimine functionality, first 2-cyanopyrimidine was converted to 2-acetylpyrimidine using methyl magnesium bromide in ether at 0 °C. Then, the condensation of 2-acetylpyrimidine in excess

pyrrole with trifluoroacetic acid catalyst produced the desired dipyrromethane, 5-methyl-5-(2-pyrimidinyl)dipyrromethane **(3)**, in good yield (35 %).

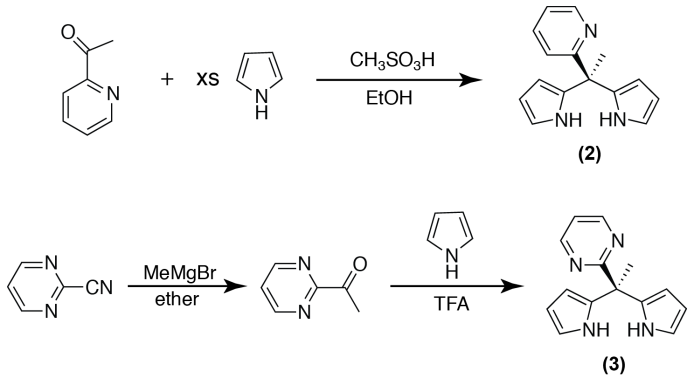

Scheme 6.2: Synthesis of dipyrromethane units with pyridine (2) and pyrimidine (3) functionalities

The same strategy was employed for both pyridine and pyrimidine cobalt calix[4]phyrin hangman derivatives (Scheme 6.3). The diacylated pentafluorophenyl dipyrromethane was reduced with $NaBH_4$ to give the dicarbinol product. The dicarbinol then undergoes Lewis acid catalyzed condensation with either dipyrromethane **(2)** or **(3)**, followed by oxidation with DDQ and quenching with triethylamine. Following purification with column chromatography the freebase calix[4]phyrin with either pyridine or pyrimidine hanging group was obtained in good to excellent yield (42% and 60%, respectively). The freebase calix[4]phyrin was reacted with cobalt acetate in acetonitrile at 60 °C for several hours to give nearly quantitative conversion (~95% Co(C4P*HM*^{py}) or Co(C4P*HM*^{pyrm})).

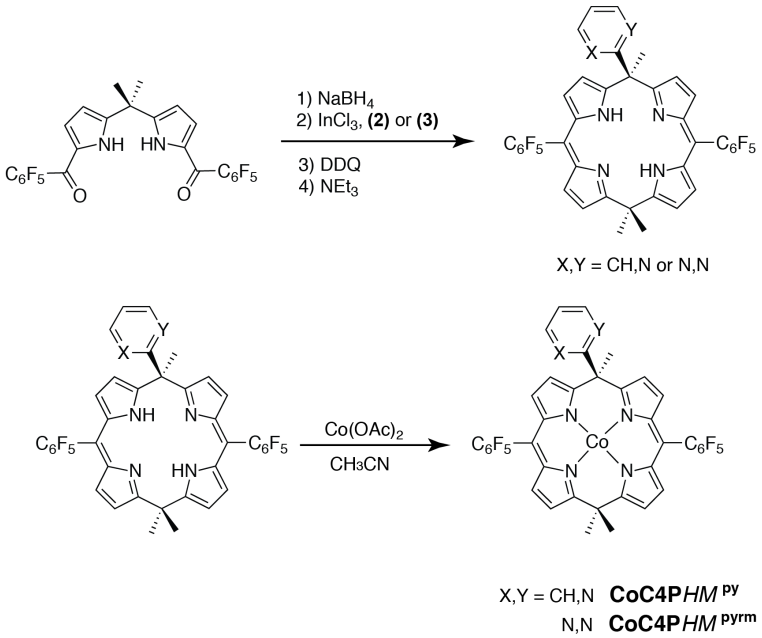

Scheme 6.3: Synthesis of cobalt calix[4]phyrin catalysts with pyridine (Co(C4P*HM*^{py})) and pyrimidine (Co(C4P*HM*^{pyrm})) hangman functionality

6.3 O_2 Reduction with Hangman Derivatives

The homogeneous ORR with cobalt calix[4]phyrin hangman derivatives (Co(C4P*HM*^{COOH}), Co(C4P*HM*^{py}) and Co(C4P*HM*^{pyrm})) was monitored using UV-vis spectroscopy[16] and compared to the results with the unmodified Co(C4P^{PF}) catalyst. The reaction was probed homogeneously as described in Chapter 5, namely using ferrocene as a one electron chemical reductant and perchloric acid as a proton source in air-saturated benzonitrile (PhCN). The rise in absorbance at 620 nm due to the oxidation of ferrocene to ferrocenium ion (Fc^+) is shown over time in Figure 6.5 for each catalyst. The final absorbance of Fc^+ for each catalyst is similar at approximately 1.67, ranging from 1.62 to 1.74 (Table 6.2).

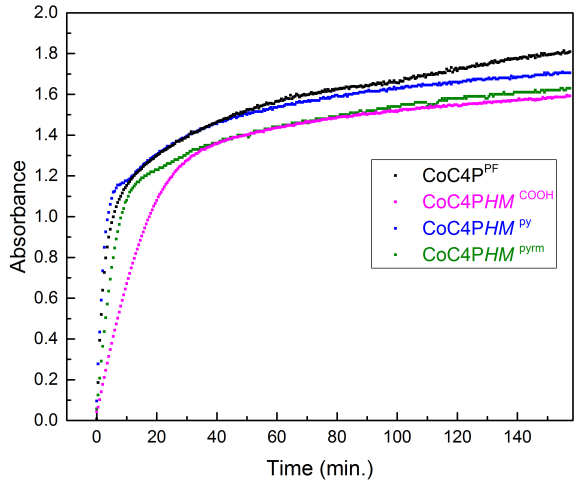

Figure 6.5: Time course of absorbance at 620 nm due to Fc oxidation catalyzed by Co(C4P^{PF}) (black), Co(C4P*HM*^{COOH}) (magenta), Co(C4P*HM*^{py}) (blue), and Co(C4P*HM*^{pyrm}) (green).

From the final absorbance, the concentration of Fc^+ in solution can be determined using the extinction coefficient (330 $M^{-1}cm^{-1}$ in PhCN). Subsequently, the number of electron equivalents transferred (n) for oxygen reduction was determined from the ratio of the known initial concentration of O_2 in solution and the final concentration of Fc^+ produced. The value of n indicates the % H_2O produced from O_2 (n = 2 for H_2O_2, n = 4 for H_2O). The results for each catalyst are shown in Table 6.2.

The results for each catalyst are essentially the same, with both the hangman modified (Co(C4P*HM*^{COOH}), Co(C4P*HM*^{py}) and Co(C4P*HM*^{pyrm})) and unmodified (Co(C4P^{PF})) cobalt catalysts producing n ~3, which corresponds to 50 % H_2O production. Unfortunately, this suggests that the hangman functionality does not influence the selectivity of the reaction under homogeneous conditions. A more detailed discussion for these results will be provided at the end of this chapter.

Table 6.2: Results of homogeneous O_2 reduction catalyzed by hangman modified and unmodified cobalt calix[4]phyrins

Compound	Final Abs	n	% H_2O
Co(C4P^{PF})	1.69 (±0.06)	3.01 (±0.1)	51
Co(C4P*HM*^{COOH})	1.63 (±0.16)	2.91 (±0.2)	46
Co(C4P*HM*^{py})	1.74 (±0.17)	3.10 (±0.3)	55
Co(C4P*HM*^{pyrm})	1.62 (±0.04)	2.90 (±0.1)	45

The hangman derivatives of cobalt calix[4]phyrin were also studied under heterogeneous conditions for the ORR and compared to the unmodified Co(C4P^{PF}). This was done by immobilizing the cobalt catalyst onto a glassy carbon disk electrode, using Nafion and multi-walled carbon nanotubes to assist with binding and catalyst loading. A solution of 0.5 M H_2SO_4 in Millipore water saturated with O_2 prior to data acquisition was used as supporting electrolyte. The linear sweep voltammograms for O_2 reduction were collected at an electrode rotation rate of 0, 100, 400, 900, and 1600 rpm at a scan rate of 20 mV/s. The glassy carbon disk electrode was swept from 0.8 to -0.2 V (vs Ag/AgCl).

Based on the results obtained for Co(C4P^{PF}) (see Chapter 5), the hangman cobalt catalysts were analyzed using Koutecky-Levich (KL)[17] analysis. This analysis involves plotting the inverse current density versus the inverse square root of the rotation rate. From the slope of the KL plot, n can be calculated (see Section 6.5.4). The KL plots for hangman modified and unmodified cobalt calix[4]phyrins are shown in Figure 6.6.

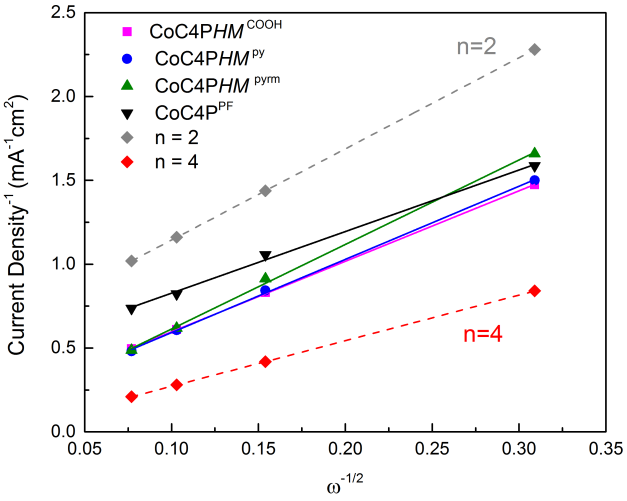

Figure 6.6: KL plots for Co(C4PHM^{COOH}) (magenta), Co(C4PHM^{py}) (blue), Co(C4PHM^{pyrm}) (green), and Co(C4P^{PF}) (black) compared to the theoretical slopes for the two-electron (black dash) and four-electron (red dash) ORR. E = 0 mV vs Ag/AgCl; scan rate is 20 mV/s

From the KL plots, the number of electrons transferred for the hangman modified cobalt calix[4]phyrin catalysts (n = 2.3-2.5, Table 6.3) was found to be lower than that of the unmodified cobalt calix[4]phyrin. This in turn means that, unexpectedly, the hangman modified catalysts are less selective for H_2O production (15-20% water production). The E_{onset} was in the same range for each catalyst (460-480 mV versus NHE).

Table 6.3: Results of heterogeneous O_2 reduction catalyzed by hangman modified and unmodified cobalt calix[4]phyrins

Compound	**n**	**% H_2O**	**E_{onset} (mV vs NHE)**
Co(C4P^{PF})	2.9 (±0.3)	45	470
Co(C4P*HM*^{COOH})	2.5 (±0.1)	20	480
Co(C4P*HM*^{py})	2.4 (±0.1)	20	460
Co(C4P*HM*^{pyrm})	2.3 (±0.1)	15	460

Our goal was to increase the selectivity for H_2O production by incorporating an acid/base functionality above the cobalt center, an approach that has been successful for cobalt porphyrins. However, under homogeneous conditions the same selectivity was found for both hangman modified and unmodified cobalt calix[4]phyrin catalysts. Even more surprising, the selectivity was decreased for the modified catalysts under heterogeneous conditions. The reasons behind this lack of further optimization is not yet understood, however, a possible explanation includes the hangman functionalities not being in proper alignment with the hydroperoxo intermediate. The solid state structure of the Co(C4P*HM*^{COOH}) shows the carboxylic acid group pointed away from the cobalt center. While this is not necessarily indicative of the configuration in solution, rotation of this hangman group does not appear to give correct alignment with the cobalt center towards the reactive intermediate as well. However, based on initial modeling this is not as strong of an argument for pyridine and (even more so) the pyrimidine hangman catalysts. Another possible explanation is that binding of O_2 occurs at the face of the cobalt calix[4]phyrin opposite to that of the hangman group. Unlike the planar cobalt porphyrins, calix[4]phyrin is puckered at the *meso* positions, providing different faces to the complex. Especially interesting is the binding of a molecule of ether through the oxygen atom to the face opposite of the hangman group. Future work in this area entails understanding the role the hangman group and binding of O_2 to the cobalt calix[4]phyrin using computational methods.

6.4 Summary

In previous work by the Nocera group,[11] cobalt porphyrins have been modified to direct protonation to the distal oxygen of the hydroperoxo intermediate by using a

hangman group. An analogous approach to increase selectivity of water production was applied to the cobalt calix[4]phyrin. A family of hangman cobalt calix[4]phyrins with carboxylic acid, pyridine and pyrimidine functionalities has been synthesized and characterized. Each catalyst was explored for O_2 reduction capabilities, both homogeneously and heterogeneously. Unfortunately, when compared to the unmodified cobalt calix[4]phyrin, the hangman modified catalysts did not show an increase in selectivity towards water production under homogenous conditions, and showed decrease selectivity under heterogeneous conditions. While the reason is not fully understood for these results, binding of O_2 to the face opposite the hangman group is a possible explanation.

6.5 Experimental Methods

6.5.1 General Methods

Unless otherwise stated, reactions were performed in oven-dried glassware either under a positive pressure of nitrogen with flasks fitted with Suba-Seal rubber septa or in a nitrogen-filled glovebox.

6.5.1.1 Materials

Reagents and solvents were purchased from Acros Organics, Cambridge Isotopes Laboratories, Fisher Scientific, Sigma-Aldrich, or Strem Chemicals, Inc. Solvents for synthesis were of reagent grade or better; solvents for air- or moisture-sensitive reactions were dried by passage through activated alumina and then stored over 4 Å molecular sieves prior to use.[18] Methyl 3-acetylbenzoate,[13] 5-methyl-5-(2-pyridyl)dipyrromethane,[15] and 2-acetylpyrimidine[19] were synthesized using previous literature procedures.

6.5.1.2 Compound Characterization

^{1}H NMR and ^{13}C NMR spectra were recorded at 25 °C on a Bruker 400 MHz spectrometer. Proton spectra are referenced to the residual proton resonance of the deuterated solvent ($CDCl_3$ = δ 7.26), and carbon spectra are referenced to the carbon resonances of the solvent ($CDCl_3$ = δ 77.16). All chemical shifts are reported using the standard δ notation in parts-per-million; positive chemical shifts are to higher frequency from the given reference. High-resolution mass spectrometry analyses were performed by the Mass Spectrometry Laboratory in the Department of Chemistry and Biochemistry at the University of Delaware.

6.5.1.3 Homogeneous O_2 Reduction Experiments

UV-vis spectroscopy was carried out on a StellarNet CCD array UV- vis spectrometer at room temperature using screw cap quartz cuvettes from Starna (path length = 1 cm). The reduction of O_2 in benzonitrile (PhCN) with ferrocene (Fc), $HClO_4$ and a catalytic amount of cobalt calix[4]phyrin was monitored by the rise in ferrocenium (Fc^+) ion concentration at λ = 620 nm (ε = 330 M^{-1} in PhCN). The concentration of O_2 in air-saturated PhCN is a known value ($1.7x10^{-3}$ M).[20]

A typical experiment for catalytic homogeneous reduction of O_2 by Fc and $HClO_4$ is as follows: To a quartz cuvette (volume ~ 4.6 mL) with a screw cap fitted with a rubber septum was added 3.6 mL of a solution of Fc (0.10 M) in PhCN. To this solution was simultaneously added 46 μL of $HClO_4$ in PhCN (2.0 M) and 1 mL of cobalt calix[4]phyrin (1.0×10^{-4} M) in PhCN. All PhCN solution were saturated with air prior to preparation. The rise in the absorbance of Fc^+ was recorded every 2 or 30 seconds. At least three trials were carried out and the reported results were an average of these trials.

6.5.1.4 Rotating Ring Disk Electrode Voltammetry

Rotating ring disk electrode (RRDE) and rotating disk electrode (RDE) experiments were performed using a CHI-720D bipotentiostat with a Pine Research Instrumentation modulated speed rotator (AFE6M). The linear sweep voltammetry (LSV) measurements were performed with a four-electrode assembly: a glassy carbon working electrode (0.2475 cm^2), a platinum ring working electrode (0.1866 cm^2), a platinum mesh auxiliary electrode, and a Ag/AgCl (1.0 M KCl) reference electrode. In some instances, the reference electrode was adjusted to the normal hydrogen electrode (NHE) according to the relationship Ag^+/Ag = 235 mV + NHE. The platinum ring working electrode was set at a fixed potential of 1.46 V vs. NHE. The designated catalyst was immobilized on the glassy carbon working electrode using a previously reported literature procedure:[11] a 3.9 mL THF solution was prepared by combining 4 mg MWCNT, 45 μL 5% Nafion and 0.47 mL of a 2.5 mM solution of the cobalt compound in THF. The prepared solution was sonicated for 30 min, then 10 μL of the solution was drop cast onto the surface of the glassy carbon disk electrode. Subsequent evaporation of the solution provided an immobilized catalyst film. A 0.5 M H_2SO_4 in Millipore water solution was employed as supporting electrolyte and was saturated with O_2 for a minimum of 30 minutes prior to acquisition of LSVs. Collection efficiencies were calibrated against a ferricyanide standard.[21] Unless otherwise noted, a constant scan rate of 20 mV/s with iR drop compensation was maintained for LSV data acquisition. E_{onset} was taken at current density equal to 0.15 mA/cm^2.

6.5.1.5 Koutecky-Levich Analysis

The number of electrons transferred was determined using the Koutecky-Levich equation:[17]

$$\frac{1}{i} = \frac{1}{i_K} + \frac{1}{i_{l,c}} = \frac{1}{i_K} + \left(\frac{1}{0.62nFAD_O^{2/3}\nu^{-1/6}C_O^*} \right) \omega^{-1/2}$$

where i is the measured current density, i_K is kinetic current density, $i_{l,c}$ is limiting current density, n is electrons transferred, F is Faraday's constant (96485 C/mol), A is the electrode area (0.2475 cm^2), D_O is the diffusion coefficient of O_2 (1.15 x 10^{-5} mol/cm^3), ν is the kinematic viscosity of electrolyte (1.0 x 10^{-2} V/s), C_O is concentration of O_2 (1.4 x 10^{-6} M), and ω is the angular rotation rate of the electrode ($2\pi f$, f is revolutions per second).

6.5.2 Synthesis of Co(C4PHM^{COOH}), Co(C4PHM^{py}), and Co(C4PHM^{pyrm})

6.5.2.1 5-Methyl-5-(3-methylester benzoate)dipyrromethane

To a solution of 4 mL pyrrole and 170 mg (1 mmol) methyl 3-acetylbenzoate was added 25 μL of trifluoroacetic acid. The solution was allowed to stir at 25 °C for 72 h after which time excess pyrrole was removed *in vacuo* to yield a green oil. This oil was dissolved in ethyl acetate and rinsed with water then brine. Ethyl acetate was removed *in vacuo.* The solid was purified by column chromatography on silica using hexanes and ethyl acetate (6:1) to give 177 mg of the desired compound (63% yield).[22] ^{1}H NMR (400 MHz; $CDCl_3$, 25 °C) δ/ppm: 7.92 (s, 1H), 7.89 (d, J = 7.7 Hz, 1H), 7.82 (broad s, 2H), 7.34 (t, J = 7.7 Hz, 1H), 7.24 (d, J = 7.7 Hz, 1H), 6.70 (td, J = 2.7, 1.5, 2H), 6.18 (q, 2.9 Hz, 2H), 5.94 (m, 2H), 3.87 (s, 3H), 2.08 (s, 3H).

6.5.2.2 5,15,15-Trimethyl-5-(3-methylester benzoate)-10,20-bis(pentafluorophenyl)calix[4]phyrin

To a solution of 281 mg (0.5 mmol) of 5,5-dimethyl-1,9-bis(pentafluorobenzoyl)dipyrromethane[23] dissolved in 30 mL THF and 9 mL MeOH was added 946 mg $NaBH_4$ (25.0 mmol). This solution was allowed to stir under an air

atmosphere at room temperature for 2 hours, followed by addition of distilled water to quench the reaction. The solution was extracted with CH_2Cl_2 twice then the organic layers were combined and rinsed with water and brine. The organic layer was collected and CH_2Cl_2 was removed *in vacuo* to give a pale-yellow oil. The oil was dissolved in 200 mL of CH_2Cl_2 and to the solution was added 147 mg (0.5 mmol) of 5-methyl-5-(3-methylester benzoic acid)dipyrromethane **(1)** and 30 mg of $InCl_3$. The reaction was allowed to stir for 2 hours. To the reaction mixture was added 226 mg DDQ and after 5 minutes, 14 mL of triethylamine was also added. The reaction was allowed to stir for an additional 15 minutes, followed by removal of solvent *in vacuo* to give a dark mauve solid. The solid was purified by column chromatography on silica using hexanes and CH_2Cl_2 (5:1) to give 121 mg of the desired compound (30% yield). ^{1}H NMR (400 MHz; $CDCl_3$, 25 °C) δ/ppm: 13.49 (s, 2H), 7.97 (d, J = 7.7 Hz, 1H), 7.94 (s, 1H) 7.54 (d, J = 8.3 Hz, 1H), 7.44 (t, J = 7.8 Hz, 1H), 6.35 (d, J = 4.3 Hz, 2H), 6.31 (d, J = 4.3 Hz, 2H), 6.24 (t, J = 3.2 Hz, 42H), 3.88 (s, 3H), 2.07 (s, 3H), 1.68 (d, J = 11.7 Hz, 6H).

6.5.2.3 5,15,15-Trimethyl-5-(3-benzoic acid)-10,20-bis(pentafluorophenyl) calix[4]phyrin (C4P*HM*^{COOH})

To a solution of 30 mL sulfuric acid, 5 mL acetic acid, and 10 mL H_2O was added 108 mg (0.13 mmol) 5,15,15-trimethyl-5-(3-methylester benzoic acid)-10,20-bis(pentafluorophenyl)calix[4]phyrin. The solution was allowed to stir in the dark at reflux for 1.5 h. The resulting solution was dissolved in ethyl acetate and rinsed several times with a brine solution. Ethyl acetate was removed *in vacuo* to give a red solid and was purified by column chromatography on silica using CH_2Cl_2 and ethyl acetate (5:1) to give 86 mg of the desired compound (80% yield). ^{1}H NMR (400 MHz;

$CDCl_3$, 25 °C) δ/ppm: 13.51 (broad s, 2H), 8.02 (d, J = 7.7 Hz, 1H), 7.99 (s, 1H), 7.58 (d, J = 7.9 Hz, 1H), 7.48 (t, 7.8 Hz, 1H), 6.36 (d, J = 4.3 Hz, 2H), 6.32 (d, J = 4.3 Hz, 2H), 6.24 (s, 4H), 2.06 (s, 3H), 1.67 (s, 6H).

6.5.2.4 Cobalt 5,15,15-trimethyl-5-(3-benzoic acid)-10,20-bis(pentafluorophenyl) calix[4]phyrin (Co(C4P*HM*^{COOH}))

A mixture of C4P*HM*^{COOH} (40 mg, 0.05 mmol) and 10 mg $Co(OAc)_2$ was allowed to stir in 15 mL CH_3CN at 65 °C for 16 h. The solvent was removed *in vacuo*. The remaining solid was dissolved in ethyl acetate and rinsed several times with a brine solution. The organic layers were combined and dried over sodium sulfate. The solvent was removed *in vacuo* and the crude material was purified by column chromatography on silica using dichloromethane and ethyl acetate (5:1) as the eluent to give a dark yellow brown solid in quantitative yield (43 mg). HR-LIFDI-MS: $[M]^+$ m/z calc for $C_{42}H_{22}F_{10}N_4O_2Co$: 863.0915. Found: 863.0930.

6.5.2.5 5,15,15-Trimethyl-5-(2-pyridyl)-10,20-bis(pentafluorophenyl) calix[4]phyrin (C4P*HM*^{py})

To a solution of 116 mg (0.21 mmol) of 5-methyl-1,9-bis(pentafluorobenzoyl)dipyrromethane[23] dissolved in 12 mL THF and 4 mL MeOH was added 400 mg $NaBH_4$. This solution was allowed to stir under an air atmosphere at room temperature for 2 hours, followed by addition of distilled water to quench the reaction. The solution was extracted with CH_2Cl_2 twice then the organic layers were combined and rinsed with water and brine. The organic layer was collected and CH_2Cl_2 was removed *in vacuo* to give a pale-yellow oil. The oil was dissolved in 100 mL of CH_2Cl_2 and to the solution was added 50 mg (0.21 mmol) of 5-methyl-5-(2-pyridyl)dipyrromethane **(2)** and ~15 mg of $InCl_3$. The reaction was allowed to stir at

room temperature for 12 hours. To the reaction mixture was added 92 mg DDQ and after 5 minutes, 6 mL of triethylamine was also added. The reaction was allowed to stir for an additional 15 minutes, followed by removal of solvent *in vacuo* to give a dark red solid. The solid was purified by column chromatography on silica using hexanes and CH_2Cl_2 (1:3) to give 66 mg of the desired compound (42% yield). ^{1}H NMR (400 MHz; $CDCl_3$, 25 °C) δ/ppm: 13.53 (broad s, 2H), 8.66 (ddd, J = 4.8, 1.9, 0.9 Hz, 1H), 7.71 (td, J = 7.7, 1.9 Hz, 1H), 7.48 (dt, J = 8.1, 1.0 Hz, 1H), 7.20 (ddd, J = 7.5, 4.8, 1.1 Hz, H), 6.42 (d, J = 4.3 Hz, 2H), 6.31 (d, J = 4.3 Hz, 2H), 6.24 (q, J = 4.3 Hz, 4H), 2.16, 1.78, 1.70.

6.5.2.6 Cobalt 5,15,15-trimethyl-5-(2-pyridyl)-10,20-bis(pentafluorophenyl) calix[4]phyrin (Co(C4P*HM*^{py}))

A mixture of C4P*HM*^{py} (50 mg, 0.07 mmol) and 10 mg $Co(OAc)_2$ was allowed to stir in 15 mL CH_3CN at 60 °C for 8 h. The solvent was removed *in vacuo*. The remaining solid was dissolved in ethyl acetate and rinsed several times with a brine solution. The organic layers were combined and dried over sodium sulfate. The solvent was removed *in vacuo* and the crude material was purified by column chromatography on silica using dichloromethane and hexane (1:1) as the eluent to give a dark yellow brown solid in 95 % yield (50 mg). HR-LIFDI-MS: $[M]^+$ m/z calc for $C_{40}H_{21}F_{10}N_5Co$: 820.0986. Found: 820.0969.

6.5.2.7 5-Methyl-5-(2-pyrimidinyl)dipyrromethane

To a solution of 15 mL of pyrrole and 580 mg (4.75 mmol) 2-acetylpyrimidine was added 40 μL of trifluoroacetic acid. The solution was allowed to stir at 25 °C for 96 h after which time excess pyrrole was removed *in vacuo* to yield a yellow oil. This oil was dissolved in ethyl acetate and rinsed with water then brine. Ethyl acetate was

removed *in vacuo*. The solid was purified by column chromatography on silica using hexanes and ethyl acetate (1:2) to give 430 mg of the desired compound (35% yield). ^{1}H NMR (400 MHz; $CDCl_3$, 25 °C) δ/ppm: 8.97 (broad s, 2H), 8.74 (d, J = 4.9 Hz, 2H), 7.19 (t, J = 4.9 Hz, 1H), 6.71 (td, J = 2.7, 1.5 Hz, 2H), 6.13 (dt, J = 3.5, 2.7 Hz, 2H), 5.94 (ddd, J = 3.4, 2.6, 1.5 Hz, 2H), 2.19 (s, 3H).

6.5.2.8 5,15,15-Trimethyl-5-(2-pyrimidinyl)-10,20-bis(pentafluorophenyl) calix[4]phyrin (C4P*HM*^{pyrm})

To a solution of 281 mg (0.5 mmol) of 5,5-dimethyl-1,9-bis(pentafluorobenzoyl)dipyrromethane[23] dissolved in 30 mL THF and 9 mL MeOH was added 946 mg $NaBH_4$ (25.0 mmol). This solution was allowed to stir under an air atmosphere at room temperature for 2 hours, followed by addition of distilled water to quench the reaction. The solution was extracted with CH_2Cl_2 twice then the organic layers were combined and rinsed with water and brine. The organic layer was collected and CH_2Cl_2 was removed *in vacuo* to give a pale-yellow oil. The oil was dissolved in 200 mL of CH_2Cl_2 and to the solution was added 119 mg (0.5 mmol) of 5-methyl-5-(2-pyrimidinyl)dipyrromethane **(3)** and 30 mg of $InCl_3$. The reaction was allowed to stir for 2 hours. To the reaction mixture was added 226 mg DDQ and after 5 minutes, 14 mL of triethylamine was also added. The reaction was allowed to stir for an additional 15 minutes, followed by removal of solvent *in vacuo* to give a dark red solid. The solid was purified by column chromatography on silica using hexanes and CH_2Cl_2 (1:3) to give 223 mg of the desired compound (60% yield). ^{1}H NMR (400 MHz; $CDCl_3$, 25 °C) δ/ppm: 13.84 (broad s, 2H), 8.83 (d, J = 4.8 Hz, 2H), 7.22 (t, J = 4.8 Hz, 1H), 6.41 (d, J = 4.3 Hz, 2H), 6.29-6.22 (m, 6H), 2.29 (s, 3H), 2.01 (s, 3H), 1.74 (s, 3H).

6.5.2.9 Cobalt 5,15,15-trimethyl-5-(2-pyrimidinyl)-10,20-bis(pentafluorophenyl) calix[4]phyrin (Co(C4P*HM*^{pyrm}))

A mixture of C4P*HM*^{pyrm} (100 mg, 0.13 mmol) and 10 mg $Co(OAc)_2$ was allowed to stir in 15 mL CH_3CN at 60 °C for 16 h. The solvent was removed *in vacuo*. The remaining solid was dissolved in ethyl acetate and rinsed several times with a brine solution. The organic layers were combined and dried over sodium sulfate. The solvent was removed *in vacuo* and the crude material was purified by column chromatography on silica using dichloromethane and hexane (2:1) as the eluent to give a dark yellow brown solid in 95 % yield (102 mg). HR-LIFDI-MS: $[M]^+$ m/z calc for $C_{40}H_{21}F_{10}N_5Co$: 821.0922. Found: 821.0924.

6.5.3 X-ray Crystallography

6.5.3.1 X-ray Structure Solution and Refinement for Co(C4P*HM*^{COOH})

Crystals were mounted using viscous oil onto a plastic mesh and cooled to the data collection temperature. Data were collected on a Smart APEX diffractometer with Mo-Kα radiation (λ = 0.71073 Å) monochromated with graphite focused using Goebel mirrors Unit cell parameters were obtained from 36 data frames, 0.5º ω, from three different sections of the Ewald sphere. The unit-cell parameters, equivalent reflections, and systematic absences in the diffraction data are consistent, uniquely, with *C*2/*c* (no. 15). Solutions in the centrosymmetric space group options yielded chemically reasonable and computationally stable results of refinement. The data sets were treated with multi-scan absorption corrections.[24] The structures were solved using direct methods and refined with full-matrix, least-squares procedures on F^2.[25] The data was treated with Squeeze to model disordered solvent molecules as diffused contributions.[26] All non-hydrogen atoms were refined with anisotropic displacement

parameters. H-atoms were placed in calculated positions with U_{iso} equal to 1.2 (1.5 for methyl H) U_{eq} of the attached atom. Atomic scattering factors are contained in the SHELXTL program library. Crystallographic data were collected by Gabriel Andrade and Dr. Glenn Yap, Department of Chemistry and Biochemistry, University of Delaware.

6.5.3.2 Crystallographic Information Tables

Table 6.4: Crystallographic data for Co(C4P*HM*^{COOH})

Formula	**Co(C4P*HM*^{COOH})**
Fw	937.68
Crystal System	monoclinic
Space Group	C 1 2/c 1
a	24.2762(16) Å
b	16.7200(11) Å
c	24.5752(17) Å
α	90°
β	112.103(2)°
γ	90°
Volume	9242.0(11) Å^3
Z	8
Temp	200(2) K
D_{calcd}	1.348 g/cm^3
2Θ range	1.58 to 27.52°
μ (Mo Kα)	0.454 mm^{-1}
Reflections	69701
Unique	10598
R (int)	0.0733
R_1	0.0679
wR_2	0.2053

6.6 References

(1) Collman, J. P.; Wagenknecht, P. S.; Hutchison, J. E. *Angew. Chemie Int. Ed. English* **1994**, *33* (15–16), 1537.

(2) Rosenthal, J.; Nocera, D. G. *Acc. Chem. Res.* **2007**, *40* (7), 543.

(3) Zhang, W.; Lai, W.; Cao, R. *Chem. Rev.* **2017**, *117* (4), 3717

(4) Collman, J.P.; Boulatov, R.; Sunderland, C.J. In *The Porphyrin Handbook*; Kadish, K. M.; Smith, K.M.; Guilard, R., Eds.; Academic Press: San Diego, CA, 2003, Vol. 11, pp 1-49.

(5) Scherson, D. A.; Palencsár, A.; Tolmachev, Y.; Stefan, I. In *Electrochemical Surface Modification*; Wiley-VCH Verlag GmbH & Co. KGaA, 2008; pp 191–288.

(6) Rosenthal, J.; Nocera, D. G. In *Progress in Inorganic Chemistry*; John Wiley & Sons, Inc., 2007; pp 483–544.

(7) Liu, H. Y.; Abdalmuhdi, I.; Chang, C. K.; Anson, F. C. *J. Phys. Chem.* **1985**, *89* (4), 665.

(8) Ni, C. L.; Abdalmuhdi, I.; Chang, C. K.; Anson, F. C. *J. Phys. Chem.* **1987**, *91* (5), 1158.

(9) Collman, J. P.; Hendricks, N. H.; Kim, K.; Bencosme, C. S. *J. Chem. Soc., Chem. Commun.* **1987**, *20*, 1537.

(10) Guilard, R.; Brandes, S.; Tardieux, C.; Tabard, A.; L'Her, M.; Miry, C.; Gouerec, P.; Knop, Y.; Collman, J. P. *J. Am. Chem. Soc.* **1995**, *117* (47), 11721.

(11) McGuire Jr., R.; Dogutan, D. K.; Teets, T. S.; Suntivich, J.; Shao-Horn, Y.; Nocera, D. G. *Chem. Sci.* **2010**, *1* (3), 411.

(12) Rosenthal, J. Proton-Coupled Electron Transfer: From Basic Principles to Small Molecule Activation. Ph.D. Thesis, Massachusetts Institute of Technology, 2007.

(13) Suzuki, T.; Muto, N.; Bando, M.; Itoh, Y.; Masaki, A.; Ri, M.; Ota, Y.; Nakagawa, H.; Iida, S.; Shirahige, K.; Miyata, N. *ChemMedChem* **2014**, *9* (3), 657.

(14) Rosenthal, J.; Chng, L. L.; Fried, S. D.; Nocera, D. G. *Chem. Commun.* **2007**, *25*, 2642.

(15) Gao, G.; Korobkov, I.; Gambarotta, S. *Inorg. Chem.* **2004**, *43* (3), 1108.

(16) Fukuzumi, S.; Okamoto, K.; Gros, C. P.; Guilard, R. *J. Am. Chem. Soc.* **2004**, *126* (33), 10441.

(17) Bard, A. J.; Faulkner, L. R. In *Electrochemical Methods: Fundamentals and Applications, 2nd edition*; Wiley: New York, 2001; pp 517-518.

(18) Pangborn, A. B.; Giardello, M. A.; Grubbs, R. H.; Rosen, R. K.; Timmers, F. J. *Organometallics* **1996,** *15* (5), 1518-1520.

(19) Reimann, E.; Ziegon, H.-L. *Justus Liebigs Ann. Chem.* **1976**, *1976* (7–8), 1351.

(20) Fukuzumi, S.; Imahori, H.; Yamada, H.; El-Khouly, M. E.; Fujitsuka, M.; Ito, O.; Guldi, D. M. *J. Am. Chem. Soc.* **2001**, *123* (11), 2571.

(21) Hancock, C. A.; Ong, A. L.; Slater, P. R.; Varcoe, J. R. *J. Mater. Chem. A* **2014**, *2* (9), 3047.

(22) Fitzsimons, M. C. Unpublished results.

(23) O'Brien, A. Y.; McGann, J. P.; Geier, G. R. *J. Org. Chem.* **2007**, *72* (11), 4084.

(24) Apex3 software suite, Madison, WI, 2015.

(25) Sheldrick, G. M. *Acta Crystallogr. Sect. A* **2008**, *64* (1), 112.

(26) Spek, A. L. *J. Appl. Crystallogr.* **2003**, *36* (1), 7.

Appendix A

ADDITIONAL O_2 REDUCTION DATA

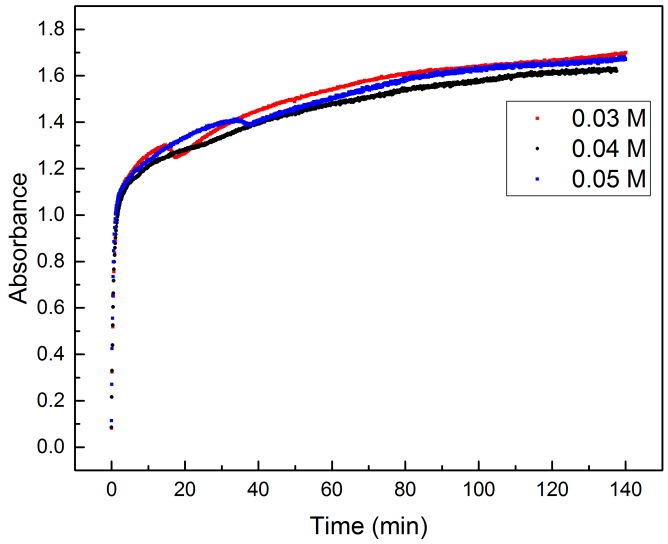

Figure A.1: Time course of absorbance at 620 nm due to Fc oxidation catalyzed by $Co(C4P^{PF})$ with various concentrations of $HClO_4$ in air-saturated PhCN

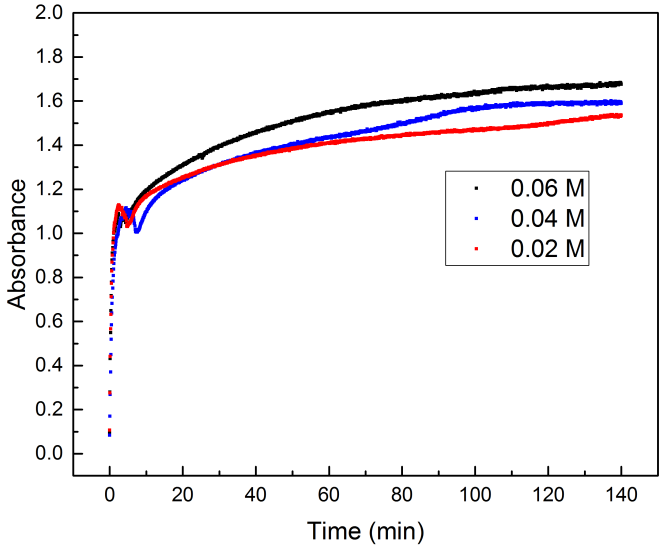

Figure A.2: Time course of absorbance at 620 nm due to Fc oxidation catalyzed by Co(C4P^{PF}) with $HClO_4$ and various concentrations of Fc in air-saturated PhCN

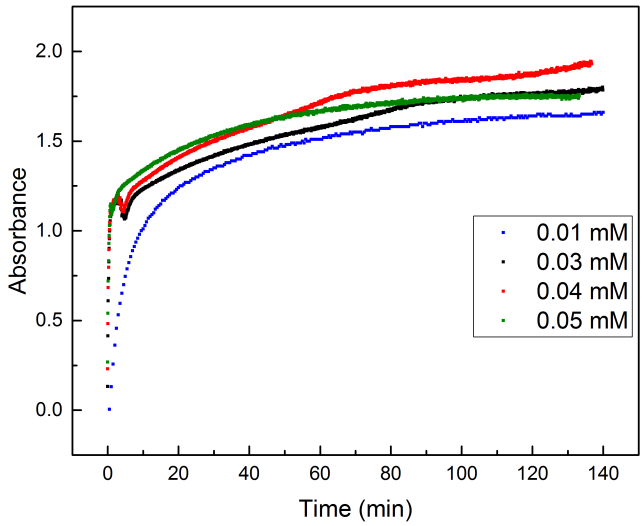

Figure A.3: Time course of absorbance at 620 nm due to Fc oxidation with $HClO_4$ catalyzed by various concentration of Co(C4P^{PF}) in air-saturated PhCN

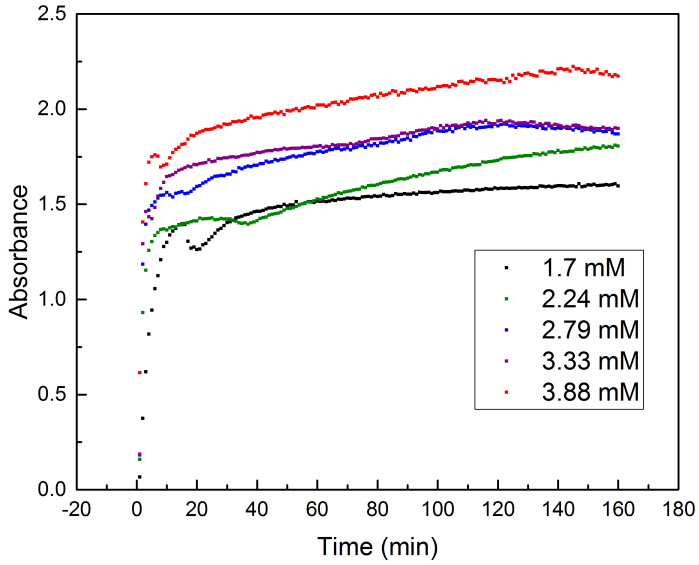

Figure A.4: Time course of absorbance at 620 nm due to Fc oxidation catalyzed by $Co(C4P^{PF})$ with $HClO_4$ and various concentrations of O_2 in PhCN

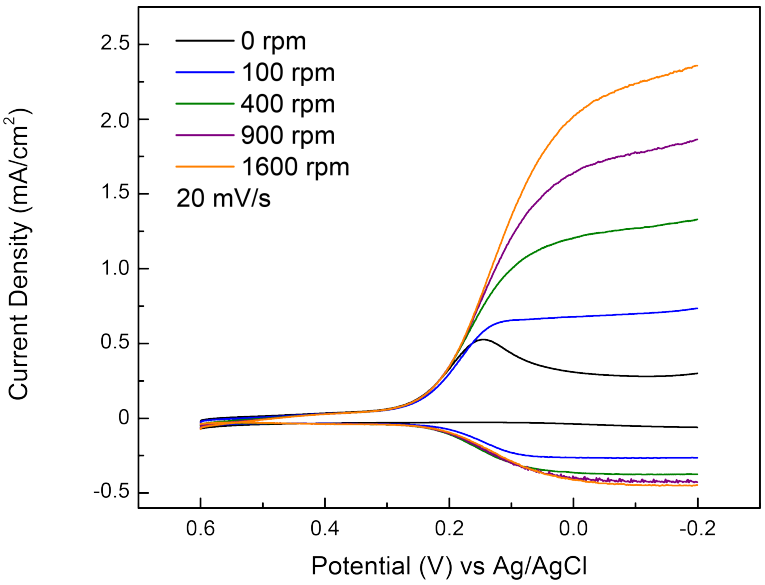

Figure A.5: LSVs of ORR activity of Co(C4P*HM*^{COOH}) at a RRDE at different rotation rates in O_2 saturated 0.5 M H_2SO_4, with a scan rate of 20 mV/s

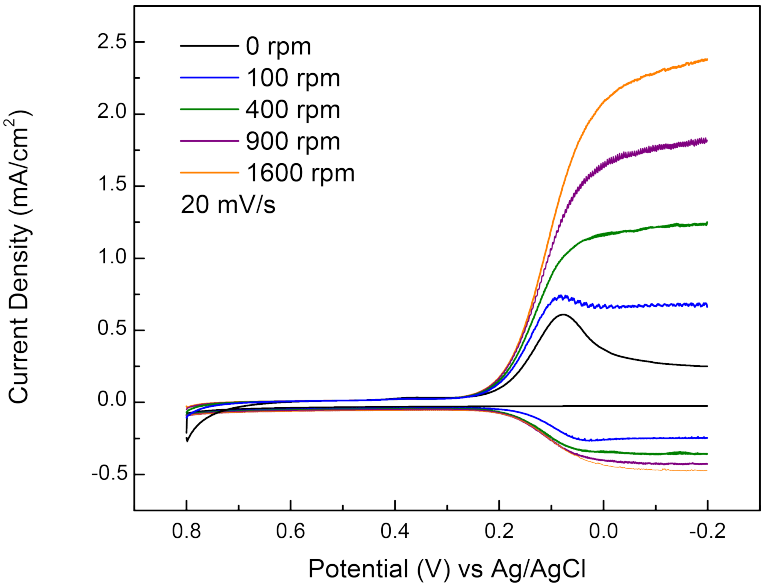

Figure A.6: LSVs of ORR activity of Co(C4P*HM*^{py}) at a RRDE at different rotation rates in O_2 saturated 0.5 M H_2SO_4, with a scan rate of 20 mV/s

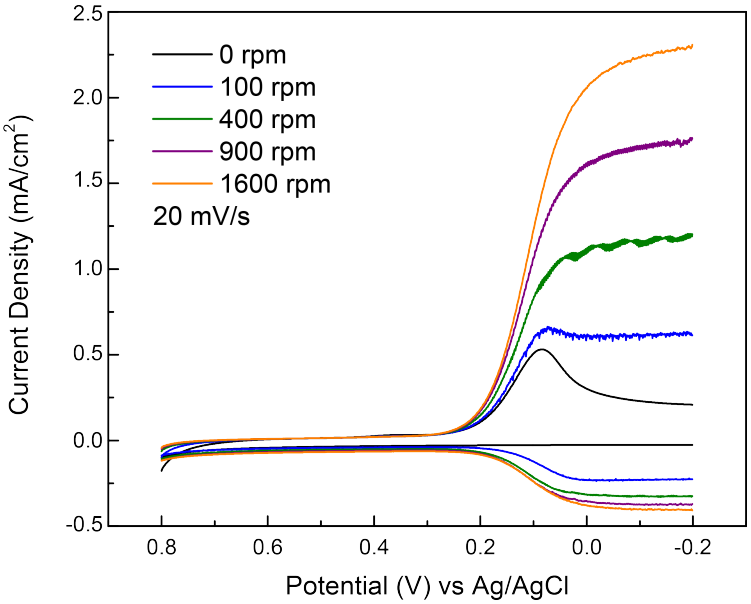

Figure A.7: LSVs of ORR activity of Co(C4P*HM*^{pyrm}) at a RRDE at different rotation rates in O_2 saturated 0.5 M H_2SO_4, with a scan rate of 20 mV/s

Appendix B

BOND LENGTHS AND ANGLES FOR CRYSTAL STRUCTURES

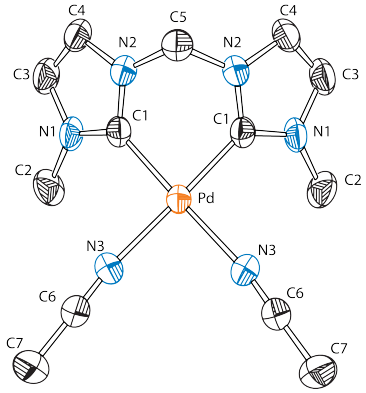

Figure B.1: Numbered crystal structure of $[(MDC^{Me})Pd(CH_3CN)_2](PF_6)_2$ with all hydrogen atoms omitted for clarity and thermal ellipsoids shown at 50% probability. Counterions and solvent molecules are also emitted for clarity.

Table B.1: Bond lengths (Å) determined for $[(MDC^{Me})Pd(CH_3CN)_2](PF_6)_2$

Bond	Length	Bond	Length
Pd-C1	1.973(6)	Pd-N3	2.062(5)
N1-C1	1.331(7)	N1-C3	1.384(9)
N1-C2	1.474(9)	N2-C1	1.338(8)
N2-C4	1.388(8)	N2-C5	1.455(7)
N3-C6	1.127(8)	N4-C8	1.133(15)
N5-C10	1.111(18)	C2-H2A	0.96
C2-H2B	0.96	C2-H2C	0.96
C3-C4	1.335(10)	C3-H3	0.93
C4-H4	0.93	C5-N2#1	1.455(7)
C5-H5A	0.97	C5-H5B	0.97
C6-C7	1.448(9)	C7-H7A	0.96
C7-H7B	0.96	C7-H7C	0.96

C8-C9	1.387(17)	C9-H9A	0.96
C9-H9B	0.96	C9-H9C	0.96
C10-C11	1.395(19)	C11-H11A	0.96
C11-H11B	0.96	C11-H11C	0.96
P1-F4#2	1.462(9)	P1-F4	1.463(9)
P1-F1	1.519(10)	P1-F3	1.562(8)
P1-F3#2	1.562(8)	P1-F2	1.568(10)
P2-F5	1.524(7)	P2-F5#2	1.524(7)
P2-F8	1.523(8)	P2-F8#2	1.523(8)
P2-F6	1.581(7)	P2-F7	1.592(7)

Table B.2: Bond angles (°) determined for $[(MDC^{Me})Pd(CH_3CN)_2](PF_6)_2$

Bond	**Length**	**Bond**	**Length**
C1-Pd-C1#1	83.8(3)	C1-Pd-N3#1	177.7(2)
C1#1-Pd-N3#1	95.0(2)	C1-Pd-N3	95.0(2)
C1#1-Pd-N3	177.7(2)	N3#1-Pd-N3	86.2(3)
C1-N1-C3	109.8(6)	C1-N1-C2	126.4(5)
C3-N1-C2	123.7(5)	C1-N2-C4	111.0(5)
C1-N2-C5	122.8(5)	C4-N2-C5	126.0(6)
C6-N3-Pd	171.3(5)	N1-C1-N2	105.9(5)
N1-C1-Pd	130.0(5)	N2-C1-Pd	124.0(4)
N1-C2-H2A	109.5	N1-C2-H2B	109.5
H2A-C2-H2B	109.5	N1-C2-H2C	109.5
H2A-C2-H2C	109.5	H2B-C2-H2C	109.5
C4-C3-N1	107.9(6)	C4-C3-H3	126.0
N1-C3-H3	126.0	C3-C4-N2	105.4(6)
C3-C4-H4	127.3	N2-C4-H4	127.3
N2#1-C5-N2	108.0(7)	N2#1-C5-H5A	110.1
N2-C5-H5A	110.1	N2#1-C5-H5B	110.1
N2-C5-H5B	110.1	H5A-C5-H5B	108.4
N3-C6-C7	179.1(7)	C6-C7-H7A	109.5
C6-C7-H7B	109.5	H7A-C7-H7B	109.5
C6-C7-H7C	109.5	H7A-C7-H7C	109.5
H7B-C7-H7C	109.5	N4-C8-C9	179.4(14)
C8-C9-H9A	109.5	C8-C9-H9B	109.5
H9A-C9-H9B	109.5	C8-C9-H9C	109.5
H9A-C9-H9C	109.5	H9B-C9-H9C	109.5
N5-C10-C11	179.6(18)	C10-C11-H11A	109.5
C10-C11-H11B	109.5	H11A-C11-H11B	109.5
C10-C11-H11C	109.5	H11A-C11-H11C	109.5

H11B-C11-H11C	109.5	F4#2-P1-F4	86.7(14)
F4#2-P1-F1	91.4(8)	F4-P1-F1	91.4(8)
F4#2-P1-F3	177.1(9)	F4-P1-F3	91.0(8)
F1-P1-F3	90.5(6)	F4#2-P1-F3#2	91.0(8)
F4-P1-F3#2	177.1(9)	F1-P1-F3#2	90.5(6)
F3-P1-F3#2	91.2(10)	F4#2-P1-F2	92.9(7)
F4-P1-F2	92.9(7)	F1-P1-F2	174.2(8)
F3-P1-F2	85.4(5)	F3#2-P1-F2	85.4(5)
F5-P2-F5#2	87.6(9)	F5-P2-F8	178.9(8)
F5#2-P2-F8	91.2(7)	F5-P2-F8#2	91.2(7)
F5#2-P2-F8#2	178.9(8)	F8-P2-F8#2	89.9(11)
F5-P2-F6	91.0(3)	F5#2-P2-F6	91.0(3)
F8-P2-F6	88.9(4)	F8#2-P2-F6	88.9(4)
F5-P2-F7	89.1(4)	F5#2-P2-F7	89.1(4)
F8-P2-F7	91.1(4)	F8#2-P2-F7	91.1(4)
F6-P2-F7	180.0(4)		

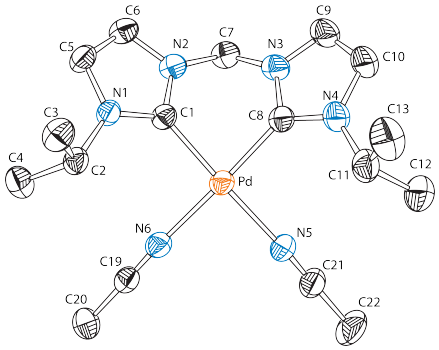

Figure B.2: Numbered crystal structure of $[(MDC^{iPr})Pd(CH_3CN)_2](PF_6)_2$ with all hydrogen atoms omitted for clarity and thermal ellipsoids shown at 50% probability. Counterions and solvent molecules are also emitted for clarity.

Table B.3: Bond lengths (Å) determined for $[(MDC^{iPr})Pd(CH_3CN)_2](PF_6)_2$

Bond	**Length**	**Bond**	**Length**
Pd1-C8	1.974(4)	Pd1-C1	1.979(3)
Pd1-N6	2.064(3)	Pd1-N5	2.073(3)
N1-C1	1.335(5)	N1-C5	1.382(5)
N1-C2	1.488(4)	N2-C1	1.349(5)

N2-C6	1.385(5)	N2-C7	1.461(5)
N3-C8	1.363(5)	N3-C9	1.373(5)
N3-C7	1.453(5)	N4-C8	1.336(5)
N4-C10	1.393(5)	N4-C11	1.482(5)
N5-C21	1.122(5)	N6-C19	1.135(5)
C2-C4	1.518(5)	C2-C3	1.535(5)
C2-H2	1.0	C3-H3A	0.98
C3-H3B	0.98	C3-H3C	0.98
C4-H4A	0.98	C4-H4B	0.98
C4-H4C	0.98	C5-C6	1.343(6)
C5-H5	0.95	C6-H6	0.95
C7-H7A	0.99	C7-H7B	0.99
C9-C10	1.355(7)	C9-H9	0.95
C10-H10	0.95	C11-C12	1.504(6)
C11-C13	1.520(7)	C11-H11	1.0
C12-H12A	0.98	C12-H12B	0.98
C12-H12C	0.98	C13-H13A	0.98
C13-H13B	0.98	C13-H13C	0.98
C19-C20	1.451(6)	C20-H20A	0.98
C20-H20B	0.98	C20-H20C	0.98
C21-C22	1.466(6)	C22-H22A	0.98
C22-H22B	0.98	C22-H22C	0.98
F1-P1	1.578(5)	F2-P1	1.568(4)
F3-P1	1.587(3)	F4-P1	1.558(5)
F5-P1	1.533(4)	F6-P1	1.582(4)
F7-P2	1.586(4)	F8-P2	1.592(3)
F9-P2	1.569(4)	F10-P2	1.573(4)
F11-P2	1.598(4)	F12-P2	1.571(4)
O1-C25	1.4194	O1-C24	1.4195
C23-C24	1.5178	C23-H23A	0.98
C23-H23B	0.98	C23-H23C	0.98
C24-H24A	0.99	C24-H24B	0.99
C25-C26	1.5179	C25-H25A	0.99
C25-H25B	0.99	C26-H26A	0.98
C26-H26B	0.98	C26-H26C	0.98

Table B.4: Bond angles (°) determined for $[(MDC^{iPr})Pd(CH_3CN)_2](PF_6)_2$

Bond	**Angle**	**Bond**	**Angle**
C8-Pd1-C1	83.90(15)	C8-Pd1-N6	176.26(13)

C1-Pd1-N6	94.01(14)	C8-Pd1-N5	94.74(14)
C1-Pd1-N5	174.95(13)	N6-Pd1-N5	87.08(13)
C1-N1-C5	109.9(3)	C1-N1-C2	126.1(3)
C5-N1-C2	123.9(3)	C1-N2-C6	110.0(3)
C1-N2-C7	123.1(3)	C6-N2-C7	127.0(3)
C8-N3-C9	110.5(4)	C8-N3-C7	122.7(3)
C9-N3-C7	126.8(3)	C8-N4-C10	110.3(4)
C8-N4-C11	125.8(3)	C10-N4-C11	123.9(4)
C21-N5-Pd1	173.8(4)	C19-N6-Pd1	176.1(3)
N1-C1-N2	106.3(3)	N1-C1-Pd1	131.7(3)
N2-C1-Pd1	121.8(3)	N1-C2-C4	109.6(3)
N1-C2-C3	109.5(3)	C4-C2-C3	113.3(3)
N1-C2-H2	108.1	C4-C2-H2	108.1
C3-C2-H2	108.1	C2-C3-H3A	109.5
C2-C3-H3B	109.5	H3A-C3-H3B	109.5
C2-C3-H3C	109.5	H3A-C3-H3C	109.5
H3B-C3-H3C	109.5	C2-C4-H4A	109.5
C2-C4-H4B	109.5	H4A-C4-H4B	109.5
C2-C4-H4C	109.5	H4A-C4-H4C	109.5
H4B-C4-H4C	109.5	C6-C5-N1	107.4(3)
C6-C5-H5	126.3	N1-C5-H5	126.3
C5-C6-N2	106.4(3)	C5-C6-H6	126.8
N2-C6-H6	126.8	N3-C7-N2	108.3(3)
N3-C7-H7A	110.0	N2-C7-H7A	110.0
N3-C7-H7B	110.0	N2-C7-H7B	110.0
H7A-C7-H7B	108.4	N4-C8-N3	105.7(3)
N4-C8-Pd1	132.2(3)	N3-C8-Pd1	121.9(3)
C10-C9-N3	106.7(4)	C10-C9-H9	126.6
N3-C9-H9	126.6	C9-C10-N4	106.7(4)
C9-C10-H10	126.6	N4-C10-H10	126.6
N4-C11-C12	110.7(4)	N4-C11-C13	110.0(4)
C12-C11-C13	111.5(4)	N4-C11-H11	108.2
C12-C11-H11	108.2	C13-C11-H11	108.2
C11-C12-H12A	109.5	C11-C12-H12B	109.5
H12A-C12-H12B	109.5	C11-C12-H12C	109.5
H12A-C12-H12C	109.5	H12B-C12-H12C	109.5
C11-C13-H13A	109.5	C11-C13-H13B	109.5
H13A-C13-H13B	109.5	C11-C13-H13C	109.5
H13A-C13-H13C	109.5	H13B-C13-H13C	109.5
N6-C19-C20	179.0(4)	C19-C20-H20A	109.5
C19-C20-H20B	109.5	H20A-C20-H20B	109.5
C19-C20-H20C	109.5	H20A-C20-H20C	109.5
H20B-C20-H20C	109.5	N5-C21-C22	178.3(5)

C21-C22-H22A	109.5	C21-C22-H22B	109.5
H22A-C22-H22B	109.5	C21-C22-H22C	109.5
H22A-C22-H22C	109.5	H22B-C22-H22C	109.5
F5-P1-F4	97.2(4)	F5-P1-F2	177.7(4)
F4-P1-F2	84.9(4)	F5-P1-F1	88.4(4)
F4-P1-F1	173.0(4)	F2-P1-F1	89.4(3)
F5-P1-F6	93.0(2)	F4-P1-F6	93.3(3)
F2-P1-F6	87.8(2)	F1-P1-F6	90.6(3)
F5-P1-F3	87.9(2)	F4-P1-F3	86.6(3)
F2-P1-F3	91.3(2)	F1-P1-F3	89.4(3)
F6-P1-F3	179.1(2)	F9-P2-F10	91.9(3)
F9-P2-F12	178.7(3)	F10-P2-F12	88.4(3)
F9-P2-F7	89.0(3)	F10-P2-F7	178.9(2)
F12-P2-F7	90.8(3)	F9-P2-F8	89.7(2)
F10-P2-F8	88.2(2)	F12-P2-F8	91.6(2)
F7-P2-F8	92.5(2)	F9-P2-F11	89.7(3)
F10-P2-F11	90.2(2)	F12-P2-F11	89.0(3)
F7-P2-F11	89.1(2)	F8-P2-F11	178.3(2)
C25-O1-C24	113.5	C24-C23-H23A	109.5
C24-C23-H23B	109.5	H23A-C23-H23B	109.5
C24-C23-H23C	109.5	H23A-C23-H23C	109.5
H23B-C23-H23C	109.5	O1-C24-C23	108.8
O1-C24-H24A	109.9	C23-C24-H24A	109.9
O1-C24-H24B	109.9	C23-C24-H24B	109.9
H24A-C24-H24B	108.3	O1-C25-C26	108.8
O1-C25-H25A	109.9	C26-C25-H25A	109.9
O1-C25-H25B	109.9	C26-C25-H25B	109.9
H25A-C25-H25B	108.3	C25-C26-H26A	109.5
C25-C26-H26B	109.5	H26A-C26-H26B	109.5
C25-C26-H26C	109.5	H26A-C26-H26C	109.5
H26B-C26-H26C	109.5		

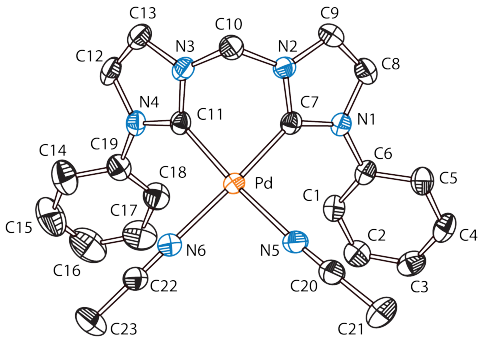

Figure B.3: Numbered crystal structure of $[(MDC^{Ph})Pd(CH_3CN)_2](PF_6)_2$ with all hydrogen atoms omitted for clarity and thermal ellipsoids shown at 50% probability. Counterions and solvent molecules are also emitted for clarity.

Table B.5: Bond lengths (Å) determined for $[(MDC^{Ph})Pd(CH_3CN)_2](PF_6)_2$

Bond	Length	Bond	Length
Pd-C11	1.965(4)	Pd-C7	1.973(4)
Pd-N6	2.050(3)	Pd-N5	2.067(4)
P1-F4	1.590(2)	P1-F5	1.591(3)
P1-F6	1.592(3)	P1-F3	1.595(3)
P1-F1	1.595(3)	P1-F2	1.601(3)
P2-F10	1.563(4)	P2-F7	1.565(3)
P2-F12	1.566(4)	P2-F11	1.571(4)
P2-F8	1.590(3)	P2-F9	1.598(3)
N1-C7	1.353(5)	N1-C8	1.394(5)
N1-C6	1.435(5)	N2-C7	1.341(5)
N2-C9	1.380(5)	N2-C10	1.451(5)
N3-C11	1.345(5)	N3-C13	1.376(5)
N3-C10	1.452(5)	N4-C11	1.351(5)
N4-C12	1.395(5)	N4-C19	1.428(5)
N5-C20	1.122(5)	N6-C22	1.126(5)
C1-C6	1.380(6)	C1-C2	1.390(7)
C1-H1	0.95	C2-C3	1.388(8)
C2-H2	0.95	C3-C4	1.367(9)
C3-H3	0.95	C4-C5	1.379(8)
C4-H4	0.95	C5-C6	1.379(6)
C5-H5	0.95	C8-C9	1.321(6)
C8-H8	0.95	C9-H9	0.95
C10-H10A	0.99	C10-H10B	0.99

C12-C13	1.337(6)	C12-H12	0.95
C13-H13	0.95	C14-C19	1.388(5)
C14-C15	1.388(6)	C14-H14	0.95
C15-C16	1.382(6)	C15-H15	0.95
C16-C17	1.385(6)	C16-H16	0.95
C17-C18	1.390(6)	C17-H17	0.95
C18-C19	1.380(6)	C18-H18	0.95
C20-C21	1.454(6)	C21-H21A	0.98
C21-H21B	0.98	C21-H21C	0.98
C22-C23	1.451(6)	C23-H23A	0.98
C23-H23B	0.98	C23-H23C	0.98

Table B.6: Bond angles (°) determined for $[(MDC^{Ph})Pd(CH_3CN)_2](PF_6)_2$

Bond	**Angle**	**Bond**	**Angle**
C11-Pd-C7	83.55(15)	C11-Pd-N6	92.52(14)
C7-Pd-N6	172.09(14)	C11-Pd-N5	176.55(14)
C7-Pd-N5	93.15(14)	N6-Pd-N5	90.87(13)
F4-P1-F5	89.65(15)	F4-P1-F6	90.52(14)
F5-P1-F6	179.12(18)	F4-P1-F3	90.58(15)
F5-P1-F3	89.23(16)	F6-P1-F3	89.90(15)
F4-P1-F1	89.26(15)	F5-P1-F1	90.90(18)
F6-P1-F1	89.97(17)	F3-P1-F1	179.79(19)
F4-P1-F2	179.35(16)	F5-P1-F2	90.33(15)
F6-P1-F2	89.51(14)	F3-P1-F2	90.07(15)
F1-P1-F2	90.09(15)	F10-P2-F7	90.8(2)
F10-P2-F12	92.5(3)	F7-P2-F12	91.4(2)
F10-P2-F11	87.9(2)	F7-P2-F11	91.6(2)
F12-P2-F11	176.9(2)	F10-P2-F8	177.4(2)
F7-P2-F8	91.3(2)	F12-P2-F8	89.0(2)
F11-P2-F8	90.5(2)	F10-P2-F9	90.4(2)
F7-P2-F9	178.7(2)	F12-P2-F9	88.3(2)
F11-P2-F9	88.7(2)	F8-P2-F9	87.50(18)
C7-N1-C8	109.4(3)	C7-N1-C6	126.6(3)
C8-N1-C6	124.0(3)	C7-N2-C9	110.8(3)
C7-N2-C10	122.4(3)	C9-N2-C10	126.7(3)
C11-N3-C13	110.8(3)	C11-N3-C10	121.3(3)
C13-N3-C10	127.9(3)	C11-N4-C12	109.5(3)
C11-N4-C19	125.4(3)	C12-N4-C19	124.8(3)
C20-N5-Pd	170.5(4)	C22-N6-Pd	174.7(3)

C6-C1-C2	118.9(5)	C6-C1-H1	120.5
C2-C1-H1	120.5	C3-C2-C1	119.5(6)
C3-C2-H2	120.2	C1-C2-H2	120.2
C4-C3-C2	120.3(6)	C4-C3-H3	119.9
C2-C3-H3	119.9	C3-C4-C5	121.0(6)
C3-C4-H4	119.5	C5-C4-H4	119.5
C6-C5-C4	118.5(6)	C6-C5-H5	120.7
C4-C5-H5	120.7	C5-C6-C1	121.7(5)
C5-C6-N1	118.8(4)	C1-C6-N1	119.5(4)
N2-C7-N1	105.3(3)	N2-C7-Pd	121.4(3)
N1-C7-Pd	133.1(3)	C9-C8-N1	107.5(4)
C9-C8-H8	126.3	N1-C8-H8	126.3
C8-C9-N2	107.0(4)	C8-C9-H9	126.5
N2-C9-H9	126.5	N2-C10-N3	108.2(3)
N2-C10-H10A	110.1	N3-C10-H10A	110.1
N2-C10-H10B	110.1	N3-C10-H10B	110.1
H10A-C10-H10B	108.4	N3-C11-N4	105.6(3)
N3-C11-Pd	122.7(3)	N4-C11-Pd	131.7(3)
C13-C12-N4	107.1(4)	C13-C12-H12	126.4
N4-C12-H12	126.4	C12-C13-N3	106.9(3)
C12-C13-H13	126.5	N3-C13-H13	126.5
C19-C14-C15	118.6(4)	C19-C14-H14	120.7
C15-C14-H14	120.7	C16-C15-C14	120.9(4)
C16-C15-H15	119.6	C14-C15-H15	119.6
C15-C16-C17	119.8(4)	C15-C16-H16	120.1
C17-C16-H16	120.1	C16-C17-C18	120.1(4)
C16-C17-H17	120.0	C18-C17-H17	120.0
C19-C18-C17	119.4(4)	C19-C18-H18	120.3
C17-C18-H18	120.3	C18-C19-C14	121.2(4)
C18-C19-N4	120.3(3)	C14-C19-N4	118.5(4)
N5-C20-C21	179.0(5)	C20-C21-H21A	109.5
C20-C21-H21B	109.5	H21A-C21-H21B	109.5
C20-C21-H21C	109.5	H21A-C21-H21C	109.5
H21B-C21-H21C	109.5	N6-C22-C23	179.0(5)
C22-C23-H23A	109.5	C22-C23-H23B	109.5
H23A-C23-H23B	109.5	C22-C23-H23C	109.5
H23A-C23-H23C	109.5	H23B-C23-H23C	109.5

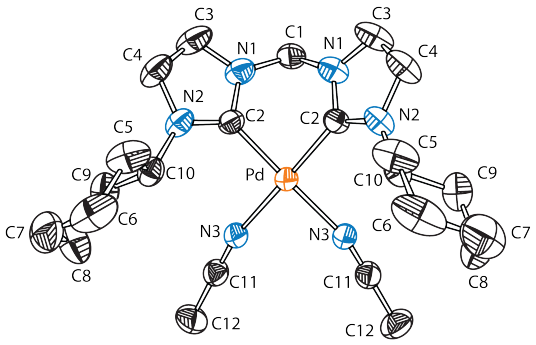

Figure B.4: Numbered crystal structure of $[(MDC^{Cy})Pd(CH_3CN)_2](PF_6)_2$ with all hydrogen atoms omitted for clarity and thermal ellipsoids shown at 50% probability. Counterions and solvent molecules are also emitted for clarity.

Table B.7: Bond lengths (Å) determined for $[(MDC^{Cy})Pd(CH_3CN)_2](PF_6)_2$

Bond	Length	Bond	Length
Pd-C2	1.971(6)	Pd-C2	1.971(6)
Pd-N3	2.057(6)	Pd-N3	2.057(6)
N1-C2	1.343(9)	N1-C3	1.386(11)
N1-C1	1.451(9)	N2-C2	1.342(9)
N2-C4	1.392(9)	N2-C10	1.495(9)
N3-C11	1.138(9)	C1-N1	1.451(9)
C1-H1A	0.99	C1-H1B	0.99
C3-C4	1.316(13)	C3-H3	0.95
C4-H4	0.95	C5-C10	1.507(9)
C5-C6	1.563(13)	C5-H5A	0.99
C5-H5B	0.99	C6-C7	1.488(18)
C6-H6A	0.99	C6-H6B	0.99
C7-C8	1.509(16)	C7-H7A	0.99
C7-H7B	0.99	C8-C9	1.546(13)
C8-H8A	0.99	C8-H8B	0.99
C9-C10	1.516(11)	C9-H9A	0.99
C9-H9B	0.99	C10-H10	1.0
C11-C12	1.434(11)	C12-H12A	0.98
C12-H12B	0.98	C12-H12C	0.98
P1-F4	1.5731	P1-F2	1.592(7)
P1-F2	1.592	P1-F1	1.602(2)
P1-F1	1.6022	P1-F3	1.604(7)
P1-F3	1.6042	P1-F6	1.609(8)

P1-F6	1.6094	P1-F5	1.6355
P1-F5	1.636(7)	F1-F1	0.25(3)
F2-F6	0.996(11)	F2-F5	1.4323
F3-F5	1.132(6)	F3-F3	1.322(17)
F5-F3	1.132(12)	F5-F2	1.4323
F6-F2	0.996(6)	F6-F6	1.479(17)
P2-F10	1.574(6)	P2-F10	1.574
P2-F12	1.581(14)	P2-F12	1.5814
P2-F8	1.601(13)	P2-F8	1.6013
P2-F7	1.6022	P2-F7	1.602(6)
P2-F11	1.626(13)	P2-F11	1.6257
P2-F9	1.632(15)	P2-F9	1.6316
F7-F7	0.85(2)	F8-F12	0.731(6)
F9-F11	0.598(5)	F10-F10	0.84(2)
F10-F12	1.740(8)	F11-F9	0.598(5)
F12-F8	0.731(6)	F12-F10	1.740(10)

Table B.8: Bond angles (°) determined for $[(MDC^{Cy})Pd(CH_3CN)_2](PF_6)_2$

Bond	**Angle**	**Bond**	**Angle**
C2-Pd-C2	83.5(4)	C2-Pd-N3	95.6(3)
C2-Pd-N3	178.1(2)	C2-Pd-N3	178.1(2)
C2-Pd-N3	95.6(3)	N3-Pd-N3	85.3(3)
C2-N1-C3	109.6(7)	C2-N1-C1	121.1(6)
C3-N1-C1	129.1(7)	C2-N2-C4	109.3(6)
C2-N2-C10	125.8(5)	C4-N2-C10	124.8(6)
C11-N3-Pd	165.7(6)	N1-C1-N1	108.4(8)
N1-C1-H1A	110.0	N1-C1-H1A	110.0
N1-C1-H1B	110.0	N1-C1-H1B	110.0
H1A-C1-H1B	108.4	N2-C2-N1	106.2(6)
N2-C2-Pd	130.5(5)	N1-C2-Pd	123.2(5)
C4-C3-N1	107.4(7)	C4-C3-H3	126.3
N1-C3-H3	126.3	C3-C4-N2	107.5(7)
C3-C4-H4	126.3	N2-C4-H4	126.3
C10-C5-C6	109.0(7)	C10-C5-H5A	109.9
C6-C5-H5A	109.9	C10-C5-H5B	109.9
C6-C5-H5B	109.9	H5A-C5-H5B	108.3
C7-C6-C5	112.5(8)	C7-C6-H6A	109.1
C5-C6-H6A	109.1	C7-C6-H6B	109.1
C5-C6-H6B	109.1	H6A-C6-H6B	107.8

C6-C7-C8	109.8(8)	C6-C7-H7A	109.7
C8-C7-H7A	109.7	C6-C7-H7B	109.7
C8-C7-H7B	109.7	H7A-C7-H7B	108.2
C7-C8-C9	110.7(9)	C7-C8-H8A	109.5
C9-C8-H8A	109.5	C7-C8-H8B	109.5
C9-C8-H8B	109.5	H8A-C8-H8B	108.1
C10-C9-C8	109.7(7)	C10-C9-H9A	109.7
C8-C9-H9A	109.7	C10-C9-H9B	109.7
C8-C9-H9B	109.7	H9A-C9-H9B	108.2
N2-C10-C5	110.0(6)	N2-C10-C9	110.6(6)
C5-C10-C9	111.9(7)	N2-C10-H10	108.1
C5-C10-H10	108.1	C9-C10-H10	108.1
N3-C11-C12	178.9(9)	C11-C12-H12A	109.5
C11-C12-H12B	109.5	H12A-C12-H12B	109.5
C11-C12-H12C	109.5	H12A-C12-H12C	109.5
H12B-C12-H12C	109.5	F4-P1-F2	96.0
F4-P1-F2	96.0	F2-P1-F2	124.34(14)
F4-P1-F1	175.4(10)	F2-P1-F1	87.8(9)
F2-P1-F1	79.7(9)	F4-P1-F1	175.4
F2-P1-F1	79.7	F2-P1-F1	87.8
F1-P1-F1	9.1(11)	F4-P1-F3	91.9
F2-P1-F3	92.7(4)	F2-P1-F3	140.8(5)
F1-P1-F3	90.5(4)	F1-P1-F3	86.7
F4-P1-F3	91.9	F2-P1-F3	140.83(13)
F2-P1-F3	92.6	F1-P1-F3	86.7(4)
F1-P1-F3	90.5	F3-P1-F3	48.7(6)
F4-P1-F6	88.1	F2-P1-F6	90.4(4)
F2-P1-F6	36.2(5)	F1-P1-F6	89.4(5)
F1-P1-F6	93.5	F3-P1-F6	177.0
F3-P1-F6	128.3(5)	F4-P1-F6	88.0
F2-P1-F6	36.23(13)	F2-P1-F6	90.4
F1-P1-F6	93.5(5)	F1-P1-F6	89.4
F3-P1-F6	128.3(6)	F3-P1-F6	177.0
F6-P1-F6	54.7(5)	F4-P1-F5	88.1
F2-P1-F5	52.67(14)	F2-P1-F5	175.3
F1-P1-F5	96.2(10)	F1-P1-F5	88.0
F3-P1-F5	40.9(5)	F3-P1-F5	89.5
F6-P1-F5	142.1(5)	F6-P1-F5	87.5
F4-P1-F5	88.2	F2-P1-F5	175.3
F2-P1-F5	52.67(12)	F1-P1-F5	88.0(10)
F1-P1-F5	96.2	F3-P1-F5	89.5(4)
F3-P1-F5	40.88(11)	F6-P1-F5	87.5(4)
F6-P1-F5	142.13(11)	F5-P1-F5	130.01(12)

F1-F1-P1	85.4	F6-F2-F5	134.3(3)
F6-F2-P1	72.8(7)	F5-F2-P1	65.2(3)
F5-F3-F3	136.5(3)	F5-F3-P1	71.1(3)
F3-F3-P1	65.7	F3-F5-F2	128.4(3)
F3-F5-P1	68.1(6)	F2-F5-P1	62.1(3)
F2-F6-F6	132.2(4)	F2-F6-P1	70.9(4)
F6-F6-P1	62.6	F10-P2-F10	30.8(8)
F10-P2-F12	90.3(6)	F10-P2-F12	66.9
F10-P2-F12	66.9(6)	F10-P2-F12	90.3
F12-P2-F12	96.9(5)	F10-P2-F8	92.7(6)
F10-P2-F8	111.8	F12-P2-F8	91.0(3)
F12-P2-F8	26.5(3)	F10-P2-F8	111.8(5)
F10-P2-F8	92.7	F12-P2-F8	26.53(9)
F12-P2-F8	91.0	F8-P2-F8	75.2(6)
F10-P2-F7	149.2(8)	F10-P2-F7	179.7
F12-P2-F7	112.9	F12-P2-F7	89.5
F8-P2-F7	68.0	F8-P2-F7	87.1
F10-P2-F7	179.7	F10-P2-F7	149.2(8)
F12-P2-F7	89.5(6)	F12-P2-F7	112.9(6)
F8-P2-F7	87.1(6)	F8-P2-F7	68.0(5)
F7-P2-F7	30.8(8)	F10-P2-F11	91.5(6)
F10-P2-F11	71.99(6)	F12-P2-F11	88.8(2)
F12-P2-F11	157.6(3)	F8-P2-F11	175.8
F8-P2-F11	103.1(6)	F7-P2-F11	108.23(5)
F7-P2-F11	88.7(6)	F10-P2-F11	72.0(5)
F10-P2-F11	91.5	F12-P2-F11	157.62(11)
F12-P2-F11	88.8	F8-P2-F11	103.1(6)
F8-P2-F11	175.8	F7-P2-F11	88.7
F7-P2-F11	108.2(5)	F11-P2-F11	78.4(6)
F10-P2-F9	89.8(6)	F10-P2-F9	112.4
F12-P2-F9	177.7	F12-P2-F9	85.3(5)
F8-P2-F9	91.3(3)	F8-P2-F9	154.62(7)
F7-P2-F9	67.8	F7-P2-F9	90.3(6)
F11-P2-F9	88.9(2)	F11-P2-F9	21.17(8)
F10-P2-F9	112.4(6)	F10-P2-F9	89.8
F12-P2-F9	85.3(5)	F12-P2-F9	177.7
F8-P2-F9	154.6(3)	F8-P2-F9	91.3
F7-P2-F9	90.3	F7-P2-F9	67.8(6)
F11-P2-F9	21.2(3)	F11-P2-F9	88.9
F9-P2-F9	92.5(5)	F7-F7-P2	74.6
F12-F8-P2	75.2(11)	F11-F9-P2	78.9(14)
F10-F10-P2	74.6	F10-F10-F12	116.1(6)
P2-F10-F12	56.7(4)	F9-F11-P2	80.0(14)

F8-F12-P2	78.3(12)	F8-F12-F10	132.6(15)
P2-F12-F10	56.3(5)		

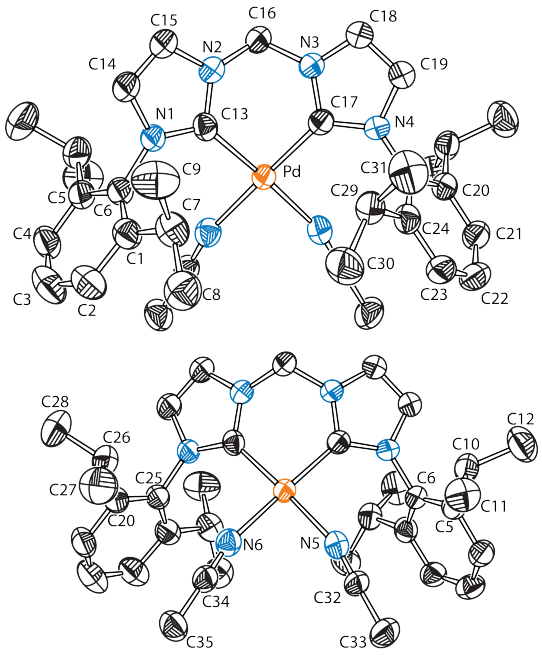

Figure B.5: Numbered crystal structure of [(MDC^{DIPP})Pd(CH$_3$CN)$_2$](PF$_6$)$_2$ with all hydrogen atoms omitted for clarity and thermal ellipsoids shown at 50% probability. Counterions and solvent molecules are also emitted for clarity.

Table B.9: Bond lengths (Å) determined for [(MDC^{DIPP})Pd(CH$_3$CN)$_2$](PF$_6$)$_2$

Bond	**Length**	**Bond**	**Length**
Pd-C13	1.972(5)	Pd-C17	1.990(5)
Pd-N6	2.039(5)	Pd-N5	2.053(5)
F1-P1	1.565(4)	F2-P1	1.598(4)
F3-P1	1.586(5)	F4-P1	1.581(4)
F5-P1	1.613(5)	F6-P1	1.587(5)
F7-P2	1.540(5)	F8-P2	1.524(5)
F9-P2	1.538(5)	F10-P2	1.542(6)
F11-P2	1.566(4)	F12-P2	1.576(4)
N1-C13	1.361(6)	N1-C14	1.398(6)

N1-C6	1.451(6)	N2-C13	1.358(6)
N2-C15	1.381(6)	N2-C16	1.461(6)
N3-C17	1.349(6)	N3-C18	1.384(7)
N3-C16	1.445(6)	N4-C17	1.347(6)
N4-C19	1.389(7)	N4-C25	1.458(6)
N5-C32	1.128(7)	N6-C34	1.137(7)
N7-C36	1.109(17)	C1-C6	1.390(7)
C1-C2	1.406(7)	C1-C7	1.514(7)
C2-C3	1.380(8)	C2-H2	0.95
C3-C4	1.380(7)	C3-H3	0.95
C4-C5	1.399(7)	C4-H4	0.95
C5-C6	1.409(7)	C5-C10	1.514(7)
C7-C8	1.530(8)	C7-C9	1.534(8)
C7-H7	1.0	C8-H8A	0.98
C8-H8B	0.98	C8-H8C	0.98
C9-H9A	0.98	C9-H9B	0.98
C9-H9C	0.98	C10-C12	1.525(7)
C10-C11	1.536(8)	C10-H10	1.0
C11-H11A	0.98	C11-H11B	0.98
C11-H11C	0.98	C12-H12A	0.98
C12-H12B	0.98	C12-H12C	0.98
C14-C15	1.362(7)	C14-H14	0.95
C15-H15	0.95	C16-H16A	0.99
C16-H16B	0.99	C18-C19	1.339(8)
C18-H18	0.95	C19-H19	0.95
C20-C21	1.399(7)	C20-C25	1.406(7)
C20-C26	1.489(9)	C21-C22	1.351(9)
C21-H21	0.95	C22-C23	1.384(9)
C22-H22	0.95	C23-C24	1.415(7)
C23-H23	0.95	C24-C25	1.386(8)
C24-C29	1.521(8)	C26-C28	1.532(8)
C26-C27	1.540(9)	C26-H26	1.0
C27-H27A	0.98	C27-H27B	0.98
C27-H27C	0.98	C28-H28A	0.98
C28-H28B	0.98	C28-H28C	0.98
C29-C31	1.531(8)	C29-C30	1.532(9)
C29-H29	1.0	C30-H30A	0.98
C30-H30B	0.98	C30-H30C	0.98
C31-H31A	0.98	C31-H31B	0.98
C31-H31C	0.98	C32-C33	1.449(8)
C33-H33A	0.98	C33-H33B	0.98
C33-H33C	0.98	C34-C35	1.456(7)
C35-H35A	0.98	C35-H35B	0.98

C35-H35C	0.98	C36-C37	1.409(16)
C37-H37A	0.98	C37-H37B	0.98
C37-H37C	0.98		

Table B.10: Bond angles (°) determined for $[(MDC^{DIPP})Pd(CH_3CN)_2](PF_6)_2$

Bond	**Angle**	**Bond**	**Angle**
C13-Pd-C17	88.0(2)	C13-Pd-N6	177.91(18)
C17-Pd-N6	93.70(19)	C13-Pd-N5	94.35(19)
C17-Pd-N5	177.12(18)	N6-Pd-N5	84.00(18)
C13-N1-C14	111.0(4)	C13-N1-C6	128.0(4)
C14-N1-C6	121.0(4)	C13-N2-C15	113.2(4)
C13-N2-C16	122.7(4)	C15-N2-C16	123.9(4)
C17-N3-C18	111.2(4)	C17-N3-C16	124.0(4)
C18-N3-C16	124.3(4)	C17-N4-C19	110.1(4)
C17-N4-C25	129.7(4)	C19-N4-C25	119.7(4)
C32-N5-Pd	164.0(4)	C34-N6-Pd	166.2(5)
F1-P1-F4	89.9(3)	F1-P1-F3	178.9(3)
F4-P1-F3	89.7(3)	F1-P1-F6	90.6(3)
F4-P1-F6	89.7(3)	F3-P1-F6	90.4(3)
F1-P1-F2	90.9(3)	F4-P1-F2	179.2(3)
F3-P1-F2	89.5(2)	F6-P1-F2	90.3(2)
F1-P1-F5	89.8(3)	F4-P1-F5	89.8(2)
F3-P1-F5	89.2(3)	F6-P1-F5	179.4(3)
F2-P1-F5	90.1(2)	F8-P2-F9	93.3(5)
F8-P2-F7	88.7(5)	F9-P2-F7	177.9(5)
F8-P2-F10	179.0(4)	F9-P2-F10	86.6(4)
F7-P2-F10	91.4(4)	F8-P2-F11	90.5(4)
F9-P2-F11	87.7(3)	F7-P2-F11	91.8(3)
F10-P2-F11	90.5(4)	F8-P2-F12	89.2(3)
F9-P2-F12	92.1(3)	F7-P2-F12	88.4(3)
F10-P2-F12	89.9(3)	F11-P2-F12	179.6(4)
C6-C1-C2	116.1(5)	C6-C1-C7	122.2(5)
C2-C1-C7	121.6(5)	C3-C2-C1	121.5(5)
C3-C2-H2	119.2	C1-C2-H2	119.2
C4-C3-C2	120.2(5)	C4-C3-H3	119.9
C2-C3-H3	119.9	C3-C4-C5	121.7(5)
C3-C4-H4	119.2	C5-C4-H4	119.2
C4-C5-C6	115.9(5)	C4-C5-C10	120.3(5)
C6-C5-C10	123.8(5)	C1-C6-C5	124.6(5)

C1-C6-N1	118.3(4)	C5-C6-N1	117.2(4)
C1-C7-C8	113.1(5)	C1-C7-C9	109.6(5)
C8-C7-C9	110.0(5)	C1-C7-H7	108.0
C8-C7-H7	108.0	C9-C7-H7	108.0
C7-C8-H8A	109.5	C7-C8-H8B	109.5
H8A-C8-H8B	109.5	C7-C8-H8C	109.5
H8A-C8-H8C	109.5	H8B-C8-H8C	109.5
C7-C9-H9A	109.5	C7-C9-H9B	109.5
H9A-C9-H9B	109.5	C7-C9-H9C	109.5
H9A-C9-H9C	109.5	H9B-C9-H9C	109.5
C5-C10-C12	110.3(5)	C5-C10-C11	112.1(5)
C12-C10-C11	110.3(5)	C5-C10-H10	108.0
C12-C10-H10	108.0	C11-C10-H10	108.0
C10-C11-H11A	109.5	C10-C11-H11B	109.5
H11A-C11-H11B	109.5	C10-C11-H11C	109.5
H11A-C11-H11C	109.5	H11B-C11-H11C	109.5
C10-C12-H12A	109.5	C10-C12-H12B	109.5
H12A-C12-H12B	109.5	C10-C12-H12C	109.5
H12A-C12-H12C	109.5	H12B-C12-H12C	109.5
N2-C13-N1	103.5(4)	N2-C13-Pd	124.6(3)
N1-C13-Pd	131.9(4)	C15-C14-N1	107.1(4)
C15-C14-H14	126.5	N1-C14-H14	126.5
C14-C15-N2	105.2(4)	C14-C15-H15	127.4
N2-C15-H15	127.4	N3-C16-N2	108.8(4)
N3-C16-H16A	109.9	N2-C16-H16A	109.9
N3-C16-H16B	109.9	N2-C16-H16B	109.9
H16A-C16-H16B	108.3	N4-C17-N3	105.1(4)
N4-C17-Pd	131.5(4)	N3-C17-Pd	123.4(4)
C19-C18-N3	106.0(5)	C19-C18-H18	127.0
N3-C18-H18	127.0	C18-C19-N4	107.6(5)
C18-C19-H19	126.2	N4-C19-H19	126.2
C21-C20-C25	115.3(6)	C21-C20-C26	120.5(5)
C25-C20-C26	124.3(5)	C22-C21-C20	122.9(6)
C22-C21-H21	118.6	C20-C21-H21	118.6
C21-C22-C23	120.1(6)	C21-C22-H22	120.0
C23-C22-H22	120.0	C22-C23-C24	121.3(6)
C22-C23-H23	119.3	C24-C23-H23	119.3
C25-C24-C23	115.6(6)	C25-C24-C29	123.8(5)
C23-C24-C29	120.6(6)	C24-C25-C20	124.8(5)
C24-C25-N4	119.6(5)	C20-C25-N4	115.5(5)
C20-C26-C28	110.1(6)	C20-C26-C27	112.6(5)
C28-C26-C27	110.8(6)	C20-C26-H26	107.7
C28-C26-H26	107.7	C27-C26-H26	107.7

C26-C27-H27A	109.5	C26-C27-H27B	109.5
H27A-C27-H27B	109.5	C26-C27-H27C	109.5
H27A-C27-H27C	109.5	H27B-C27-H27C	109.5
C26-C28-H28A	109.5	C26-C28-H28B	109.5
H28A-C28-H28B	109.5	C26-C28-H28C	109.5
H28A-C28-H28C	109.5	H28B-C28-H28C	109.5
C24-C29-C31	112.4(5)	C24-C29-C30	113.6(5)
C31-C29-C30	108.5(5)	C24-C29-H29	107.4
C31-C29-H29	107.4	C30-C29-H29	107.4
C29-C30-H30A	109.5	C29-C30-H30B	109.5
H30A-C30-H30B	109.5	C29-C30-H30C	109.5
H30A-C30-H30C	109.5	H30B-C30-H30C	109.5
C29-C31-H31A	109.5	C29-C31-H31B	109.5
H31A-C31-H31B	109.5	C29-C31-H31C	109.5
H31A-C31-H31C	109.5	H31B-C31-H31C	109.5
N5-C32-C33	177.9(6)	C32-C33-H33A	109.5
C32-C33-H33B	109.5	H33A-C33-H33B	109.5
C32-C33-H33C	109.5	H33A-C33-H33C	109.5
H33B-C33-H33C	109.5	N6-C34-C35	178.8(6)
C34-C35-H35A	109.5	C34-C35-H35B	109.5
H35A-C35-H35B	109.5	C34-C35-H35C	109.5
H35A-C35-H35C	109.5	H35B-C35-H35C	109.5
N7-C36-C37	179.(2)	C36-C37-H37A	109.5
C36-C37-H37B	109.5	H37A-C37-H37B	109.5
C36-C37-H37C	109.5	H37A-C37-H37C	109.5
H37B-C37-H37C	109.5		

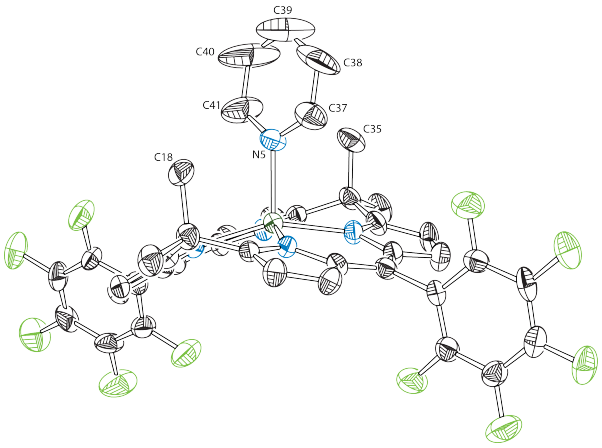

Figure B.6: Partially numbered crystal structure of Zn(C4P^{PF}) with all hydrogen atoms omitted for clarity and thermal ellipsoids shown at 50% probability.

Table B.11: Bond lengths (Å) determined for Zn(C4P^{PF})

Bond	Length	Bond	Length
Zn-N4	2.079(5)	Zn-N2	2.083(5)
Zn-N3	2.083(5)	Zn-N1	2.090(5)
Zn-N5	2.098(5)	F1-C6	1.339(7)
F2-C7	1.340(8)	F3-C8	1.335(7)
F4-C9	1.340(7)	F5-C10	1.346(7)
F6-C24	1.338(7)	F7-C25	1.363(8)
F8-C26	1.350(8)	F9-C27	1.357(8)
F10-C28	1.362(8)	N1-C1	1.339(8)
N1-C4	1.399(8)	N2-C15	1.345(7)
N2-C12	1.391(7)	N3-C19	1.359(8)
N3-C22	1.391(7)	N4-C33	1.356(8)
N4-C30	1.403(7)	N5-C41	1.322(9)
N5-C37	1.348(9)	C1-C2	1.410(9)
C1-C34	1.519(9)	C2-C3	1.358(9)
C3-C4	1.409(9)	C4-C5	1.382(8)
C5-C12	1.419(9)	C5-C11	1.504(8)
C6-C7	1.362(9)	C6-C11	1.389(9)
C7-C8	1.361(9)	C8-C9	1.372(10)
C9-C10	1.386(9)	C10-C11	1.374(8)
C12-C13	1.414(8)	C13-C14	1.340(8)
C14-C15	1.420(9)	C15-C16	1.522(8)
C16-C19	1.510(9)	C16-C18	1.542(9)

C16-C17	1.544(9)	C19-C20	1.402(8)
C20-C21	1.376(9)	C21-C22	1.423(8)
C22-C23	1.399(9)	C23-C30	1.396(8)
C23-C29	1.497(8)	C24-C25	1.359(9)
C24-C29	1.395(9)	C25-C26	1.353(10)
C26-C27	1.344(10)	C27-C28	1.376(9)
C28-C29	1.381(9)	C30-C31	1.411(9)
C31-C32	1.366(9)	C32-C33	1.407(9)
C33-C34	1.520(9)	C34-C35	1.554(9)
C34-C36	1.555(9)	C37-C38	1.397(12)
C38-C39	1.349(16)	C39-C40	1.358(17)
C40-C41	1.390(13)		

Table B.12: Bond angles (°) determined for Zn(C4P^{PF})

Bond	**Angle**	**Bond**	**Angle**
N4-Zn-N2	158.80(19)	N4-Zn-N3	89.22(19)
N2-Zn-N3	86.83(19)	N4-Zn-N1	85.5(2)
N2-Zn-N1	89.67(19)	N3-Zn-N1	156.06(19)
N4-Zn-N5	100.4(2)	N2-Zn-N5	100.7(2)
N3-Zn-N5	106.2(2)	N1-Zn-N5	97.7(2)
C1-N1-C4	105.9(5)	C1-N1-Zn	127.7(4)
C4-N1-Zn	126.2(4)	C15-N2-C12	105.8(5)
C15-N2-Zn	127.7(4)	C12-N2-Zn	126.5(4)
C19-N3-C22	106.5(5)	C19-N3-Zn	126.3(4)
C22-N3-Zn	125.7(4)	C33-N4-C30	105.4(5)
C33-N4-Zn	127.3(4)	C30-N4-Zn	127.0(4)
C41-N5-C37	118.3(7)	C41-N5-Zn	123.0(6)
C37-N5-Zn	118.3(5)	N1-C1-C2	111.3(6)
N1-C1-C34	123.9(6)	C2-C1-C34	124.7(6)
C3-C2-C1	106.5(6)	C2-C3-C4	107.7(6)
C5-C4-N1	124.5(6)	C5-C4-C3	126.8(6)
N1-C4-C3	108.6(5)	C4-C5-C12	128.5(6)
C4-C5-C11	115.7(6)	C12-C5-C11	115.8(5)
F1-C6-C7	118.7(6)	F1-C6-C11	118.9(6)
C7-C6-C11	122.4(6)	F2-C7-C8	118.9(6)
F2-C7-C6	120.7(7)	C8-C7-C6	120.4(7)
F3-C8-C7	121.3(7)	F3-C8-C9	119.2(6)
C7-C8-C9	119.4(6)	F4-C9-C8	120.2(6)
F4-C9-C10	120.4(7)	C8-C9-C10	119.3(6)

F5-C10-C11	118.6(6)	F5-C10-C9	118.9(6)
C11-C10-C9	122.5(6)	C10-C11-C6	115.8(6)
C10-C11-C5	122.9(6)	C6-C11-C5	121.1(5)
N2-C12-C13	109.0(5)	N2-C12-C5	124.2(5)
C13-C12-C5	126.7(6)	C14-C13-C12	107.6(6)
C13-C14-C15	106.9(6)	N2-C15-C14	110.6(5)
N2-C15-C16	122.4(5)	C14-C15-C16	127.0(6)
C19-C16-C15	112.1(5)	C19-C16-C18	108.2(5)
C15-C16-C18	109.2(5)	C19-C16-C17	109.9(5)
C15-C16-C17	109.6(5)	C18-C16-C17	107.7(5)
N3-C19-C20	110.5(6)	N3-C19-C16	122.1(5)
C20-C19-C16	127.3(6)	C21-C20-C19	107.5(6)
C20-C21-C22	106.5(6)	N3-C22-C23	125.0(6)
N3-C22-C21	109.0(5)	C23-C22-C21	126.0(6)
C30-C23-C22	127.7(6)	C30-C23-C29	115.7(6)
C22-C23-C29	116.7(6)	F6-C24-C25	119.0(6)
F6-C24-C29	119.0(6)	C25-C24-C29	122.1(7)
C26-C25-C24	120.6(7)	C26-C25-F7	120.2(6)
C24-C25-F7	119.2(7)	C27-C26-F8	119.9(8)
C27-C26-C25	119.8(6)	F8-C26-C25	120.3(7)
C26-C27-F9	119.7(7)	C26-C27-C28	120.0(7)
F9-C27-C28	120.3(7)	F10-C28-C27	118.6(7)
F10-C28-C29	119.0(6)	C27-C28-C29	122.4(7)
C28-C29-C24	115.1(6)	C28-C29-C23	122.0(6)
C24-C29-C23	122.8(6)	C23-C30-N4	123.7(6)
C23-C30-C31	127.0(6)	N4-C30-C31	109.3(6)
C32-C31-C30	107.1(6)	C31-C32-C33	107.2(6)
N4-C33-C32	111.0(6)	N4-C33-C34	123.9(6)
C32-C33-C34	125.1(6)	C1-C34-C33	113.8(5)
C1-C34-C35	108.1(6)	C33-C34-C35	109.8(6)
C1-C34-C36	110.3(6)	C33-C34-C36	108.4(6)
C35-C34-C36	106.1(5)	N5-C37-C38	121.2(9)
C39-C38-C37	120.7(11)	C38-C39-C40	117.0(11)
C39-C40-C41	121.5(11)	N5-C41-C40	121.1(10)

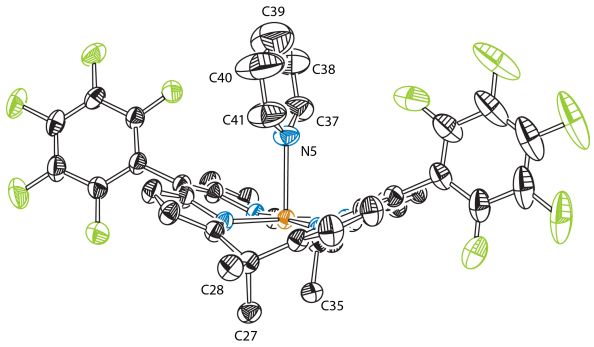

Figure B.7: Partially numbered crystal structure of Cu(C4P^{PF}) with all hydrogen atoms omitted for clarity and thermal ellipsoids shown at 50% probability.

Table B.13: Bond lengths (Å) determined for Cu(C4P^{PF})

Bond	Length	Bond	Length
Cu1-N2	1.978(2)	Cu1-N4	1.980(2)
Cu1-N3	1.979(2)	Cu1-N1	1.986(2)
Cu1-N5	2.3992(18)	Cu2-N9	1.973(2)
Cu2-N8	1.977(2)	Cu2-N10	1.984(2)
Cu2-N7	1.984(2)	Cu2-N11	2.3805(17)
N1-C1	1.342(3)	N1-C4	1.393(3)
N2-C9	1.346(3)	N2-C6	1.389(3)
N3-C11	1.343(3)	N3-C14	1.402(3)
N4-C19	1.336(3)	N4-C16	1.397(3)
N7-C42	1.344(3)	N7-C45	1.393(3)
N8-C50	1.338(3)	N8-C47	1.394(3)
N9-C52	1.340(3)	N9-C55	1.396(3)
N10-C60	1.342(3)	N10-C57	1.390(3)
C1-C2	1.424(4)	C1-C20	1.510(4)
C2-C3	1.357(5)	C3-C4	1.431(4)
C4-C5	1.379(4)	C5-C6	1.381(4)
C5-C26	1.506(4)	C6-C7	1.428(4)
C7-C8	1.361(5)	C8-C9	1.412(4)
C9-C10	1.514(4)	C10-C11	1.507(4)
C10-C28	1.526(4)	C10-C27	1.543(4)
C11-C12	1.409(4)	C12-C13	1.363(4)
C13-C14	1.410(4)	C14-C15	1.392(4)
C15-C16	1.391(4)	C15-C34	1.496(4)
C16-C17	1.414(4)	C17-C18	1.376(4)
C18-C19	1.416(4)	C19-C20	1.511(4)

C20-C36	1.529(4)	C20-C35	1.542(4)
C21-F1	1.334(5)	C21-C22	1.373(5)
C21-C26	1.387(5)	C22-F2	1.344(6)
C22-C23	1.375(8)	C23-F3	1.341(5)
C23-C24	1.370(9)	C24-F4	1.330(6)
C24-C25	1.381(6)	C25-F5	1.338(6)
C25-C26	1.375(5)	C29-F6	1.337(4)
C29-C34	1.375(4)	C29-C30	1.387(4)
C30-F7	1.335(4)	C30-C31	1.378(5)
C31-F8	1.339(3)	C31-C32	1.371(4)
C32-F9	1.345(3)	C32-C33	1.379(4)
C33-F10	1.339(3)	C33-C34	1.382(4)
N5-C37	1.39	N5-C41	1.39
C37-C38	1.39	C38-C39	1.39
C39-C40	1.39	C40-C41	1.39
C42-C43	1.420(4)	C42-C61	1.508(4)
C43-C44	1.370(4)	C44-C45	1.425(4)
C45-C46	1.384(4)	C46-C47	1.393(4)
C46-C67	1.500(4)	C47-C48	1.416(4)
C48-C49	1.381(5)	C49-C50	1.412(4)
C50-C51	1.513(4)	C51-C52	1.511(4)
C51-C69	1.539(4)	C51-C68	1.548(4)
C52-C53	1.413(4)	C53-C54	1.370(4)
C54-C55	1.413(4)	C55-C56	1.388(4)
C56-C57	1.389(4)	C56-C75	1.505(3)
C57-C58	1.420(4)	C58-C59	1.373(4)
C59-C60	1.421(4)	C60-C61	1.503(4)
C61-C77	1.529(4)	C61-C76	1.546(4)
C62-F11	1.329(5)	C62-C67	1.386(5)
C62-C63	1.402(5)	C63-F12	1.337(6)
C63-C64	1.346(8)	C64-F13	1.334(5)
C64-C65	1.375(8)	C65-F14	1.348(6)
C65-C66	1.382(5)	C66-F15	1.344(5)
C66-C67	1.370(5)	C70-F16	1.340(3)
C70-C71	1.379(4)	C70-C75	1.390(4)
C71-F17	1.335(3)	C71-C72	1.366(5)
C72-F18	1.353(3)	C72-C73	1.368(5)
C73-F19	1.337(4)	C73-C74	1.379(4)
C74-F20	1.343(3)	C74-C75	1.373(4)
N11-C78	1.39	N11-C82	1.39
C78-C79	1.39	C79-C80	1.39
C80-C81	1.39	C81-C82	1.39

Table B.14: Bond angles (°) determined for Cu(C4P^{PF})

Bond	Angle	Bond	Angle
N2-Cu1-N4	177.40(10)	N2-Cu1-N3	90.28(9)
N4-Cu1-N3	89.98(9)	N2-Cu1-N1	89.66(9)
N4-Cu1-N1	89.99(9)	N3-Cu1-N1	177.96(9)
N2-Cu1-N5	91.54(9)	N4-Cu1-N5	91.04(9)
N3-Cu1-N5	90.08(9)	N1-Cu1-N5	91.97(8)
N9-Cu2-N8	90.06(9)	N9-Cu2-N10	89.80(9)
N8-Cu2-N10	177.21(10)	N9-Cu2-N7	177.75(9)
N8-Cu2-N7	90.05(9)	N10-Cu2-N7	89.99(9)
N9-Cu2-N11	90.60(8)	N8-Cu2-N11	91.46(9)
N10-Cu2-N11	91.33(8)	N7-Cu2-N11	91.64(8)
C1-N1-C4	107.2(2)	C1-N1-Cu1	126.88(18)
C4-N1-Cu1	123.13(18)	C9-N2-C6	107.5(2)
C9-N2-Cu1	127.50(19)	C6-N2-Cu1	123.17(17)
C11-N3-C14	106.6(2)	C11-N3-Cu1	126.92(18)
C14-N3-Cu1	122.58(17)	C19-N4-C16	106.9(2)
C19-N4-Cu1	127.14(18)	C16-N4-Cu1	123.69(18)
C42-N7-C45	107.0(2)	C42-N7-Cu2	127.45(18)
C45-N7-Cu2	122.72(18)	C50-N8-C47	107.1(2)
C50-N8-Cu2	127.76(19)	C47-N8-Cu2	122.96(18)
C52-N9-C55	106.5(2)	C52-N9-Cu2	128.06(18)
C55-N9-Cu2	123.15(17)	C60-N10-C57	107.0(2)
C60-N10-Cu2	126.41(18)	C57-N10-Cu2	123.00(18)
N1-C1-C2	110.2(3)	N1-C1-C20	120.7(2)
C2-C1-C20	129.0(3)	C3-C2-C1	107.0(3)
C2-C3-C4	107.4(3)	C5-C4-N1	122.7(2)
C5-C4-C3	129.0(3)	N1-C4-C3	108.1(2)
C4-C5-C6	126.8(3)	C4-C5-C26	116.6(3)
C6-C5-C26	116.6(3)	C5-C6-N2	123.9(3)
C5-C6-C7	128.1(3)	N2-C6-C7	107.9(3)
C8-C7-C6	107.2(3)	C7-C8-C9	107.4(3)
N2-C9-C8	110.0(3)	N2-C9-C10	121.5(2)
C8-C9-C10	128.5(3)	C11-C10-C9	109.5(2)
C11-C10-C28	110.6(2)	C9-C10-C28	110.5(2)
C11-C10-C27	108.0(2)	C9-C10-C27	109.5(2)
C28-C10-C27	108.7(2)	N3-C11-C12	110.4(2)
N3-C11-C10	120.4(2)	C12-C11-C10	129.0(2)
C13-C12-C11	107.2(2)	C12-C13-C14	107.4(2)
C15-C14-N3	123.2(2)	C15-C14-C13	128.3(2)
N3-C14-C13	108.4(2)	C14-C15-C16	126.8(2)
C14-C15-C34	115.9(2)	C16-C15-C34	117.2(2)

C15-C16-N4	122.8(2)	C15-C16-C17	128.4(3)
N4-C16-C17	108.7(2)	C18-C17-C16	107.0(3)
C17-C18-C19	106.6(3)	N4-C19-C18	110.8(2)
N4-C19-C20	121.1(2)	C18-C19-C20	128.0(2)
C1-C20-C19	108.7(2)	C1-C20-C36	111.2(2)
C19-C20-C36	110.5(2)	C1-C20-C35	108.6(2)
C19-C20-C35	109.2(2)	C36-C20-C35	108.7(2)
F1-C21-C22	118.5(4)	F1-C21-C26	119.6(3)
C22-C21-C26	121.9(5)	F2-C22-C21	120.0(5)
F2-C22-C23	120.6(4)	C21-C22-C23	119.4(5)
F3-C23-C24	119.9(6)	F3-C23-C22	119.6(6)
C24-C23-C22	120.5(4)	F4-C24-C23	121.2(5)
F4-C24-C25	119.8(6)	C23-C24-C25	119.0(5)
F5-C25-C26	119.5(4)	F5-C25-C24	118.2(5)
C26-C25-C24	122.3(5)	C25-C26-C21	117.0(4)
C25-C26-C5	121.6(3)	C21-C26-C5	121.4(3)
F6-C29-C34	120.5(3)	F6-C29-C30	116.9(3)
C34-C29-C30	122.6(3)	F7-C30-C31	120.3(3)
F7-C30-C29	120.7(3)	C31-C30-C29	119.0(3)
F8-C31-C32	119.8(3)	F8-C31-C30	120.3(3)
C32-C31-C30	119.8(3)	F9-C32-C31	119.6(3)
F9-C32-C33	120.5(3)	C31-C32-C33	119.9(3)
F10-C33-C32	117.9(3)	F10-C33-C34	120.1(2)
C32-C33-C34	122.0(3)	C29-C34-C33	116.7(2)
C29-C34-C15	121.6(3)	C33-C34-C15	121.7(3)
C37-N5-C41	120.0	C37-N5-Cu1	120.51(13)
C41-N5-Cu1	118.63(13)	N5-C37-C38	120.0
C39-C38-C37	120.0	C38-C39-C40	120.0
C41-C40-C39	120.0	C40-C41-N5	120.0
N7-C42-C43	110.4(2)	N7-C42-C61	120.3(2)
C43-C42-C61	129.3(2)	C44-C43-C42	107.0(3)
C43-C44-C45	106.9(3)	C46-C45-N7	123.0(2)
C46-C45-C44	128.1(3)	N7-C45-C44	108.7(2)
C45-C46-C47	126.5(3)	C45-C46-C67	116.9(3)
C47-C46-C67	116.6(3)	C46-C47-N8	123.6(2)
C46-C47-C48	127.8(3)	N8-C47-C48	108.5(3)
C49-C48-C47	107.1(3)	C48-C49-C50	106.5(3)
N8-C50-C49	110.7(3)	N8-C50-C51	122.0(2)
C49-C50-C51	127.3(3)	C52-C51-C50	110.6(2)
C52-C51-C69	109.8(2)	C50-C51-C69	109.8(2)
C52-C51-C68	107.8(2)	C50-C51-C68	109.8(2)
C69-C51-C68	109.0(2)	N9-C52-C53	110.9(2)
N9-C52-C51	121.2(2)	C53-C52-C51	127.7(2)

C54-C53-C52	106.6(2)	C53-C54-C55	107.3(2)
C56-C55-N9	123.7(2)	C56-C55-C54	127.5(2)
N9-C55-C54	108.7(2)	C55-C56-C57	126.6(2)
C55-C56-C75	115.7(2)	C57-C56-C75	117.6(2)
C56-C57-N10	122.4(2)	C56-C57-C58	128.5(3)
N10-C57-C58	108.9(2)	C59-C58-C57	106.9(2)
C58-C59-C60	106.7(2)	N10-C60-C59	110.5(2)
N10-C60-C61	121.2(2)	C59-C60-C61	128.3(2)
C60-C61-C42	108.7(2)	C60-C61-C77	110.6(2)
C42-C61-C77	110.8(2)	C60-C61-C76	109.9(2)
C42-C61-C76	108.4(2)	C77-C61-C76	108.5(2)
F11-C62-C67	119.9(3)	F11-C62-C63	118.7(4)
C67-C62-C63	121.3(4)	F12-C63-C64	121.1(4)
F12-C63-C62	118.8(5)	C64-C63-C62	120.1(5)
F13-C64-C63	120.3(6)	F13-C64-C65	119.9(6)
C63-C64-C65	119.8(4)	F14-C65-C64	120.7(4)
F14-C65-C66	119.5(5)	C64-C65-C66	119.8(5)
F15-C66-C67	119.4(3)	F15-C66-C65	118.4(4)
C67-C66-C65	122.3(4)	C66-C67-C62	116.7(3)
C66-C67-C46	121.8(3)	C62-C67-C46	121.5(3)
F16-C70-C71	118.5(3)	F16-C70-C75	119.4(2)
C71-C70-C75	122.1(3)	F17-C71-C72	120.5(3)
F17-C71-C70	120.4(3)	C72-C71-C70	119.2(3)
F18-C72-C71	120.0(3)	F18-C72-C73	119.5(3)
C71-C72-C73	120.5(3)	F19-C73-C72	119.8(3)
F19-C73-C74	120.7(3)	C72-C73-C74	119.5(3)
F20-C74-C75	119.9(3)	F20-C74-C73	118.0(3)
C75-C74-C73	122.1(3)	C74-C75-C70	116.7(3)
C74-C75-C56	121.8(2)	C70-C75-C56	121.5(2)
C78-N11-C82	120.0	C78-N11-Cu2	118.73(12)
C82-N11-Cu2	121.27(12)	C79-C78-N11	120.0
C78-C79-C80	120.0	C81-C80-C79	120.0
C80-C81-C82	120.0	C81-C82-N11	120.0

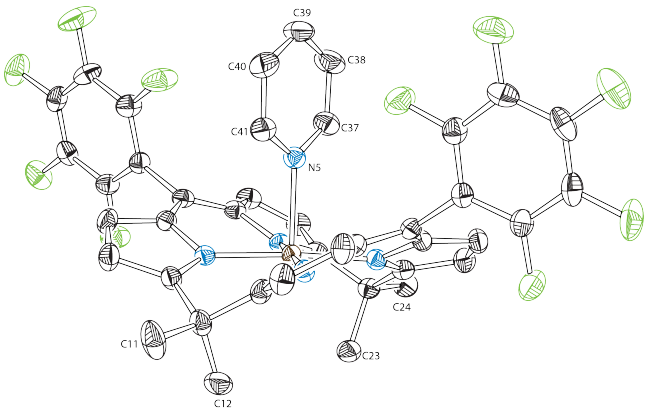

Figure B.8: Partially numbered crystal structure of Co(C4P^{PF}) with all hydrogen atoms omitted for clarity and thermal ellipsoids shown at 50% probability.

Table B.15: Bond lengths (Å) determined for Co(C4P^{PF})

Bond	Length	Bond	Length
Co-N4	1.9239(19)	Co-N2	1.9249(19)
Co-N3	1.9273(19)	Co-N1	1.9334(19)
Co-N5	2.155(2)	F1-C25	1.340(3)
F2-C26	1.345(3)	F3-C27	1.343(3)
F4-C28	1.341(3)	F5-C29	1.342(3)
F6-C31	1.341(3)	F7-C32	1.338(3)
F8-C33	1.334(3)	F9-C34	1.349(3)
F10-C35	1.341(3)	N1-C1	1.343(3)
N1-C4	1.398(3)	N2-C9	1.338(3)
N2-C6	1.398(3)	N3-C13	1.338(3)
N3-C16	1.397(3)	N4-C21	1.343(3)
N4-C18	1.400(3)	N5-C37	1.334(3)
N5-C41	1.336(3)	C1-C2	1.418(3)
C1-C22	1.504(3)	C2-C3	1.372(3)
C2-H2	0.95	C3-C4	1.411(3)
C3-H3	0.95	C4-C5	1.399(3)
C5-C6	1.387(3)	C5-C30	1.496(3)
C6-C7	1.423(3)	C7-C8	1.360(3)
C7-H7	0.95	C8-C9	1.422(3)
C8-H8	0.95	C9-C10	1.510(3)
C10-C13	1.510(3)	C10-C11	1.528(4)
C10-C12	1.549(4)	C11-H11A	0.98
C11-H11B	0.98	C11-H11C	0.98

C12-H12A	0.98	C12-H12B	0.98
C12-H12C	0.98	C13-C14	1.420(3)
C14-C15	1.372(3)	C14-H14	0.95
C15-C16	1.415(3)	C15-H15	0.95
C16-C17	1.389(3)	C17-C18	1.393(3)
C17-C36	1.495(3)	C18-C19	1.422(3)
C19-C20	1.368(4)	C19-H19	0.95
C20-C21	1.415(3)	C20-H20	0.95
C21-C22	1.513(3)	C22-C24	1.529(3)
C22-C23	1.548(3)	C23-H23A	0.98
C23-H23B	0.98	C23-H23C	0.98
C24-H24A	0.98	C24-H24B	0.98
C24-H24C	0.98	C25-C26	1.377(3)
C25-C30	1.386(3)	C26-C27	1.369(4)
C27-C28	1.368(4)	C28-C29	1.376(3)
C29-C30	1.382(3)	C31-C36	1.381(3)
C31-C32	1.381(4)	C32-C33	1.376(4)
C33-C34	1.369(4)	C34-C35	1.375(3)
C35-C36	1.385(3)	C37-C38	1.382(4)
C37-H37	0.95	C38-C39	1.371(4)
C38-H38	0.95	C39-C40	1.376(4)
C39-H39	0.95	C40-C41	1.383(4)
C40-H40	0.95	C41-H41	0.95

Table B.16: Bond angles (°) determined for Co(C4P^{PF})

Bond	**Angle**	**Bond**	**Angle**
N4-Co-N2	176.10(8)	N4-Co-N3	89.43(8)
N2-Co-N3	89.96(8)	N4-Co-N1	90.37(8)
N2-Co-N1	90.08(8)	N3-Co-N1	177.69(8)
N4-Co-N5	92.73(8)	N2-Co-N5	91.14(8)
N3-Co-N5	91.38(8)	N1-Co-N5	90.93(8)
C1-N1-C4	107.21(19)	C1-N1-Co	127.42(16)
C4-N1-Co	123.47(15)	C9-N2-C6	106.78(19)
C9-N2-Co	128.04(16)	C6-N2-Co	123.79(16)
C13-N3-C16	106.93(19)	C13-N3-Co	127.59(16)
C16-N3-Co	122.89(16)	C21-N4-C18	106.65(19)
C21-N4-Co	128.19(16)	C18-N4-Co	124.15(16)
C37-N5-C41	117.6(2)	C37-N5-Co	121.34(17)
C41-N5-Co	121.04(17)	N1-C1-C2	109.8(2)

N1-C1-C22	120.7(2)	C2-C1-C22	129.4(2)
C3-C2-C1	107.3(2)	C3-C2-H2	126.3
C1-C2-H2	126.3	C2-C3-C4	107.0(2)
C2-C3-H3	126.5	C4-C3-H3	126.5
N1-C4-C5	122.1(2)	N1-C4-C3	108.6(2)
C5-C4-C3	128.9(2)	C6-C5-C4	125.4(2)
C6-C5-C30	116.4(2)	C4-C5-C30	118.1(2)
C5-C6-N2	122.7(2)	C5-C6-C7	128.4(2)
N2-C6-C7	108.5(2)	C8-C7-C6	107.2(2)
C8-C7-H7	126.4	C6-C7-H7	126.4
C7-C8-C9	107.0(2)	C7-C8-H8	126.5
C9-C8-H8	126.5	N2-C9-C8	110.6(2)
N2-C9-C10	120.5(2)	C8-C9-C10	128.9(2)
C13-C10-C9	108.0(2)	C13-C10-C11	111.1(2)
C9-C10-C11	111.3(2)	C13-C10-C12	109.1(2)
C9-C10-C12	108.1(2)	C11-C10-C12	109.2(2)
C10-C11-H11A	109.5	C10-C11-H11B	109.5
H11A-C11-H11B	109.5	C10-C11-H11C	109.5
H11A-C11-H11C	109.5	H11B-C11-H11C	109.5
C10-C12-H12A	109.5	C10-C12-H12B	109.5
H12A-C12-H12B	109.5	C10-C12-H12C	109.5
H12A-C12-H12C	109.5	H12B-C12-H12C	109.5
N3-C13-C14	110.5(2)	N3-C13-C10	120.3(2)
C14-C13-C10	129.2(2)	C15-C14-C13	106.8(2)
C15-C14-H14	126.6	C13-C14-H14	126.6
C14-C15-C16	107.1(2)	C14-C15-H15	126.5
C16-C15-H15	126.5	C17-C16-N3	122.0(2)
C17-C16-C15	128.8(2)	N3-C16-C15	108.7(2)
C16-C17-C18	124.9(2)	C16-C17-C36	117.2(2)
C18-C17-C36	117.9(2)	C17-C18-N4	122.3(2)
C17-C18-C19	129.1(2)	N4-C18-C19	108.4(2)
C20-C19-C18	107.2(2)	C20-C19-H19	126.4
C18-C19-H19	126.4	C19-C20-C21	106.9(2)
C19-C20-H20	126.6	C21-C20-H20	126.6
N4-C21-C20	110.8(2)	N4-C21-C22	121.0(2)
C20-C21-C22	128.2(2)	C1-C22-C21	109.87(19)
C1-C22-C24	110.4(2)	C21-C22-C24	110.5(2)
C1-C22-C23	108.3(2)	C21-C22-C23	108.5(2)
C24-C22-C23	109.2(2)	C22-C23-H23A	109.5
C22-C23-H23B	109.5	H23A-C23-H23B	109.5
C22-C23-H23C	109.5	H23A-C23-H23C	109.5
H23B-C23-H23C	109.5	C22-C24-H24A	109.5
C22-C24-H24B	109.5	H24A-C24-H24B	109.5

C22-C24-H24C	109.5	H24A-C24-H24C	109.5
H24B-C24-H24C	109.5	F1-C25-C26	118.3(2)
F1-C25-C30	119.7(2)	C26-C25-C30	121.9(2)
F2-C26-C27	119.6(2)	F2-C26-C25	120.5(2)
C27-C26-C25	119.9(2)	F3-C27-C28	120.2(3)
F3-C27-C26	119.9(2)	C28-C27-C26	119.8(2)
F4-C28-C27	119.8(2)	F4-C28-C29	120.5(3)
C27-C28-C29	119.6(2)	F5-C29-C28	118.1(2)
F5-C29-C30	119.5(2)	C28-C29-C30	122.4(2)
C29-C30-C25	116.4(2)	C29-C30-C5	120.6(2)
C25-C30-C5	122.9(2)	F6-C31-C36	119.8(2)
F6-C31-C32	117.4(2)	C36-C31-C32	122.8(2)
F7-C32-C33	120.0(2)	F7-C32-C31	120.6(3)
C33-C32-C31	119.4(3)	F8-C33-C34	120.4(3)
F8-C33-C32	120.1(3)	C34-C33-C32	119.4(2)
F9-C34-C33	119.9(2)	F9-C34-C35	120.0(3)
C33-C34-C35	120.0(2)	F10-C35-C34	118.0(2)
F10-C35-C36	119.5(2)	C34-C35-C36	122.5(2)
C31-C36-C35	115.8(2)	C31-C36-C17	120.3(2)
C35-C36-C17	123.8(2)	N5-C37-C38	123.0(3)
N5-C37-H37	118.5	C38-C37-H37	118.5
C39-C38-C37	119.1(3)	C39-C38-H38	120.5
C37-C38-H38	120.5	C38-C39-C40	118.6(3)
C38-C39-H39	120.7	C40-C39-H39	120.7
C39-C40-C41	119.1(3)	C39-C40-H40	120.4
C41-C40-H40	120.4	N5-C41-C40	122.6(3)
N5-C41-H41	118.7	C40-C41-H41	118.7

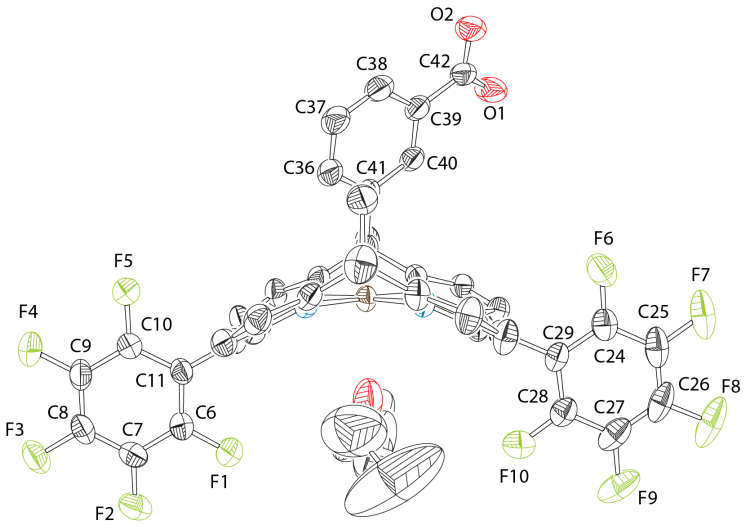

Figure B.9: Partially numbered crystal structure of Co(C4P*HM*^{COOH}) with all hydrogen atoms omitted for clarity and thermal ellipsoids shown at 50% probability.

Table B.17: Bond lengths (Å) determined for Co(C4P*HM*^{COOH})

Bond	Length	Bond	Length
Co-N4	1.921(2)	Co-N1	1.919(3)
Co-N3	1.930(3)	Co-N2	1.932(3)
Co-O3	2.449(4)	N1-C1	1.343(4)
N1-C4	1.397(4)	N2-C15	1.342(4)
N2-C12	1.404(4)	N3-C19	1.339(4)
N3-C22	1.394(4)	N4-C33	1.337(4)
N4-C30	1.396(4)	O1-C42	1.258(5)
O2-C42	1.275(5)	O2-H2A	0.84
F1-C6	1.332(4)	F2-C7	1.336(4)
F3-C8	1.336(4)	F4-C9	1.345(4)
F5-C10	1.341(4)	F6-C24	1.332(5)
F7-C25	1.346(5)	F8-C26	1.339(4)
F9-C27	1.336(5)	F10-C28	1.344(4)
C1-C2	1.409(5)	C1-C34	1.511(4)
C2-C3	1.371(5)	C2-H2	0.95
C3-C4	1.416(5)	C3-H3	0.95
C4-C5	1.398(5)	C5-C12	1.380(5)
C5-C11	1.497(4)	C6-C7	1.380(5)
C6-C11	1.386(5)	C7-C8	1.369(5)

C8-C9	1.369(5)	C9-C10	1.376(5)
C10-C11	1.385(5)	C12-C13	1.423(5)
C13-C14	1.357(5)	C13-H13	0.95
C14-C15	1.421(5)	C14-H14	0.95
C15-C16	1.509(5)	C16-C19	1.508(5)
C16-C18	1.532(5)	C16-C17	1.548(5)
C17-H17A	0.98	C17-H17B	0.98
C17-H17C	0.98	C18-H18A	0.98
C18-H18B	0.98	C18-H18C	0.98
C19-C20	1.426(5)	C20-C21	1.374(5)
C20-H20	0.95	C21-C22	1.407(5)
C21-H21	0.95	C22-C23	1.387(5)
C23-C30	1.388(5)	C23-C29	1.502(4)
C24-C29	1.378(5)	C24-C25	1.392(5)
C25-C26	1.371(7)	C26-C27	1.357(6)
C27-C28	1.383(5)	C28-C29	1.381(5)
C30-C31	1.420(4)	C31-C32	1.372(5)
C31-H31	0.95	C32-C33	1.422(4)
C32-H32	0.95	C33-C34	1.520(4)
C34-C41	1.539(5)	C34-C35	1.531(5)
C35-H35A	0.98	C35-H35B	0.98
C35-H35C	0.98	C36-C41	1.391(4)
C36-C37	1.400(6)	C36-H36	0.95
C37-C38	1.353(5)	C37-H37	0.95
C38-C39	1.387(5)	C38-H38	0.95
C39-C40	1.391(5)	C39-C42	1.482(5)
C40-C41	1.392(5)	C40-H40	0.95
O3-C43	1.424(2)	O3-C45	1.429(2)
C43-C44	1.510(2)	C43-H43A	0.99
C43-H43B	0.99	C44-H44A	0.98
C44-H44B	0.98	C44-H44C	0.98
C45-C46	1.507(2)	C45-H45A	0.99
C45-H45B	0.99	C46-H46A	0.98
C46-H46B	0.98	C46-H46C	0.98

Table B.18: Bond angles (°) determined for Co(C4P*HM*^{COOH})

Bond	Angle	Bond	Angle
N4-Co-N1	89.33(11)	N4-Co-N3	90.57(11)
N1-Co-N3	178.84(12)	N4-Co-N2	179.61(11)
N1-Co-N2	90.28(11)	N3-Co-N2	89.82(11)
N4-Co-O3	90.91(11)	N1-Co-O3	89.86(12)
N3-Co-O3	88.98(12)	N2-Co-O3	89.06(12)
C1-N1-C4	106.2(3)	C1-N1-Co	128.3(2)
C4-N1-Co	124.5(2)	C15-N2-C12	106.3(3)
C15-N2-Co	127.7(2)	C12-N2-Co	124.2(2)
C19-N3-C22	106.7(3)	C19-N3-Co	127.5(2)
C22-N3-Co	124.6(2)	C33-N4-C30	106.0(2)
C33-N4-Co	128.5(2)	C30-N4-Co	124.9(2)
C42-O2-H2A	109.5	N1-C1-C2	111.2(3)
N1-C1-C34	120.7(3)	C2-C1-C34	128.1(3)
C3-C2-C1	106.6(3)	C3-C2-H2	126.7
C1-C2-H2	126.7	C2-C3-C4	107.2(3)
C2-C3-H3	126.4	C4-C3-H3	126.4
C5-C4-N1	122.8(3)	C5-C4-C3	127.9(3)
N1-C4-C3	108.8(3)	C4-C5-C12	125.2(3)
C4-C5-C11	116.8(3)	C12-C5-C11	118.0(3)
F1-C6-C7	118.3(3)	F1-C6-C11	119.5(3)
C7-C6-C11	122.2(3)	F2-C7-C8	119.9(3)
F2-C7-C6	120.7(3)	C8-C7-C6	119.4(3)
F3-C8-C7	119.5(3)	F3-C8-C9	120.5(3)
C7-C8-C9	120.0(3)	F4-C9-C10	120.2(3)
F4-C9-C8	119.7(3)	C10-C9-C8	120.1(3)
F5-C10-C9	118.7(3)	F5-C10-C11	119.6(3)
C9-C10-C11	121.7(3)	C6-C11-C10	116.7(3)
C6-C11-C5	120.6(3)	C10-C11-C5	122.7(3)
C5-C12-N2	122.6(3)	C5-C12-C13	128.6(3)
N2-C12-C13	108.6(3)	C14-C13-C12	107.3(3)
C14-C13-H13	126.4	C12-C13-H13	126.4
C13-C14-C15	107.1(3)	C13-C14-H14	126.5
C15-C14-H14	126.5	N2-C15-C14	110.7(3)
N2-C15-C16	120.7(3)	C14-C15-C16	128.6(3)
C19-C16-C15	108.0(3)	C19-C16-C18	111.5(3)
C15-C16-C18	111.1(3)	C19-C16-C17	108.4(3)
C15-C16-C17	108.9(3)	C18-C16-C17	108.9(3)
C16-C17-H17A	109.5	C16-C17-H17B	109.5
H17A-C17-H17B	109.5	C16-C17-H17C	109.5
H17A-C17-H17C	109.5	H17B-C17-H17C	109.5

C16-C18-H18A	109.5	C16-C18-H18B	109.5
H18A-C18-H18B	109.5	C16-C18-H18C	109.5
H18A-C18-H18C	109.5	H18B-C18-H18C	109.5
N3-C19-C20	110.8(3)	N3-C19-C16	121.2(3)
C20-C19-C16	127.9(3)	C21-C20-C19	105.9(3)
C21-C20-H20	127.1	C19-C20-H20	127.1
C20-C21-C22	107.7(3)	C20-C21-H21	126.2
C22-C21-H21	126.2	N3-C22-C23	122.3(3)
N3-C22-C21	108.9(3)	C23-C22-C21	128.3(3)
C30-C23-C22	125.5(3)	C30-C23-C29	115.3(3)
C22-C23-C29	119.1(3)	F6-C24-C29	120.5(3)
F6-C24-C25	118.7(4)	C29-C24-C25	120.8(4)
C26-C25-F7	120.5(4)	C26-C25-C24	120.1(4)
F7-C25-C24	119.4(4)	C25-C26-F8	118.6(4)
C25-C26-C27	120.4(3)	F8-C26-C27	121.1(5)
F9-C27-C26	120.2(4)	F9-C27-C28	120.8(4)
C26-C27-C28	119.0(4)	F10-C28-C29	119.8(3)
F10-C28-C27	117.6(4)	C29-C28-C27	122.6(4)
C24-C29-C28	117.1(3)	C24-C29-C23	121.6(3)
C28-C29-C23	121.2(3)	C23-C30-N4	123.1(3)
C23-C30-C31	127.4(3)	N4-C30-C31	109.1(3)
C32-C31-C30	107.2(3)	C32-C31-H31	126.4
C30-C31-H31	126.4	C31-C32-C33	105.9(3)
C31-C32-H32	127.0	C33-C32-H32	127.0
N4-C33-C32	111.7(3)	N4-C33-C34	120.6(3)
C32-C33-C34	127.5(3)	C1-C34-C33	108.3(3)
C1-C34-C41	112.1(3)	C33-C34-C41	105.7(3)
C1-C34-C35	110.0(3)	C33-C34-C35	110.6(3)
C41-C34-C35	110.0(3)	C34-C35-H35A	109.5
C34-C35-H35B	109.5	H35A-C35-H35B	109.5
C34-C35-H35C	109.5	H35A-C35-H35C	109.5
H35B-C35-H35C	109.5	C41-C36-C37	120.4(3)
C41-C36-H36	119.8	C37-C36-H36	119.8
C38-C37-C36	120.8(4)	C38-C37-H37	119.6
C36-C37-H37	119.6	C37-C38-C39	119.8(4)
C37-C38-H38	120.1	C39-C38-H38	120.1
C40-C39-C38	120.2(3)	C40-C39-C42	118.9(3)
C38-C39-C42	120.8(4)	C39-C40-C41	120.5(3)
C39-C40-H40	119.8	C41-C40-H40	119.8
C36-C41-C40	118.3(3)	C36-C41-C34	123.0(3)
C40-C41-C34	118.7(3)	O2-C42-O1	123.6(3)
O2-C42-C39	116.8(3)	O1-C42-C39	119.5(4)
C43-O3-C45	99.5(6)	C43-O3-Co	147.0(5)

C45-O3-Co	113.4(5)	O3-C43-C44	108.2(7)
O3-C43-H43A	110.1	C44-C43-H43A	110.1
O3-C43-H43B	110.1	C44-C43-H43B	110.1
H43A-C43-H43B	108.4	C43-C44-H44A	109.5
C43-C44-H44B	109.5	H44A-C44-H44B	109.5
C43-C44-H44C	109.5	H44A-C44-H44C	109.5
H44B-C44-H44C	109.5	O3-C45-C46	115.1(6)
O3-C45-H45A	108.5	C46-C45-H45A	108.5
O3-C45-H45B	108.5	C46-C45-H45B	108.5
H45A-C45-H45B	107.5	C45-C46-H46A	109.5
C45-C46-H46B	109.5	H46A-C46-H46B	109.5
C45-C46-H46C	109.5	H46A-C46-H46C	109.5
H46B-C46-H46C	109.5		

Appendix C

NMR SPECTRA

* Asterisks note adventitious solvent

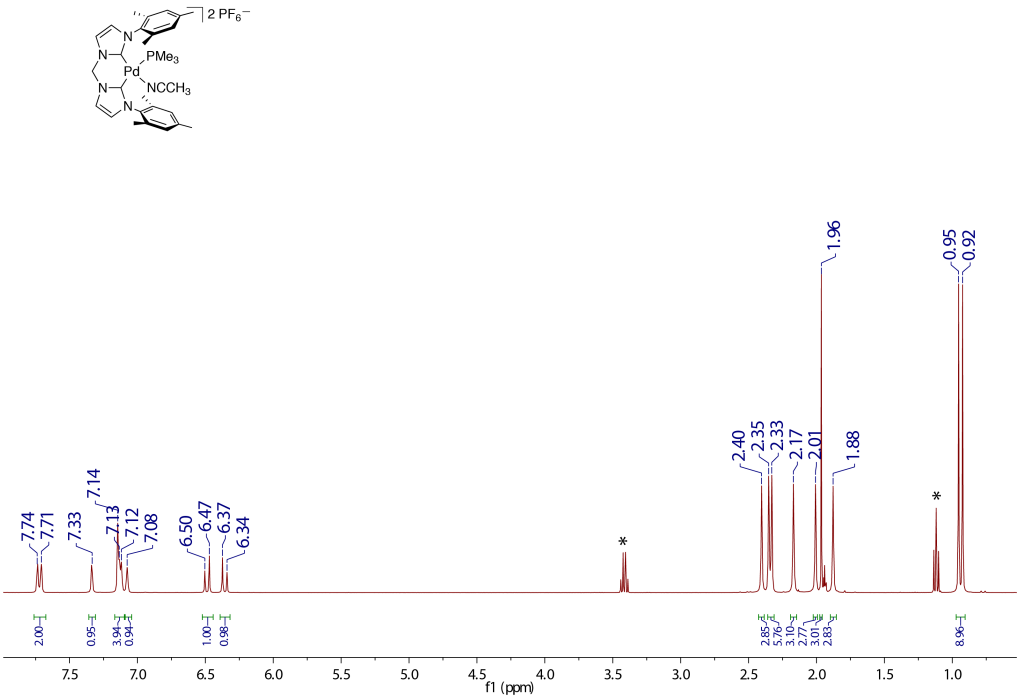

Figure C.1: ^{1}H-NMR spectrum for [(MDC^{Mes})Pd(CH_3CN)(PMe_3)](PF_6)$_2$ in CD_3CN

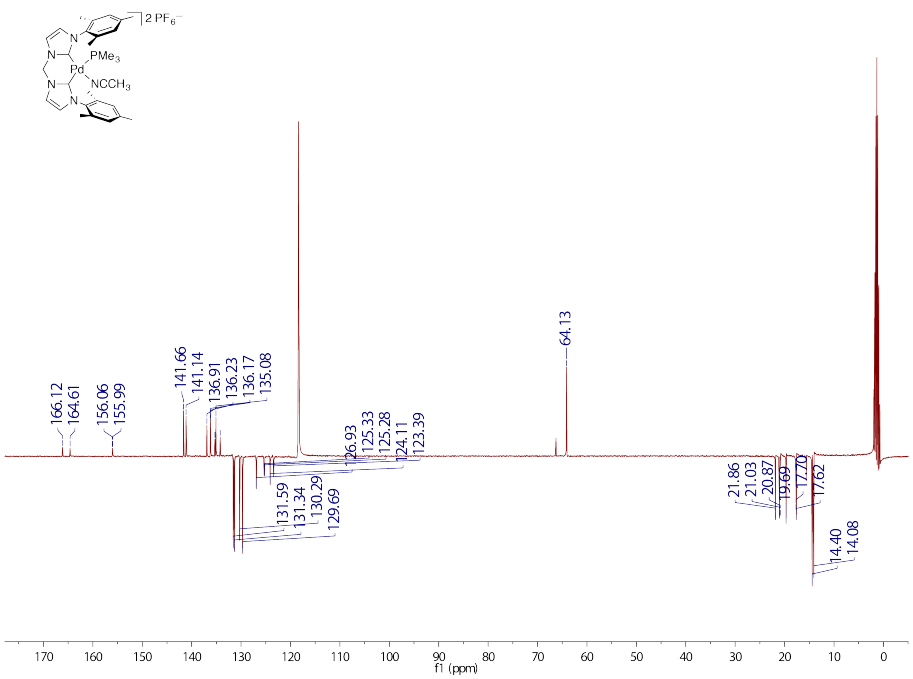

Figure C.2: ^{1}C-NMR spectrum for [(MDC^{Mes})Pd(CH_3CN)(PMe_3)](PF_6)$_2$ in CD_3CN

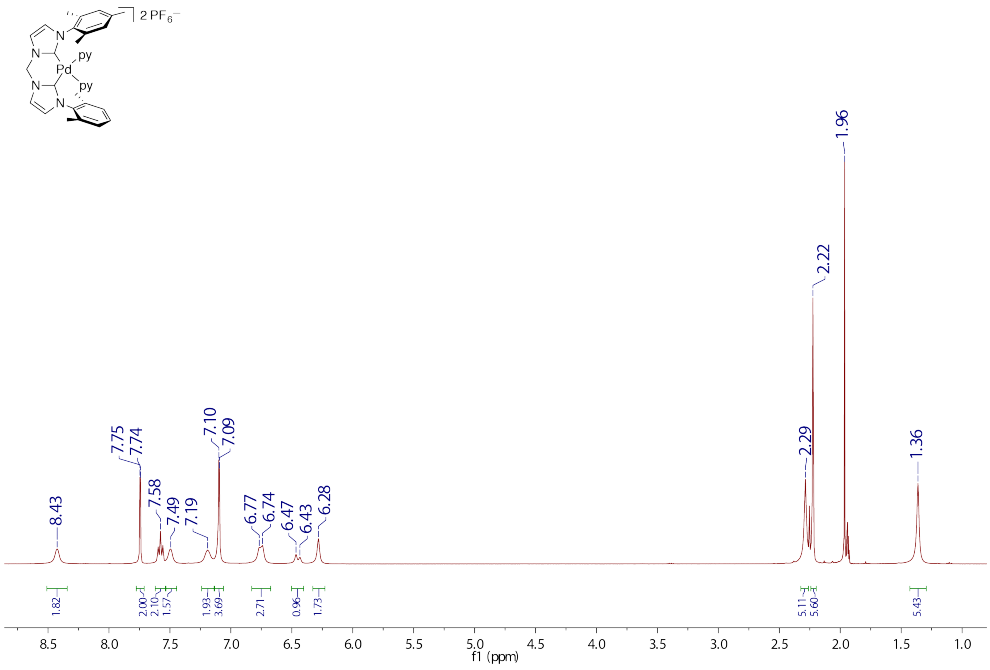

Figure C.3: ^{1}H-NMR spectrum for [(MDC^{Mes})Pd(py)$_2$](PF_6)$_2$ in CD_3CN

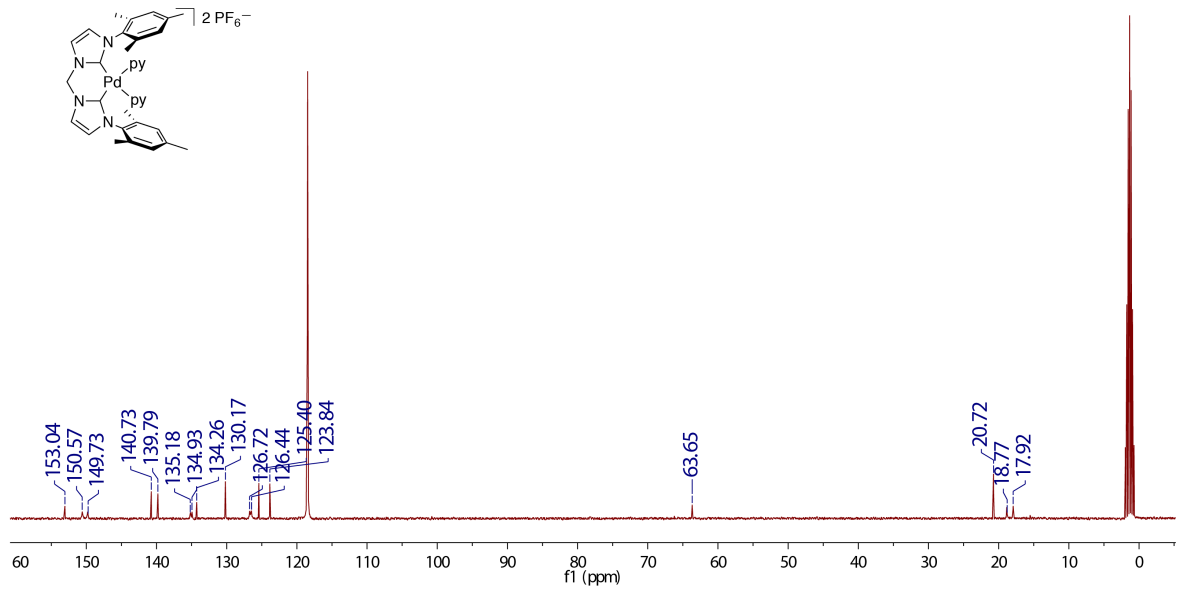

Figure C.4: ^{13}C-NMR spectrum for $[(MDC^{Mes})Pd(py)_2](PF_6)_2$ in CD_3CN

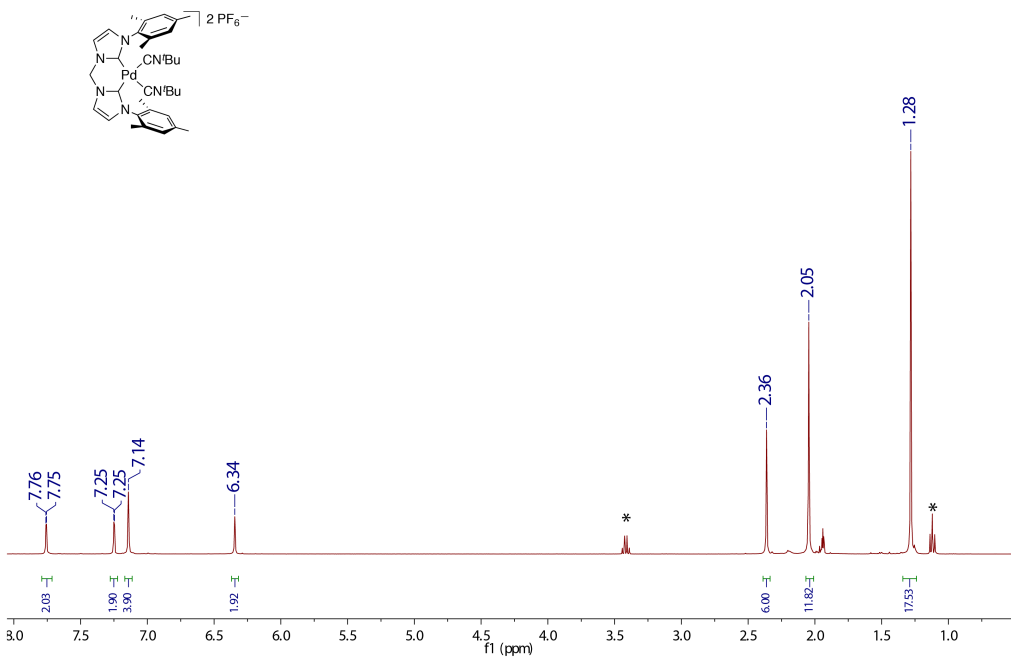

Figure C.5: ^{1}H-NMR spectrum for $[(MDC^{Mes})Pd(tBuNC)_2](PF_6)_2$ in CD_3CN

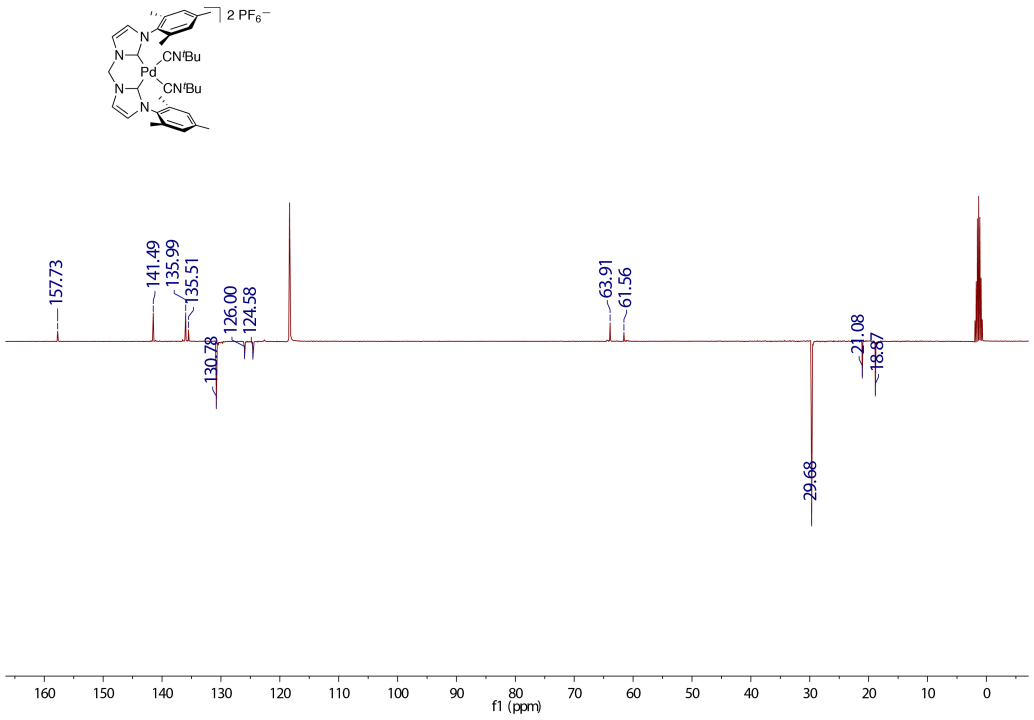

Figure C.6: ^{13}C-NMR spectrum for $[(MDC^{Mes})Pd(tBuNC)_2](PF_6)_2$ in CD_3CN

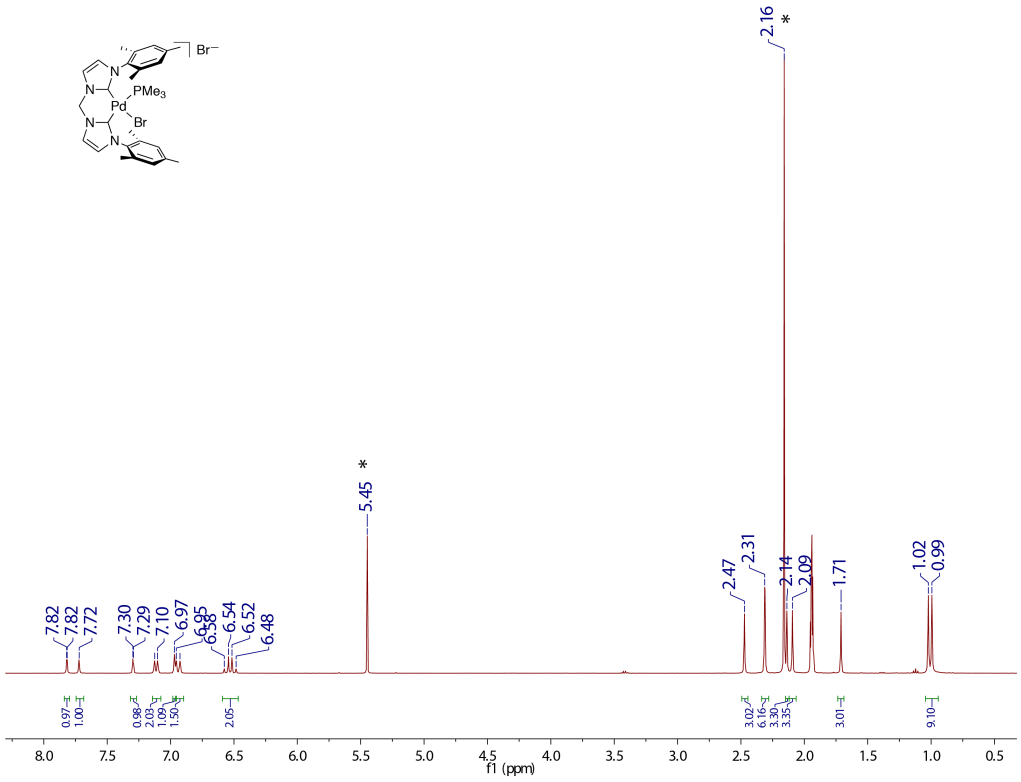

Figure C.7: ^{1}H-NMR spectrum for [(MDC^{mes})PdBr(PMe$_3$)]Br in CD_3CN

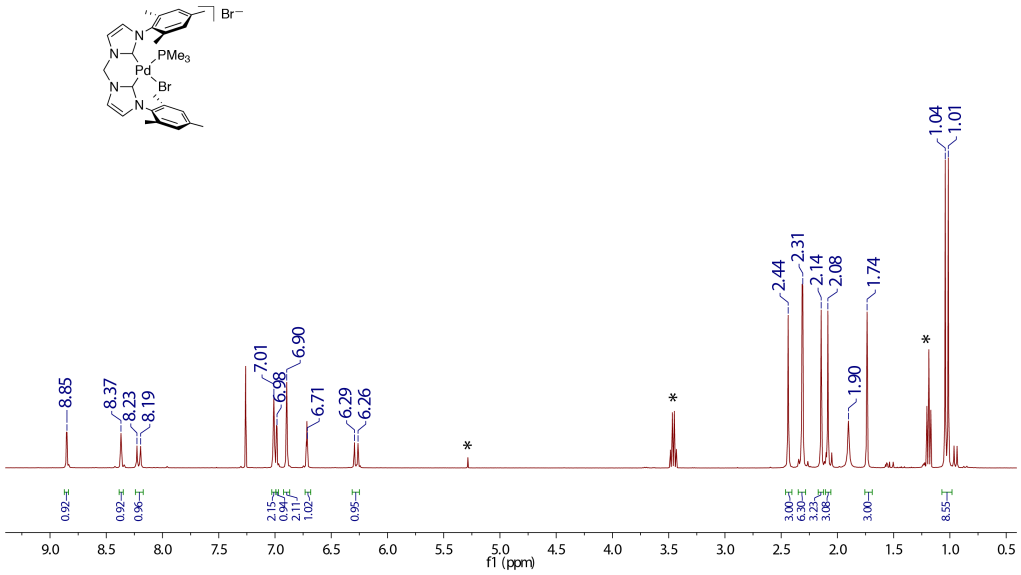

Figure C.8: ^{1}H-NMR spectrum for [(MDC^{mes})PdBr(PMe$_3$)]Br in $CDCl_3$

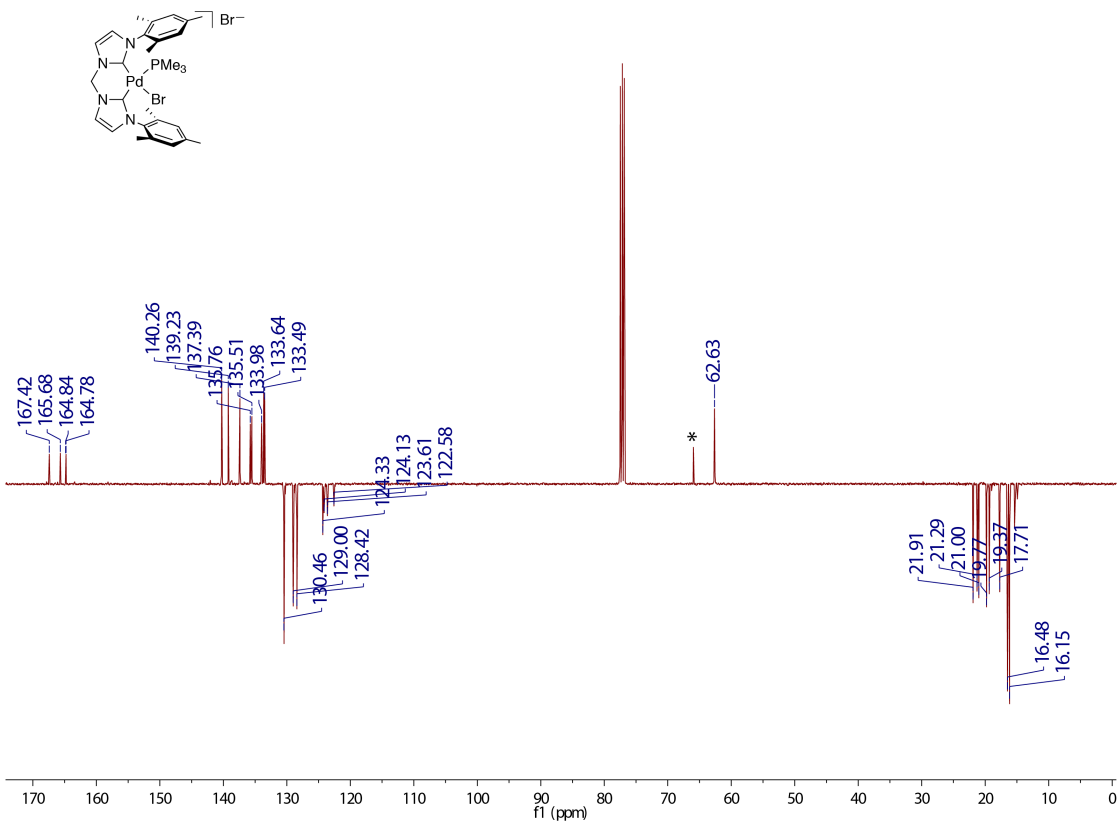

Figure C.9: ^{13}C-NMR spectrum for [(MDC^{mes})PdBr(PMe$_3$)]Br in CDCl$_3$

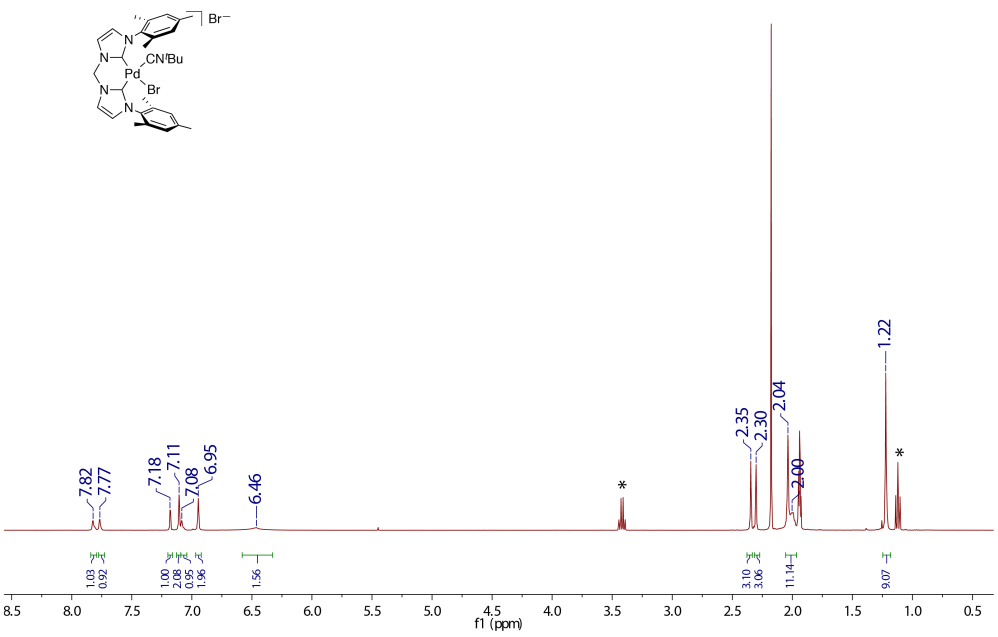

Figure C.10: ^{1}H-NMR spectrum for [(MDC^{mes})PdBr(^{t}BuNC)]Br in CD_3CN

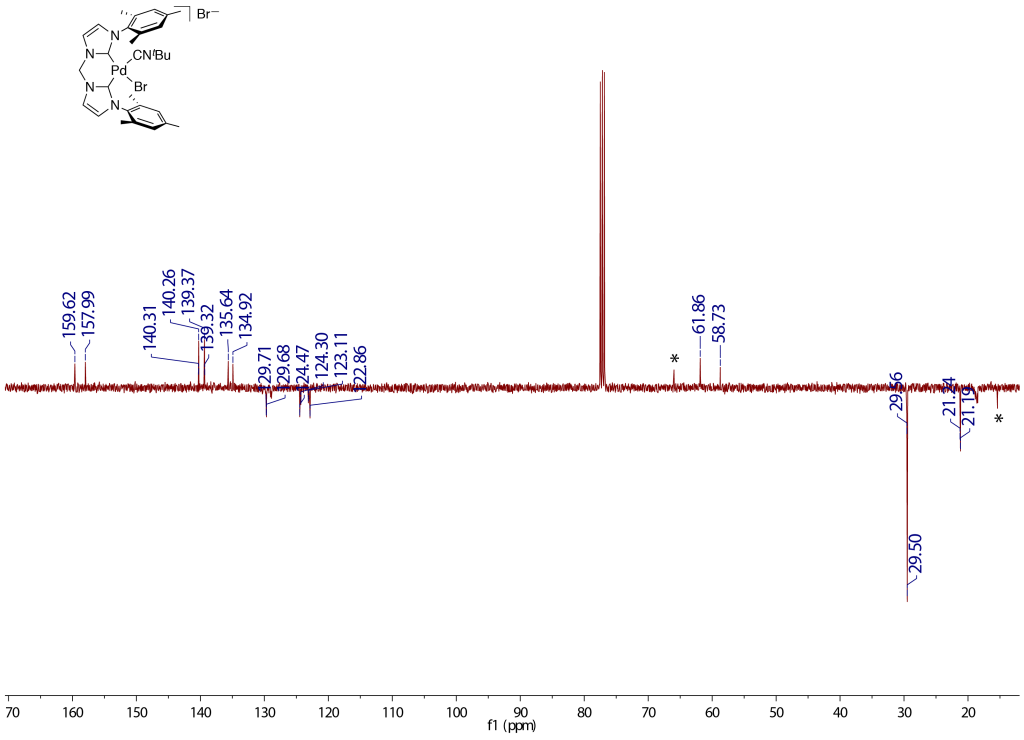

Figure C.11: ^{13}C-NMR spectrum for [(MDC^{mes})PdBr(^{t}BuNC)]Br in $CDCl_3$

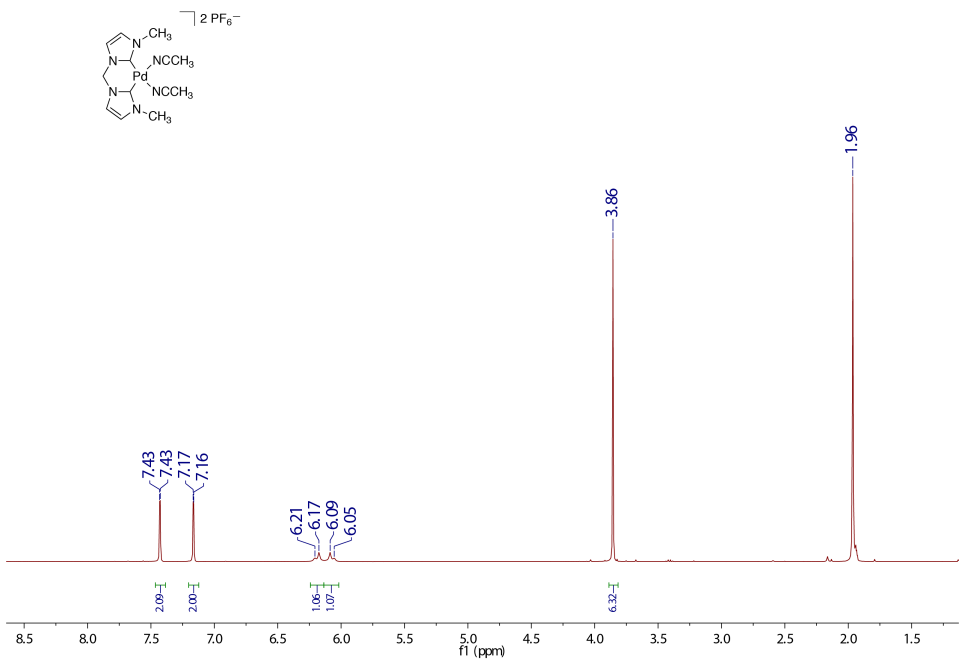

Figure C.12: ^{1}H-NMR spectrum for $[(MDC^{Me})Pd(CH_3CN)_2](PF_6)_2$ in CD_3CN

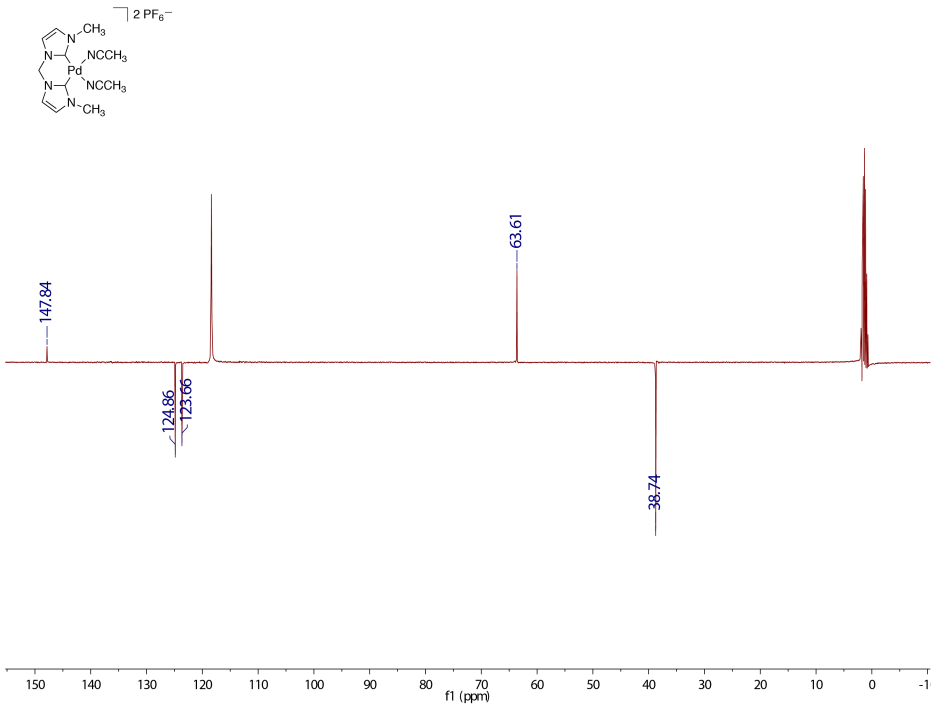

Figure C.13: ^{13}C-NMR spectrum for $[(MDC^{Me})Pd(CH_3CN)_2](PF_6)_2$ in CD_3CN

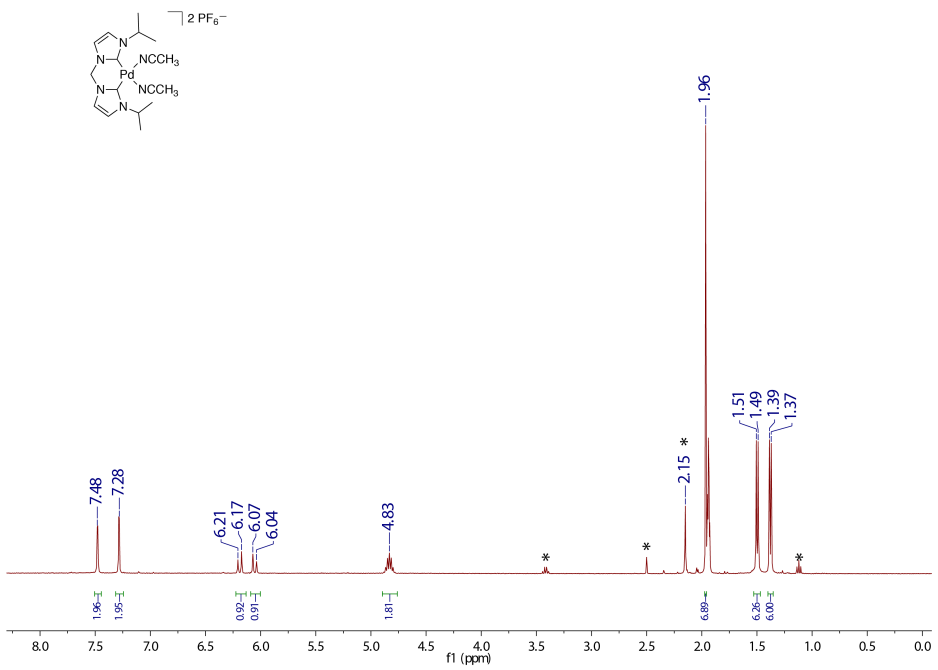

Figure C.14: ^{1}H-NMR spectrum for $[(MDC^{iPr})Pd(CH_3CN)_2](PF_6)_2$ in CD_3CN

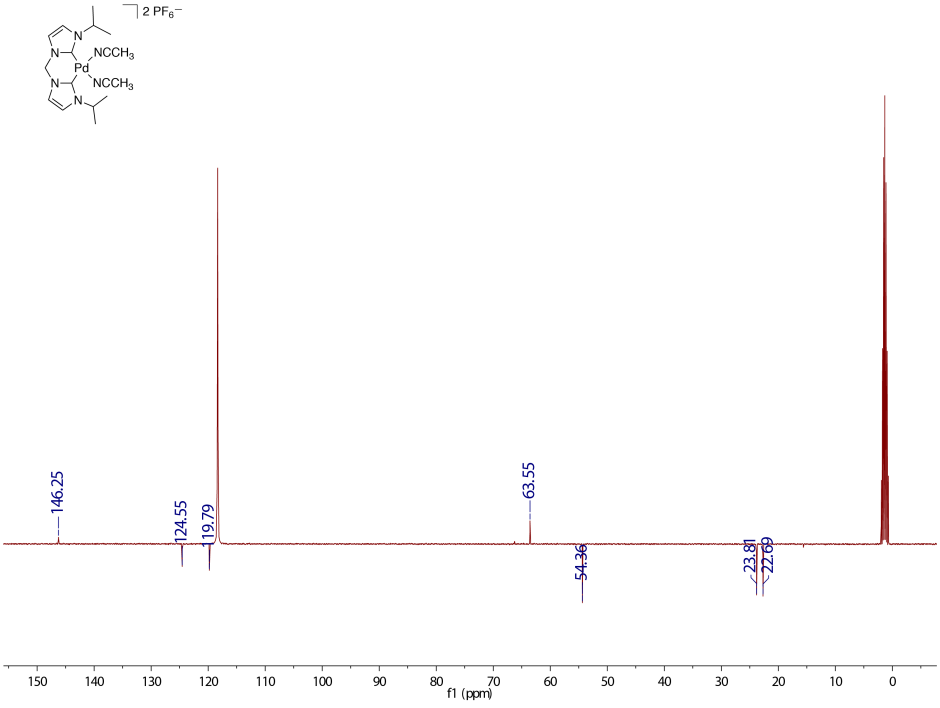

Figure C.15: ^{13}C-NMR spectrum for $[(MDC^{iPr})Pd(CH_3CN)_2](PF_6)_2$ in CD_3CN

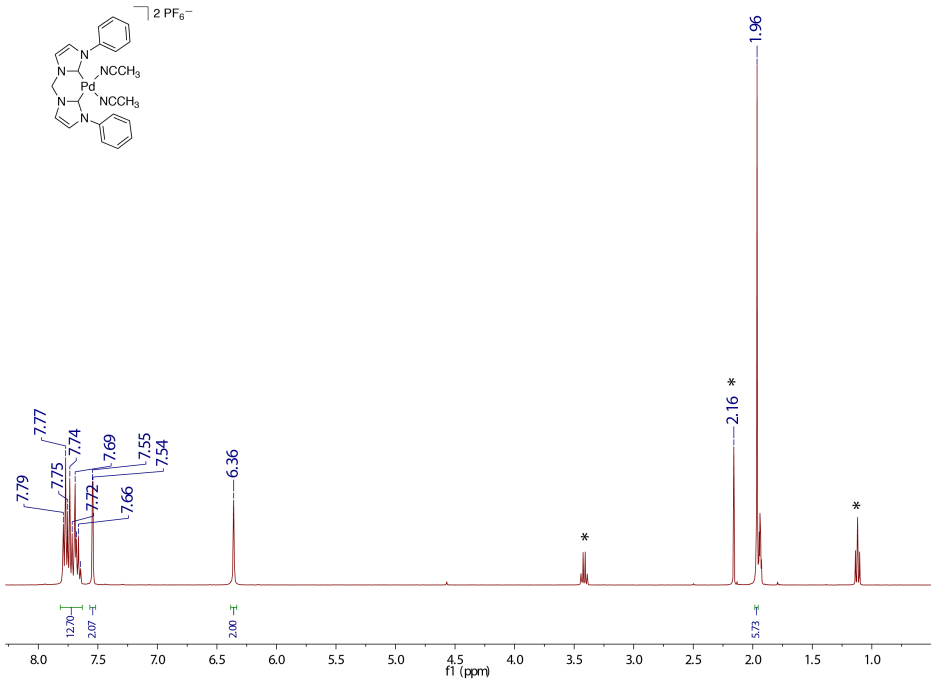

Figure C.16: ^{1}H-NMR spectrum for $[(MDC^{Ph})Pd(CH_3CN)_2](PF_6)_2$ in CD_3CN

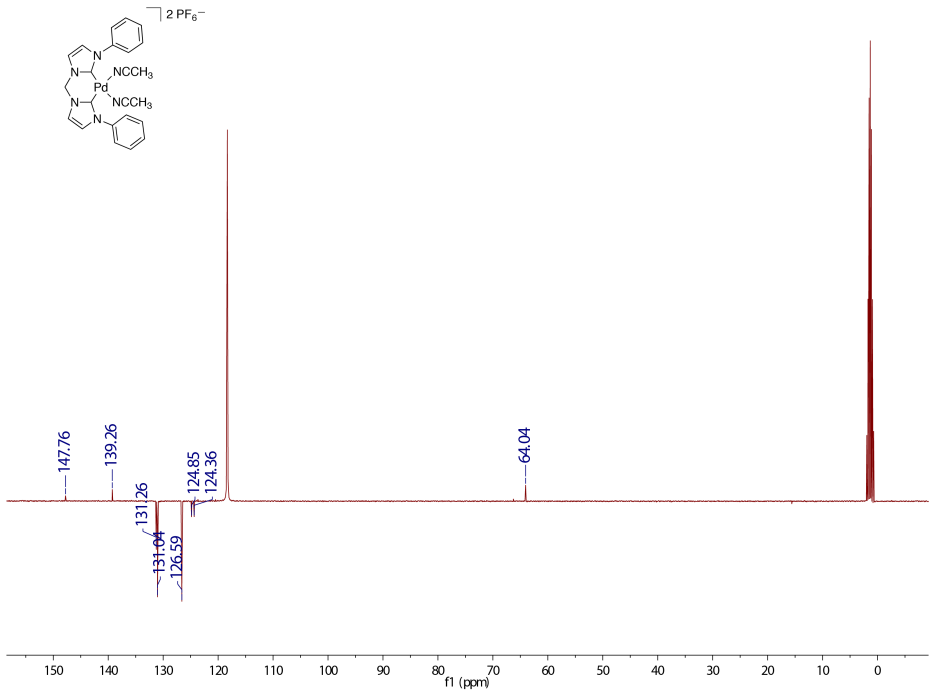

Figure C.17: ^{13}C-NMR spectrum for $[(MDC^{Ph})Pd(CH_3CN)_2](PF_6)_2$ in CD_3CN

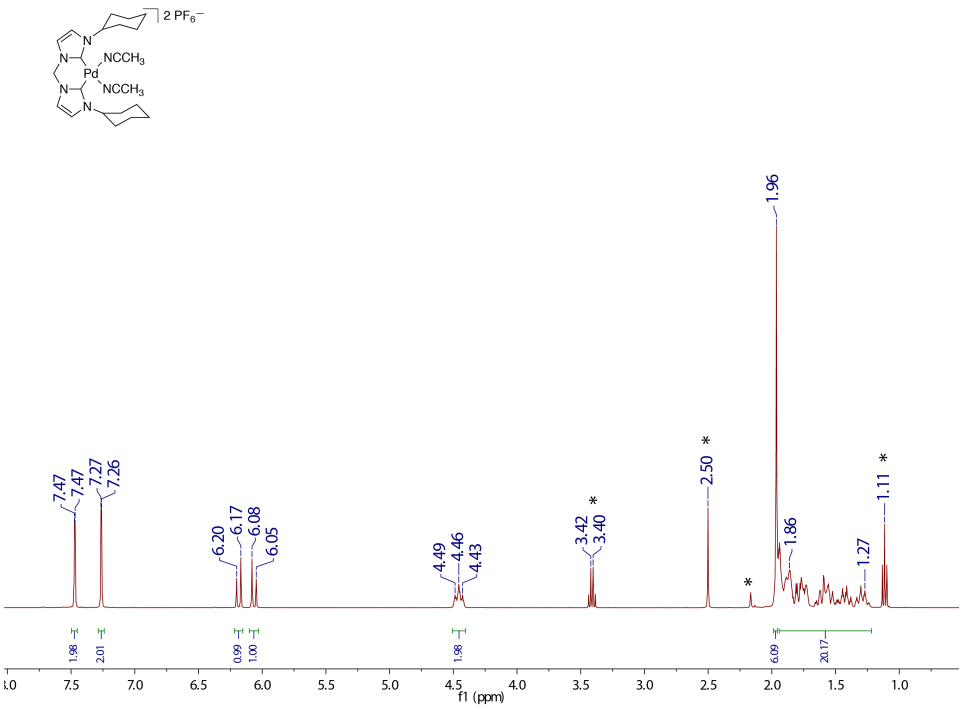

Figure C.18: ^{1}H-NMR spectrum for $[(MDC^{Cy})Pd(CH_3CN)_2](PF_6)_2$ in CD_3CN

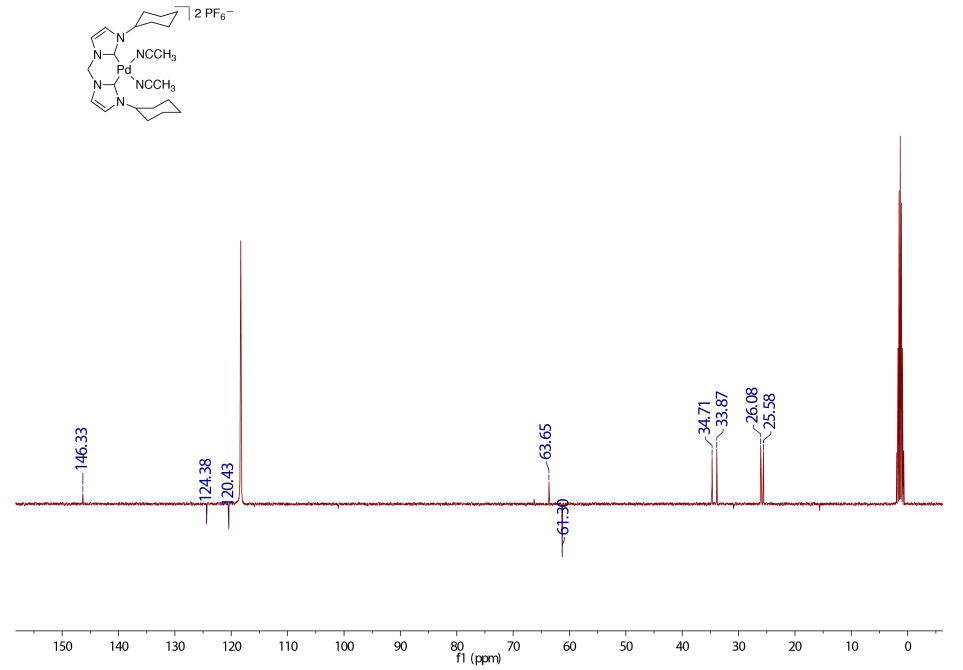

Figure C.19: ^{13}C-NMR spectrum for $[(MDC^{Cy})Pd(CH_3CN)_2](PF_6)_2$ in CD_3CN

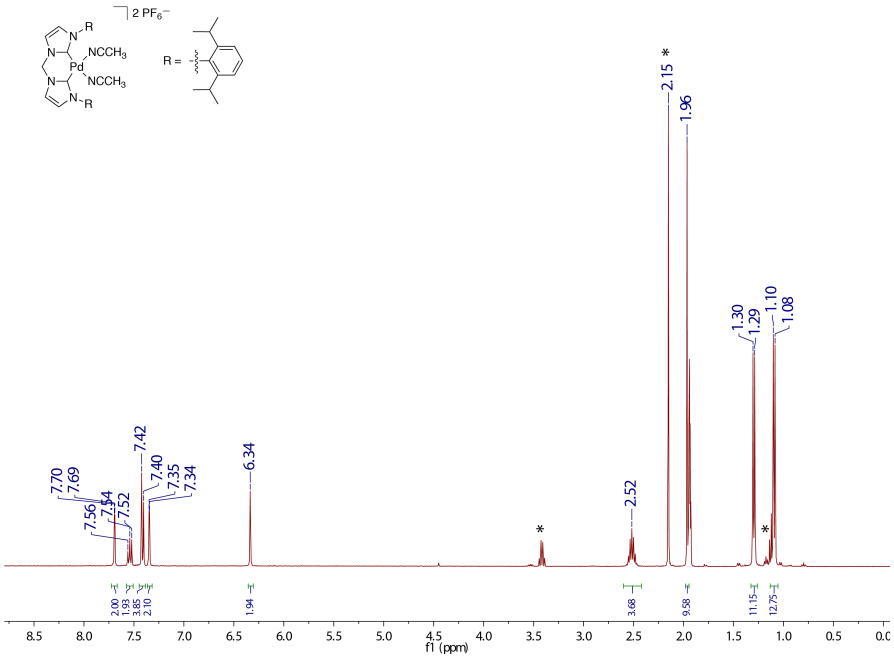

Figure C.20: ^{1}H-NMR spectrum for $[(MDC^{DIPP})Pd(CH_3CN)_2](PF_6)_2$ in CD_3CN

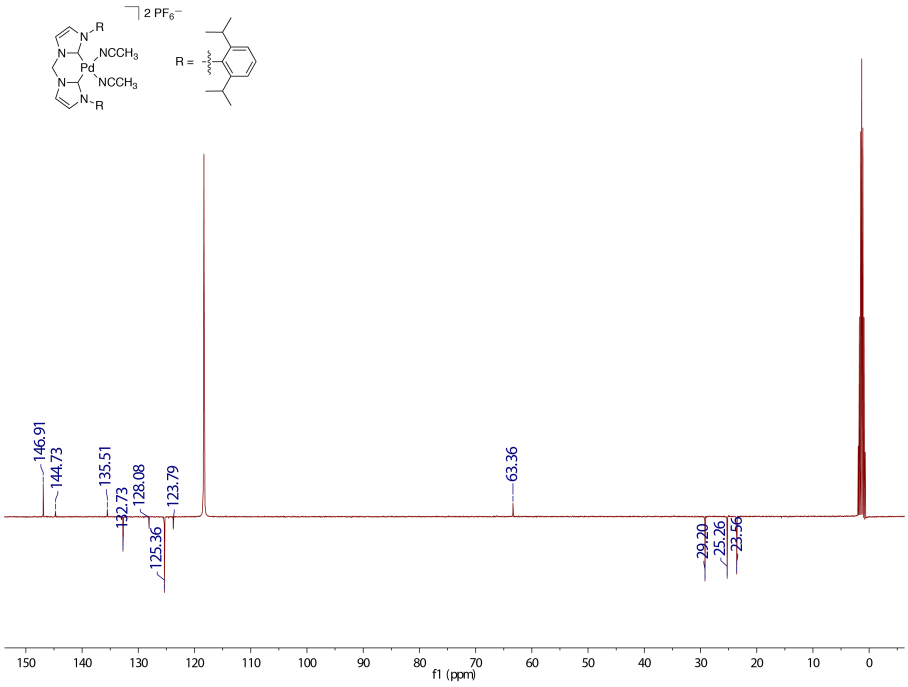

Figure C.21: ^{13}C-NMR spectrum for $[(MDC^{DIPP})Pd(CH_3CN)_2](PF_6)_2$ in CD_3CN

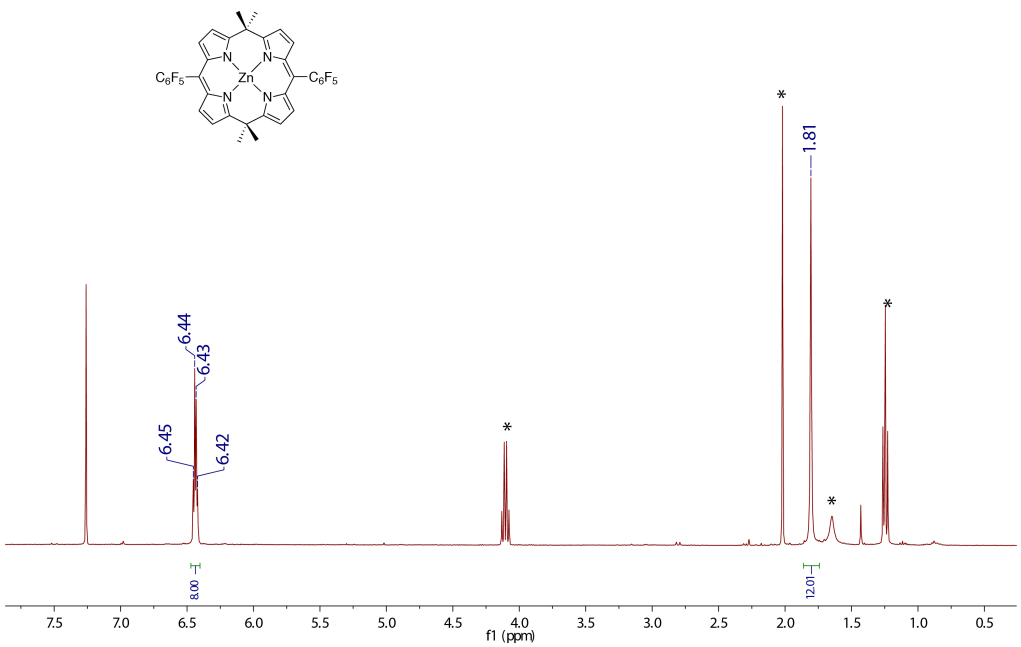

Figure C.22: ^{1}H-NMR spectrum for Zn(C4P^{PF}) in $CDCl_3$

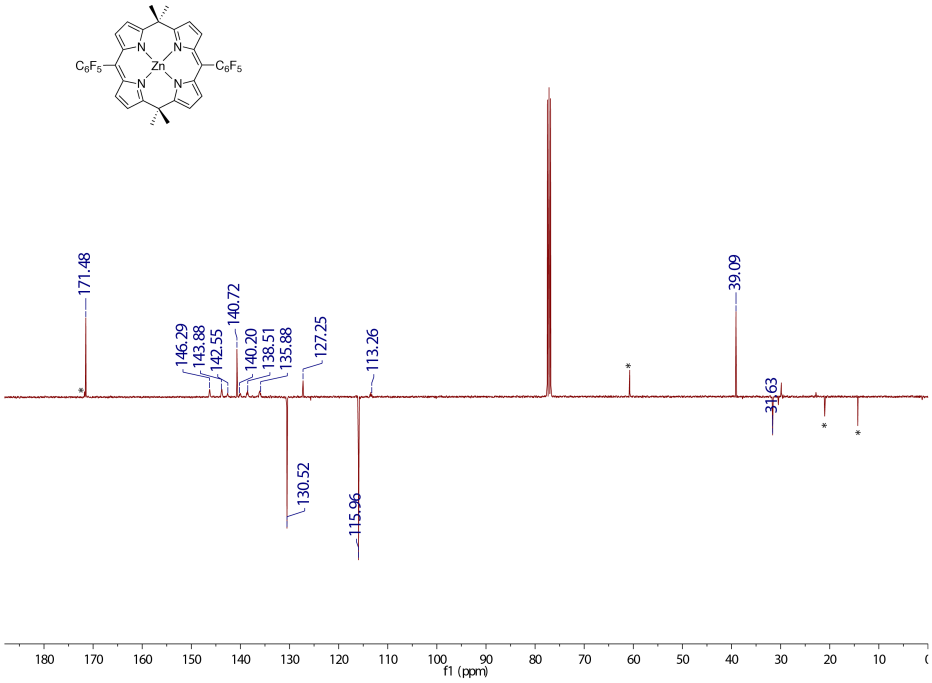

Figure C.23: ^{13}C-NMR spectrum for Zn(C4P^{PF}) in $CDCl_3$

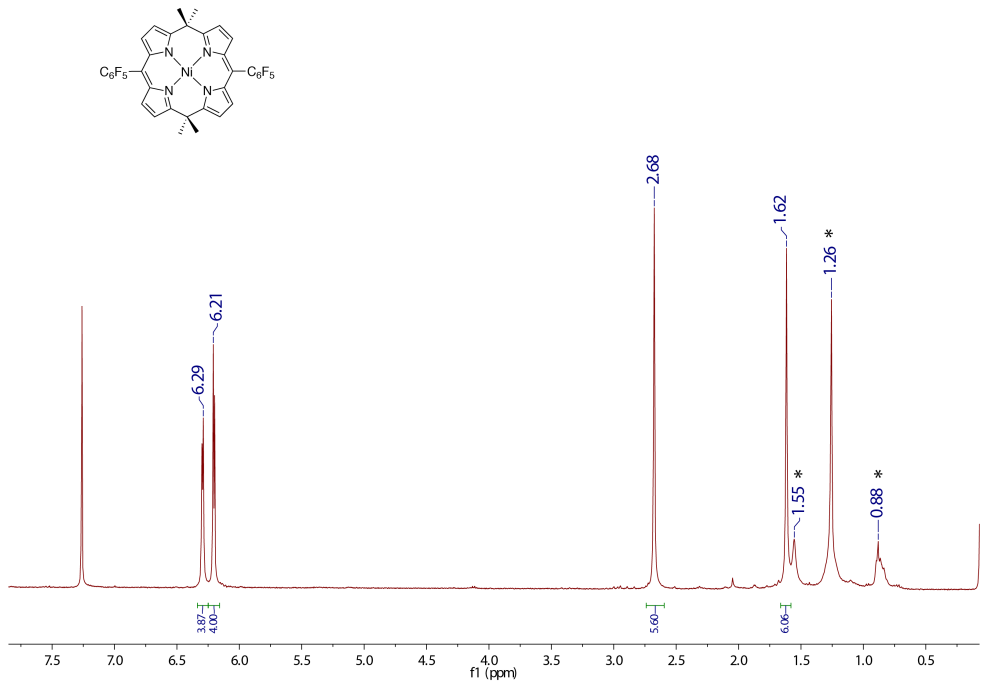

Figure C.24: ^{1}H-NMR spectrum for Ni(C4P^{PF}) in $CDCl_3$

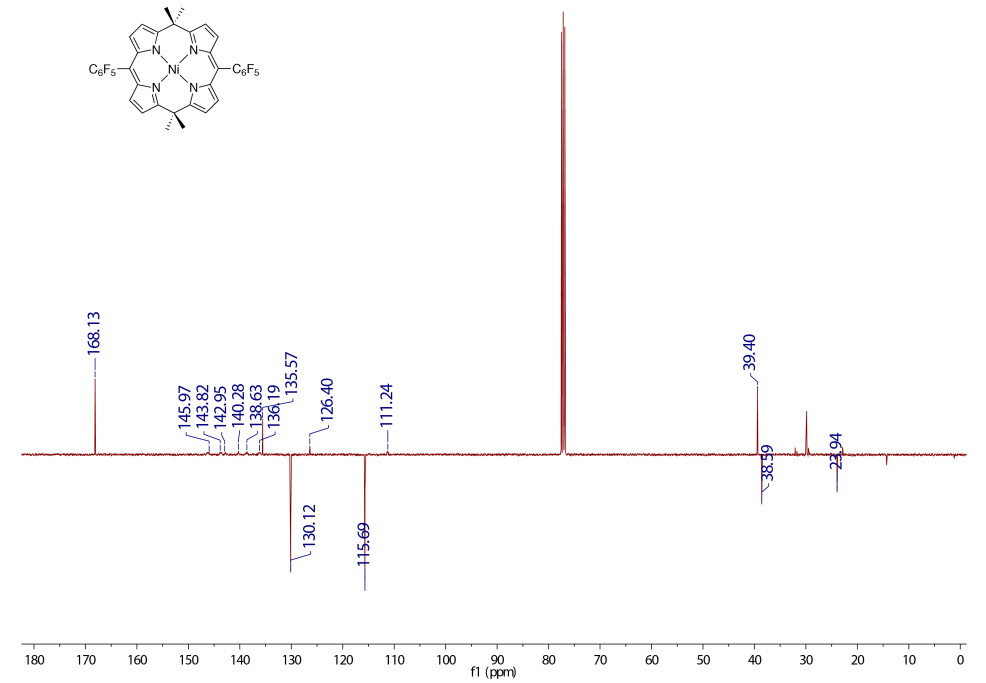

Figure C.25: ^{13}C-NMR spectrum for Ni(C4P^{PF}) in $CDCl_3$

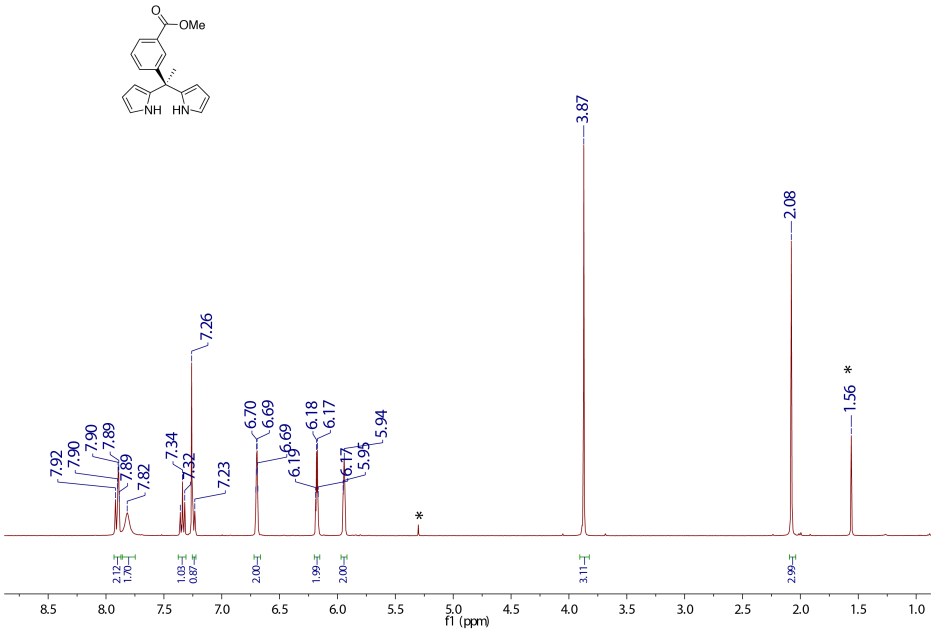

Figure C.26: ^{1}H-NMR spectrum for 5-methyl-5-(3-methylester benzoate) dipyrromethane in $CDCl_3$

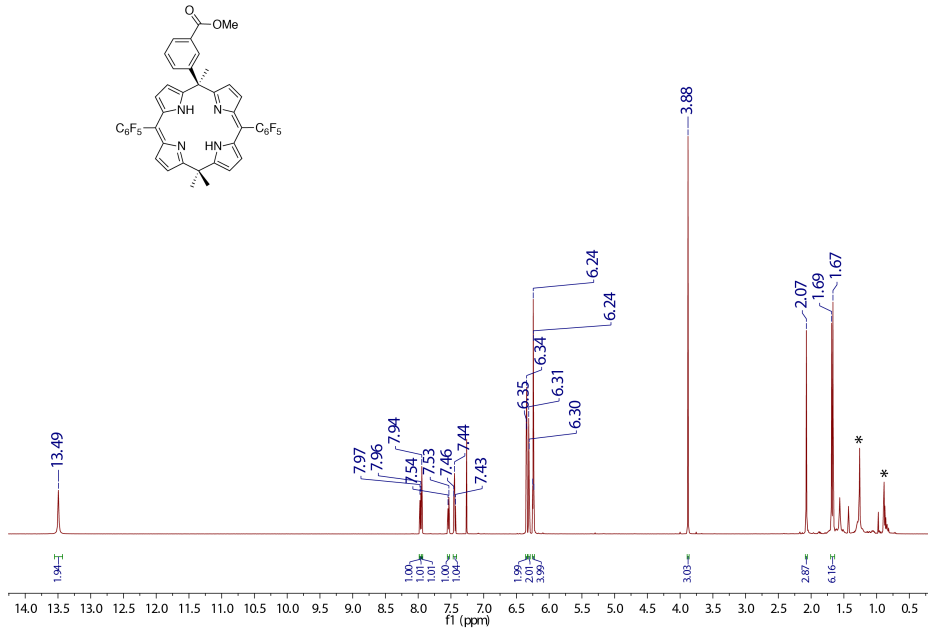

Figure C.27: ^{1}H-NMR spectrum for 5,15,15-trimethyl-5-(3-methylester benzoate)-10,20-bis(pentafluorophenyl)calix[4]phyrin in $CDCl_3$

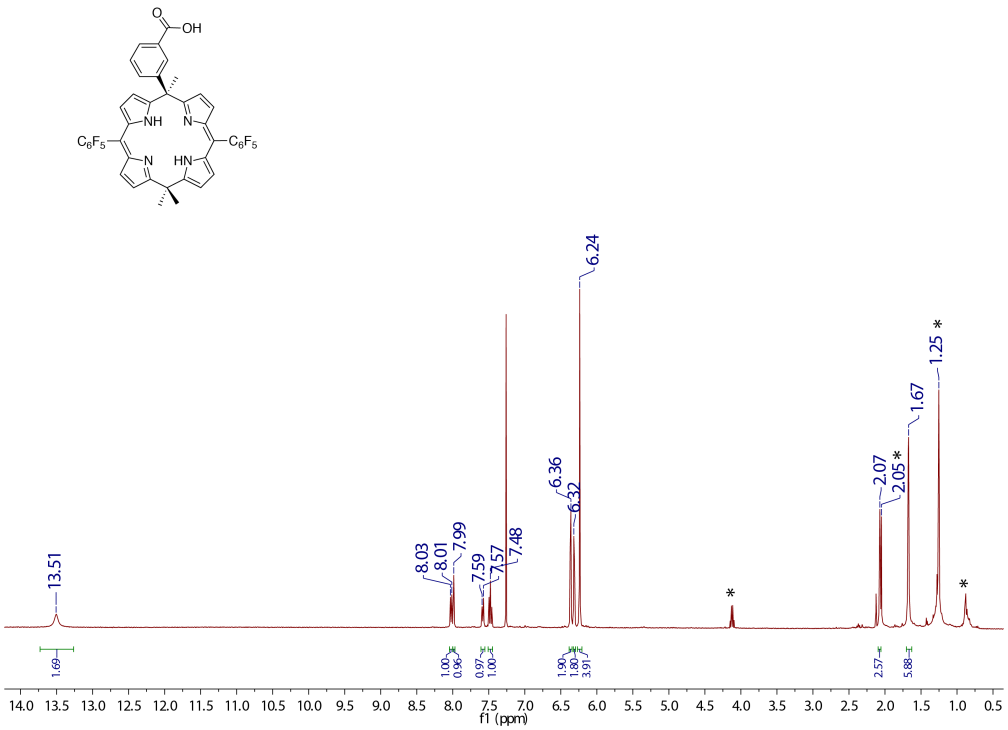

Figure C.28: ^{1}H-NMR spectrum for C4P*HM*^{COOH} in $CDCl_3$

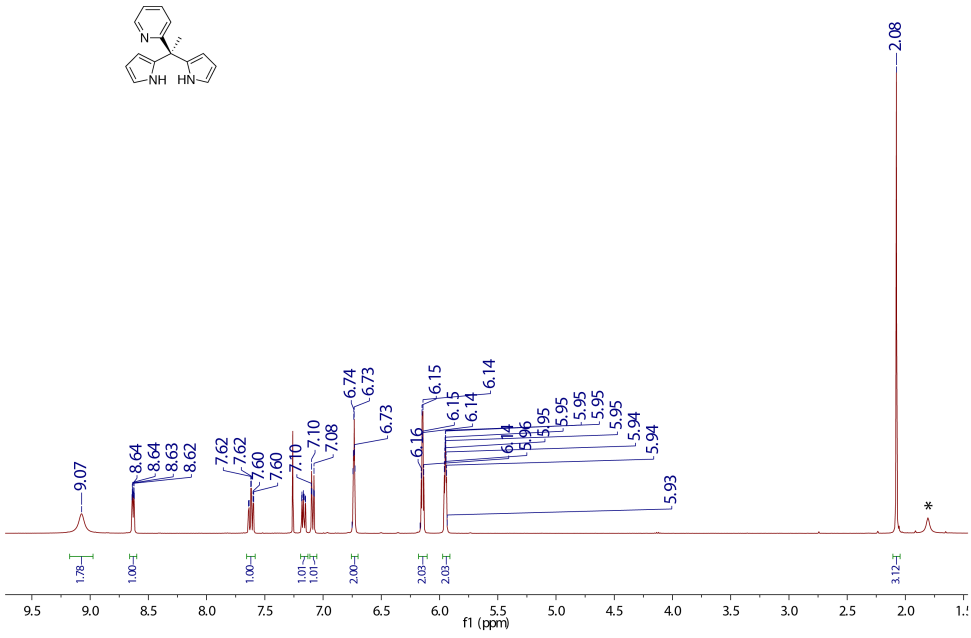

Figure C.29: ^{1}H-NMR spectrum for 5-methyl-5-(2-pyridyl)dipyrromethane in $CDCl_3$

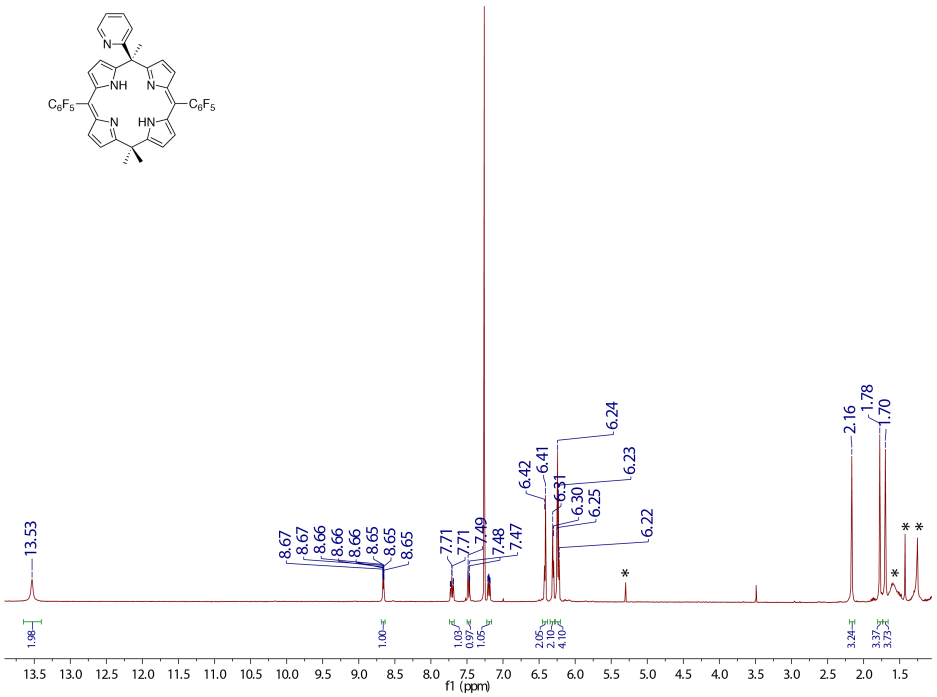

Figure C.30: ^{1}H-NMR spectrum for C4P*HM*^{py} in $CDCl_3$

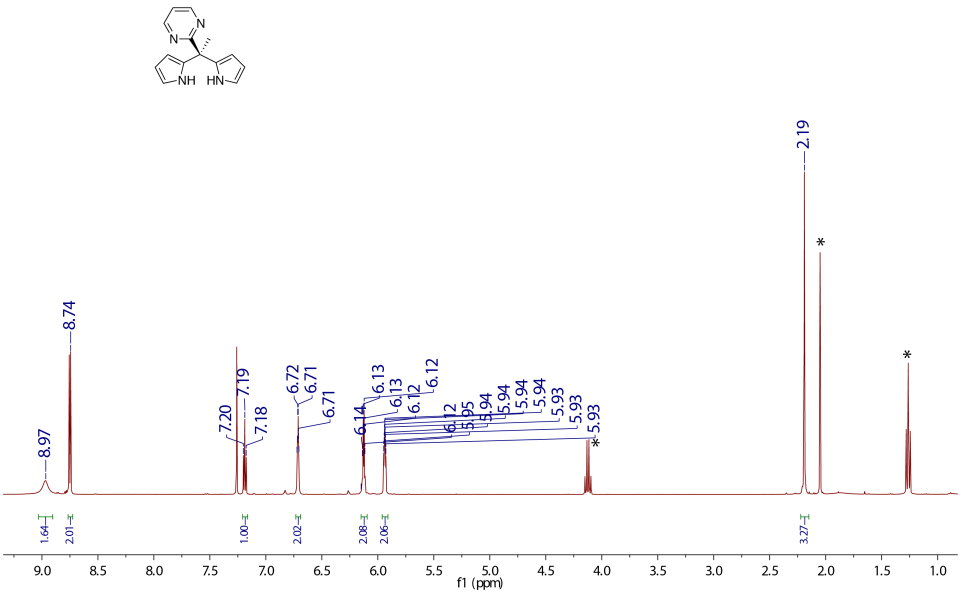

Figure C.31: ^{1}H-NMR spectrum for 5-methyl-5-(2-pyrimidinyl)dipyrromethane in $CDCl_3$

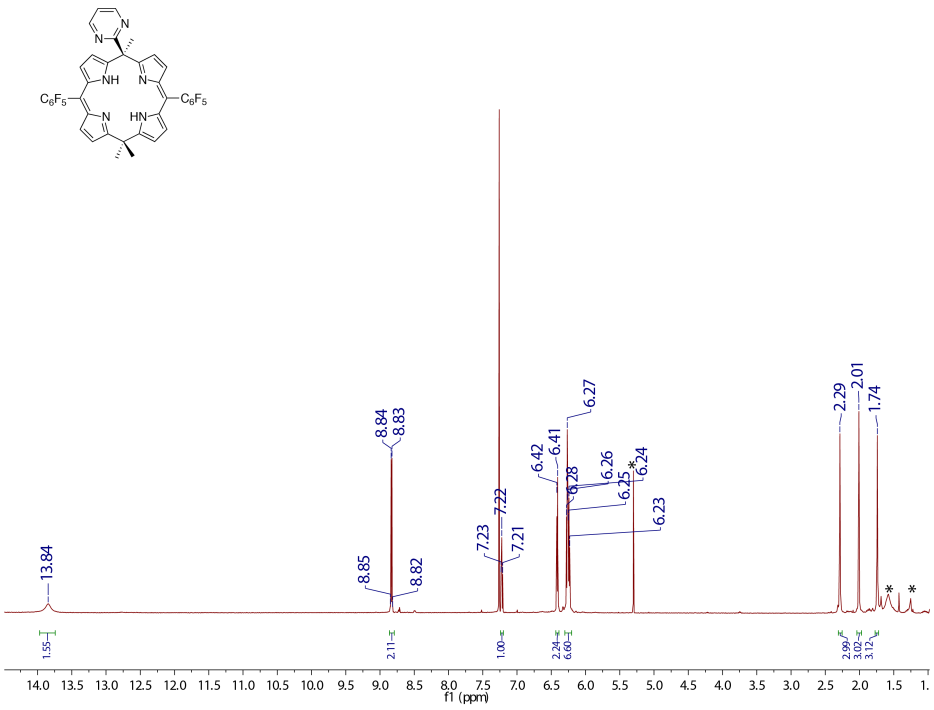

Figure C.32: ^{1}H-NMR spectrum for C4P*HM*^{pyrm} in $CDCl_3$